

# On large-scale wave coupling across the stratopause

Habilitationsschrift zur Erlangung der Venia Legendi

vorgelegt von

Jens Oberheide

Bergische Universität Wuppertal

Fachbereich C – Mathematik und Naturwissenschaften (Physik)

September 2006

Diese Dissertation kann wie folgt zitiert werden:

urn:nbn:de:hbz:468-20070724

[<http://nbn-resolving.de/urn/resolver.pl?urn=urn%3Anbn%3Ade%3Ahbz%3A468-20070724>]

# Contents

<b>1</b>	<b>Introduction</b>	<b>1</b>
<b>2</b>	<b>Troposphere - thermosphere coupling by large-scale waves</b>	<b>4</b>
2.1	Tides . . . . .	5
2.2	Planetary waves . . . . .	9
<b>3</b>	<b>Satellite-borne observations and modeling of the middle atmosphere</b>	<b>13</b>
3.1	Instrument overview . . . . .	13
3.1.1	LIMS . . . . .	13
3.1.2	CRISTA . . . . .	14
3.1.3	SABER . . . . .	15
3.1.4	TIDI . . . . .	16
3.2	Model overview . . . . .	17
3.2.1	GSWM . . . . .	17
3.2.2	TIME-GCM . . . . .	18
3.2.3	Extended CMAM . . . . .	21
3.3	The sampling problem: How to compare models with observations? . .	21
<b>4</b>	<b>Nonmigrating tides</b>	<b>27</b>
4.1	Diurnal temperature tides in the equatorial lower thermosphere from CRISTA . . . . .	27
4.1.1	Data analysis . . . . .	27
4.1.2	Error estimate . . . . .	30
4.1.3	Results and discussion . . . . .	31
4.1.4	What did we learn from CRISTA? . . . . .	40
4.2	Diurnal temperature tides in the stratosphere and mesosphere from LIMS	41
4.2.1	Data analysis . . . . .	42
4.2.2	Evolution of tides and planetary waves . . . . .	43
4.2.3	Implications of the LIMS results . . . . .	49
4.3	Diurnal tidal climatologies from TIDI wind data . . . . .	50
4.3.1	Tidal analysis . . . . .	50
4.3.2	Error analysis . . . . .	53
4.3.3	Monthly climatologies . . . . .	54
4.3.4	Comparison with UARS . . . . .	56

4.3.5	Model/observation comparison . . . . .	59
4.3.6	Some conclusions from the diurnal analyses . . . . .	72
4.4	Semidiurnal tidal climatologies from TIDI wind data . . . . .	73
<b>5</b>	<b>Mesospheric surf zone and inversion layers</b>	<b>80</b>
5.1	November 1994 case study . . . . .	81
5.2	Generalization of the case study results . . . . .	88
<b>6</b>	<b>Comparison of kinetic temperature from 15 <math>\mu\text{m}</math> CO<sub>2</sub> limb emissions and OH*(3,1) rotational temperature in nearly coincident air masses</b>	<b>98</b>
6.1	GRIPS instrument and data . . . . .	98
6.2	Coincidence criteria . . . . .	100
6.3	GRIPS - SABER comparisons . . . . .	101
6.4	Discussion and implications for joint analyses . . . . .	105
<b>7</b>	<b>Summary</b>	<b>107</b>
<b>8</b>	<b>Acknowledgment</b>	<b>110</b>
<b>A</b>	<b>Appendix</b>	<b>111</b>
A1	List of acronyms . . . . .	112
A2	Classical tidal theory . . . . .	113
A3	Tidal component deconvolution . . . . .	118
A4	TIDI climatologies: diurnal . . . . .	123
A5	TIDI climatologies: semidiurnal . . . . .	138
<b>9</b>	<b>References</b>	<b>151</b>

# List of Figures

1.1	Schematic of atmospheric coupling processes . . . . .	2
2.1	Schematic of vertical wave coupling . . . . .	5
2.2	Structure of the migrating tide . . . . .	6
2.3	Rectified eddy forcing due to tides . . . . .	7
2.4	PW propagation mechanism . . . . .	11
3.1	CRISTA local solar time . . . . .	14
3.2	SABER local solar time . . . . .	15
3.3	TIDI local solar time . . . . .	16
3.4	Effect of GW parameterization on the mean zonal wind . . . . .	20
3.5	Satellite sampling versus model representation . . . . .	23
3.6	TIME-GCM sampled along SABER and TIDI footprints . . . . .	24
3.7	Artifacts of incompletely sampled tides . . . . .	25
3.8	Satellite sampled versus full model carbon monoxide . . . . .	26
4.1	Tidal signatures in CRISTA-1 temperatures . . . . .	28
4.2	CRISTA - model comparisons, November . . . . .	33
4.3	CRISTA - model comparisons, August . . . . .	39
4.4	LIMS latitude - altitude plots of wavenumber 1 results . . . . .	42
4.5	LIMS time evolution of monthly mean w2 and s0 amplitudes . . . . .	44
4.6	LIMS/GSWM intercomparison of w2 amplitudes . . . . .	45
4.7	LIMS tidal and QSPW (high latitudes) time evolution . . . . .	46
4.8	LIMS tidal and QSPW (subtropical latitudes) time evolution . . . . .	47
4.9	Correlation between w2 and QSPW-1 from LIMS . . . . .	48
4.10	TIDI meridional winds at 95 km . . . . .	51
4.11	TIDI composite data . . . . .	52
4.12	UARS and TIDI meridional wind amplitudes and phases . . . . .	57
4.13	UARS and TIDI zonal wind amplitudes and phases . . . . .	57
4.14	Diurnal tidal amplitudes from UARS and TIDI: meridional wind . . . . .	58
4.15	Diurnal tidal amplitudes from UARS and TIDI: zonal wind . . . . .	58
4.16	w2 meridional: TIDI versus models at 95 km . . . . .	61
4.17	w2 meridional: TIDI versus models in Jan and Sep . . . . .	61
4.18	s0 meridional: TIDI versus models at 95 km . . . . .	62
4.19	s0 meridional: TIDI versus models in Jan and Sep . . . . .	62

4.20	e2 meridional: TIDI versus models at 95 km . . . . .	63
4.21	e2 meridional: TIDI versus models in Jan and Sep . . . . .	63
4.22	e3 meridional: TIDI versus models at 95 km . . . . .	64
4.23	e3 meridional: TIDI versus models in Jan and Sep . . . . .	64
4.24	w2 zonal: TIDI versus models at 95 km . . . . .	65
4.25	w2 zonal: TIDI versus models in Jan and Sep . . . . .	65
4.26	s0 zonal: TIDI versus models at 95 km . . . . .	66
4.27	s0 zonal: TIDI versus models in Jan and Sep . . . . .	66
4.28	e2 zonal: TIDI versus models at 95 km . . . . .	67
4.29	e2 zonal: TIDI versus models in Jan and Sep . . . . .	67
4.30	e3 zonal: TIDI versus models at 95 km . . . . .	68
4.31	e3 zonal: TIDI versus models in Jan and Sep . . . . .	68
4.32	Time evolution of semidiurnal tidal amplitudes: meridional wind . .	74
4.33	Time evolution of semidiurnal tidal amplitudes: zonal wind . . . . .	76
4.34	UARS and TIDI semidiurnal wind amplitudes: w3 . . . . .	77
4.35	UARS and TIDI semidiurnal wind amplitudes: w1 . . . . .	78
5.1	CRISTA & TIME-GCM dynamics on Nov. 9, 1994 . . . . .	82
5.2	Zonal mean zonal momentum tendency from CRISTA . . . . .	83
5.3	Mesospheric surf zone . . . . .	84
5.4	Mesospheric inversion layers . . . . .	85
5.5	GW net momentum forcing . . . . .	86
5.6	MILs due to PW-1 & PW-2 activity . . . . .	87
5.7	Monthly variation of 2003 MIL heights . . . . .	90
5.8	Monthly variation of 2003 MIL magnitudes . . . . .	91
5.9	Tidal effects on MIL height and amplitude . . . . .	92
5.10	2003 NH TIME-GCM dynamics and MILs . . . . .	94
5.11	MILs during a stratospheric warming event . . . . .	95
5.12	TIME-GCM surf zone . . . . .	97
6.1	GRIPS OH*(3,1) rotational temperatures since 1980 . . . . .	99
6.2	Example of GRIPS/SABER spatial coincidence . . . . .	101
6.3	GRIPS/SABER temperature comparison I . . . . .	103
6.4	GRIPS/SABER temperature comparison II . . . . .	104
A2.1	Hough functions . . . . .	117
A3.1	Principle of deconvolution . . . . .	119

A4.1	TIDI diurnal climatology: w2 meridional . . . . .	124
A4.2	TIDI diurnal climatology: s0 meridional . . . . .	125
A4.3	TIDI diurnal climatology: e2 meridional . . . . .	126
A4.4	TIDI diurnal climatology: e3 meridional . . . . .	127
A4.5	TIDI diurnal climatology: w2 zonal . . . . .	128
A4.6	TIDI diurnal climatology: s0 zonal . . . . .	129
A4.7	TIDI diurnal climatology: e2 zonal . . . . .	130
A4.8	TIDI diurnal climatology: e3 zonal . . . . .	131
A4.9	TIDI diurnal climatology: w4 meridional . . . . .	132
A4.10	TIDI diurnal climatology: w3 meridional . . . . .	133
A4.11	TIDI diurnal climatology: e1 meridional . . . . .	134
A4.12	TIDI diurnal climatology: w4 zonal . . . . .	135
A4.13	TIDI diurnal climatology: w3 zonal . . . . .	136
A4.14	TIDI diurnal climatology: e1 zonal . . . . .	137
A5.1	TIDI semidiurnal climatology: w4 meridional . . . . .	139
A5.2	TIDI semidiurnal climatology: w3 meridional . . . . .	140
A5.3	TIDI semidiurnal climatology: w1 meridional . . . . .	141
A5.4	TIDI semidiurnal climatology: s0 meridional . . . . .	142
A5.5	TIDI semidiurnal climatology: e1 meridional . . . . .	143
A5.6	TIDI semidiurnal climatology: e2 meridional . . . . .	144
A5.7	TIDI semidiurnal climatology: w4 zonal . . . . .	145
A5.8	TIDI semidiurnal climatology: w3 zonal . . . . .	146
A5.9	TIDI semidiurnal climatology: w1 zonal . . . . .	147
A5.10	TIDI semidiurnal climatology: s0 zonal . . . . .	148
A5.11	TIDI semidiurnal climatology: e1 zonal . . . . .	149
A5.12	TIDI semidiurnal climatology: e2 zonal . . . . .	150

## List of Tables

4.1	Observed and real zonal wavenumbers for diurnal period . . . . .	29
4.2	Diurnal amplitude and phase errors: CRISTA . . . . .	30
4.3	Vertical wavelengths of the diurnal tidal components: November 1994 .	34
4.4	Vertical wavelengths of the diurnal tidal components: August 1997 . . .	37
4.5	Diurnal amplitude and phase errors: TIDI . . . . .	54
4.6	Tidal forcing mechanisms for diurnal w2, s0, e2, and e3 . . . . .	60
4.7	Semidiurnal amplitude and phase errors: TIDI . . . . .	73
6.1	Effects of different coincidence criteria . . . . .	102

# 1 Introduction

As an interface between Earth's environment and space, the mesosphere and lower thermosphere (MLT) region of the atmosphere is particularly sensitive to external influences from the Sun above and the atmospheric layers below. Located between approximately 50-120 km above the surface, it is not only a region relevant for aerospace (i.e., rocket trajectories, suborbital hypersonic planes), radio transmission, space weather effects, and aurora [Song *et al.*, 2001] but also for understanding Earth's atmosphere in general [Johnson and Killeen, 1995; Siskind *et al.*, 2000; Shepherd *et al.*, 2002; Takahashi *et al.*, 2004]. Its dynamics, chemistry and thermal structure can change rapidly due to naturally-occurring and/or human-induced changes to the energy contained within this region [Khosravi *et al.*, 2002]. Atmospheric waves play an essential role in this context. They propagate up and away from their tropospheric and stratospheric source regions and transport energy and momentum to the upper part of the atmosphere. About  $10^{16}$  J of energy propagates up daily from the lower atmosphere in the form of small-scale gravity waves (GWs), large-scale planetary waves (PWs) and tides [Jarvis, 2001]. This roughly equals the  $10^{17}$  J of energy that is injected per day during a geomagnetic storm (occurring in average every 5 days) from space through auroral processes. Particle precipitation, radiation, chemistry and dynamics play all an important role in driving the global circulation in the MLT that itself feeds back into tropospheric and stratospheric processes that are related to extended-range weather forecast [Baldwin *et al.*, 2003a,b] and climate research. A prominent example for the latter is the mesospheric preconditioning for the unprecedented Southern Hemisphere ozone hole split in late September 2002 [Liu and Roble, 2005]. The implications of this event, which is in contrast to the trend for the last 20 years toward a stronger and colder Antarctic vortex, are not yet understood. Figure 1.1 overviews the relevant coupling processes and parameters.

Our present understanding of the MLT region, and its coupling with the atmospheric layers below and above, is far from being complete. For many years, its inaccessibility caused the lack of a comprehensive database. The traditional division into troposphere-stratosphere research by meteorologists and thermosphere-ionosphere-magnetosphere research by space physicists resulted in an in-between gap. Hence, the MLT is the least explored region of Earth's atmosphere. Some important open science questions are:

- What are the spatio-temporal variations of temperature, winds, and chemical constituents and what causes them?
- What are the sources and magnitudes of atmospheric waves and how do they interact with each other?
- What is the relative importance of radiation, chemistry, and dynamics for the momentum and energy budget?
- How large is the anthropogenic effect?
- Can we quantify the MLT effect on climate?

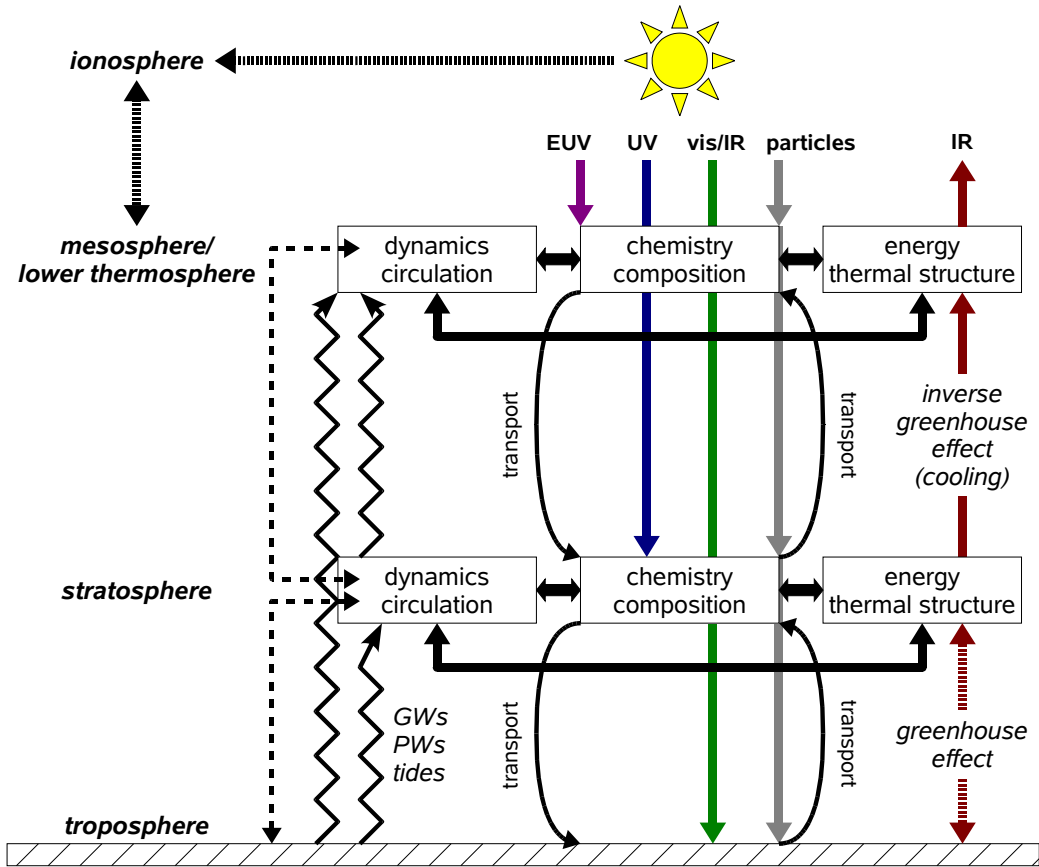


Figure 1.1: Schematic of atmospheric coupling processes.

Far from being complete, these and other issues motivated the increasing MLT research efforts during the past few years. Models have been developed that extend from the ground to the thermosphere [Roble and Ridley, 1994; Fomichev et al., 2002; Sassi et al., 2002]. Ground-based instruments have been upgraded, i.e. daylight capable lidar systems [She, 2004]. Satellites have been built to measure minor constituents, temperature, and wind in the MLT region on a global scale (i.e., NIMBUS-7, UARS, CRISTA-SPAS, TIMED; see list of acronyms in appendix A1) although their numbers are small compared to the platforms dedicated to lower atmosphere and ionosphere-magnetosphere research. International scientific programs have been initiated such as the Planetary Scale Mesopause Observing System (PSMOS) [Shepherd et al., 2002] and recently the Climate and Weather of the Sun-Earth System (CAWSES) [Basu and Pallamraju, 2006].

These combined research efforts should greatly enhance our knowledge of the MLT and allow to view Earth's atmosphere as a whole. In the long-term they may also result in a MLT equivalent of the data assimilation systems in the troposphere-stratosphere [Swinbank and O'Neill, 1994] and ionosphere [Richmond, 1992]. This approach of merging observations with models was exceedingly successful in improving the models and to study fundamental atmospheric processes. Applying the same concept to the MLT is thus very attractive but also very challenging. First steps toward it have already been made using ensemble Kalman filters (R.S. Lieberman, private communication) and general circulation models (T.G. Shepherd, private communication). All

these approaches, however, suffer from the lack of a comprehensive database and the current ignorance of some basic physical processes.

A key role in this context and in understanding the MLT region plays the large-scale vertical wave coupling across the stratopause by PWs and tides [*Smith, 2003; McLandress et al., 2006*]. Its better understanding is the leading objective of this work using data from several satellite instruments and models of differing character. Section 2 reviews the basic characteristics of tides and planetary waves with emphasis on vertical coupling between the lower and upper atmosphere. Section 3 overviews the satellite instruments (LIMS, CRISTA, SABER, TIDI) and models (GSWM, TIME-GCM, extended CMAM) used and discusses the principle difficulties in comparing satellite data with models in the MLT region.

Section 4 provides a comparative observation/model analysis of nonmigrating (non-Sun-synchronous) tides that are among the least understood phenomena in the MLT. Observation-based tidal definitions are derived from the data of three satellite instruments (LIMS, CRISTA: temperature; TIDI: winds) and compared to the models. The comparison consolidates predictions [*Hagan and Roble, 2001*] that interactions of solar driven migrating tides with PWs play an important role in nonmigrating tidal forcing. This process and additional latent heat release in the troposphere [*Hagan and Forbes, 2002; 2003*] imply that large-scale tropospheric systems that do not propagate into the MLT can nevertheless influence the dynamics, chemistry, and energetics in this height region via their imprint upon the tidal fields. Especially the measurements of the TIDI instrument on board TIMED provide a data set that is unprecedented in that it is amenable to global nonmigrating tidal wind analysis over a range of MLT altitudes. The derived tidal climatologies are expected to aid modelers in tuning source functions and dissipative parameters to match observations.

Section 5 focuses on the formation of the mesospheric surf zone and its relationship with temperature inversion layers as a result of PW/GW interaction and troposphere-stratosphere dynamics. A case study using temperature and constituent data from the CRISTA instrument is generalized using a one-year long run of the TIME-GCM. Section 6 presents a three-year comparison between coincident satellite-borne (SABER) and ground-based (GRIPS) temperature measurements in the mesosphere and discusses its implications for secular trend estimates and joint analyses of multiple satellite instruments. Each section includes its own discussion and conclusion part. The relevant findings are summarized in section 7.

## 2 Troposphere - thermosphere coupling by large-scale waves

As a rotating stratified fluid, the atmosphere supports a variety of wave motions on different spatio-temporal scales. Many of these waves in temperature, wind, and density are excited in the troposphere and stratosphere and may propagate up into the mesosphere and lower thermosphere region where they dissipate. As a result, atmospheric waves transport energy and momentum from the lower into the upper atmosphere and deposit them into the mean flow. Figure 2.1 illustrates some of the relevant mechanisms. Wave periods and horizontal wavelengths range from minutes to hours and a few to some hundred kilometers (GWs) over harmonics of a solar day (tides) to days and weeks (PWs). Tides and planetary waves are global phenomena with horizontal wavelengths on the order of Earth's circumference. Generated by topography - mean flow and surface interactions, convection, or radiative processes, all these waves basically grow exponentially in amplitude when propagating upward, to satisfy energy conservation. Wave amplitudes in the MLT can therefore be large before dissipation sets in. One condition for the latter is when the phase speed of the wave matches the mean flow velocity. The mean flow then serves as a barrier to vertical propagation and the wave is absorbed. Thermal conductivity, and molecular and eddy diffusion also play an important role, as ion drag, radiative damping and the drag associated with breaking GWs do. The last two processes are sometimes approximated and referred to as Newtonian cooling and Rayleigh friction.

The vertical coupling by large-scale tides and planetary waves is the main focus of this work. Their basic characteristics are reviewed in sections 2.1 and 2.2 below. Tides and PWs may strongly interact with each other but also with the small-scale GWs through various processes such as wave filtering, generation of secondary waves, and mean flow interactions. The crucial role of GWs for the dynamics and thermal structure of the MLT is thus briefly overviewed in the following.

Gravity waves have the buoyancy force as the restoring force. Among others, their mean excitation mechanisms include flow distortions induced by mountain ranges, convection, and wind shear. A prominent example for their role in MLT physics is the cold summer mesopause. Defined as the boundary between the mesosphere and the thermosphere, it is the coldest place on Earth. Summer temperatures in polar latitudes drop to 120-130 K [Lübken, 1999] which is some 80 K colder than expected from radiative equilibrium. The cooling is a consequence of GW dissipation that in turn exerts a force on the mean meridional flow via momentum flux divergence. This results in a summer-to-winter pole mean meridional circulation and an upward motion of air at the summer pole, to satisfy continuity. The corresponding adiabatic expansion then leads to the cooling. GW dissipation also causes the reversal of the mean zonal wind field from westerly in the mesosphere to easterly in the lower thermosphere (winter) and vice versa in summer. Typical GW wavelengths are below the horizontal resolution of most atmospheric models. It is thus necessary to parameterize their sub-grid effects which is a general problem of middle atmosphere models (see section 3.2.2). An observational confirmation of these parameterization schemes is very difficult because global measurements of GW distributions are very sparse and still suffer from a lack of horizontal resolution [Preusse *et al.*, 2006]. A tutorial intro-

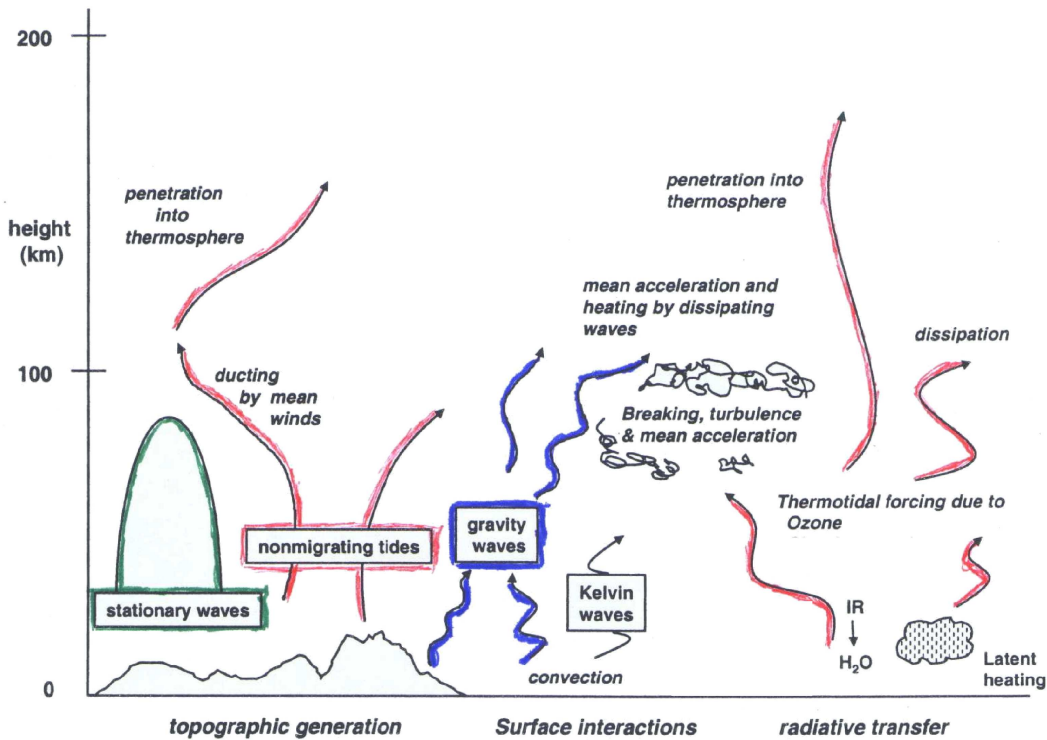


Figure 2.1: Schematic of various processes related to wave coupling between the lower and upper atmosphere. Green: stationary planetary waves; red: tides; blue: gravity waves. Figure adopted from *Forbes* [2002], copyright 2002 American Geophysical Union. Reproduced/modified by permission of American Geophysical Union.

duction of GWs and their role in middle atmosphere circulation is given by *Holton and Alexander* [2000]. GW effects on the large-scale wave coupling are discussed more closely in sections 3, 4, and 5.

## 2.1 Tides

Tides are global-scale waves in temperature, winds, and density with periods that are harmonics of a solar day. They are among the most striking dynamical features in the MLT. Tidal winds are on the order of the time-averaged zonal wind and dominate the meridional wind field. Tides also modify the upward propagation of GWs and their momentum deposition in the upper atmosphere via critical layer filtering mechanisms [*Fritts and Vincent*, 1987] and via modulation of the buoyancy frequency [*Preusse et al.*, 2001]. They play a major role in the diurnal cycle of chemical active species [*Angelats i Coll and Forbes*, 1998; *Marsh and Russell*, 2000; *Zhang et al.*, 2001]. Temperature oscillations may change reaction rates with simultaneous transport of air parcels some 1000 km in the horizontal and some kilometers in the vertical [*Ward*, 1999]. As a result, tides have a major impact (up to 40% from the migrating diurnal tide alone) on the total heating in the MLT [*Smith et al.*, 2003].

The classical tidal theory [*Chapman and Lindzen*, 1970] outlined in appendix A2 already predicts the existence of two classes of tidal oscillations, the migrating and nonmigrating tides. Migrating or Sun-synchronous tides propagate westward with

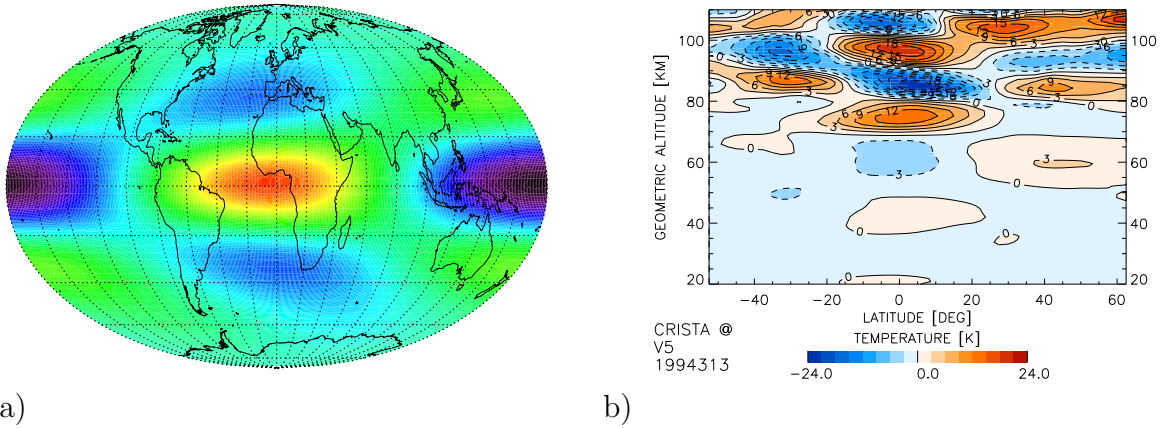


Figure 2.2: a). Model simulation [Hagan *et al.*, 1999] for the migrating diurnal tide in October at 82 km and 0 h Universal time. Shown is the temperature oscillation. Contour interval is between -14 K (black) and +14 K (red). b) Observed vertical structure. Results shown are from CRISTA measurements in November.

the apparent motion of the Sun and are primarily driven by the absorption of solar infrared and ultraviolet radiation in tropospheric water and water vapor and stratospheric ozone. Their zonal wavenumbers are therefore equal to their frequencies (in cycles per day), that is, wavenumber 1 for the migrating diurnal (24 hour period) and wavenumber 2 for the migrating semidiurnal (12 hour period) tides. Migrating tides have been intensively studied using temperature and wind data from various ground-based [Chang and Avery, 1997; Manson *et al.*, 1999; Tsuda *et al.*, 1999] and satellite [Hitchman and Leovy, 1985; Dudhia *et al.*, 1993; Burrage *et al.*, 1995; Khatatov *et al.*, 1997; Wu *et al.*, 1998; Shepherd *et al.*, 1999; Ward *et al.*, 1999; Oberheide *et al.*, 2000; Zhang and Shepherd, 2005] instruments as well as with models [Forbes, 1982; Vial and Forbes, 1989, Hagan *et al.*, 1995; Akmaev *et al.*, 1996; McLandress, 1997; Hagan *et al.*, 2001].

Figure 2.2a exemplifies the horizontal structure of the migrating diurnal tide: a zonal wavenumber 1 signature maximizes at the equator with secondary wave maxima occurring at 30°S and 30°N that are out-of-phase with the wave at the equator. The whole pattern moves westward with the apparent motion of the Sun when time progresses. Figure 2.2b shows its vertical extent as measured by the CRISTA satellite instrument in November 1994. Alternating patterns of positive and negative temperature perturbations occur at the equator and at mid-latitudes indicating a vertical wavelength of about 25 km. The wave grows with increasing altitude, maximizes at 90 km and starts to dissipate at altitudes above. Section 4.1.3 gives a more detailed discussion.

An interpretation of the vertical and horizontal structures shown in Figure 2.2 in terms of the classical tidal theory might be illustrative at this point, in spite of its inherent shortcomings. The classical tidal theory is overviewed in appendix A2 by summarizing the comprehensive review of Forbes [1995]. It predicts a vertical wavelength of 27.9 km for the first symmetric tidal mode (Hough function) of the migrating diurnal tide with an equatorial maximum and two out-of-phase secondary maxima at  $\sim 30^\circ\text{S}$  and  $\sim 30^\circ\text{N}$  (Figure A2.1). This is reflected in the model (Figure

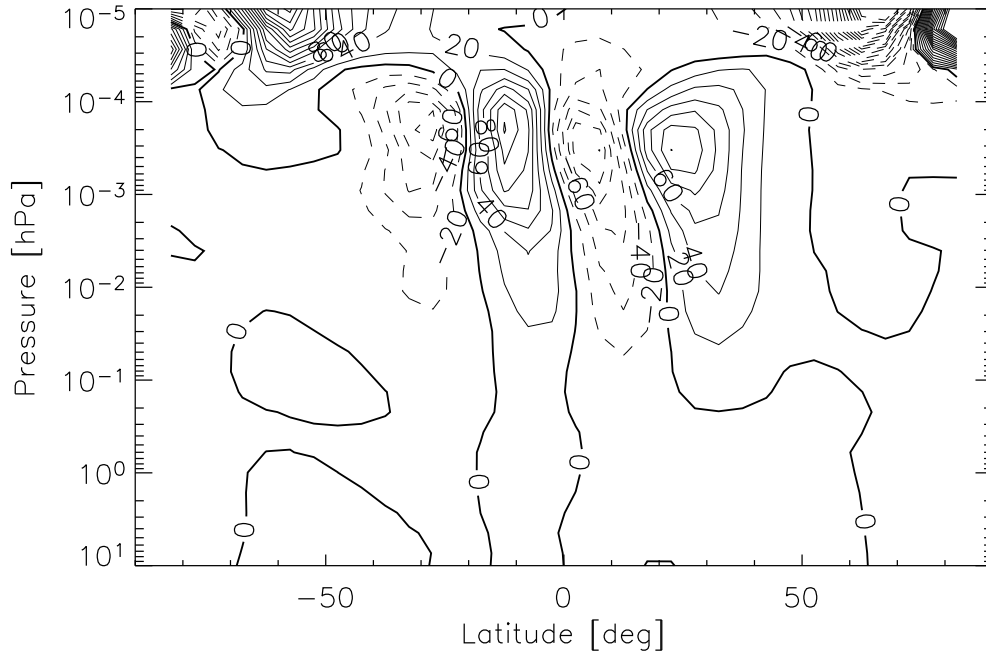


Figure 2.3: Rectified eddy forcing computed from a TIME-GCM simulation for 5 November 1994. Contour interval is  $20 \text{ ms}^{-1}\text{day}^{-1}$ . Negative values are dashed. Signatures equatorward of  $30^\circ$  are governed by the migrating diurnal tide. They maximize around 100 km altitude. High altitude/latitude imbalances are dominated by auroral processes.

2.2a) and in the observation (Figure 2.2b). Hemispheric asymmetries and dissipative features evident in the latter are not covered by the classical theory but the general agreement is nevertheless satisfactory.

Figure 2.3 illustrates one tidal effect on the MLT circulation. It shows the "rectified eddy forcing" (divergence of Reynolds stress) in the zonal mean meridional momentum equation as computed from a TIME-GCM simulation for 5 November 1994. Rectified eddy forcing from TIME-GCM agrees well with results from the Kyushu University atmospheric circulation model [Miyahara *et al.*, 2000] where the forcing equatorward of  $30^\circ$  predominantly originates from the migrating diurnal tide. It introduces a considerable deviation, exceeding 20 m/s at its peak in TIME-GCM, of the zonal mean zonal wind field in the MLT from geostrophic balance (not shown). TIME-GCM signatures at high altitudes and latitudes in Figure 2.3 are likely non-tidal and caused by auroral processes.

The nonmigrating or non-Sun-synchronous tides are far less understood due to the limited amount of observations, model deficiencies, and some ignorance of their role in upper atmosphere dynamics, chemistry, and energetics. Their better understanding is a primary objective of this work (section 4). Nonmigrating tides do not follow the apparent westward motion of the Sun but may propagate westward, eastward, or remain standing. Their zonal wavenumbers do not equal their frequencies (in cycles per day) and they may be forced by a variety of quite different mechanisms. The aggregate effects of nonmigrating tides introduce a longitudinal variability of the amplitudes and phases of the total tidal fields [Khattatov *et al.*, 1996; Ward *et al.*, 1999; Manson *et al.*, 1999].

Tidal components are classified according to their propagation direction and zonal wavenumber  $s$ . A zonal wavenumber  $s > 0$  indicates eastward propagation and  $s < 0$  means westward propagation. The nomenclature used in the following is standard: a letter/number combination is assigned to each tidal component. The letter gives the propagation direction ( $w$ : westward,  $e$ : eastward,  $s$ : standing) and the number is the absolute value of the zonal wavenumber  $|s| \geq 0$ ; i.e.  $w3$  is the westward propagating nonmigrating component of zonal wavenumber 3,  $s0$  is the standing oscillation (having naturally zonal wavenumber 0), and  $e3$  is the eastward propagating component of zonal wavenumber 3. With the same nomenclature, the migrating diurnal tide is  $w1$  and the migrating semidiurnal tide is  $w2$ .

The two leading nonmigrating tidal sources are latent heat release in the tropical troposphere [*Hagan and Forbes*, 2002; 2003] and non-linear interactions between quasi-stationary planetary waves (QSPWs) and the migrating tide [*Hagan and Roble*, 2001; *Lieberman et al.*, 2004]. Additional sources are longitudinal variations in the heating from ozone and water vapor due to land-sea differences and topography [*Kato et al.*, 1982, *Tsuda and Kato*, 1989], and non-linear interactions between the migrating tide and gravity waves [*McLandress and Ward*, 1994]. *Oberheide and Gusev* [2002] suggested non-linear interactions between latent heat forced nonmigrating tides and QSPWs as an additional mechanism but this has not yet been proven or falsified. The role of absorption of solar insolation in forcing the nonmigrating tides has not yet finally been resolved. Model results of *Hagan et al.* [1997] point to a rather small contribution but revised radiative heating rates by *Lieberman et al.* [2003] indicate that the radiative source may need to be revisited.

The amount of data suitable for nonmigrating tidal analysis has so far been quite limited which is primarily due to shortcomings of both satellite-borne and ground-based instruments. Satellite instruments suffer from their lack of local time coverage, but they provide the longitudinal coverage being essential to separate the nonmigrating components from the tidal signal. Composite data of 30-60 days from instruments on board slowly precessing satellites provide a local time coverage of 24 hours and may be Fourier analyzed [*Forbes et al.*, 2003; *Oberheide et al.*, 2005; 2006b]. Such satellite results must therefore be interpreted in a rather climatological sense. A recently developed non-Fourier method [*Oberheide et al.*, 2002b] allows tidal analysis on a daily basis, but the method critically depends on data quality and orbit geometry. It has been successfully applied to Cryogenic Infrared Spectrometers and Telescopes for the Atmosphere (CRISTA) and Limb Infrared Monitor of the Stratosphere (LIMS) data [*Oberheide and Gusev*, 2002; *Lieberman et al.*, 2004]. Ground-based observations partly provide 24 hour local time coverage every day, but it is impossible to de-alias nonmigrating and migrating tides from the observations. Networks of ground-based stations may help, but to avoid tidal aliasing, numerous stations must be equally spaced in longitude. Such a requirement is difficult to meet and basically limited to the analysis of semidiurnal components in high northern and southern latitudes [*Wu et al.*, 2003; *Murphy et al.*, 2003].

The few global observations of nonmigrating tides that are available therefore originate from satellite instruments. Using LIMS data, *Lieberman* [1991] showed the combined nonmigrating tidal amplitudes equal to or in excess of the migrating diurnal amplitude at altitudes below 80 km with vertical phase progression suggesting a

tidal forcing below the stratosphere. These findings were confirmed by *Oberheide and Gusev* [2002] and *Oberheide et al.* [2002b] who derived nonmigrating tides between 50 and 120 km altitude from CRISTA temperatures. The CRISTA results could be understood by a combination of both latent heat and QSPW/tidal interaction forcing with the sources of the observed large w3, w4, and w5 amplitudes remaining in the dark. *Lieberman et al.* [2004] revisited the LIMS data and found evidence for wave-wave interaction forcing in the stratosphere. *Forbes et al.* [2003], *Manson et al.* [2002, 2004], and *Huang and Reber* [2004] were able to retrieve nonmigrating tidal amplitudes and phases from the two wind instruments on board the Upper Atmosphere Research Satellite (UARS): the High Resolution Doppler Imager (HRDI) and the Wind Imaging Interferometer (WINDII). The specifics of the UARS instruments, however, confined their analyses to an altitude of 95 km but they clearly showed the month-to-month variability of the nonmigrating tides as well as the resulting longitude modulation of the diurnal tidal amplitude. With a different analysis approach, *Talaat and Lieberman* [1999] retrieved nonmigrating tidal information between 60 and 120 km from HRDI but without being able to clearly identify the zonal wavenumbers of the tidal components. Note that the results of the UARS analyses are partly contradictory in tidal amplitudes. Differences reach 50%, but in all these studies the nonmigrating tides partly exceeded the migrating tide. This emphasizes their important role in MLT dynamics. Recently, *Forbes and Wu* [2006] established internal consistency between the nonmigrating tides in Microwave Limb Sounder (MLS) temperatures at 86 km and the UARS tidal winds at 95 km within the context of the classical tidal theory.

State-of-the-art tidal models like the global scale wave model (GSWM, see section 3.2.1 for details), or the model of *Grieger et al.* [2004] as well as general circulation models like the thermosphere-ionosphere-mesosphere-electrodynamics general circulation model (TIME-GCM, see section 3.2.2 for details), the whole atmosphere chemistry climate model (WACCM; R. Garcia, private communication), and the extended canadian middle atmosphere model (extended CMAM, see section 3.2.3 for details) can now reproduce nonmigrating tides but with a number of deficiencies in terms of predicted amplitudes, the presence of specific nonmigrating tidal components, and seasonal and inter-annual variability. Observation-based tidal definitions and climatologies such as provided in section 4 are therefore required to aid modelers in tuning source functions and dissipative parameters to match observations.

## 2.2 Planetary waves

The linear wave theory (appendix A2) already describes another class of large-scale waves: the free traveling planetary (Rossby) waves. Without external forcing, one obtains the free (Lamb wave) solution in Equation A2.33 that in turn defines the periods of the normal modes (Hough functions) for different zonal wavenumbers  $s$ . Periods are on the order of several days. Prominent solutions are the 5-day wave, 10-day wave, 16-day wave ( $|s| = 1$ ), the 4-day wave ( $|s| = 2$ ), and the quasi two-day wave (QTDW,  $|s| = 3$ ). The given periods are approximate values. Normal Rossby modes propagate westward. Typical phase speeds ( $60^\circ$  latitude) are  $23 \text{ ms}^{-1}$  for the 10-day wave and  $39 \text{ ms}^{-1}$  for the QTDW. This is small compared to the phase speed of the

tides, that is,  $464 \text{ ms}^{-1}$  at the equator and  $232 \text{ ms}^{-1}$  at  $60^\circ$  latitude for the migrating diurnal tide. It thus becomes clear that the presence of zonal winds has a rather moderate effect on the tides but it may become very important for the planetary waves: wave breaking occurs once the phase speed matches or approaches the zonal mean zonal wind speed. Such critical wind layers can easily occur for planetary waves in the real atmosphere but not for the tides. See *Forbes* [1995] for more details. Free planetary waves are not further considered, apart from their possible aliasing effects in the tidal analysis presented in section 4. This also applies to the Kelvin waves and mixed Rossby-gravity waves that can be described within the same theoretical framework.

Of more particular interest for this work are the forced planetary Rossby waves. Their behavior is significantly different from that of the free planetary waves described above. The characteristics of forced planetary waves may be summarized as follows: (i) zonal wavelengths are of the scale of the Earth's circumference; (ii) PWs in the extratropics are in approximate geostrophic balance; (iii) forcing occurs in the troposphere by topography, land-sea temperature contrast, and synoptic eddies; (iv) restoring force is the latitudinal gradient of background potential vorticity; (v) horizontal propagation is westward with respect to the background zonal wind; (vi) vertical propagation into the stratosphere and mesosphere only occurs for the longest spatial scales.

Some basic characteristics of forced PWs can already be derived from a simple barotropic model on the  $\beta$ -plane. Assuming an incompressible fluid with purely horizontal flow, the zonal and meridional momentum equations are combined to form the vorticity equation which is further simplified by replacing the spherical geometry with Cartesian geometry and by writing the Coriolis parameter  $f = 2\Omega \sin \varphi$  as  $f = f_0 + \beta y$  ( $\beta$ -plane approximation) with angular velocity of the Earth  $\Omega$  and latitude  $\varphi$ . Hence, the absolute, barotropic vorticity  $q$  of an air parcel is materially conserved:

$$\frac{Dq}{Dt} = \left( \frac{\partial}{\partial t} + u \frac{\partial}{\partial x} + v \frac{\partial}{\partial y} \right) q = 0 \quad (2.1)$$

with

$$q = \zeta + f = \frac{\partial v}{\partial x} - \frac{\partial u}{\partial y} + f_0 + \beta y \quad (2.2)$$

and relative vorticity  $\zeta$ , zonal wind  $u$ , and meridional wind  $v$ . See *Andrews et al.* [1987] for details. For small amplitude disturbances on a constant zonal mean flow and with  $(u, v) = (-\partial\Psi/\partial y, \partial\Psi/\partial x)$  as derivatives of the stream function  $\Psi$ , Equations 2.1 and 2.2 lead to

$$\left( \frac{\partial}{\partial t} + \bar{u} \frac{\partial}{\partial x} \right) \left( \frac{\partial^2 \Psi'}{\partial x^2} + \frac{\partial^2 \Psi'}{\partial y^2} \right) + \beta \frac{\partial \Psi'}{\partial x} = 0 \quad (2.3)$$

that is solved by

$$\Psi'(x, y, t) = \Re \left\{ \tilde{\Psi} e^{i(kx + ly - ckt)} \right\}. \quad (2.4)$$

Primed quantities denote small disturbances and overbared quantities are a zonal mean. The wave in Equation 2.4 depends on the zonal and meridional wavenumbers  $k$  and  $l$ , and on the phase speed

$$c = \bar{u} - \frac{\beta}{k^2 + l^2}. \quad (2.5)$$

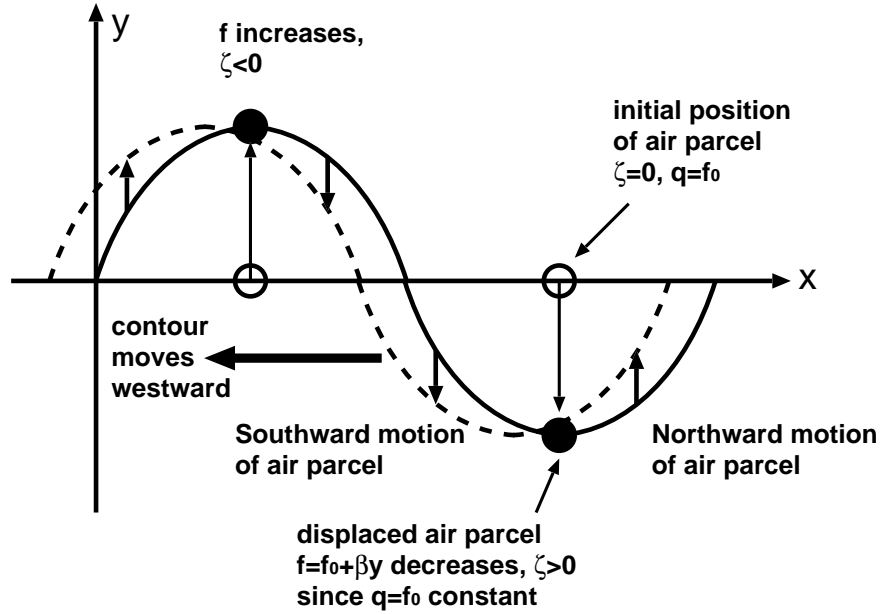


Figure 2.4: Planetary Rossby wave propagation mechanism. Restoring force is the latitudinal gradient of the background potential vorticity. For details see text.

Conservation of barotropic vorticity thus results in the westward propagation (with respect to the zonal mean flow) of planetary Rossby waves. Figure 2.4 illustrates the basic mechanism.

A further extension of this simple theory [e.g. *Andrews et al.*, 1987] leads to the quasi-geostrophic potential vorticity equation and to a condition for the vertical propagation of PWs. For a stationary wave ( $c = 0$ ), one obtains the Charney-Drazin criterion [*Charney and Drazin*, 1961]:

$$0 < \bar{u} < \bar{u}_c \quad (2.6)$$

$$\bar{u}_c \equiv \frac{\beta}{(k^2 + l^2) + \frac{f_0^2}{(2HN)^2}} \quad (2.7)$$

with constant scale height  $H$  and buoyancy frequency  $N$ . Vertically propagating, stationary planetary waves (SPWs) can only exist in winds that are westerly (eastward) and that are not too strong. Wave decay and breaking sets in once the waves approach altitudes with mean zonal wind velocities close to zero (critical wind layer). The Charney-Drazin criterion also implies that only SPWs with long horizontal wavelengths may propagate upward. This is well known from observations which show that SPWs are usually composed of zonal wavenumbers between one and three in the winter hemisphere and that they are absent in the summer hemisphere when the wind is easterly (westward). See *Labitzke* [1980] for an early climatology of the planetary wave evolution in the stratosphere and mesosphere. *Scott and Haynes* [2002] give a more sophisticated model description of planetary waves including hemispheric differences. Stationary planetary wave 1 and 2 evolution is discussed more closely in section 5 using CRISTA measurements and TIME-GCM simulations.

Important SPW forcing mechanisms are topography and the land-sea temperature contrast. SPWs may interfere with the free traveling planetary waves resulting in an

amplitude modulation [*Madden and Labitzke, 1981; Smith, 1985*]. An example for that is shown in the LIMS analysis in section 4.2. SPWs are often referred to as quasi-stationary planetary waves (QSPWs) because their phase speeds may be slightly above zero (with periods on the order of weeks) and because they may exhibit a vacillating behavior.

SPWs maximize in the 60° latitude regime. Their departure from zonal symmetry (i.e., in temperature) can be considered as a displacement (wave 1) or an elongation (wave 2) of the polar vortex. SPWs deposit their momentum and energy into the mean flow when dissipating and also provide an important filtering mechanism for upward propagating GWs. This is discussed more closely in section 5 in the context of upper mesospheric planetary wave forcing.

Stationary planetary waves strongly interact with the tides. The basic mechanism is the same as in an AM radio transmitter. The non-linear interaction of two waves of zonal wavenumbers  $s_1, s_2$  and frequencies  $\sigma_1, \sigma_2$  predominantly leads to the generation of two secondary waves of wavenumber  $s_1 + s_2$  with frequency  $\sigma_1 + \sigma_2$ , and  $s_1 - s_2$  with frequency  $\sigma_1 - \sigma_2$ . This may be exemplified for the interaction between the migrating diurnal tide ( $s_1 = -1, \sigma_1 = 1/24 \text{ hour}^{-1}$ ) and the SPW of zonal wavenumber one ( $s_2 = 1, \sigma_2 = 0$ ). The resulting secondary waves are of zonal wavenumber  $s = -2$  and frequency  $\sigma = 1/24 \text{ hour}^{-1}$  and  $s = 0, \sigma = 1/24 \text{ hour}^{-1}$  and thus the w2 and s0 nonmigrating components of the diurnal tide. Observational evidence for this mechanism is presented in section 4.

## 3 Satellite-borne observations and modeling of the middle atmosphere

Global measurements of upper atmosphere parameters started immediately with the beginning of the space-age, that is, by deriving thermospheric density from satellite drag. Such measurements are still used for secular trend analysis [*Keating et al.*, 2000]. Satellites since provided invaluable diagnostics of MLT forcing, dynamics, chemistry, and energetics using various techniques in the microwave (MW), infrared (IR), visible (VIS), and ultraviolet (UV) spectral regimes. Approaches include the measurement of MW and IR limb emissions, UV/VIS/IR solar, lunar and stellar occultation, UV/VIS nadir and limb scattering, and Global Positioning System (GPS) occultation.

Numerous instruments have so far measured dynamical fields such as temperature, geopotential and winds, and chemical species in the altitude range above the stratopause. A digest of the most relevant instruments and missions for studying vertical coupling processes across the stratopause certainly includes LIMS, CRISTA, and the instruments on board the UARS and TIMED satellites. Data from the Odin, ENVISAT, and EOS-Aura satellites can also be expected to contribute to this field once they become widely available to the community. Section 3.1 overviews the instruments and data used in the following sections: LIMS, CRISTA, and SABER and TIDI on board TIMED.

The interpretation of the satellite diagnostics and the elucidation of the impact of the associated processes on the MLT requires complementary modeling efforts. On the other hand, the models require observations and diagnostics for the assessment of the current model physics and chemistry and as a guideline for the improvement and tuning of parameterization schemes. This interdependency calls for a close collaboration between modeler, experimenter, and data analyst. Data from the linear (GSWM) and the two non-linear (TIME-GCM, extended CMAM) models used for the present analyses are provided by the model owners and analyzed in close collaboration with them. The models are overviewed in section 3.2.

One immediate problem with the comparative analysis of satellite data and model predictions is the asymptotic sampling of the satellite instruments, that is, the irregular spacing of the measurements in space and time. A technique to deal with this problem is presented in section 3.3.

### 3.1 Instrument overview

#### 3.1.1 LIMS

The Limb Infrared Monitor of the Stratosphere (LIMS) instrument on board the NIMBUS-7 satellite was operational from Oct. 24, 1978 until May 28, 1979 [*Gille and Russell*, 1984]. The spacecraft was launched into a 955 km altitude Sun-synchronous orbit (99.1° inclination) with local solar times of the instrument footprints fixed at 13:00 (ascending) and 22:40 (descending). Ascending (asc) orbit nodes are the instrument footprints when the satellite moves from south to north and descending (dsc) orbit nodes are the footprints for north-south movement. LIMS is a limb-viewing

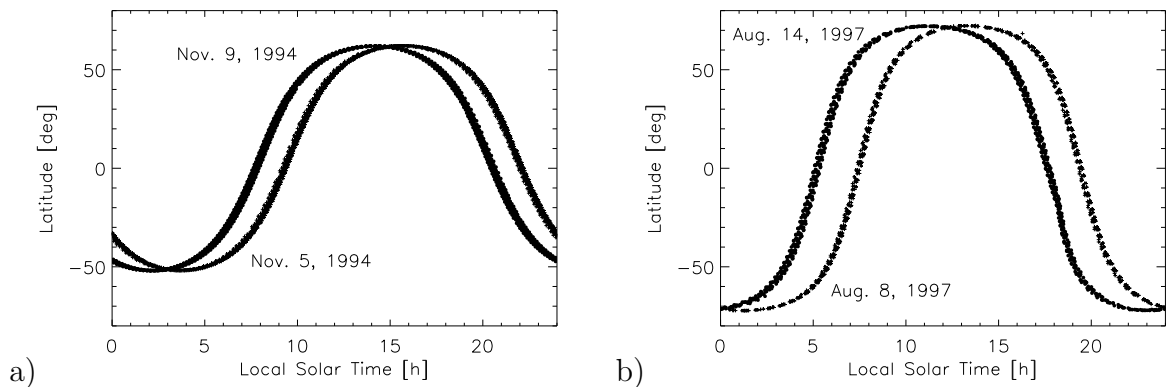


Figure 3.1: Local solar time (LST) of CRISTA temperature measurements in the MLT. Each symbol represents one temperature profile. a) CRISTA-1 for November 5 and 9, 1994. b) CRISTA-2 for August 8 and 14, 1997.

radiometer measuring the 6-15  $\mu\text{m}$  spectral region in six channels with day- and nighttime capability. Temperature is the only parameter used here (section 4.2) but the instrument also measures various chemical constituents ( $\text{O}_3$ ,  $\text{H}_2\text{O}$ ,  $\text{NO}_2$ ,  $\text{HNO}_3$ ). The temperature is retrieved from the 15  $\mu\text{m}$   $\text{CO}_2$  emissions between 10-80 km assuming local thermodynamical equilibrium conditions (LTE) [Remsberg *et al.*, 2004]. The vertical resolution is 3.7 km and the along track resolution is 144 km. An overview of the 2002 re-analysis of the LIMS data (called version V6) is given by Lieberman *et al.* [2004]. The precision of the temperature data is 1.4 K at 3 and 1 hPa, 1.3 K at 0.4 and 0.1 hPa, and 0.7 K at 0.04 hPa. The accuracy of a single temperature profile is 2.5 K. LIMS data cover 64°S to 84°N latitude. They may be downloaded from <http://lims.gats-inc.com>.

### 3.1.2 CRISTA

The limb sounding Cryogenic Infrared Spectrometers and Telescopes for the Atmosphere (CRISTA) instrument was flown twice as part of the two U.S. Space Shuttle missions STS-66 (3-14 November 1994, CRISTA-1) and STS-85 (7-19 August 1997, CRISTA-2). It was developed and built by the University of Wuppertal. CRISTA was mounted on the free-flying ASTRO-SPAS platform that was released at the beginning and captured at the end of each flight. During both missions, the instrument was in a 300 km circular orbit inclined 57° to the equator. CRISTA-1 data cover the latitudinal range 52°S to 62°N. Continuous maneuvering of the spacecraft extended the latitudinal coverage to 72°S to 72°N for CRISTA-2. Depending on the measuring mode, the vertical resolution of the measurements is between 1.5 - 2.5 km with an along track resolution of 200-400 km. See Offermann *et al.* [1999] and Grossmann *et al.* [2002] for the specifics of the instrument and mission overviews.

The daily local solar time (LST) precession of 22 minutes for a given orbit node and latitude is such that the daily asc and dsc LSTs can be considered to be longitude independent. Figure 3.1 shows the instrument footprint LSTs as a function of latitude. The maximum LST separation of 12 hours occurs close to the equator at about 5°N and decreases toward higher latitudes. Owing to the short mission durations, CRISTA data have no complete LST coverage.

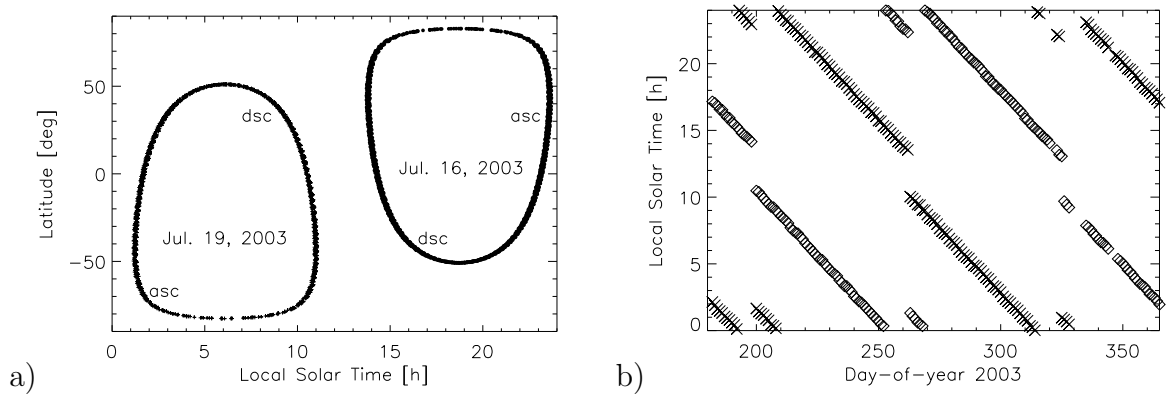


Figure 3.2: Local solar time (LST) of SABER footprints. a) Footprints of valid data for Jul. 16, 2003 and Jul. 19, 2003. Note the different yaw cycle. b) LST coverage at  $0^{\circ}\text{N}$  for the second half of 2003: crosses: ascending orbit nodes; diamonds: descending orbit nodes.

The instrument measures selected atmospheric constituents and temperature from below the tropopause up to the thermosphere in the spectral region from  $4 - 71 \mu\text{m}$  [Riese *et al.*, 1999]. CRISTA data cover day- and nighttime and may be downloaded from <http://www.crista.uni-wuppertal.de>. The most recent MLT temperature data set goes up to 120 km altitude with a precision of about 1 K at 87 km and 3 K at 110 km. The accuracy is about 4.5 K at 87 km and 14 K at 110 km. Temperature in the MLT is retrieved from the  $15 \mu\text{m}$   $\text{CO}_2$  emissions accounting for the deviation from the local thermodynamical equilibrium (non-LTE) [Gusev *et al.*, 2006]. The CRISTA data are probably the best source of precise global day- and nighttime temperature measurements from the lower stratosphere up into the lower thermosphere.

### 3.1.3 SABER

NASA's Thermosphere Ionosphere Mesosphere Energetics and Dynamics (TIMED) satellite was launched on Dec. 7, 2001 into a 625 km circular orbit inclined  $74^{\circ}$  to the equator (<http://www.timed.jhuapl.edu>). Its mission has recently been extended to 2010. The instrument on board the TIMED spacecraft designed to measure temperatures and chemical species in the MLT is a 10-channel radiometer: the Sounding the Atmosphere using Broadband Emission Radiometry (SABER) instrument [Mlynczak, 1997]. SABER measures day- and nighttime Earth limb emission vertical profiles in the near to mid-infrared over the range  $1.27 \mu\text{m}$  to  $17 \mu\text{m}$ . Temperatures are deduced from  $15 \mu\text{m}$   $\text{CO}_2$  emissions with respect to the non-LTE conditions in this height region [Mertens *et al.*, 2004]. The routine temperature retrieval covers the altitude regime from 10-105 km with a vertical resolution of about 2 km and an along-track resolution of about 400 km. SABER temperature errors of data versions v01.04 and v01.06 [Mertens *et al.*, 2004] used here are not yet routinely provided. Preliminary estimates (M. G. Mlynczak, private communication) are 5 K for the systematic error (accuracy) and 2 K for the the relative error (precision) at 87 km altitude. Data may be downloaded from <http://saber.larc.nasa.gov>.

The TIMED spacecraft changes its orientation with respect to the orbital flight direction every 60 days from forward to backward and vice versa (yaw cycle). SABER

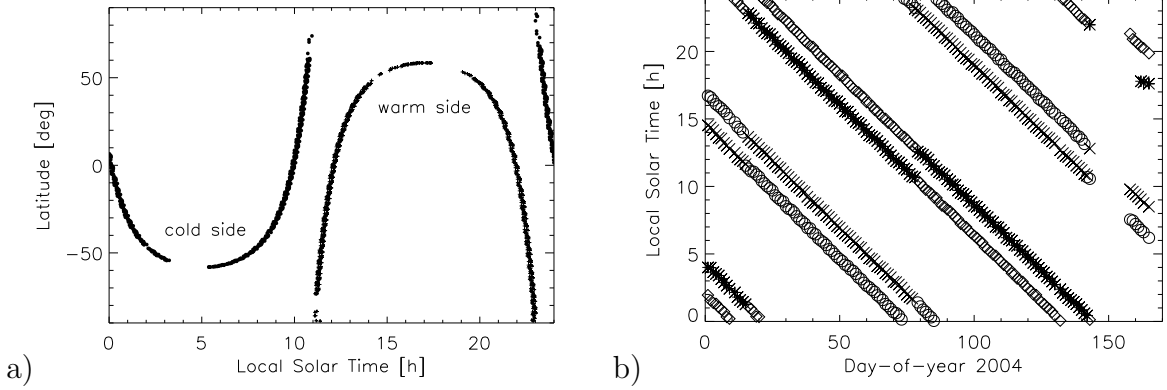


Figure 3.3: Local solar time (LST) of TIDI footprints for cold side and warm side measurements. a) Footprints of valid data for Jan. 22, 2004. b) LST coverage at  $20^\circ\text{N}$  for the first half of 2004: circles: asc, cold; crosses: asc, warm; diamonds: dsc, cold; asterisks: dsc, warm.

always views on the anti-Sun side of the spacecraft (perpendicular to the orbit) resulting in an asymmetric latitudinal coverage from  $83^\circ\text{S}$  to  $52^\circ\text{N}$  and  $52^\circ\text{S}$  to  $83^\circ\text{N}$  for consecutive yaw phases. Figure 3.2a shows the SABER local solar time (LST) coverage for two different yaws. For a given day and latitude, measurements taken on the ascending (asc) and descending (dsc) orbit nodes can be considered as to be longitude independent. The daily LST variation is 12 minutes per day such that full LST coverage is realized every 60 days (Figure 3.2b).

### 3.1.4 TIDI

The instrument on board the TIMED satellite with the primary objective to measure winds in the MLT region is the TIMED Doppler Interferometer (TIDI). It was developed and built by the University of Michigan [Killeen *et al.*, 1999]. Neutral winds are measured by limb scanning various upper atmosphere airglow layers and monitoring the Doppler shift. The instrument is day- and nighttime capable which makes the wind data set unprecedented. The TIDI data used here are  $\text{O}_2$  (0-0) band P9 vector winds (level3, data versions 00\_01 (2002), 01\_01 to 01\_03 (2003), 03\_03 (2004), 03\_04 (2005)) between 85 and 105 km that were produced by the National Center for Atmospheric Research (NCAR). They may be downloaded from <http://timed.hao.ucar.edu/tidi/>.

TIDI has four telescopes that are orthogonally oriented ( $45^\circ$  with respect to the orbit). This allows the instrument to measure wind vectors on both sides of the satellite track (i.e., cold and warm sides). The viewing directions of the two telescopes on the same side of the spacecraft are perpendicular to one another such that the same locations are observed with a time delay of a few minutes when the satellite moves forward. The samplings at the two directions are then used to form the neutral wind vector in terms of the zonal (eastward) and meridional (northward) components.

Data are taken from pole-to-pole with a vertical resolution of 2.5 km and an along track resolution of about 800 km. Measuring simultaneously on both sides of the satellite track provides four local solar time (LST) samplings equatorward of  $\pm 60^\circ$  and two at latitudes poleward of  $\pm 60^\circ$ . For a given latitude, the LSTs of measurements

taken on the ascending (asc) and descending (dsc) orbit nodes can be considered to be longitude independent for warm and cold side data respectively (Figure 3.3a). The daily LST variation for a given latitude, side, and orbit node is 12 minutes toward earlier LST as time progresses. Complete (24 hours) LST coverage is obtained every 60 days which corresponds to one satellite yaw cycle (Figure 3.3b). More details about the instrument, its measurements, and recent results are given by *Killeen et al.* [2006].

TIDI has continuously taken data since March 2002 with one larger data gap in early 2003. Unfortunately, the instrument suffered from a light leak that resulted in a higher signal background than expected. *Skinner et al.* [2003] describe the optical performance, that is, the decrease in throughput due to ice deposition on some parts of the optics and the efforts to sublimate the frost that led to an improved instrument performance since April 2003. Finding the zero wind position for space-borne Fabry-Perot interferometers has always been a challenging task. The TIDI zero wind determination is improving with every new version of the data products but some uncertainty still remains. In the tidal analysis (see section 4), however, one does not need to be overly concerned about this issue as it is accounted for in the analysis procedure. The light leak also increased the noise level of the inverted wind data (30 m/s during the day, double that during the night) but this does not affect the results as shown by the error analysis presented in section 4.3.

## 3.2 Model overview

### 3.2.1 GSWM

The NCAR Global Scale Wave Model (GSWM) [*Hagan et al.*, 1995] is a two-dimensional, linearized, steady-state numerical tidal and planetary wave model which extends from the ground to the thermosphere. It solves the extended Navier-Stokes equations and has been continuously developed during the last decade by updating the initial gravity wave stress parameterization and by updating the zonal background climatologies of zonal wind and ozone with UARS measurements. Model results may be downloaded from <http://web.hao.ucar.edu/public/research/tiso/gswm/gswm.html>. GSWM provides monthly climatologies of 13 diurnal and 13 semidiurnal tidal components (westward propagating wavenumbers 1 to 6; the standing diurnal tide; and the eastward propagating wavenumbers 1 to 6), that is, the migrating tide and 12 nonmigrating tidal components. Amplitudes and phases for zonal, meridional and vertical winds, temperature, and geopotential are given from pole to pole with 3° latitudinal resolution and up to 125 km with about 4 km altitude resolution.

GSWM accounts for tidal dissipation attributable to ion drag, molecular and eddy viscosity and conductivity, and radiative damping. It employs eddy diffusion coefficients  $K_{zz}$  to explicitly calculate the divergences of the associated heat and momentum fluxes. The model also includes an effective Rayleigh friction coefficient to account for gravity wave drag effects on the tides. Further details of these parameterizations are given by *Hagan et al.* [1999].

The model includes tidal forcing schemes which account for all known sources of thermal excitation. Migrating tidal sources in the standard model configuration

include the IR heating by the absorption of solar insolation in tropospheric water and water vapor, the UV absorption in stratospheric and lower mesospheric ozone, and UV forcing in the lower thermosphere [Hagan, 1996]. An extended version of the model also includes the thermospheric absorption of extreme UV and tidal forcing associated with lower thermosphere exothermic reactions [Hagan *et al.*, 2001]. The most recent model version (GSWM-02) accounts for latent heat release due to deep convective activity in the tropical troposphere.

Latent heating is the most significant nonmigrating tidal source in the model while the response to radiative nonmigrating tidal forcing is small [Hagan *et al.*, 1997]. The parameterization of tidal forcing due to latent heat release is described by Hagan and Forbes [2002, 2003]. Briefly, a climatology of 3-hourly measurements of infrared cloud brightness temperatures is converted to rainfall rates. A Fourier fit then provides the diurnal and semidiurnal rainfall rate harmonics of zonal wavenumbers westward 6 to eastward 6 which in turn are used to calculate tidal heating functions.

Model simulations with radiative and latent heat forcing are always performed separately. This does not pose a problem because GSWM is a linear model. For the same reason, GSWM does not account for any non-linear tidal forcing processes such as wave-wave interaction. They are only included in non-linear models such as in the TIME-GCM.

### 3.2.2 TIME-GCM

The NCAR thermosphere-ionosphere-mesosphere-electrodynamics general circulation model (TIME-GCM) is a three-dimensional, time-dependent general circulation model to simulate Earth's atmosphere from 30-500 km altitude [Roble and Ridley, 1994; Roble, 1996]. As the result of more than 20 years of research and development, it combines all of the features of its predecessors, the TGCM [Dickinson *et al.*, 1981], TIGCM [Roble *et al.*, 1988], and TIE-GCM [Richmond *et al.*, 1992], but with the lower model boundary extended downward to 30 km altitude. The model time-step is four minutes. It uses a finite differencing technique to obtain a self-consistent solution for the coupled, nonlinear equations of hydrodynamics, thermodynamics, continuity of the neutral gas and for the coupling between the dynamics and the composition. Furthermore, TIME-GCM includes a self-consistent aeronomic scheme for the electrodynamic interactions between the thermosphere and ionosphere.

The output of the TIME-GCM consists of 30 fields on a three-dimensional latitude, longitude, pressure grid. Geographic longitude begins at 180°W and continues around the globe with a 5° resolution. Geographic latitude resolution is also 5°, from 87.5°S to 87.5°N. The vertical dimension is in a log pressure scale ( $\ln(p_0/p)$ ,  $p_0 = 5 \cdot 10^{-7}$  hPa) from -17 at the bottom (approximately 30 km) to +5 at the top (varying in altitude up to about 500 km). The vertical resolution is 0.5 (about 3-4 km in the mesosphere), for a total of 45 pressures.

Because the model does not extend to the ground, suitable lower boundary conditions must be employed, particularly for GWs, PWs, and tides that are excited in the troposphere and lower stratosphere and propagate upward into the model domain. Hagan and Roble [2001] overview the inherent assumptions invoked at the

lower TIME-GCM boundary near 30 km. Subgrid-scale GWs are parameterized with a modified Lindzen scheme that is extended to include molecular damping effects in the lower thermosphere. The GW parameterization scheme can be tuned to better match observations, i.e. by modifying the GW spectrum or by inducing hemispheric asymmetries in the GW amplitudes. Daily values of 10 hPa geopotential height data from the National Center for Environmental Prediction (NCEP) are used to specify the location, amplitude, and movement of PW structures. GSWM (with radiative forcing only) provides the lower boundary conditions for the migrating diurnal and semidiurnal tidal fields. Thus, TIME-GCM accounts for tropospheric radiative forcing of migrating tides but it does not account for the tropospheric forcing of nonmigrating tides and the latent heat source. Wave components forced by those processes are suppressed in the model output. The model, however, includes all tidal sources above its lower boundary, including solar radiative and non-linear forcing processes such as wave-wave interaction. *Hagan and Roble* [2001] have shown that the w2 and s0 nonmigrating diurnal tidal components are predominantly forced by the latter mechanism.

TIME-GCM also includes realistic solar and geomagnetic forcing that prevailed for the specific model day. The daily 10.7-cm radio solar radio flux is used as a proxy for the solar irradiance variability. 3-hour  $Kp$  values are used to specify variable auroral precipitation, cross-cap potential fields, and hemispheric power at the model upper boundary near 500 km. The daily  $Ap$  index is used as a proxy for the geomagnetic activity.

Using NCEP data and solar and geomagnetic indices as model input allows the simulation of specific days and years and to facilitate direct comparisons with observations. In support of the TIMED mission, there are currently 3 1/2 years (January 2002 to June 2005) of model results available (R.G. Roble, private communication). Model fields are stored with one hour time resolution which is unique for general circulation models, due to the very large data amount. Data from this simulation are used later in the section and in sections 4 and 5. They have also been used to mimic TIMED observations by sampling the model output along the satellite instruments footprints (see section 3.3 for details). Although the current simulations are realistic in the sense that they base upon the best knowledge of the prevailing geophysical conditions, it is anticipated that the comparative analyses between the TIME-GCM and the TIMED data will significantly improve the present process understanding. The model results are thus not final in any way but will be continuously improved in the future, particularly in the light of current model further developments. These include doubling the horizontal and vertical resolutions, the inclusion of nonmigrating tides at the lower model boundary, and an improved GW parameterization scheme (M.E. Hagan, private communication).

TIME-GCM has also been run for the time periods of both CRISTA flights [*Oberheide et al.*, 2002b, 2003a; *Hagan et al.*, 2002]. The most recent simulation for CRISTA-1 (November 1994) uses a version of the model with doubled vertical resolution. The GW parameterization scheme has been tuned to better match geostrophic winds derived from the CRISTA geopotential data and the observed PW signatures [*Oberheide et al.*, 2006a]. Inducing hemispheric asymmetries in the GW amplitudes significantly improved the agreement between the model and the measurement for the geostrophic winds (Figure 3.4) and for PWs and tides (not shown). The model

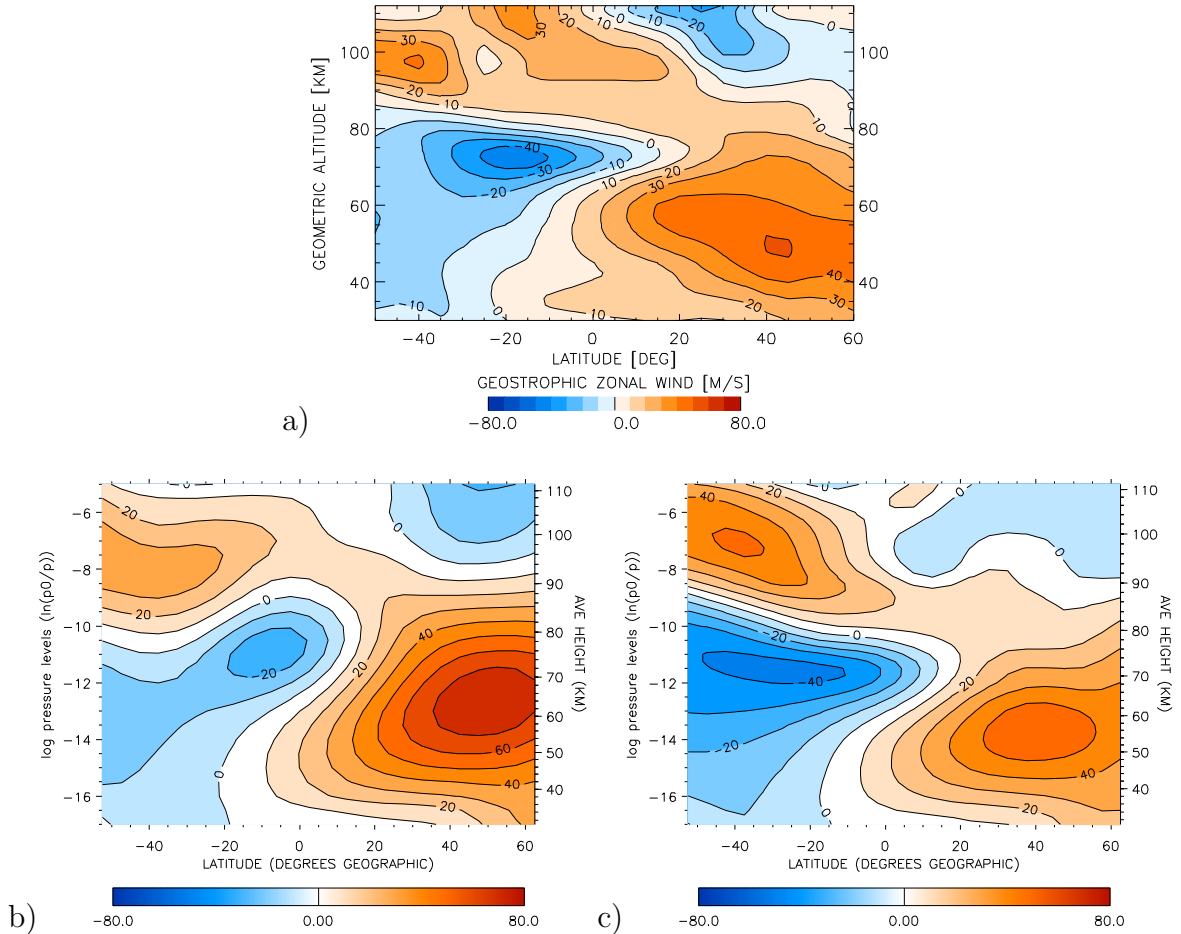


Figure 3.4: a) Geostrophic mean zonal wind from CRISTA on November 9, 1994. b) Mean zonal wind from TIME-GCM *before* tuning the GW parameterization scheme. c) Mean zonal wind *after* the tuning. Note the different vertical coordinates.

run with tuned GW parameterization scheme gives a much better representation of the SH and NH jet locations and wind speeds. Apart from the analyses presented in section 5, work in progress will use the improved GW parameterization for the long-term TIMED simulations.

Forcing TIME-GCM with specified lower and upper boundary conditions is very useful for comparative analyses with observations and thus to improve process understanding. There are nevertheless some shortcomings in the approach, particularly with the lower boundary conditions. Using climatological GSWM tides will lead to an underestimate of short-term tidal variability and the associated energy and momentum transfer in the MLT. Neglecting the latent heat source results in unrealistic small nonmigrating tides and an underestimate of possible interactions of these components with the mean flow. Furthermore, the high variability of tropospheric convection does not only affect nonmigrating tides but also the convectively forced GWs. Accounting for the lower atmosphere variability therefore requires the coupling of models like the TIME-GCM with troposphere/stratosphere models which also allows to run long-term climate simulations. It is possible to couple the TIME-GCM with such a model, the climate community model version 3 (CCM3) [Liu and Roble, 2002]. A more recent development is the new whole atmosphere chemistry climate model (WACCM) [Sassi

*et al.*, 2002] that combines the upper atmosphere physics and chemistry of TIME-GCM with tropospheric and stratospheric physics and chemistry from CCM3 in one single model. Very few coupled models exist that extend from the ground to the thermosphere. One of those is the extended CMAM. It is used for the comparative analyses in section 4 because considerable tidal analysis has already been done with the model output.

### 3.2.3 Extended CMAM

The extended Canadian Middle Atmosphere Model (extended CMAM) [*Fomichev et al.*, 2002] is based on the standard version of the CMAM. It extends from the ground to about 200 km with 70 levels in the model (2.5 km resolution in the mesosphere, 17 levels in the troposphere). The extended CMAM is a spectral model with T32 triangular truncation which translates to a horizontal resolution of about 6°. Parameterizations of most of the important physical processes from the surface to the lower thermosphere are included. They include EUV, Schumann-Runge (SR) band radiation, CO<sub>2</sub> NLTE effects, parameterized chemical heating, molecular viscosity, molecular thermal diffusion and ion drag. The present model version does not have interactive chemistry and it simulates only the neutral atmosphere (i.e., no ionized gases or auroral effects). A recent paper by *McLandress et al.* [2006] overviews the extended CMAM capabilities to simulate the large-scale dynamics of the MLT.

An important component of the model is the non-orographic gravity wave drag (GWD) parameterization that brings about the mesospheric zonal mean zonal wind reversal and provides additional wave forcing for the quasi-biennial and mesospheric semi-annual oscillations in the tropics. In the model the Doppler-spread parameterization of Hines is used (see *Fomichev et al.* [2002] for details). The vertical eddy diffusivity and heating that are produced by the Hines parameterization are also employed.

Tropospheric convective parameterization schemes have a strong impact on the middle atmosphere through the generation of waves by latent heating. The extended CMAM uses the scheme of *Zhang and McFarlane* [1995] that can produce a realistic amount of temporal variability of precipitation. However, *Horinouchi et al.* [2003] emphasize that different convective parameterizations produce very different spectra of upward propagating waves in GCMs. One goal of the ongoing collaboration with the model owners is to test such schemes through comparative analysis with the nonmigrating tides from the TIDI data. The present nonmigrating tide simulations are described by *Ward et al.* [2005]. They are compared to the CRISTA and TIDI results in section 4.

## 3.3 The sampling problem: How to compare models with observations?

A comparative analysis and even a comparison of model output with satellite-borne observations is not as straightforward as one might expect. This particularly applies to the mesosphere and thermosphere where short-term variations due to dynamical

effects such as fast traveling PWs, tides and GWs, and due to radiation and particle precipitation are large. The full output of atmospheric models is usually provided on a regular space-time grid or, for spectral models, as Fourier components. A satellite instrument, however, samples the atmosphere asynchronously (i.e., irregular distribution of the measurements in space and time). As a consequence, fast processes in the atmosphere are observed in a completely different way as compared to their model representation.

The global-scale wave perturbation field  $\tilde{T}$  (tides and PWs) as it shows up in a model is a function of Universal Time (UT). At a particular latitude it is

$$\tilde{T} = \sum_{s,n} T_{s,n} \cos[\omega_n(t_{UT} - t_{s,n}) - s\lambda], \quad (3.1)$$

where  $T_{s,n}$  is the wave amplitude,  $\omega_n$  is the frequency,  $t_{s,n}$  is the time of maximum amplitude with respect to  $0^\circ$  longitude,  $s$  is the zonal wavenumber, and  $\lambda$  is the longitude (in radians). A negative (positive) value of  $s$  represents westward (eastward) phase progression. The index  $n$  (may be non-integer) defines the wave frequency by

$$\omega_n = \frac{2\pi n}{24 \text{ hours}}, \quad (3.2)$$

such that  $n = 1$  is the diurnal and  $n = 2$  is the semidiurnal tide. Planetary waves are indicated by values of  $n$  between 0 and 1, i.e. the prominent Quasi-Two-Day-Wave (QTDW) is  $n = 0.5$ . The sampling of such a wave perturbation by a satellite is best demonstrated in a simple example (for a more thorough discussion see *Oberheide et al.* [2003b]).

Neglecting Earth's movement around the Sun, a satellite orbit is fixed in space with the Earth rotating beneath it. The period of a satellite in a low Earth orbit (some hundred kilometers) is approximately 90 minutes. Within this time, the Earth rotates  $22.5^\circ$  such that the LST of a satellite footprint at a given latitude and orbit node remains the same from one orbit to the next. A fast westward moving wave of zonal wavenumber 1 and 24 hour period (i.e., the migrating diurnal tide) is thus always measured in the same phase when observed from a satellite instrument. The observed phase is different for ascending and descending orbit nodes. In this sense, satellites always make measurements as a function of LST and not as function of UT. The relationship between both time frames (in hours) is given by

$$t_{LST} = t_{UT} + \frac{\lambda}{2\pi} \cdot 24 \text{ h}. \quad (3.3)$$

The example wave is therefore observed as a zonally symmetric feature and not as a zonal wavenumber 1 as in the model time frame that is UT. The same argument also applies to other fast traveling waves and Equation 3.1 transforms to

$$\tilde{T} = \sum_{s,n} T_{s,n} \cos[\omega_n(t_{LST} - t_{s,n}) - (s + n)\lambda]. \quad (3.4)$$

A satellite observes a global-scale wave of zonal wavenumber  $s$  and frequency  $\omega_n$  as a wavenumber  $s + n$  feature ( $n = -s$  for migrating tides). Figure 3.5 shows these sampling artifacts for several diurnal and semidiurnal tidal components. Four

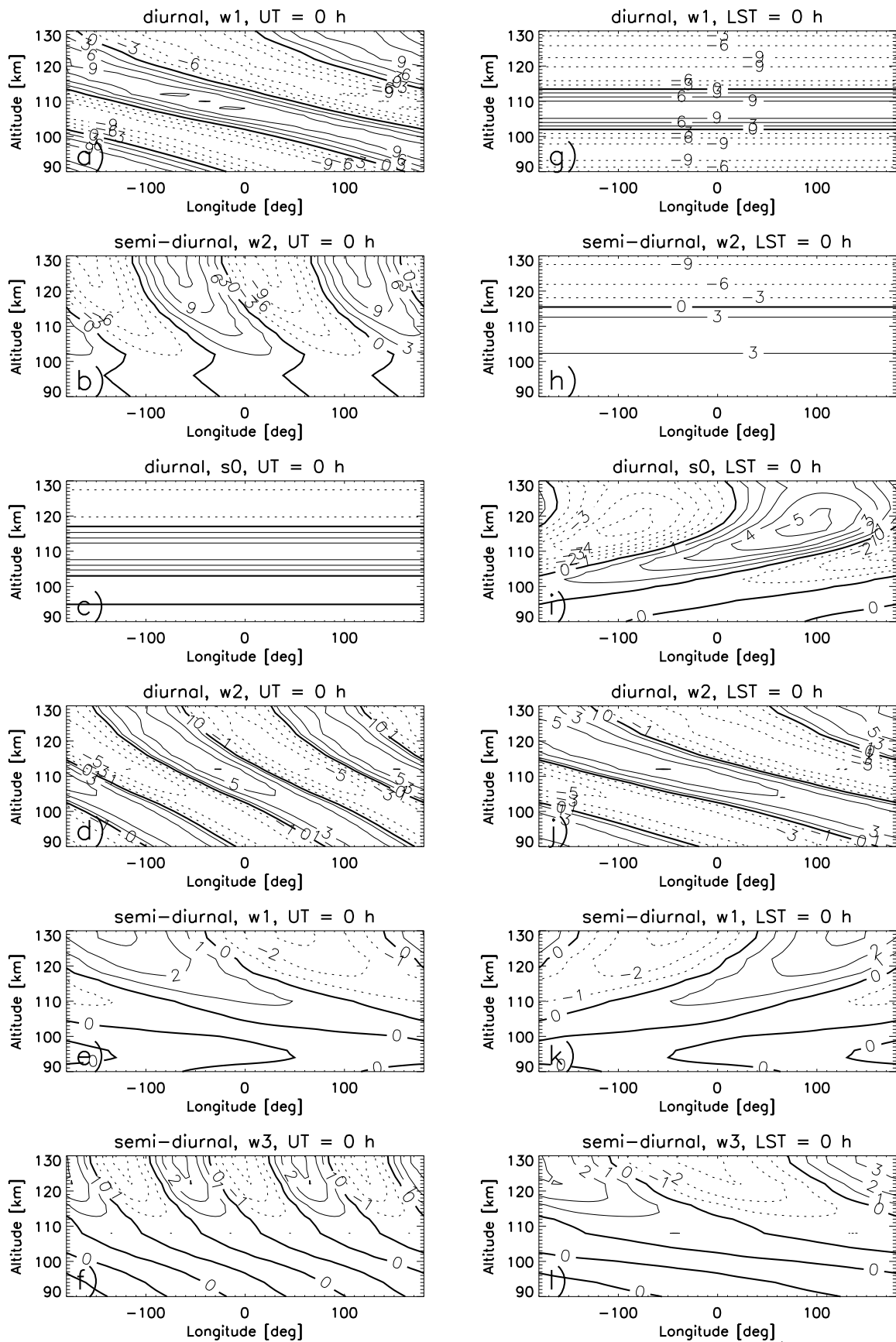


Figure 3.5: Diurnal and semidiurnal tidal temperature perturbations (11 January 1993) at  $2.5^\circ\text{N}$  as simulated by the TIME-GCM for (a-f) a constant UT of 0 h and for (g-l) a constant LST of 0 h. Four nonmigrating tidal components (s0, w2 diurnal; w1, w2 semidiurnal) are sampled as zonal wavenumber 1 by a satellite instrument.

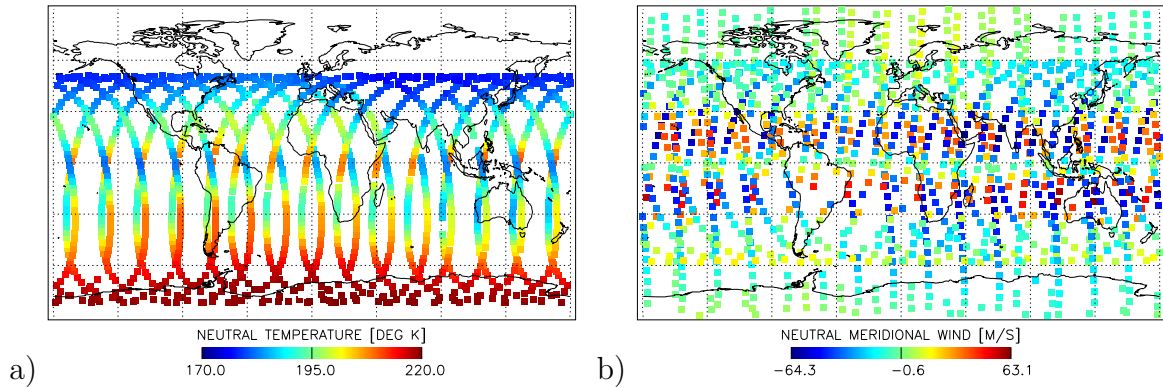


Figure 3.6: a) TIME-GCM temperature sampled along the SABER tangent points. Data and sampling shown are for 16 April 2002 at model level -8 ( $\sim 93$  km altitude). b) Same for the meridional wind sampled along the TIDI tangent points. Gaps over South America occur when the satellite flies through the South Atlantic Anomaly.

nonmigrating tidal components of different frequencies and zonal wavenumbers are sampled as a wave of zonal wavenumber 1. Migrating tides are always observed as zonally symmetric oscillations. Another example is the QTDW of zonal wavenumber 3 which is observed as a zonal wavenumber 2.5 feature (not shown in the Figure). Any tidal analysis of satellite measurements needs to deconvolve the observed wave patterns into the corresponding components, that is, the wavenumber/frequency pairs.

The asymptotic satellite sampling makes this deconvolution quite challenging and will likely result in spectral leakage when using Fourier methods [Salby, 1982]. This motivated the development of the Satellite and Universal Time (SATUT) sampling procedure for GSWM and TIME-GCM [Oberheide *et al.*, 2003b]. The basic idea is to provide the winds, temperatures, and trace constituents that would be measured if the satellite flew through the model atmosphere. Additional (i.e., not measured by the instrument) model fields are also provided. Locations (latitude and longitude) and UT of the instrument tangent points (footprints) are extracted from the measured data. The model histories of GSWM and TIME-GCM are linearly interpolated in space and time to the instrument footprints. Missing or "bad" instrument data are treated as missing values and are not included. Sampled TIME-GCM and GSWM data are available for CRISTA [Hagan *et al.*, 2002; Oberheide *et al.*, 2006a], SABER [Oberheide *et al.*, 2003b], and TIDI [Oberheide *et al.*, 2005, 2006b] with an altitude coverage larger than the measurements. Selected data sets may be downloaded from <http://timed.hao.ucar.edu/cedar/satut/>. Figure 3.6 shows an example for SABER and TIDI sampling of the TIME-GCM. Tidal signatures are evident as the differences between data on the ascending and descending orbit nodes. A number of middle atmosphere models (i.e., WACCM) nowadays possess similar sampling routines.

Using satellite sampled model output for the comparative analysis of observational and model data has a number of benefits. First, it provides an excellent algorithm testbed. Analyzing the sampled model output in exactly the same way as the measured data allows to estimate possible artifacts (i.e., aliasing) that are associated with the asymptotic satellite sampling and with the assumptions inherent in the analysis approach. This is because one can contrast these results with the analysis of the



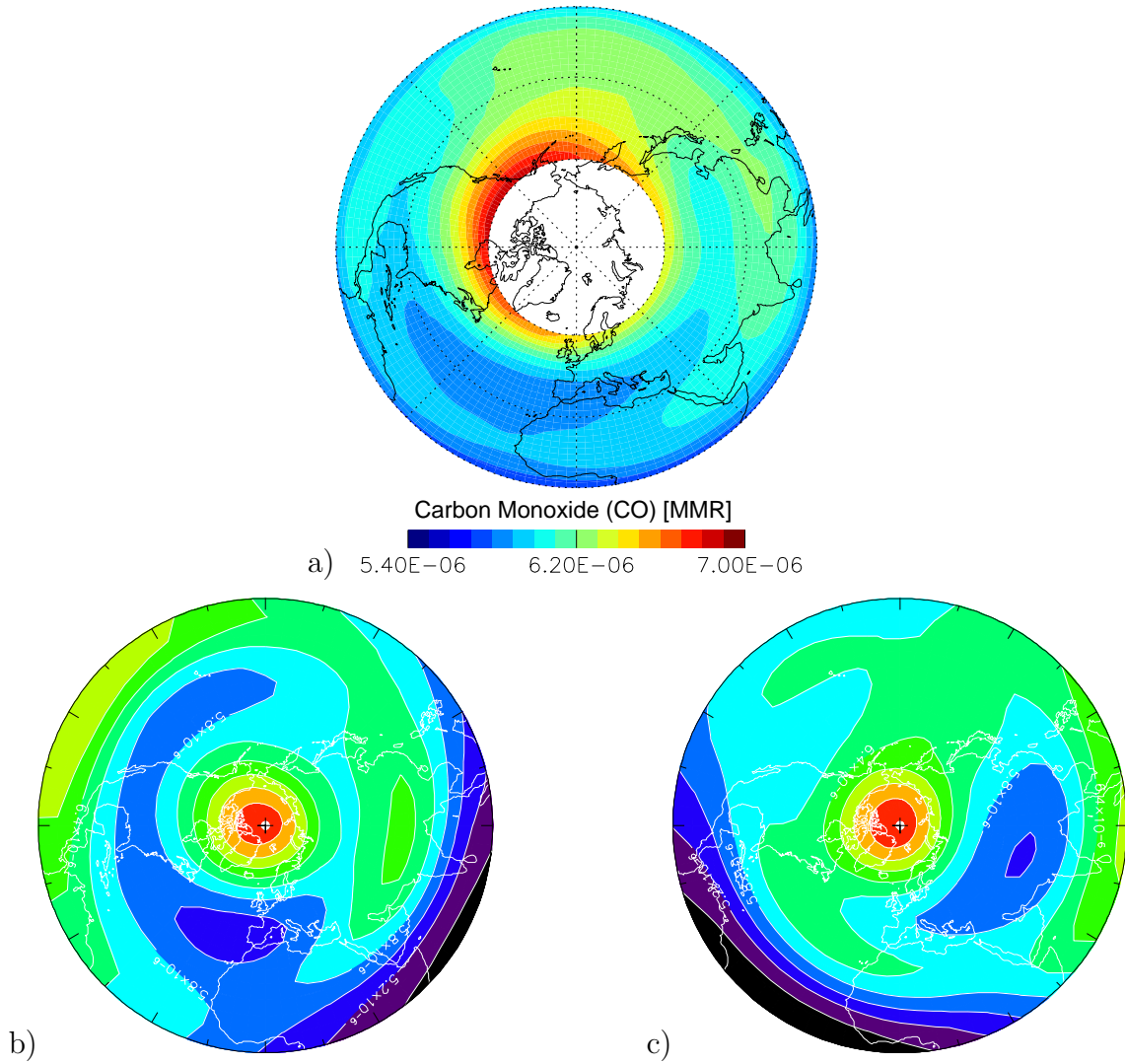


Figure 3.8: a) TIME-GCM Carbon monoxide (CO) mass mixing ratio at model level -10 (80 km) for 9 November 1994, sampled along the CRISTA footprints. The contour interval is 0.15 ppm. b) Full model output for 10 h UT. Note the different color scheme: Mass mixing range is from 4.6 to 7.8 ppm with an interval of 0.3 ppm. c) Same as b) but for 18 h UT.

also need to be accounted for. This is inherently done by sampling the model along the satellite instrument footprints. Figure 3.8 shows the differences between carbon monoxide (CO) model distributions in the LST and UT frames. TIME-GCM CO mass mixing ratio sampled along the CRISTA footprints (Figure 3.8a) differs significantly from the full model output for fixed UTs (Figures 3.8b,c). This is basically due to tidal wind transport that results in the very different tongues of CO poor and rich air for the two different UTs shown.

## 4 Nonmigrating tides

### 4.1 Diurnal temperature tides in the equatorial lower thermosphere from CRISTA

The CRISTA temperature data remain to this date the most precise satellite measurements in the lower thermosphere [Gusev *et al.*, 2006]. Their vertical extent to 120 km altitude allows for the first time an analysis of the migrating and several nonmigrating tidal components in a region of Earth's atmosphere where prior to CRISTA no global day- and nighttime temperatures were available. The specifics of the instrument's measuring schemes limit the tidal analysis to two days (Nov. 9, 1994 and Aug. 14, 1997). These snapshots and a comparison to the tidal predictions of three models of differing character (GSWM, TIME-GCM, extended CMAM) nevertheless provide new information about the magnitude of the tides, their relative contribution, and the principle forcing mechanisms.

#### 4.1.1 Data analysis

A satellite instrument observes tides in the LST frame such that Equation 3.4 applies (section 3.3). For CRISTA, this Equation cannot be solved by Fourier fitting the data because the lack of LST coverage prevents any spectral tidal analysis. It was thus necessary to develop a non-spectral analysis method to deconvolve the different tidal components from the observed wave structure [Oberheide *et al.*, 2002b]. Its specifics are reviewed below, because they are essential for the understanding and the interpretation of the results. The tidal deconvolution method is also becoming more and more used in the community and has already been applied to the data of the LIMS instrument [Lieberman *et al.*, 2004]. Work in progress focuses on its application to the wind data from the HRDI instrument on board UARS (R.S. Lieberman, private communication).

CRISTA nonmigrating tidal analysis is basically a four step method: (1) interpolate the ascending (asc) and descending (dsc) temperature measurements separately to a regular horizontal grid; (2) difference the gridded asc and dsc data; (3) fit several zonal wavenumbers to the differenced data; and (4) deconvolve the waves in the asc-dsc difference fields in their westward/eastward/standing components with respect to the satellite sampling.

(1) The interpolation to the regular  $5^\circ \times 5^\circ$  horizontal grid is done by averaging the asc and dsc data separately with a two-dimensional weighting function that resembles a triangle with a half width of  $15^\circ$  in latitude and  $25^\circ$  in longitude. It is the same function that has been used to derive geostrophic winds from CRISTA data [Oberheide *et al.*, 2002a]. The averaging preserves quasi-stationary, large-scale horizontal structures such as PWs, but smoothes out small-scale fluctuations such as GWs or turbulence. The comparatively large half widths of the filter function ensure that nearly the same number of data points on the asc and dsc parts of the orbits are averaged.

(2) The gridded asc ( $T_{asc}$ ) and dsc ( $T_{dsc}$ ) temperatures are then subtracted from each other:  $\Delta T = T_{asc} - T_{dsc}$ . At  $7.5^\circ\text{N}$  (November 1994) and  $2.5^\circ\text{N}$  (August 1997),

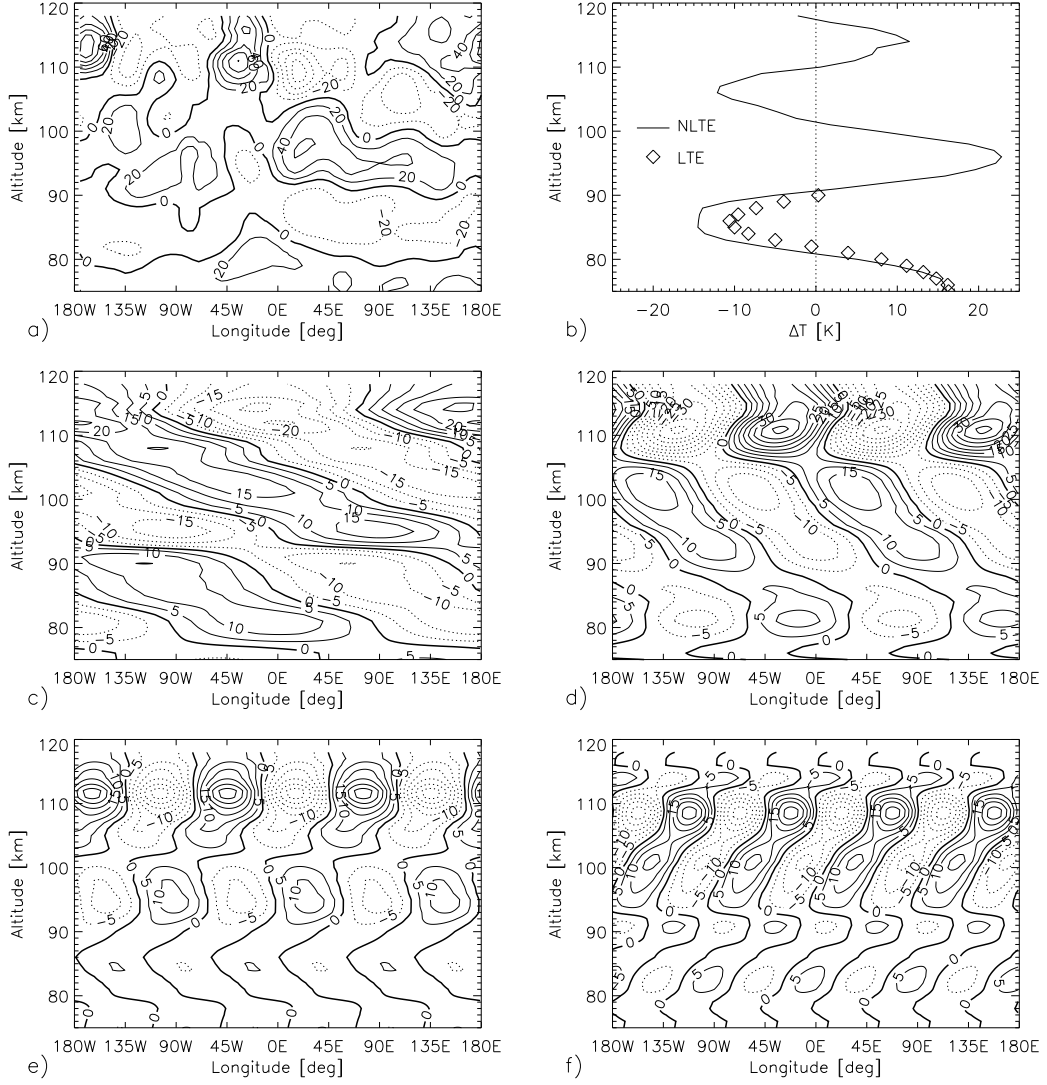


Figure 4.1: Temperature differences between the asc and dsc orbit nodes at  $7.5^\circ\text{N}$  for Nov. 9, 1994. a): Observation, contour interval is 20 K. b) Zonal mean temperature difference ( $s' = 0$ ) in comparison with the LTE values from *Oberheide et al.* [2000]. c-f) Wavenumber  $s' = 1 - 4$  fits to the observational data. Contour interval is 5 K.

the CRISTA orbit geometry (section 3.1.2) is such that asc and dsc data are 12 hours apart in LST. Consequently, all semidiurnal tidal components, independent of their zonal wavenumber, vanish in  $\Delta T$  because they are observed in the same phase on the asc and dsc orbit nodes. The wave patterns in  $\Delta T$  can thus be attributed to the diurnal tide alone, assuming that terdiurnal tides are negligible. Recent results from MLS [*Forbes and Wu, 2006*] show terdiurnal amplitudes between 0.5 and 1 K at 86 km altitude which justifies to disregard them. Quaterdiurnal tides can also be neglected because they are measured in the same phase on the asc and dsc orbit nodes and vanish in  $\Delta T$ .

(3) Figure 4.1a shows the measured  $\Delta T$  (Nov. 9, 1994) along with zonal wavenumber  $s' = 0 - 4$  least-square fits to the data (Figure 4.1b-f). Note that the minima/maxima in the measured  $\Delta T$  are two times the sum of the tidal amplitudes if

all tidal components are in phase. At several longitudes (i.e., 180°W, 45°W, 115 km),  $\Delta T$  reaches 80 K which already points to very large nonmigrating tidal effects in the lower thermosphere.

Below 80 km, the  $s' = 0$  fit result (Figure 4.1b) agrees well with the results reported by *Oberheide et al.* [2000] based upon temperatures that were retrieved assuming local thermodynamical equilibrium (LTE). Above 80 km, non-LTE becomes more important resulting in the apparent underestimate of the LTE wave amplitude compared to the non-LTE fit. Wavenumber  $s' = 1$  (Figure 4.1c) reveals a maximum signature of 25 K at 115 km. The  $s' = 2$  pattern (Figure 4.1d) is most pronounced at 112 km (40 K). The  $s' = 3$  (Figure 4.1e) and  $s' = 4$  (Figure 4.1f) fits peak slightly higher and lower than 110 km with perturbations of about 25-30 K. CRISTA-2 results (August 1997) are similar but with different wave amplitudes (not shown).

(4) Further analysis of the fit results is now required to account for the satellite sampling of diurnal oscillations. In general, an observed diurnal wavenumber  $s'$  is a linear combination of two diurnal tidal components:  $s = s' - 1$  and  $s = -s' - 1$  (section 3.3). A zonal wavenumber  $s > 0$  indicates eastward propagation and  $s < 0$  indicates westward propagation. Table 4.1 summarizes the relationship between observed and "real" atmospheric zonal wavenumbers.

The challenge in the CRISTA tidal analysis is the deconvolution of the  $s' = 1 - 4$  fits into their corresponding nonmigrating tidal components  $s$ . Briefly, the squared fit amplitudes  $T_0^2(s')$  can be expressed as a function of the tidal component amplitudes  $T_{-s'-1,1}$ ,  $T_{s'-1,1}$ , and a phase factor  $\Psi(s')$  that is basically the sum of the tidal component phases  $t_{-s'-1,1}$  and  $t_{s'-1,1}$ :

$$T_0^2(s') = T_{-s'-1,1}^2 + T_{s'-1,1}^2 + 2T_{-s'-1,1}T_{s'-1,1} \cos \Psi(s') = A + B \cos \Psi(s'). \quad (4.1)$$

At altitudes where the cosine term in Equation 4.1 vanishes or equals  $\pm 1$ , one can calculate  $A$  and  $B$  and, after linear interpolation to altitude  $z$ , the tidal amplitudes and phases. Appendix A3 gives the mathematical details and also elucidates the inherent limitations of the deconvolution method: (i) vertical gradients of the tidal component amplitudes must be reasonably small (i.e., an exponential amplitude growth with height introduces an amplitude error of  $\sim 10\%$ ); (ii) upward propagation and thus tidal forcing from below is assumed. These limitations only apply to the analysis of the nonmigrating tides. The migrating tide (w1, observed as  $s' = 0$ ) is analyzed with a different method that is described in detail by *Oberheide et al.* [2000]. Hence, it is not reviewed again.

Table 4.1: Relationship between  $s'$  and  $s$  for diurnal period.

$s'$	$s$	tidal components
0	-1	w1
1	-2; 0	w2; s0
2	-3; 1	w3; e1
3	-4; 2	w4; e2
4	-5; 3	w5; e3

### 4.1.2 Error estimate

Apart from the uncertainties introduced by the deconvolution method, there are two additional error sources that need to be considered: aliasing effects of non-tidal phenomena such as fast-moving or transient PWs, and a likely underestimate of the resulting amplitudes due to the inherent smoothing of the horizontal data gridding. The latter, on the other hand, also reduces the temperature noise error such that it is negligible after propagation through the deconvolution method. Estimates of the aliasing and gridding errors are deduced from model simulations.

Using the SATUT procedure (section 3.3), GSWM nonmigrating tides and TIME-GCM temperatures are sampled along the CRISTA footprints and then linearly superposed. The resulting satellite sampled model temperatures give a realistic representation of tidal amplitude growth and relative phasing, and of non-tidal signatures. They are then analyzed in exactly the same way as the measured CRISTA temperatures. By contrasting the derived amplitudes and phases with the full model output, one obtains the error estimates shown in Table 4.2. They account for sampling effects (including small measurement gaps), PW aliasing in the gridded asc and dsc data, and the assumptions of the deconvolution method. Adding the CRISTA random noise (section 3.1.2) to the sampled model data does not significantly change the errors that are thus governed by the method.

The horizontal gridding with its inherent smoothing leads to an underestimate of the tidal amplitudes. As a purely geometric effect, it can be accounted for by a scaling factor. The uncertainties of the scaling factors are included in the amplitude errors. All tidal amplitudes shown in the following are scaled by the factors given in Table 4.2. For a comparison of scaled and unscaled amplitudes see *Oberheide and Gusev* [2002]. Phases are not affected by the scaling. A more detailed discussion of scaling factors and their accuracy is given in the context of the TIDI error analysis in section 4.3.2. CRISTA amplitude errors are slightly height dependent (0.8 - 1 K for all nonmigrating components). To simplify matters, a height independent value of 1 K is used in the following. The w1 error is taken from *Oberheide and Gusev* [2002].

Table 4.2: Scaling Factors applied to the derived diurnal tidal amplitudes, and amplitude and phase errors. Given values are for the scaled amplitudes and apply to CRISTA-1 and CRISTA-2 results.

component	scaling factor	amplitude error [K]	phase error [hours]
w5	1.40	1.0	2.5
w4	1.17	1.0	2.0
w3	1.05	1.0	1.0
w2	1.05	1.0	1.0
w1	1.00	1.7	1.0
s0	1.05	1.0	4.0
e1	1.05	1.0	1.0
e2	1.17	1.0	2.0
e3	1.40	1.0	3.5

### 4.1.3 Results and discussion

*CRISTA-1, November 1994*

Figure 4.2 shows the derived amplitudes and phases for the eight nonmigrating diurnal components w5, w4, w3, w2, s0, e1, e2, e3 and the migrating tide w1 for Nov. 9, 1994 along with the predictions of the GSWM, TIME-GCM and extended CMAM models. GSWM nonmigrating tides are for November from the model run with latent heat forcing only (section 3.2.1). They do not include any tidal forcing due to solar insolation absorption. In contrast, the GSWM migrating tide (w1) is radiatively forced only. TIME-GCM tides are from the model run for the CRISTA-1 time period described in section 3.2.2 with migrating tides at the lower boundary specified by GSWM (radiative forcing only, without latent heating) and 10 hPa temperatures and geopotential data from NCEP. Both models thus account for quite different tidal sources: nonmigrating tides in TIME-GCM are predominantly forced by the non-linear interaction between the migrating tide and PWs [Hagan and Roble, 2001] whereas GSWM only includes the latent heat source associated with deep convective systems in the tropical troposphere. The latter source is not accounted for in TIME-GCM. The differing character of the GSWM and TIME-GCM tidal predictions allows an analysis of the predominant tidal forcing mechanisms by comparing them to the CRISTA results. Note that neither model does account for tropospheric radiative forcing of nonmigrating tides.

All these tidal sources, and possible interactions between them, are included in the extended CMAM model. Opposing its tidal predictions to the GSWM and TIME-GCM results thus provides additional information about the forcing mechanisms responsible for the observed tidal signatures and the propagation characteristics of the tides. However, some differences between the models may also be attributable to different parameterization and dissipation schemes. CMAM results are available every four days. Figure 4.2 shows November means with the model standard deviation during this month indicated by the grey shading. Nonmigrating tides in CMAM exhibit a considerable variability, particularly the w2, e1, and e2 components. The model output has not yet been analyzed for the w5 and w4 tidal components.

The observed phases in Figure 4.2 decrease with height, as it is assumed in the deconvolution of the nonmigrating tides. This is consistent with an upward energy propagation and a tidal forcing lower in the atmosphere. It agrees with the predictions of all models. TIME-GCM phases for w5, w4, w3, and s0 are more variable than those of GSWM and CMAM. They partly show phase jumps (i.e., w3 at 90 km) at altitudes with very small amplitudes ( $\leq 1$  K). The significance of the TIME-GCM phase jumps is therefore questionable. They may be an artifact of the spectral analysis.

With the exception of the rather weak s0 component, all observed nonmigrating amplitudes increase with height. The w3, w2, e2, and e3 components have the largest amplitudes and reach 10-15 K at 110 km altitude. The slight amplitude decrease just above 110 km may be associated with the tidal maxima or with some unresolved vertical fine structure. The w5, w4, and e1 amplitudes also increase with height but with maximum values around 5-7 K only. Above 100 km, the combined nonmigrating amplitudes may exceed the migrating tide by an order of magnitude (80 K compared to 8 K). The migrating tide (w1) peaks at 90 km (14 K) with a secondary maximum at 110 km (9 K) and a relative minimum (6 K) between 100 and 110 km altitude.

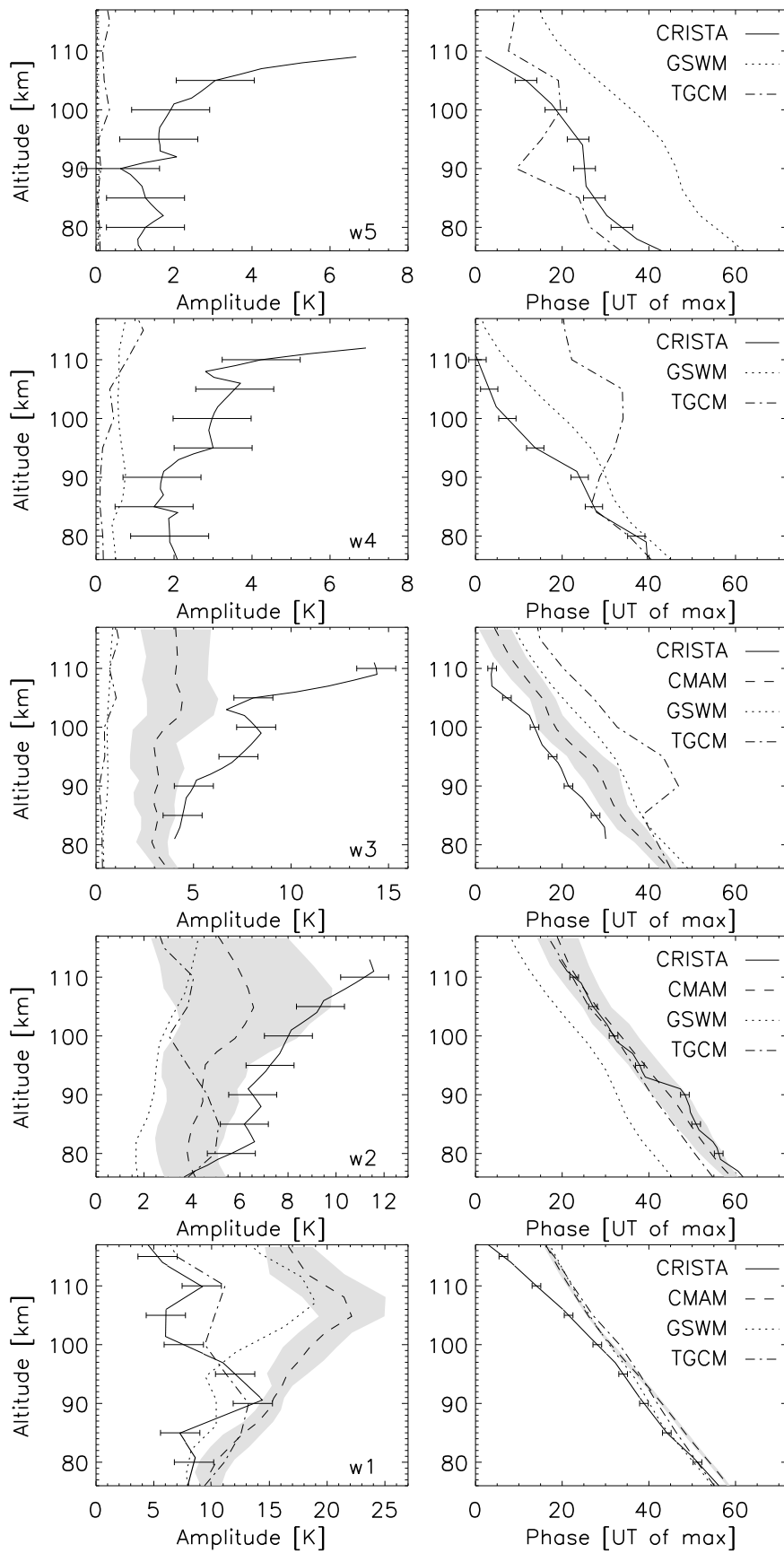


Figure 4.2: Continued on next page.

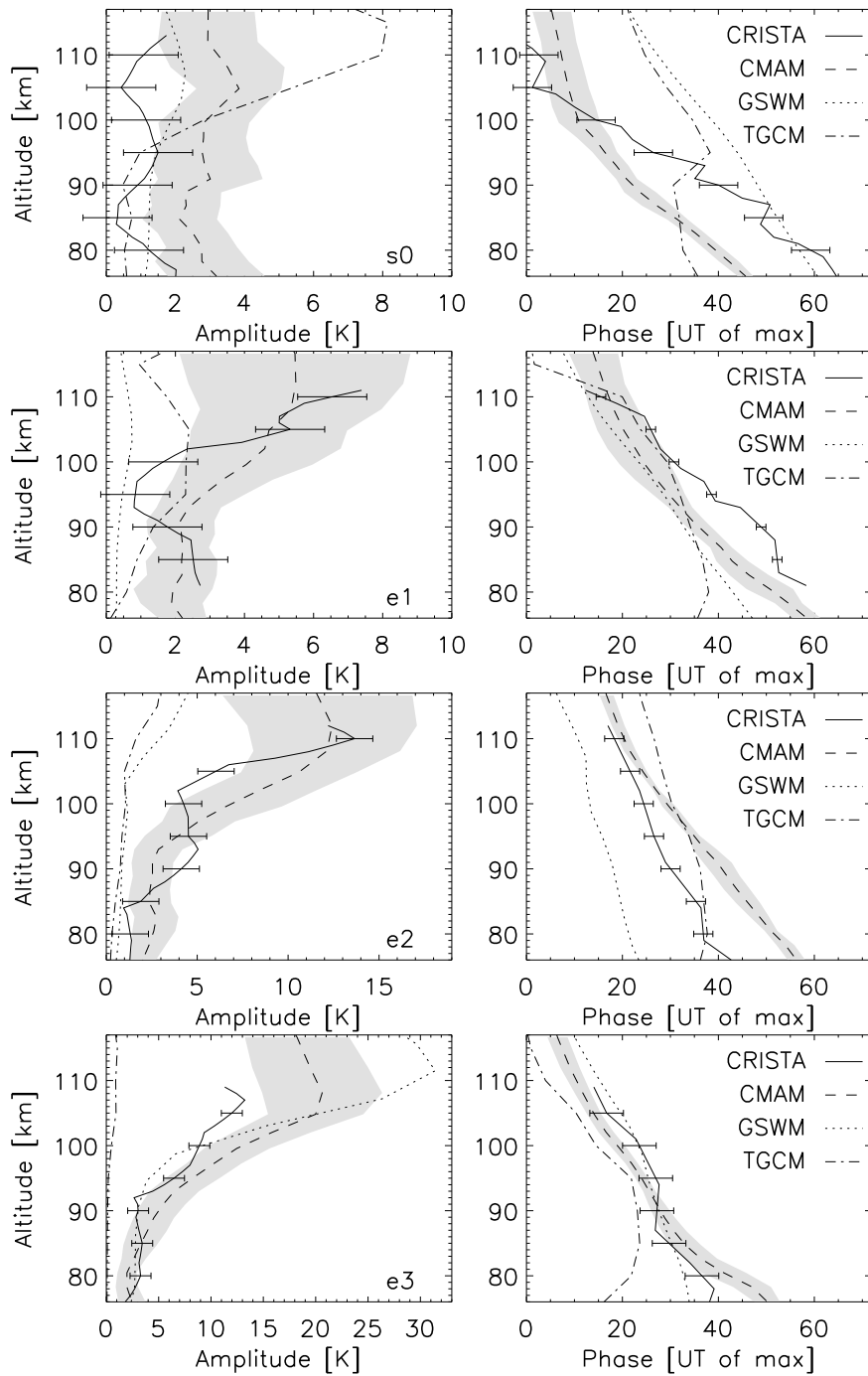


Figure 4.2: Continued from previous page. Comparison of diurnal temperature tides from CRISTA (Nov. 9, 1994, solid line) at  $7.5^\circ\text{N}$  with the model predictions. Error bars are drawn in 5 km increments. Dashed: extended CMAM (November monthly mean); shaded: extended CMAM monthly standard deviation; dotted: GSWM (November, w1 with radiative forcing only, other components with latent heat forcing only); dashed-dotted: TIME-GCM, Nov. 9, 1994.

A componentwise comparison of the observed amplitude and phase structure with the model predictions (Figure 4.2) can now provide information about the tidal sources and the model capabilities to predict a realistic tidal temperature field in the MLT. One important indicator for that is the mean vertical wavelength (Table 4.3). The

consistency of observed and modeled wavelengths is in a sense more important than an absolute agreement because the absolute phasing certainly depends on the specifics of the tidal forcing during each day. An example for that is the occurrence and time evolution of convective systems. Vertical wavelengths rather depend on the specifics of the background atmospheres and dissipation schemes in the models [*Oberheide et al.*, 2000]. Hence, they are more suitable indicators for the propagation characteristics of the tides through the real and the model atmospheres.

GSWM response for w5, w4, w3, and e1 is negligible ( $< 1$  K) such that from the linear tidal model point of view latent heat release in the tropical troposphere is not of much importance. TIME-GCM shows no significant response for w5, w4, w3, and e3 ( $< 1$  K). Because the only nonmigrating tidal sources in TIME-GCM are radiative forcing above 30 km and non-linear interactions between the migrating tide and QSPWs, this points to a rather small contribution of these sources to the four components. The extended CMAM response, on the other hand, is always non-negligible (w5 and w4 are not yet available). Before discussing the details of the nonmigrating tide comparisons, it makes sense to compare the migrating tide (w1) results first.

**w1.** GSWM and extended CMAM generally overestimate the migrating tide. The best amplitude agreement with the observation is provided by the TIME-GCM. This agreement, however, was not obtained until the model GW parameterization scheme was tuned to better match CRISTA geostrophic winds and PW structure (section 3.2.2). Model amplitudes were much larger (similar to GSWM) above the mesopause before the tuning. It clearly underlines the importance of GWs for the propagation and dissipation of tides. The model tuning not only affects the zonal mean zonal wind field and thus the background atmosphere but also the PW field that in turn acts as a longitude dependent filter for upward propagating waves. Whether these changes or the GW drag itself are primarily responsible for the tidal amplitude decrease toward the observation has not yet been resolved. The Canadian warming situation in the NH stratosphere in early November 1994 with its large increase of PW-1 amplitude likely

Table 4.3: Mean vertical wavelengths of the diurnal tidal components from CRISTA, extended CMAM, GSWM, and TIME-GCM at 7.5°N as derived from Figure 4.2 (November). † indicates TIME-GCM values that are affected by phase jumps. See text for details.

component	CRISTA [km]	extended CMAM [km]	GSWM [km]	TIME-GCM [km]
w5	24.9	N/A	21.2	†59.0
w4	19.4	N/A	22.7	†93.7
w3	24.9	24.1	24.8	†28.7
w2	20.6	23.2	26.5	25.8
w1	19.4	22.1	26.3	25.2
s0	12.1	20.1	24.4	†84.8
e1	16.7	20.3	24.3	27.1
e2	35.6	23.2	62.8	58.4
e3	34.9	24.3	40.6	34.7

plays an important role in this context, that is, by the filtering of upward propagating GWs. Section 5.1 gives a more detailed discussion of the Canadian warming and its effects on the GWs. It is thus not surprising that GSWM and extended CMAM do not reproduce the observed migrating tidal amplitude because they have not been tuned to the November 1994 geophysical conditions. However, the vertical wavelengths from all models agree well with the CRISTA observation below 100 km. No model reproduces the shortened CRISTA wavelength above 100 km. In TIME-GCM, this discrepancy is independent of the GW parameterization. Phases from the tuned and untuned model simulations do not differ very much. One may speculate about possible reasons for the observed wavelength decrease, that is, lower thermospheric winds or radiative effects, but it is so far not understood.

**w5 and w4.** From the current comparisons with GSWM and TIME-GCM, the observed tidal amplitude increase above 100 km remains unexplained. GSWM vertical wavelengths basically agree with the observed ones. The much longer TIME-GCM wavelengths in Table 4.3 are caused by phase jumps that are probably an artifact of the model spectral analysis of very small wave signatures. Both models show a decreasing phase with height which in turn indicates an upward energy propagation and a tidal forcing lower in the atmosphere. This is consistent with the basic assumption of the deconvolution method. *Oberheide and Gusev* [2002] speculated that one possible tidal source might be the non-linear interaction between the large w3 component and QSPWs 1 and 2. Upper stratospheric QSPWs in early November 1994 extended well into low and middle latitudes (see section 5.1) such that an efficient forcing might be possible. If this is the case, it is not surprising that neither GSWM nor TIME-GCM reproduce the observed amplitudes. The w3 response in TIME-GCM is negligible and, as a linear model, GSWM does not account for wave-wave interaction forcing. Additional tidal sources, such as radiative forcing in tropospheric water vapor, may also contribute to the observed w5 and w4 amplitudes. Model results by *Hagan et al.* [1997] point to a rather small contribution but revised heating rates by *Lieberman et al.* [2003] indicate that this source may need to be revisited.

**w3.** Only the extended CMAM predicts a non-negligible w3 amplitude of height independent 4 K. This is in reasonable agreement with the observation below 90 km but it differs from the observed amplitude increase to 15 K above 105 km. Again, all models reproduce the observed vertical wavelength of  $\sim 25$  km with tidal forcing in the lower atmosphere. The small GSWM response indicates that latent heat release is not a very important source but additional model runs of the extended CMAM are required to identify the dominant forcing mechanism(s). To date, the observed w3 amplitudes are not understood.

**w2.** TIME-GCM response below 90 km is strong (5 K) with GSWM amplitudes around 2 K. Both model responses (3 K each) are about equal above 100 km. As shown by *Oberheide et al.* [2002b] this suggests that the non-linear interaction between the migrating tide and QSPW-1 is an important forcing mechanism for the observed w2 component below the mesopause. The QSPW-1 in November 1994 extends well into subtropical latitudes with a peak altitude above the stratopause. This behavior is reproduced by the TIME-GCM (see section 5.1 for a detailed discussion of the QSPW-1 in November 1994). It can thus provide an efficient forcing of nonmigrating tides because the migrating tide is already large at these latitudes and altitudes. The la-

tent heat release source becomes equally important at altitudes above the mesopause. This is supported by the extended CMAM that predicts an amplitude twice as large as GSWM and TIME-GCM above 100 km. The extended CMAM monthly mean amplitude is smaller than the observed one but its considerable variability includes days with much larger amplitudes. The vertical wavelength in all models is slightly larger than the wavelength measured by CRISTA but there is still a reasonable agreement.

**s0.** The observed amplitude is small (1 K) and altitude independent. This is basically reproduced by the GSWM and the extended CMAM. The large TIME-GCM amplitude above 100 km is not observed and suggests a different migrating tide - QSPW-1 interaction forcing in the model. Below 90 km, extended CMAM and CRISTA vertical wavelengths are similar but different at altitudes above. GSWM and TIME-GCM wavelengths are much longer. The small amplitudes prevent a further discussion of the observational results.

**e1.** CRISTA and extended CMAM amplitudes agree with each other when accounting for the considerable model variability. The TIME-GCM amplitude maximizes around 100 km and decreases above. Its response is likely caused by the non-linear interaction between the migrating tide and QSPW-2. The small GSWM response suggests that wave-wave interaction forcing is also responsible for the comparatively large extended CMAM amplitude although additional model simulations are required to finally resolve this issue. The vertical wavelength from CRISTA is slightly shorter than those of the models.

**e2.** The e2 component shows the best agreement between CRISTA and extended CMAM. GSWM and TIME-GCM amplitudes are small below 105 km with an increase above, but they are significantly smaller than the observed one. Their vertical wavelengths are much longer ( $\sim 60$  km) than those of the extended CMAM ( $\sim 23$  km) and CRISTA ( $\sim 36$  km). For understanding this difference, it might be illustrative to examine the structure of the e2 component in terms of the classical tidal theory (appendix A2). In an idealized atmosphere, a tidal component is a superposition of various Hough functions that in turn are the eigenfunctions of Laplace's tidal equation. The relative strength of the various Hough functions governs the latitudinal structure and the vertical wavelength of a tidal component. As a general rule, propagating Hough functions (phase decreases with height) maximize at low latitudes whereas trapped Hough functions (constant phase with height) maximize at middle to high latitudes. CRISTA and extended CMAM results are thus consistent with a larger contribution of propagating Hough functions whereas GSWM and TIME-GCM seem to include a larger contribution of trapped Hough functions. A more quantitative assessment is not possible because the real lower thermosphere grossly deviates from the isothermal atmosphere assumption of the classical theory.

**e3.** The comparison suggests that the e3 component is forced by latent heat release in the tropical troposphere alone: the only tidal response comes from GSWM and extended CMAM. Both models apparently underestimate the tidal dissipation at altitudes above 100 km because the modeled amplitudes are too large. The CRISTA vertical wavelength is in-between that of GSWM and extended CMAM. This may be associated with a slightly different propagating/trapped Hough function distribution in the models or with the specifics of the background atmosphere. The good agreement with the vertical wavelength from TIME-GCM is probably fortuitous.

The general dynamical situation in August 1997 was characterized by unusually large QSPW-1 and 2 amplitudes in the SH stratosphere that maximize around 40 km with 1800 gpm amplitude (QSPW-1) at 65°S and 1000 gpm (QSPW-2) at 55°S [Riese *et al.*, 2002]. Although these amplitudes are about twice as large as in November 1994 (NH, see section 5.1 for details), there are two important differences that affect the forcing of nonmigrating tides through wave-wave interaction. The QSPWs in August 1997 are more confined to middle and high latitudes and peak at lower altitudes than in November 1994. They also decay rapidly above their peak altitude with amplitudes < 200 gpm above 60 km. As a result, one must expect a less efficient QSPW-migrating tide interaction forcing because the migrating tide is small below 60 km and poleward of 50°. This is confirmed by the observation (Figure 4.3) that always shows smaller nonmigrating tidal amplitudes than in November 1994, particularly for the westward propagating components that should be more affected by QSPW-migrating tide interaction.

Much of the discussion of the November 1994 results also applies for August 1997. Only the migrating tide (w1) and the three largest nonmigrating components (w2, e1, e3) are discussed more closely in the following. The remaining components (w5, w4, s0, e2) are shown for completeness. As for CRISTA-1, the basic assumption of decreasing phases with height, and thus upward energy propagation and tidal forcing from below, is consistent with the model predictions. The observed mean vertical wavelengths (Table 4.4) in August 1997 are generally similar to the November 1994 results, except for w5 (larger), s0 (larger), and e2 (smaller). The small amplitudes of those components prevent a further discussion.

**w1.** The migrating tide has a maximum amplitude of 17 K at 110 km. It is thus stronger than in November 1994 which is surprising because the migrating tide usually maximizes at the equinox. CRISTA-1 tides, however, are analyzed at 7.5°N and CRISTA-2 tides at 2.5°N such that the larger amplitudes in August 1997 may be a simple latitude effect. The vertical wavelengths of all three models agree well with the observation below 100 km (Figure 4.3). As in November 1994, they are somewhat larger than the observation at altitudes above although the difference is smaller. In contrast to the November 1994 case, TIME-GCM (5 K) now grossly underestimates

Table 4.4: As Table 4.3, but for CRISTA-2 (Aug. 14, 1997) and 2.5°N.

component	CRISTA [km]	extended CMAM [km]	GSWM [km]	TIME-GCM [km]
w5	48.4	N/A	23.2	23.5
w4	24.2	N/A	25.0	25.1
w3	21.0	26.0	26.6	25.0
w2	24.8	23.9	28.0	26.0
w1	20.9	22.6	27.0	25.1
s0	31.2	20.6	25.3	22.6
e1	14.1	18.7	22.2	41.3
e2	20.1	67.7	53.6	36.2
e3	40.7	39.4	23.6	23.8

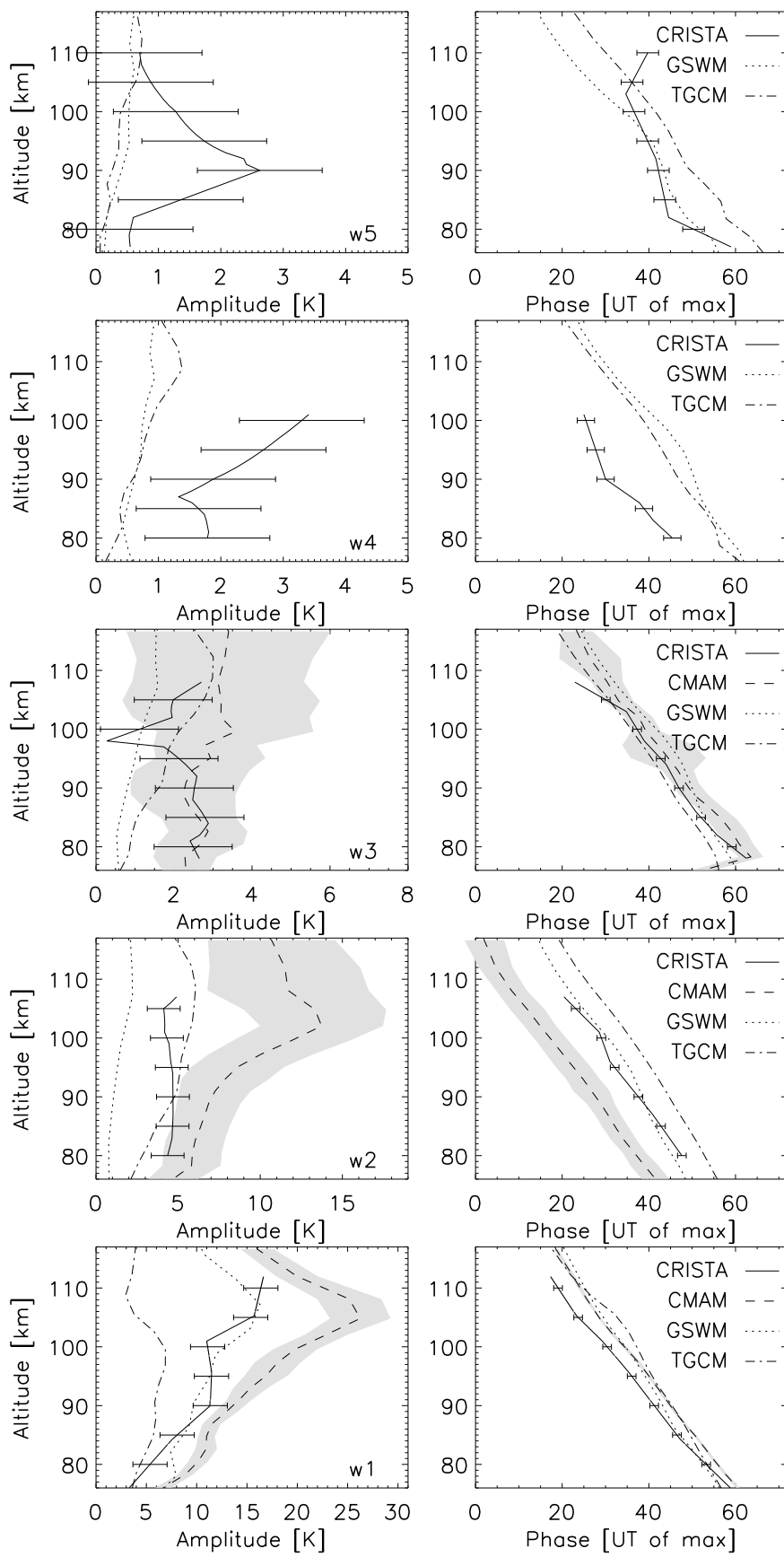


Figure 4.3: Continued on next page.

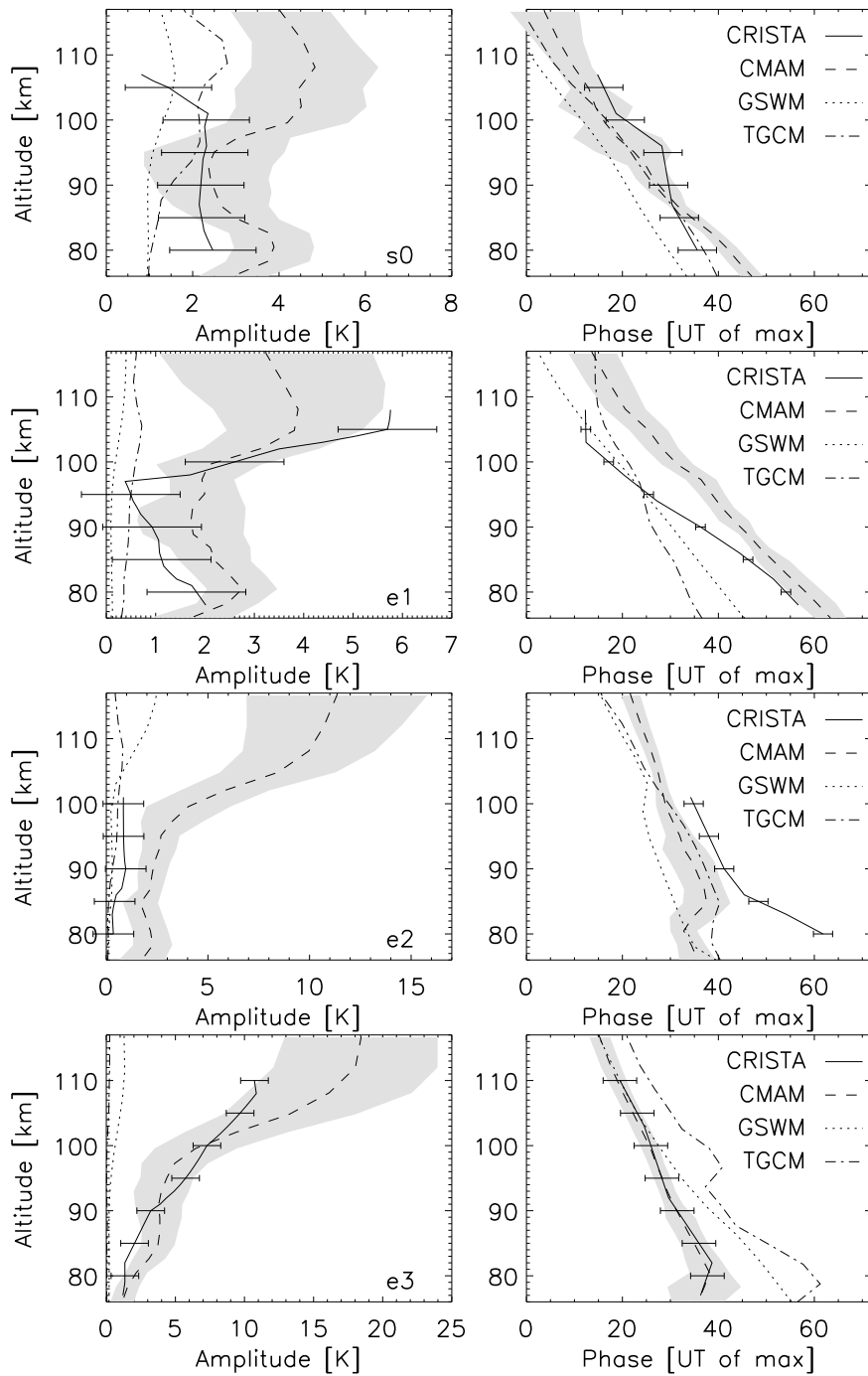


Figure 4.3: Continued from previous page. As Figure 4.2, but for Aug. 14, 1997 (CRISTA, TIME-GCM), and GSWM and extended CMAM results for August. Latitude is  $2.5^{\circ}\text{N}$ .

the tidal amplitude. This is not due to the tidal forcing at its lower boundary because the latter is provided by GSWM that in turn is in excellent agreement with the CRISTA observation. The most likely explanation is given by *Hagan et al.* [2002] who suggested that the TIME-GCM simulation for CRISTA-2 overestimates the tidal dissipation in the upper mesosphere and lower thermosphere. The GW parameterization was not tuned to better match CRISTA geostrophic wind fields as for CRISTA-1 but was run with the standard model set-up. The extended CMAM, on the other hand,

overestimates the migrating tidal amplitude by almost a factor of two. It is not clear whether this is predominantly due to an underestimate of tidal dissipation or due to an overestimate of the latent heat source (not included in GSWM and TIME-GCM).

**w2.** The observed w2 tidal amplitude of 4-5 K is almost constant with height. It is well reproduced by the TIME-GCM although this good quantitative agreement may be fortuitous due to the abovementioned overestimate of the tidal dissipation in the model. Along with the small GSWM response it nevertheless indicates that non-linear wave-wave interaction is an important forcing mechanism. Latent heat release appears to be less important over the entire height range. The extended CMAM amplitude above 95 km is considerably larger than the observed one. This differs from the November 1994 case when the model prediction was smaller. The larger model amplitude suggests an underestimate of tidal dissipation (as for w1) but this issue cannot be resolved without additional model runs. The good agreement between the vertical wavelengths of all models and CRISTA points to a similar contribution of the leading tidal mode (Hough function) in all four datasets.

**e1.** As in November 1994, CRISTA and extended CMAM amplitudes agree with each other when accounting for the considerable model variability. Even the amplitude minimum around 95 km is reproduced by the model. GSWM and TIME-GCM responses are very small. The TIME-GCM vertical wavelength (41 km) is much larger than in GSWM, extended CMAM, and CRISTA with the latter somewhat shorter than in the models. It may thus indicate that the realistic extended CMAM amplitude is rather dominated by the latent heat source which in turn appears to be underestimated in GSWM.

**e3.** Extended CMAM and CRISTA amplitudes and phases are in excellent agreement with some model tendency toward larger amplitudes around 110 km (15 K compared to 10 K). GSWM and TIME-GCM responses are negligible. Because a wave-wave interaction forcing of e3 is rather unlikely, GSWM seems to underestimate the latent heat response in the MLT around solstice. The same result was obtained when comparing TIDI wind data with the models (see section 4.3.5).

#### 4.1.4 What did we learn from CRISTA?

CRISTA temperature data provide for the first time a detailed view of diurnal temperature tides in an altitude region of Earth's atmosphere that was not accessible to global analysis before. Nonmigrating tides dominate the tidal temperature field above the mesopause. Their combined amplitudes may exceed the migrating tide by an order of magnitude. This demonstrates the importance of nonmigrating tides for studying the dynamics, energetics, and chemistry in this height region and for interpreting ground-based, in-situ, and satellite-borne observations.

The tidal phase progression cannot be derived from CRISTA observations alone, but consistency with the models is only obtained for tidal forcing from below. Hence, nonmigrating tides contribute significantly to the coupling between the lower and upper atmosphere. Tropospheric weather systems may have a large effect on the MLT region via their imprint upon the tidal fields. It may even exceed the effect of solar radiation absorption. Inherently limited by the short measuring periods, the

CRISTA results can, of course, only provide a snapshot of the tidal activity that is also confined to equatorial latitudes. Differences between the observed nonmigrating tidal amplitudes around equinox (November 1994) and around solstice (August 1997) should not be overinterpreted: they are more indicative for the seasonal cycle of the nonmigrating tides with generally larger amplitudes in November.

The short mission duration also imposes some restrictions to the model comparisons. Comparing two specific days of data with a climatological model and GCMs certainly stresses the model capabilities to an extreme. It nevertheless shows that both latent heat release in the tropical troposphere and non-linear interactions between QSPWs and the migrating tide are important tidal sources. The models have a general tendency to underestimate the westward propagating components in the lower thermosphere and thus the wave-wave interaction source. Their capabilities, particularly of the extended CMAM, to reproduce realistic eastward tidal components are better although differences remain. These differences may partly be attributable to a latitude effect because the exact location of a tidal maximum certainly depends on the specifics of the background atmosphere in the model [*Hagan and Roble, 2001*]. However, the model capability to reproduce a realistic seasonal cycle of the tides is probably more important. The TIDI results in section 4.3 clearly point to that fact. They are consistent with the CRISTA findings but also underline the need for longer time-series and climatologies. One instrument that can provide a longer temperature data set is the LIMS instrument on board the NIMBUS-7 satellite. Its measurements provide additional information about the relative importance of the latent heat and wave-wave interactions sources and where the latter forcing occurs in the atmosphere.

## 4.2 Diurnal temperature tides in the stratosphere and mesosphere from LIMS

The Limb Infrared Monitor of the Stratosphere (LIMS) instrument on board the NIMBUS-7 satellite operated from October 24, 1978 until May 28, 1979 (section 3.1.1). Its objectives were to measure height profiles of temperature, ozone, water vapor, and nitrogen species in the middle atmosphere. A recent re-analysis of the LIMS data (V6) provides mesospheric temperatures to higher altitudes and with higher spatial resolution than before [*Lieberman et al., 2004*]. These temperatures are retrieved assuming local thermodynamical equilibrium (LTE) and are limited to altitudes below 80 km. The length, continuity and daily, near-global coverage (64°S-84°N) of the LIMS temperature record renders this data set nevertheless very useful for analyzing the global structure and the short-term variations in the diurnal tidal fields during the NH winter of 1978-1979. Of particular interest in this context are the major stratospheric warming events that occurred in January and February 1979. *Lieberman et al. [2004]* studied the variability of the diurnal nonmigrating tides during this time period. The magnitude of the corresponding QSPW events provides an opportunity to search for empirical support to the idea that QSPW-migrating tide interactions are a source of nonmigrating tides. It is in a sense an extension of the CRISTA study wherein the non-linear interaction source is examined by comparative model/observation analysis alone. The LIMS data also shed some light on the conditions and regions where such a forcing may occur.

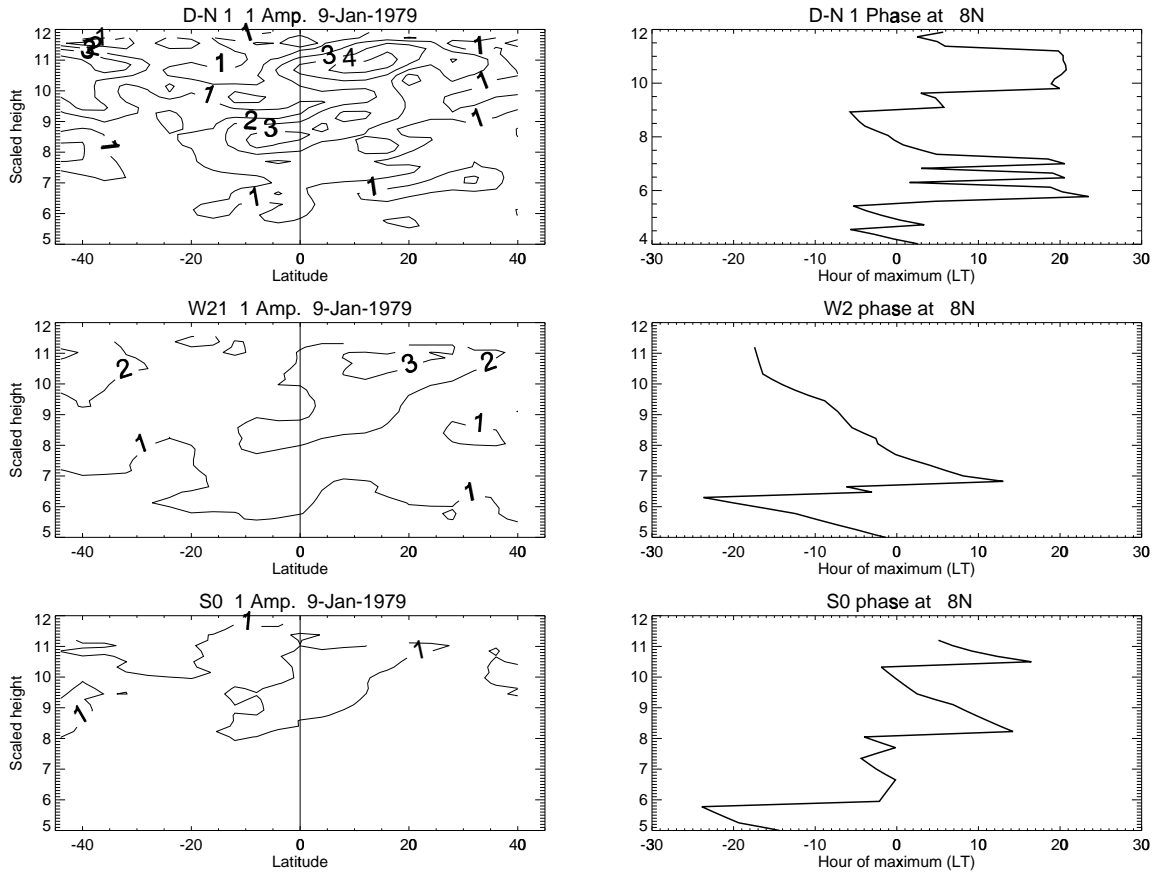


Figure 4.4: Left column: Latitude - altitude plots of the amplitude of the zonal wavenumber one asc-dsc temperature difference (top), w2 component (center), and s0 component (bottom) of the diurnal tide on January 9, 1979. Contour interval is 1 K, vertical range is from approximately 35 km to 84 km. Right column: Phase (hour of maximum) versus altitude at 8°N of the zonal wavenumber one asc-dsc difference (top), w2 (center), and s0 (bottom) components.

#### 4.2.1 Data analysis

LIMS was in a Sun-synchronous orbit with the LST of the ascending and descending orbit nodes fixed at 13:00 and 22:40 for all latitudes. This sampling pattern did not change over the course of the measurements. As for CRISTA, the lack of LST coverage prevents a spectral tidal analysis and Equation 3.4 (section 3.3) cannot be solved by Fourier fitting the data. The deconvolution method introduced in section 4.1.1 is thus applied to each day and latitude of the LIMS measurements to derive nonmigrating tidal amplitudes and phases. For LIMS, one further difficulty in the analysis arises because the LSTs of the asc and dsc measurements are only 10 h apart. Although the deconvolution method (appendix A3) can easily be extended to account for that (see *Oberheide et al.* [2002b] for details), it nevertheless imposes a further restriction: the semidiurnal signal in the asc-dsc difference fields is set to zero. This assumption is justified because (i) the semidiurnal effect in the asc-dsc temperature difference  $\Delta T$  is  $\leq 10\%$  (from Equation 7 in *Oberheide et al.* [2003b]) for 10 h LST difference and (ii) the semidiurnal tidal amplitudes are small in the mesosphere [*Forbes and Wu*, 2006].

Figure 4.4 illustrates the deconvolution of the observed zonal wavenumber one asc-dsc temperature difference pattern on January 9, 1979 as function of latitude and altitude. One scale height translates to 7 km altitude. Following section 4.1, an observed zonal wavenumber one diurnal pattern corresponds to an interference of the s0 and w2 diurnal components. The top panel represents the global amplitude and the phase at 8°N for observed wavenumber one ( $T_0$  and  $\Psi$  in Equation 4.1). The amplitude exhibits multiple maxima in altitude, one at approximately 8 scale heights, and the other at about 11 scale heights. However, following the deconvolution, the amplitudes of w2 (center row, left) and s0 (bottom row, left) vary smoothly with altitude. The amplitude of w2 is approximately twice as strong as that of s0. The phase of the asc-dsc difference at 8°N (top row, right) decreases with altitude between 7 and 9 scale heights, but is otherwise rather variable. The w2 phase (center row, right) decreases nearly uniformly with altitude with a vertical wavelength of approximately 14 km in the stratosphere (below 7 scale heights) and of about 25 km in the mesosphere (above 7 scale heights). The phase of the weaker s0 component is more variable, and decreases systematically with altitude only in the 8-11 scale height range where the amplitudes are largest. The s0 phase below 8 scale heights is not significant because the corresponding amplitudes are well below 1 K. A detailed error analysis for LIMS has not been made. It is reasonable to assume that the LIMS amplitude and phase errors are similar to the CRISTA errors shown in Table 4.2 because they are governed by the method. Note that the LIMS amplitudes shown have not been scaled. This introduces an additional 5% uncertainty in the w2 and s0 amplitudes.

#### 4.2.2 Evolution of tides and planetary waves

Figure 4.5 shows the evolution of the monthly mean migrating, w2, and s0 diurnal temperature tides at 10.7 scale heights (approximately 75 km). The migrating tide is inferred from the asc-dsc difference of the zonal mean temperatures (divided by 2), and therefore represents a snapshot referenced to approximately 13:00 LST. Hence, it is not a tidal amplitude (which also explains the negative values) but rather a proxy for the migrating tidal signal (see *Hitchman and Leovy* [1985] for details). The w2 and s0 components plotted in Figure 4.5 represent tidal amplitudes derived using the deconvolution method.

The migrating tide in Figure 4.5 maximizes in March with a peak amplitude of 9 K at the equator. This is consistent with the spring equinox maximum and the well-known semi-annual variability of the migrating tide. A secondary peak in November is likely associated with the fall equinox maximum. The w2 amplitude, however, exhibits a different seasonal behavior. It maximizes in December at about 15°N with an amplitude that is about one-half of the migrating tide. The s0 amplitude evolution is similar to that of w2, but its amplitude is much smaller and on the edge of being significant. The following discussion thus focuses on the w2 nonmigrating component alone.

Before discussing the time evolution of w2 in terms of possible wave-wave interaction forcing, it is interesting to compare it with the climatological GSWM results (section 3.2.1) and thus the latent heat forced contribution. GSWM w2 (Figure 4.6, top panel) has a strong response symmetric about the equator. The largest ampli-

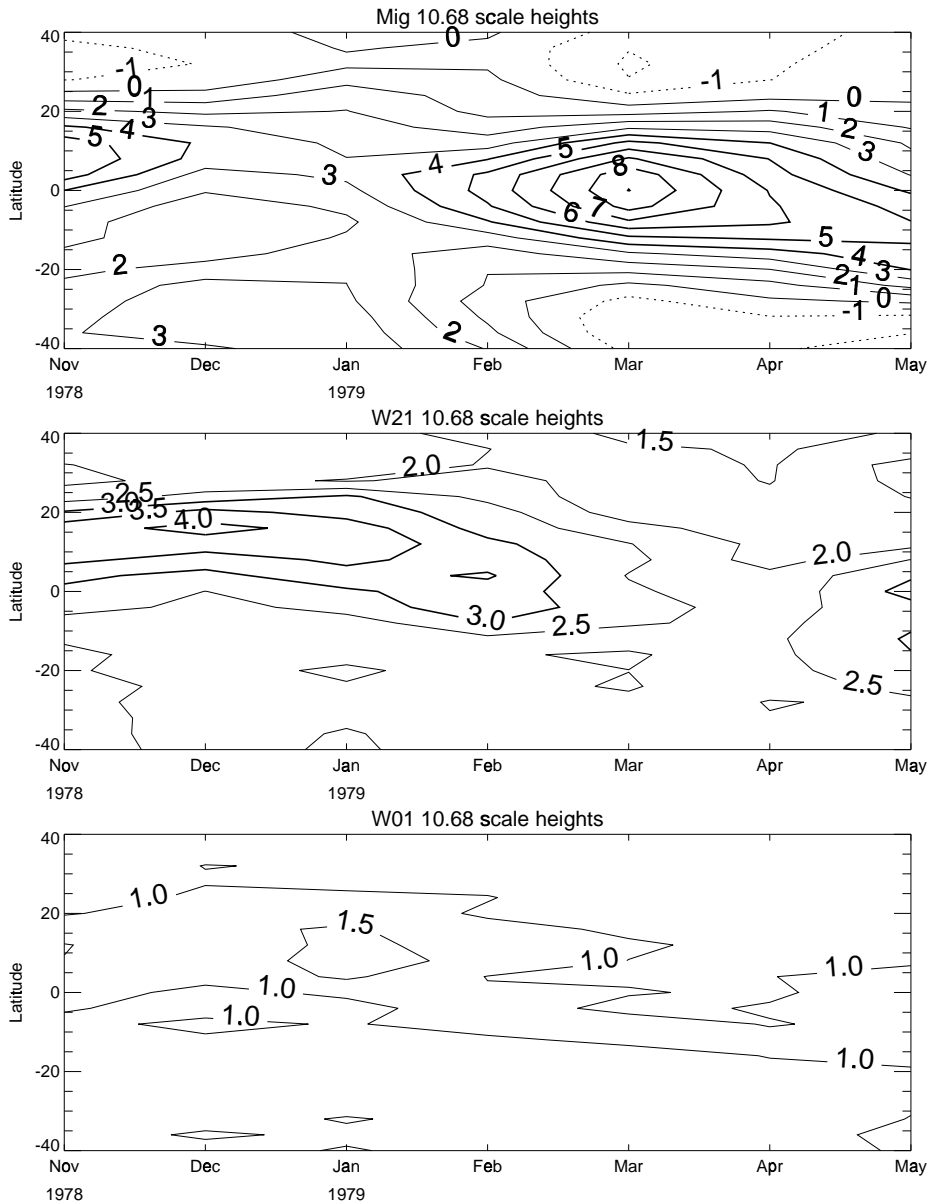


Figure 4.5: Time evolution of monthly mean migrating w1 (top), w2 (center) and s0 (bottom) diurnal temperature amplitudes at 10.7 scale heights (approximately 75 km).

tudes are found at the equator during March and April with a maximum value of  $\leq 3$  K and around fall equinox with values between 1.5 and 2 K. A secondary maximum occurs during spring equinox near 30°N. The model result differs from the observation (Figure 4.6, center panel) in several ways. Instead of maximizing at equinoxes, the LIMS data maximize (4 K) in December and are weakest during March and April. Although the observed w2 amplitude also maximizes at low latitudes, it has a broader latitudinal extent than its model counterpart and it also exhibits more latitudinal variability: slightly northward of the equator in boreal winter and slightly southward in May.

There are a number of possible reasons for the discrepancies between the observed and modeled w2 amplitudes: differences between the observed and modeled zonal

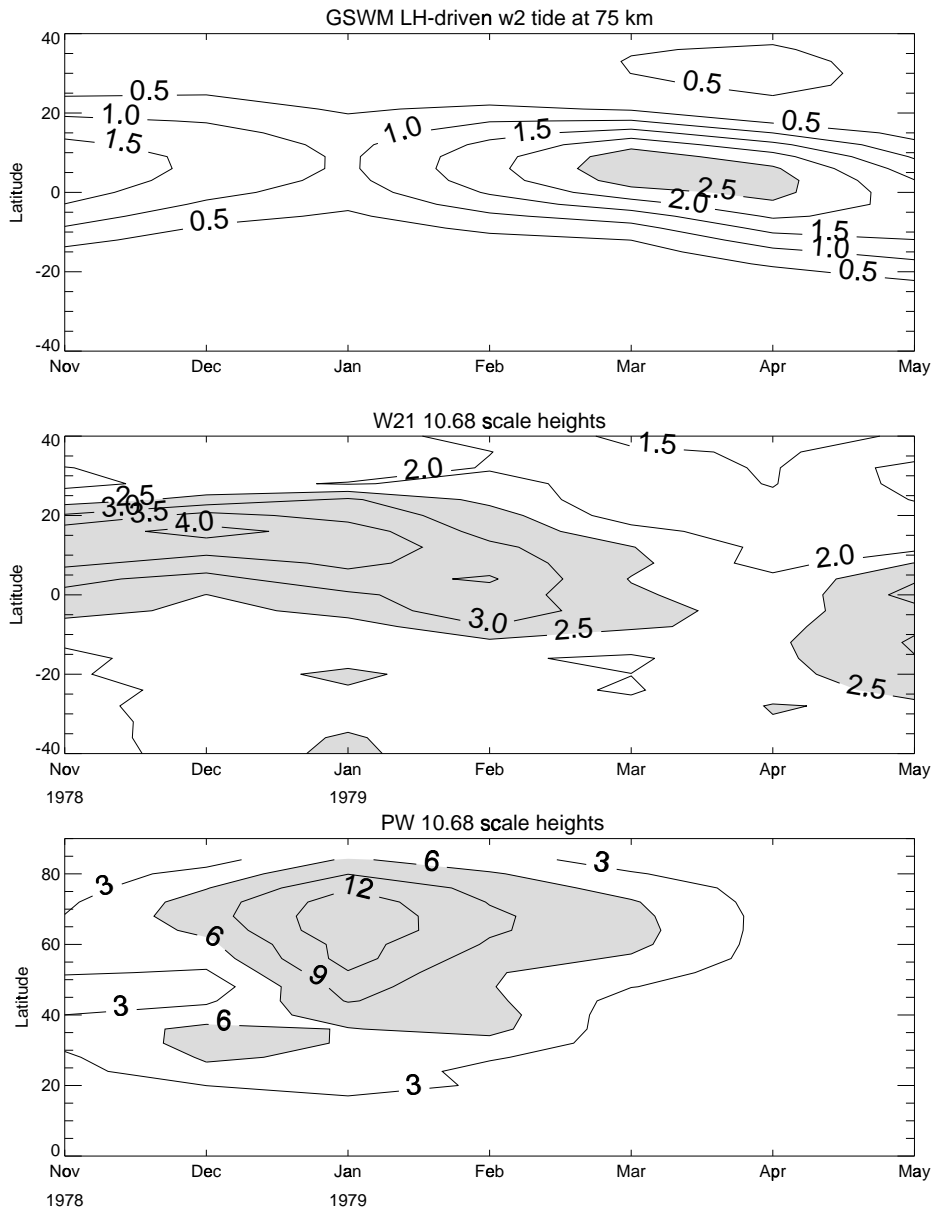


Figure 4.6: Time evolution of the monthly mean GSWM latent heat driven w2 temperature amplitude (top), LIMS w2 temperature amplitude (center). Values larger than 2.5 K are shaded. Bottom: LIMS QSPW-1 temperature amplitudes. Values larger than 6 K are shaded.

mean winds, and tidal sources and sinks. It is likely that the non-linear interaction between the migrating tide and QSPWs plays an important role in this context. Such processes are not included in GSWM. Furthermore, the CRISTA results for November 1994 (section 4.1.3) already indicate that non-linear wave-wave interaction forcing is comparably more important than the latent heat source at altitudes below the mesopause. The w2 amplitudes from CRISTA (7.5°N, November 1994) at 75 km is about 3.5 K which agrees well with the LIMS amplitude at the same latitude in November. Inspection of the bottom panel in Figure 4.6 gives additional confidence in the role of non-linear forcing processes. The periods of enhanced QSPW-1 activity coincide with the periods of largest w2 amplitudes. One of the strongest observed w2

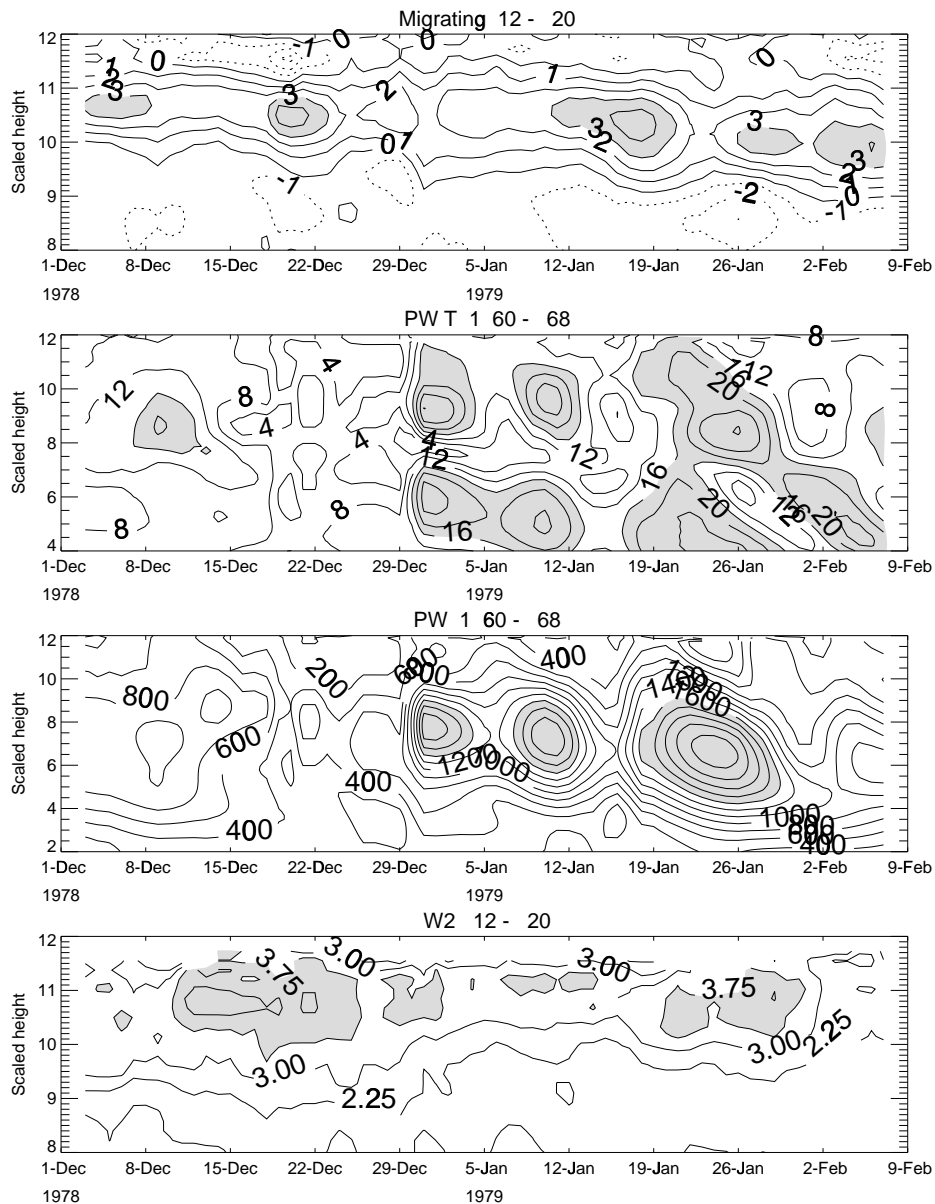


Figure 4.7: Top: Scale height versus time plot of the migrating diurnal tide referenced to approximately 13:00 LST, averaged between  $12^{\circ}\text{N}$  and  $20^{\circ}\text{N}$ . Values larger than 3 K are shaded. Second: QSPW-1 temperature amplitude from LIMS averaged between  $60^{\circ}\text{N}$  and  $68^{\circ}\text{N}$ . Values larger than 16 K are shaded. Third: QSPW-1 geopotential amplitude averaged between  $60^{\circ}$  and  $68^{\circ}\text{N}$ . Values larger than 1600 m are shaded. Bottom:  $w_2$  temperature amplitude averaged between  $12^{\circ}\text{N}$  and  $20^{\circ}\text{N}$ . Values larger than 3.75 K are shaded. All time series are smoothed using a 5-day running mean. Note the different vertical scales in each panel.

amplitude peaks occurs in December, when the QSPW-1 amplitude (in excess of 6 K) penetrates to about  $30^{\circ}\text{N}$ .

A more detailed examination of the possible role of non-linear QSPW-migrating tide interaction in forcing  $w_2$  requires a closer look on the daily evolution of these components. Figure 4.7 shows the evolution of the migrating tide (top) in the tropics, of the QSPW-1 in temperature (second) and geopotential (third) at high latitudes, and

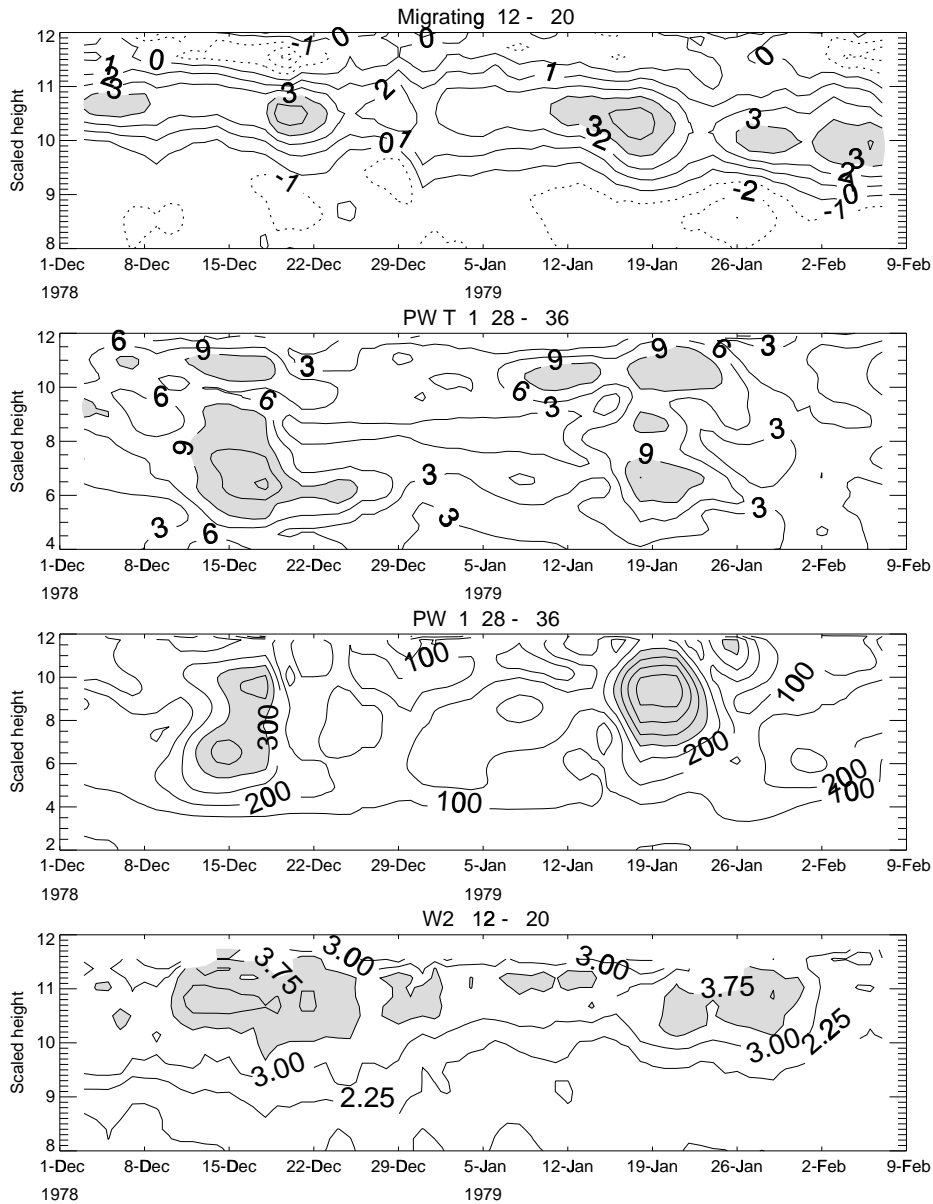


Figure 4.8: As Figure 4.7, but with the QSPW-1 amplitudes averaged between 28°N and 36°N. Second: Values larger than 9 K are shaded. Third: Values larger than 400 m are shaded.

of the  $w_2$  component (bottom) again in the tropics. The tropical latitudes correspond to the regions of largest  $w_2$  activity in Figure 4.6. They are also far enough removed from regions of strong QSPW amplitudes so as to avoid aliasing of rapidly evolving QSPW amplitudes in the daily asc-dsc differences. For example, a QSPW-1 growing or decaying at a rate of  $6 \text{ K day}^{-1}$  would account for 50% of an asc-dsc difference pattern whose amplitude is 3 K from which  $w_2$  and  $s_0$  amplitudes are inferred.

The week-to-week variations of the migrating tide in Figure 4.7 are rather modest. The maximum values between 10 and 11 scale heights (roughly 65-75 km) can be viewed as proxies for the migrating temperature amplitude. Values in excess of 3 K are observed in early and late December 1978, in the middle and later parts of January 1979, and in early February 1979. A relative amplitude minimum occurs

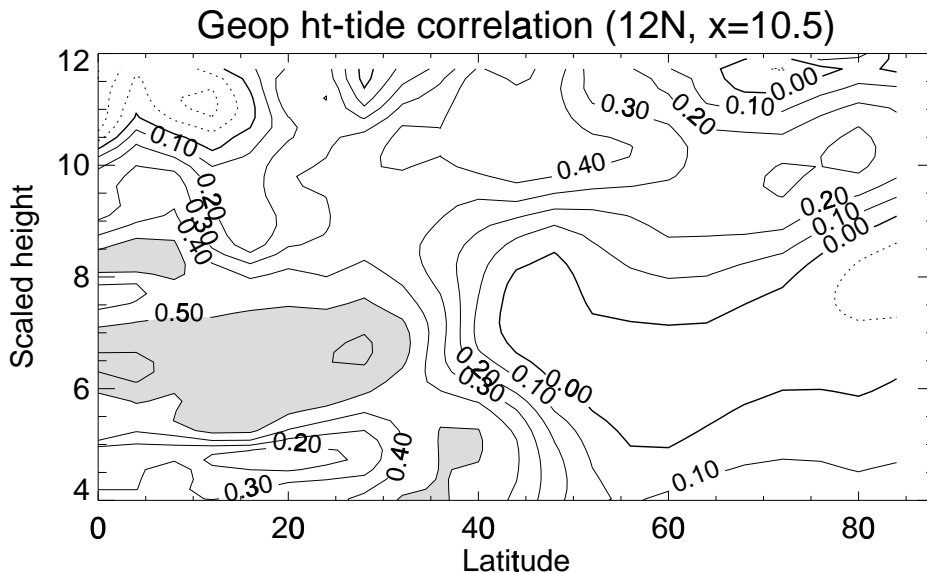


Figure 4.9: Correlation between time series of QSPW-1 geopotential amplitude and  $w_2$  temperature amplitude at 10.5 scale heights and  $12^\circ\text{N}$ . Values larger than 0.5 are shaded. Time series span December 1, 1978 - February 10, 1979 and are smoothed with a 5-day running mean.

on December 29, 1979. The QSPW-1 evolutions in temperature (second panel) and geopotential (third panel) exhibit a 16-day modulation during January. This behavior comes from an interference between a stationary PW-1 and a traveling 16-day wave [Madden and Labitzke, 1981; Smith, 1985]. The geopotential is a function of the vertically integrated temperature perturbation and thus varies more smoothly in time and in altitude. The descending wave pattern in late January and early February corresponds to the abovementioned stratospheric warming events.

The  $w_2$  evolution in Figure 4.7 (bottom) shows amplitude enhancements centered between December 10 and 25, 1978, around December 29, 1978, January 12, 1979, and between January 19 and 30, 1979. These amplitude increases generally coincide with the enhancement of QSPW-1 and are clearly visible in January. The strong QSPW-1 enhancement in temperature between December 8 and 13, 1978 is not as visible in the geopotential due to the strong vertical localization but it may be related to the  $w_2$  amplitude increase on about December 10, 1978.

However, Figure 4.6 suggested that the largest  $w_2$  amplitudes in December 1978 are rather associated with the QSPW-1 amplitude penetration in lower latitudes. This becomes even more striking when comparing the tidal activity to the QSPW-1 amplitudes averaged between  $28^\circ\text{N}$  and  $36^\circ\text{N}$  (Figure 4.8). The mid-December enhancements of  $w_2$  (bottom) and QSPW-1 (second and third panel) now coincide well. The weaker  $w_2$  amplitude increase around January 12, 1979 may be linked to a corresponding QSPW-1 temperature amplification at 10 scale heights. This also applies to January 19, 1979 when a  $w_2$  enhancement is initiated.

Both Figures 4.7 and 4.8 thus suggest a connection between the  $w_2$  amplitude evolution at tropical northern latitudes and QSPW-1 enhancements at both subtropical and high latitudes. A more quantitative attempt to link the tidal and planetary

wave evolution is shown in Figure 4.9. It shows the correlation of w2 diurnal temperature amplitudes at 12°N and 10.5 scale heights (75 km) with the global QSPW-1 geopotential amplitudes. The correlations are computed between 5-day running mean time series of w2 and QSPW-1 over the December 1, 1978 to February 10, 1979 period shown in Figures 4.7 and 4.8. Regions of positive correlation extend well into the middle and high latitudes above 8 scale heights (55 km). However, the highest positive correlations are found at latitudes equatorward of 30°N and between 6 and 8 scale heights (roughly 45 to 55 km).

### 4.2.3 Implications of the LIMS results

Insofar as migrating tide and QSPW-1 interactions are a source for w2, the correlation pattern in Figure 4.9 suggests that this process is facilitated by the low-latitude presence of QSPW-1. This result is not unexpected because one might anticipate that the interaction between these waves is enhanced by their joint presence at low latitudes. The migrating tide is most pronounced around the equator and in the subtropics. On the other hand, QSPWs that propagate into the middle atmosphere often break or encounter critical levels at extratropical latitudes where migrating tides are weak. During December 1978, however, QSPW-1 penetrated the latitude range of the migrating tide (Figure 4.6). As pointed out in section 4.1.3, this also applies for November 1994 with the resulting large w2 amplitudes observed by CRISTA. The comparably small w2 amplitudes in August 1997 are also consistent with this interpretation, because the QSPW activity during this period was confined to extratropical latitudes (section 4.1.3). LIMS and CRISTA results for the w2 component forcing are thus consistent although the latter were obtained by model/observation intercomparisons and not from the observations alone.

The constraints imposed by the LIMS orbit geometry, particularly the lack of amplitude and phase information of the migrating tide, prevent a more thorough analysis. The correlation between w2 and QSPW-1 during the boreal winter of 1978 and 1979 nevertheless lends empirical support to the idea that QSPW-migrating tide interactions are a source of nonmigrating tides. Observational evidence for the interaction would be enhanced if the evolution of both migrating and nonmigrating tides could be documented at middle latitudes where the planetary waves maximize. This could also identify the potential contribution of the vertically trapped migrating diurnal tide in the upper stratosphere to the non-linear interactions. This in-situ forced tidal contribution (by ozone heating) maximizes around 45° latitude where the planetary wave amplitudes are largest.

Furthermore, non-linear interactions are facilitated through momentum as well as heat exchange between the migrating tide and QSPWs. Although the migrating diurnal temperature tide may not in general maximize in the vicinity of the planetary wave amplitude, the corresponding zonal and meridional winds have broad maxima around 20° to 25° which in turn is closer to the latitude range of the QSPW winds. As a result, non-linear interactions may occur in locations where strong signatures of the migrating diurnal temperature tide are not necessarily found. Tidal wind fields are discussed in the next section 4.3.

### 4.3 Diurnal tidal climatologies from TIDI wind data

With the launch of the TIMED satellite in December 2001, continuous temperature and wind data sets amenable to MLT tidal analyses became available. The wind-measuring instrument, the TIMED Doppler Interferometer (TIDI, section 3.1.4), is operating since early 2002. Its day- and nighttime capability allows to derive non-migrating tidal wind climatologies over a range of MLT altitudes. Limitations of previous satellite-borne wind instruments have restricted such climatologies to 95 km altitude before. Hence, the TIDI results represent the first evidence of the vertical wind structure of nonmigrating tides over a 20 km range in the mesopause region.

In the following, TIDI measurements of zonal and meridional winds in the mesosphere and lower thermosphere are analyzed for diurnal nonmigrating tides (1 June 2002 to 15 June 2005). Climatologies of monthly mean amplitudes and phases for seven tidal components are derived at altitudes between 85 and 105 km and latitudes between 45°S and 45°N (w4, w3, w2, s0, e1, e2, and e3). The latitude range of the analysis has been restricted to avoid aliasing of rapidly evolving QSPWs. The TIDI results are cross-checked by comparing them to the existing 95 km UARS climatology of *Forbes et al.* [2003]. A comparative analysis of the TIDI climatologies with GSWM, TIME-GCM, and extended CMAM tidal predictions provides further insight into the latent heat and QSPW-tidal interaction forcing contributions to the observed tides and their seasonal variability.

#### 4.3.1 Tidal analysis

The TIDI data quality improves with every new data version available but the current noise level (section 3.1.4) is still too high to apply the tidal deconvolution method introduced in section 4.1.1. Instead, the zonal and meridional TIDI winds are analyzed using a Fourier method. Such a spectral approach is far less sensitive to random noise (section 4.3.2). The orbit precession rate of TIMED requires that tidal parameters obtained via a Fourier method be accumulated over 60 days (full LST coverage). The inherent averaging and smoothing renders the approach in a sense even more suitable for obtaining climatologies.

The tides are derived as described by *Oberheide et al.* [2006b]. However, the specifics of the analysis method are reviewed herein, because they are essential for understanding the results. It is basically a two-dimensional Fourier transform of a 60-day composite data set. The composite data set is composed and analyzed as follows:

1. For each measuring day, split the TIDI wind data into four subsets of ascending (asc) and descending (dsc) orbit node measurements for the TIDI warm and cold sides respectively. All four data subsets have different local times for a given latitude.
2. For each subset, combine 5 days of consecutive TIDI wind measurements to produce zonal and meridional winds in each of the latitude and longitude bands that saw satellite overpasses (Figure 4.10a). Combining several days of data

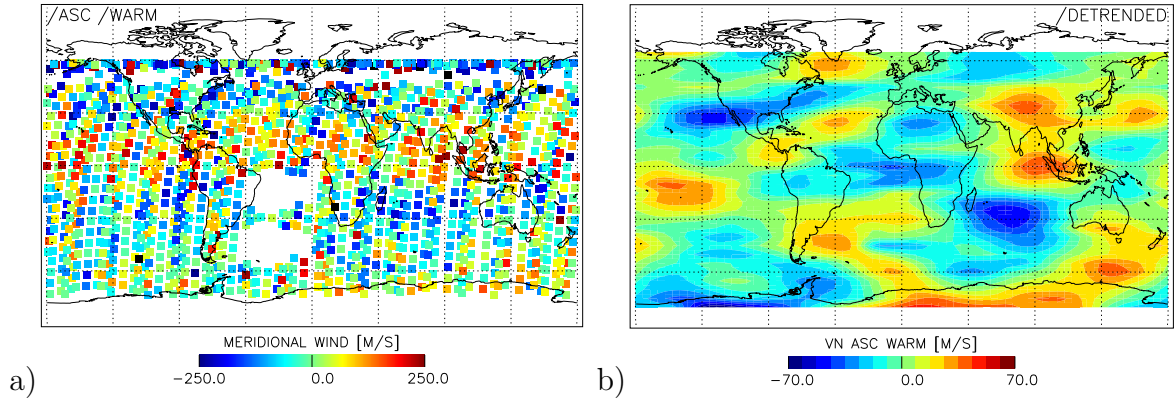


Figure 4.10: a) One subset of 5 days of consecutive TIDI meridional wind measurements (20–24 January 2004) at 95 km. Only data taken on the warm side and on the ascending part of the orbits are shown. Each mark represents a complete height profile of wind measurements. Gaps over South America occur when the satellite flies through the South Atlantic Anomaly. They do not affect the analysis. b) Mapped subset with the zonal mean removed.

increases the number of data points per longitude/latitude band and thus reduces the noise level. It also closes data gaps. Note that combining 5 days of data results in one hour LST smoothing but this does not affect the analysis. Combining 3 days of data yielded almost identical amplitudes and phases (not shown).

3. Map the 4 subsets separately onto a horizontal grid of  $5^\circ \times 5^\circ$  using a two-dimensional triangular filter function with a full width of  $7.5^\circ$  in the North-South direction and  $45^\circ$  in East-West direction. This yields 36 grid points in latitudinal and 72 grid points in longitudinal direction. Each grid point represents the average of about 40 TIDI wind measurements.
4. Remove the zonal mean from the 4 mapped subsets (Figure 4.10b). The zonal mean removal accounts for potential zero wind line differences between the warm and cold side data. It also removes the migrating tides from the mapped data because migrating tides are observed as zonally symmetric features. They would therefore be aliased by temporal variations of the background (i.e., diurnal mean) winds. See *Oberheide et al.* [2003b] and section 3.3 for details of tidal sampling issues in the data from slowly precessing satellites.
5. Repeat steps 1 to 4 as a 5-day running mean for a 60 day period. The TIMED orbit geometry is such that 60 days of combined TIDI asc/dsc, warm/cold side data subsets have 24 hours of LST coverage.
6. Combine 60 days of mapped data subsets and sort the merged data set in local time. Interpolate the sorted data set onto a fixed LST grid, including averaging if more than one data subset is available for a given LST bin. The resulting composite data set is therefore evenly spaced in LST (24 hours LST coverage) and longitude ( $360^\circ$  coverage) for each latitude and altitude. Analyzing warm and cold side data separately yields results within the error bars discussed in section 4.3.2 (not shown).

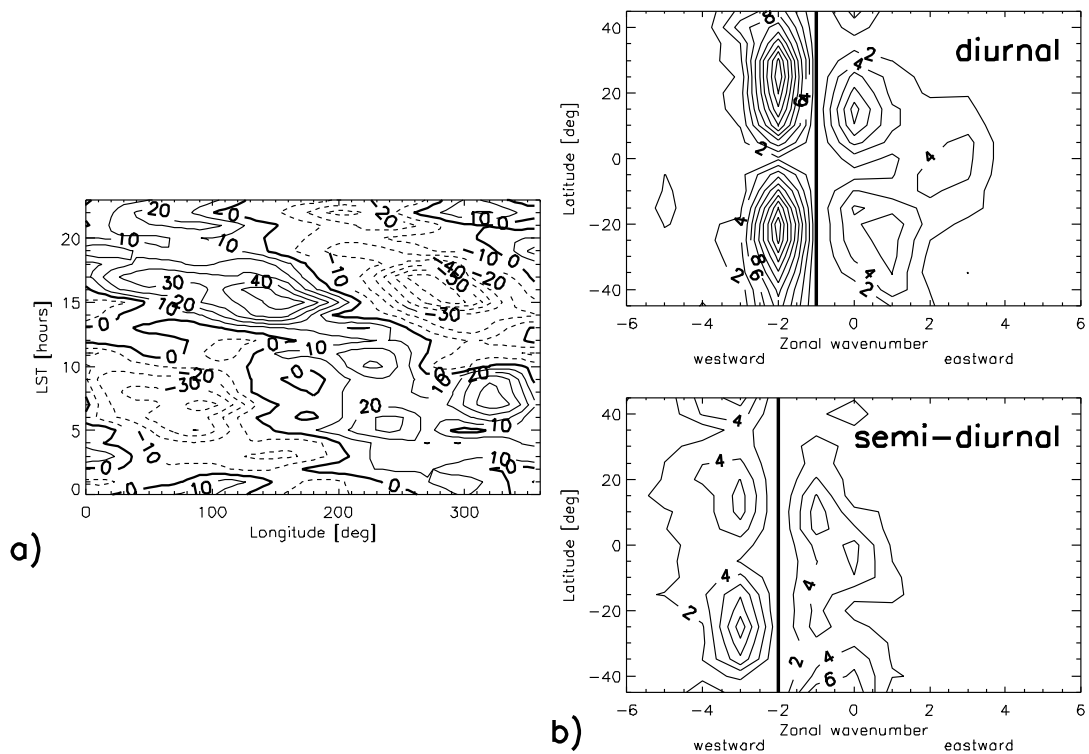


Figure 4.11: a) TIDI composite data from the period 15 January 2004 to 18 March 2004 (later assigned to 15 February 2004) at  $20^\circ\text{N}$  and 95 km for the meridional wind. Note that the observed wavenumbers have not yet been shifted. b) Corresponding amplitudes (m/s) as function of wavenumber and latitude for diurnal and semidiurnal frequencies. Observed wavenumbers have been shifted to account for the satellite sampling. The positions of the migrating tides are indicated by the thick vertical line.

7. Compute wavenumber/frequency pairs with two-dimensional Fourier transform. Owing to the 60-day averaging, the results must be interpreted in a climatological sense. Short-time variations will be smoothed out. Account for the fact that the observed wavenumber is shifted by  $-1$  as compared to the real zonal wavenumber (i.e., diurnal  $w_2$  is observed as  $w_1$ ). This is due to the satellite sampling (section 3.3). Assign the amplitudes and phases to the day in the middle of the 60-day period.
8. Repeat steps 1 to 7 as a 60-day running mean for the 3-year analysis period and average the derived amplitudes and phases into monthly bins.

As an example for the composite data, Figure 4.11a shows a longitude/LST plot at 95 km for the meridional (northward) wind at  $20^\circ\text{N}$  (step 6 above). Fourier analysis then provides amplitudes and phases for different frequencies. The resulting wavenumbers, however, must be shifted by 1 to account for the satellite sampling (step 7 above). Figure 4.11b shows the shifted amplitudes for diurnal and semidiurnal frequencies as function of latitude. It should be emphasized again that the removal of the zonal means (step 4 above) also results in the removal of the migrating tides. The migrating components cannot be analyzed with the analysis method and are not present in the figure. Semidiurnal tides are discussed in section 4.4. The analysis is

carried out for about 3 years of TIDI data (1 June 2002 to 15 June 2005). In early 2003, the satellite was moved such that TIDI was looking toward the Earth's surface. This prevented the tidal analysis during the first 3 months of the year. Apart from this gap, the TIDI data have an almost continuous temporal coverage.

### 4.3.2 Error analysis

There are basically three error sources that introduce some uncertainty in the derived tidal amplitudes and phases: measurement noise, artifacts from the asynoptic satellite sampling, and the analysis method itself. The analysis method accounts for the absolute error (accuracy) while the measurement noise and the asynoptic satellite sampling govern the relative error (precision).

The analysis method itself introduces a considerable damping of the derived amplitudes because of the large widths of the triangular filter in the horizontal mapping routine (analysis step 3). This damping becomes more serious for larger wavenumbers and also depends on the latitudinal structure of the tides. Components with a broad amplitude and phase distribution as function of latitude will be less affected than components with sharp amplitude minima/maxima and phase transitions. All derived tidal amplitudes and phases must therefore be corrected for the damping. The uncertainty of the correction must be considered as the accuracy. The correction and its uncertainty is determined using both model simulations and the measured data.

First, monthly tidal wind amplitudes and phases from the GSWM model are linearly interpolated to each day of the year. From these data, tidal wind perturbations for the LST, altitude, longitude, and latitude of the TIDI measurements are extracted for each day of an equivalent three-year period (using the SATUT procedure introduced in section 3.3, with data gaps). They are the synthesis of 13 diurnal and 13 semidiurnal tidal components (w6 to e6). The model mapping provides a data set identical to the TIDI data but with the measured zonal and meridional winds replaced with the model diurnal and semidiurnal tidal wind perturbations ("flying the satellite through the model"). This model data set is then analyzed as the measured TIDI data. The derived amplitudes are compared month by month to the full model output (monthly means of 60-day running mean averages). The comparison provides a correction for each tidal component that can be described by a scaling factor independent of month, latitude, and altitude. Phases remain unaffected, but with some scatter (1 to 2 hours depending on the component) introduced by the asynoptic satellite sampling.

Next, the scaling factors derived from the model simulations are applied in the sense of an initial guess to the monthly TIDI climatologies (called run 1). The scaled amplitudes and the (unscaled) phases from run 1 are then used to compute tidal wind perturbations for the TIDI footprints, as for the model simulation described above. Analyzing the data again as described in section 4.3.1 provides new monthly climatologies (called run 2) that are compared to the (unscaled) results from run 1. With perfect scaling of run 1, no systematic differences should occur. However, because GSWM and TIDI amplitude and phase distributions partly differ, run 1 and 2 results also differ. These differences are used to further improve the scaling of run 1 and the whole procedure is repeated. The systematic difference between the resulting monthly climatologies (run 3) and run 1 is on average smaller than 3%, indicating

good scaling factors. The standard deviation of scaling factors derived month by month gives the uncertainty of the mean scaling factors provided in Table 4.5 and therefore the amplitude accuracy of the monthly climatologies. All tidal amplitudes presented in the remainder of this work are from run 1 and have been scaled with the values given in Table 4.5. Phases do not require scaling.

Table 4.5 also provides the amplitude and phase precisions. They are the mean standard deviations between the (scaled) amplitudes and phases from runs 1 and 3 deduced for each month, latitude, and altitude. The precisions therefore include both the measurement noise and the noise introduced by the asynoptic satellite sampling. Propagating the measurement noise separately through the analysis yielded a consistent amplitude error of about 1 m/s. The inherent smoothing of the measurements due to the horizontal gridding and the use of 60 days of composite data significantly reduces the noise level.

### 4.3.3 Monthly climatologies

The tidal analysis covers the nonmigrating tidal components w4, w3, w2, s0, e1, e2, and e3 for the zonal (eastward) and meridional (northward) winds. Higher wavenumbers, although permitted by the Nyquist theorem, are not further considered because their scaling factors become very large (i.e.,  $> 5$  for e4). Figures of the 14 analyzed tidal components are omitted from the running text for better readability. Instead, they are shown in appendix A4 in the same order as they are discussed below. Electronic data files with numerical values are available on the web ([http://www.atmos.physik.uni-wuppertal.de/causes/nmt\\_mlt/](http://www.atmos.physik.uni-wuppertal.de/causes/nmt_mlt/)).

**w2, meridional (Figure A4.1)** The largest amplitudes (18 m/s) are found in January, February, and September to December, maximizing at about 20°S and 20°N around 95 km altitude. During these months, this component is anti-symmetric with respect to the equator, as indicated by the phase jumps at 0° latitude. The phase behavior in June, when the amplitudes are smallest (8 m/s), is rather symmetric about the equator. Phases decrease with increasing altitude. This indicates an upward propagation in the observed altitude range and thus tidal forcing from below.

Table 4.5: Scaling Factors applied to the derived diurnal tidal amplitudes, and meridional ( $v$ ) and zonal ( $u$ ) wind errors of the monthly climatologies. Given values are for the scaled amplitudes.

component	scaling factor		amplitude accuracy		amplitude precision		phase precision	
	$v$	$u$	$v$ [%]	$u$ [%]	$v$ [ $\frac{m}{s}$ ]	$u$ [ $\frac{m}{s}$ ]	$v$ [hours]	$u$ [hours]
w4	2.00	2.02	9	9	0.9	0.7	2.1	2.1
w3	1.41	1.43	14	7	1.0	0.8	2.0	2.0
w2	1.24	1.26	11	13	1.3	1.1	1.4	1.5
s0	1.20	1.19	13	16	1.4	1.1	1.4	1.6
e1	1.46	1.37	16	15	1.1	0.8	1.7	1.8
e2	2.01	1.83	14	16	0.9	0.8	1.8	1.4
e3	3.26	3.18	11	12	1.0	0.9	1.5	1.1

**s0, meridional (Figure A4.2)** The latitudinal structure exhibits a large seasonal variation. Peaking in August (16 m/s), the s0 meridional component has two maxima at 20°S and 20°N in March, April, May, and again in August, September, and October with the Southern Hemisphere (SH) maximum much more pronounced than the Northern Hemisphere (NH) maximum. The peak altitude is between 90 and 95 km with a rather anti-symmetric phase distribution with respect to the equator. During the remainder of the year, the phases suggest a more symmetric behavior of the s0 component with larger vertical wavelengths. A single amplitude maximum that varies with height is located at about 10°S to 20°S. With few exceptions, phases decrease with increasing altitude thus indicating a prevailing tidal forcing from below.

**e2, meridional (Figure A4.3)** The e2 meridional amplitudes are generally symmetric about and centered on the equator with the symmetry mirrored in the phases. Exceptions are March and April, where a second amplitude maximum occurs at 40°S and above 100 km. These secondary maxima are out-of-phase with the equatorial peaks that are usually located between 95 to 100 km. All the equatorial amplitude maxima are between 6 to 8 m/s without much seasonal variation. The vertical phase distributions again suggest a tidal forcing from below.

**e3, meridional (Figure A4.4)** The e3 meridional component is always symmetric with respect to the equator with the largest amplitudes (10 m/s) occurring between November and March. The altitude of maximum amplitude varies between 95 km (November) and  $\geq 105$  km (April) with tidal forcing coming from below. Latitudinal phase jumps are observed at altitudes with small amplitudes which might indicate an increasing contribution of anti-symmetric modes at higher latitudes.

**w2, zonal (Figure A4.5)** Like its meridional counterpart, the w2 zonal component also shows largest amplitudes (10 m/s) in January, February, and September to December. Amplitude maxima are found at about 95 km but at slightly higher latitudes (30°S and 30°N). In contrast to the meridional wind, the w2 zonal component is symmetric with respect to the equator. The amplitudes between March and August are relatively small, with the exception of June, where an equatorial maximum is observed above 100 km altitude. Tidal forcing is also from below, as indicated by the decreasing phases with increasing altitude.

**s0, zonal (Figure A4.6)** Similar to the s0 meridional component, the s0 zonal component is quite variable. Amplitude maxima (6-10 m/s) are observed between 30°-40°S and 30°-40°N but their altitude varies from  $\leq 85$  km (April, SH) to  $\geq 105$  km (March, NH) with the SH maximum usually found at lower altitudes. The phase distributions are also highly variable. They indicate a rather symmetric behavior of the s0 zonal component at altitudes below 95 km with increasing anti-symmetric contributions toward higher altitudes. Although the phases usually decrease with increasing altitude (upward propagation, tidal forcing from below), there are some exceptions, e.g. in November, NH, which may indicate an in-situ forcing or even a forcing from above.

**e2, zonal (Figure A4.7)** The e2 zonal component is symmetric about the equator with a long vertical wavelength. Amplitude maxima occur at about 20°S and 20°N with the altitude of maximum amplitude usually located above the upper boundary of the analysis. Tidal forcing is from below with maximum amplitudes of 6 m/s.

**e3, zonal (Figure A4.8)** The e3 zonal component is the single largest component observed in the TIDI data. Amplitudes reach almost 20 m/s in August. From April to November, this component is symmetric about the equator with a long vertical wavelength, peaking at altitudes  $\geq 105$  km. This behavior, however, is completely different during the remainder of the year. The vertical wavelength is much smaller and the equatorial amplitude maximum changes into two anti-symmetric maxima located at about 20°S and 20°N. These maxima peak at lower altitudes (95 to 100 km). The vertical phase distributions nevertheless suggest that the tidal forcing is always from below.

**w4, w3, e1; zonal and meridional (Figures A4.9 - A4.14)** The basic features of the w4, w3, and e1 zonal and meridional tidal components may be summarized as follows: the measured w4, w3, and e1 zonal components have relatively small amplitudes (2-4 m/s) which also applies to the w4 meridional component. However, the w3 and e1 meridional amplitudes can be up to 10 m/s (September) with both components generally being anti-symmetric with respect to the equator. Tidal forcing is always from below.

#### 4.3.4 Comparison with UARS

A validation of the TIDI climatology is difficult because observations of nonmigrating tides have so far been very sparse. This is, however, different at 95 km altitude where climatological amplitude information deduced from HRDI and WINDII on UARS is available. *Forbes et al.* [2003] provide monthly mean zonal and meridional wind amplitudes for the s0, w2, and e3 diurnal components based upon data taken between 1991 and 1994. The specifics of the UARS instruments prevented an analysis at other altitudes. Fortunately, 95 km is a good altitude for comparing the TIDI and UARS results. Many tidal components peak or already have large amplitudes near 95 km.

It should nevertheless be noted that comparing the UARS data to the TIDI results does not meet the hard requirements of validation. The measurements are almost 11 years apart in time. This might be acceptable for climatologies that are taken during the same phase of the solar cycle, but there may or may not have been long term changes in the middle atmosphere. Furthermore, both TIDI and HRDI use the same technique to measure MLT winds. Validation would require comparisons with data obtained using different measurement techniques. This work will be carried out when, if any, such data become available, e.g. from chains of radar instruments.

In order to get a general view of the TIDI and UARS results, as a first step it is helpful to compare the 3-year average climatological mean amplitudes and phases. Figure 4.12 shows the comparison for the meridional wind amplitudes (a) and phases (b). The comparison for the zonal wind is provided in Figure 4.13. Both instruments measure an almost identical latitudinal distribution for all three components, but with the UARS amplitudes being roughly 50% smaller than the TIDI amplitudes. The corresponding climatological mean phases agree within the combined error bars, except for s0 in the NH. There is also a slight offset between UARS and TIDI in the SH s0 meridional phases. While such a deviation might be expected, considering the 11-year time lag between both data sets, the very stable w2 and e3 phases are remarkable

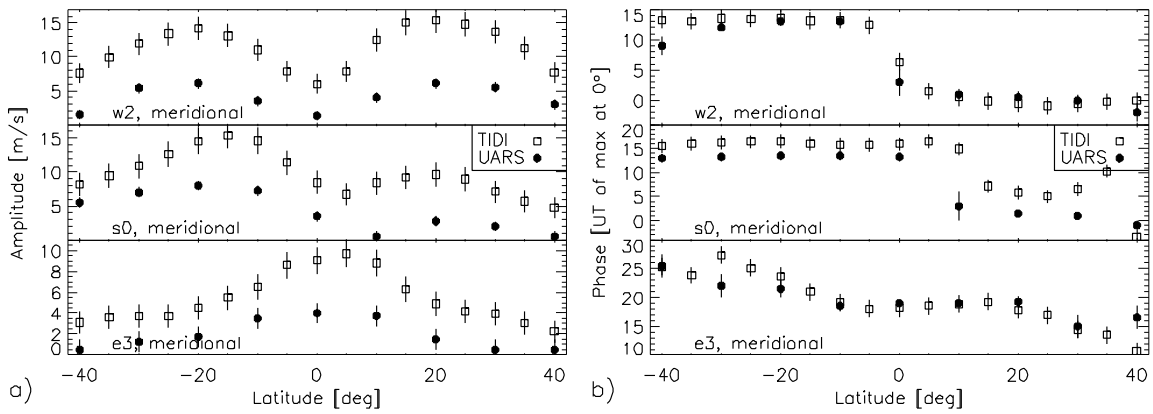


Figure 4.12: 3-year mean meridional wind amplitudes (a) and phases (b) at 95 km from TIDI (2002-2005) and UARS (HRDI & WINDII, 1991-1994, redrawn from *Forbes et al.* [2003]).

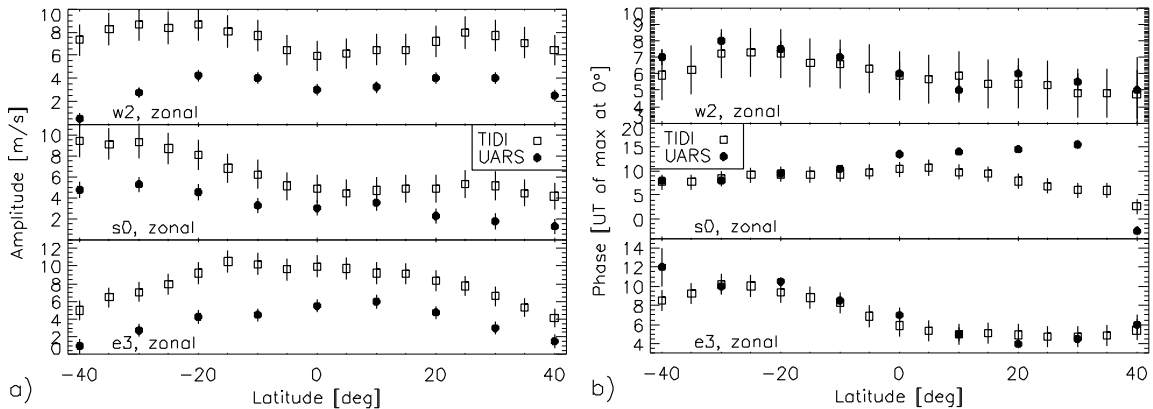


Figure 4.13: As Figure 4.12, but for the zonal wind.

There may be several reasons for the amplitude differences between TIDI and the UARS analysis. Recent results by *Huang and Reber* [2004] of nonmigrating tides in HRDI winds also indicate larger amplitudes (30%-50%) than those reported by *Forbes et al.* [2003]. In contrast, the analysis of *Manson et al.* [2004] of the same data set is more consistent with the *Forbes et al.* [2003] results. These inconsistencies have yet to be resolved, but it has been speculated by *Huang and Reber* [2004] that the specifics of the horizontal data binning might be an issue (similar to those that lead to the TIDI scaling factors in section 4.3.2). Hence, a reanalysis of the UARS data in the same way the TIDI data have been analyzed might be worthwhile. It is of course also possible that the amplitude differences between TIDI and HRDI come from the 11-year time difference of the measurements, although such a dramatic amplitude increase would be surprising.

*Forbes et al.* [2003] also provide time series for the diurnal components s0, w2, and e3. They are shown in Figure 4.14 for the meridional and in Figure 4.15 for the zonal wind together with the corresponding TIDI amplitudes. The largest differences between both data sets occur in the s0 zonal component. The NH maxima in April and August are not present in the UARS analysis which, on the other hand, shows

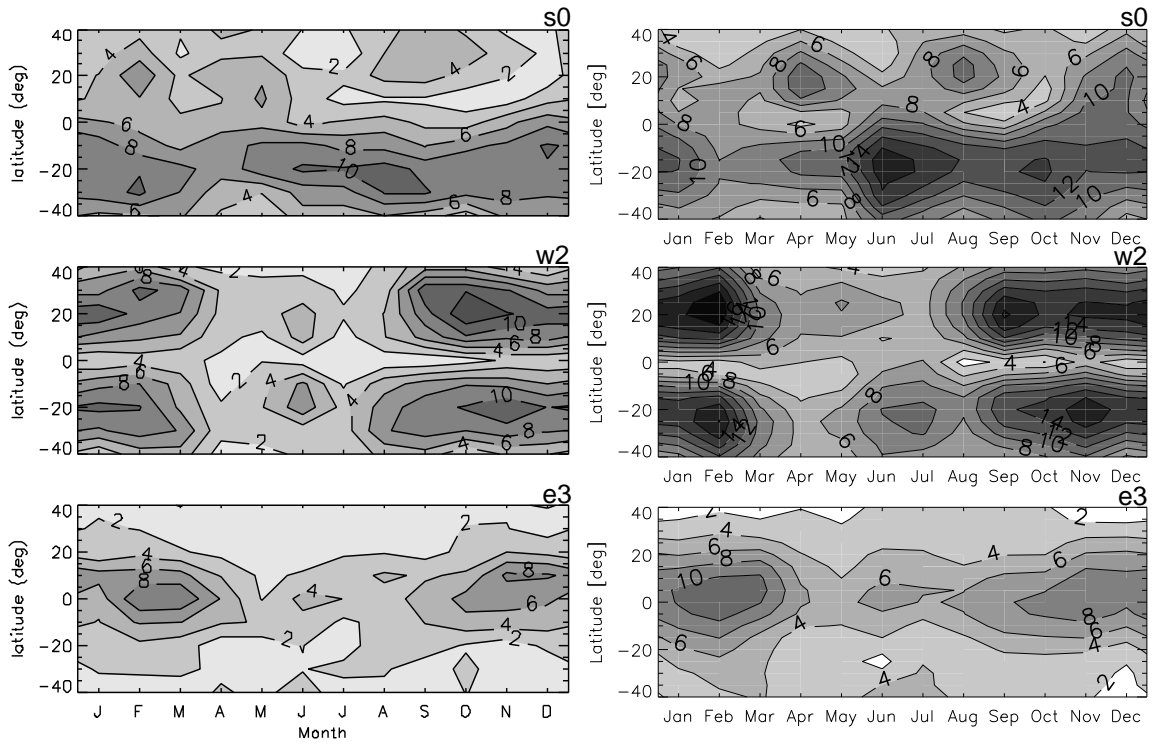


Figure 4.14: Diurnal tidal amplitudes (m/s) for the meridional wind at 95 km. Left column: UARS (HRDI & WINDII, 1991-1994, taken from *Forbes et al.* [2003], copyright 2003 American Geophysical Union. Reproduced/modified by permission of American Geophysical Union.); right column: TIDI (2002-2005). From top to bottom: s0, w2, e3.

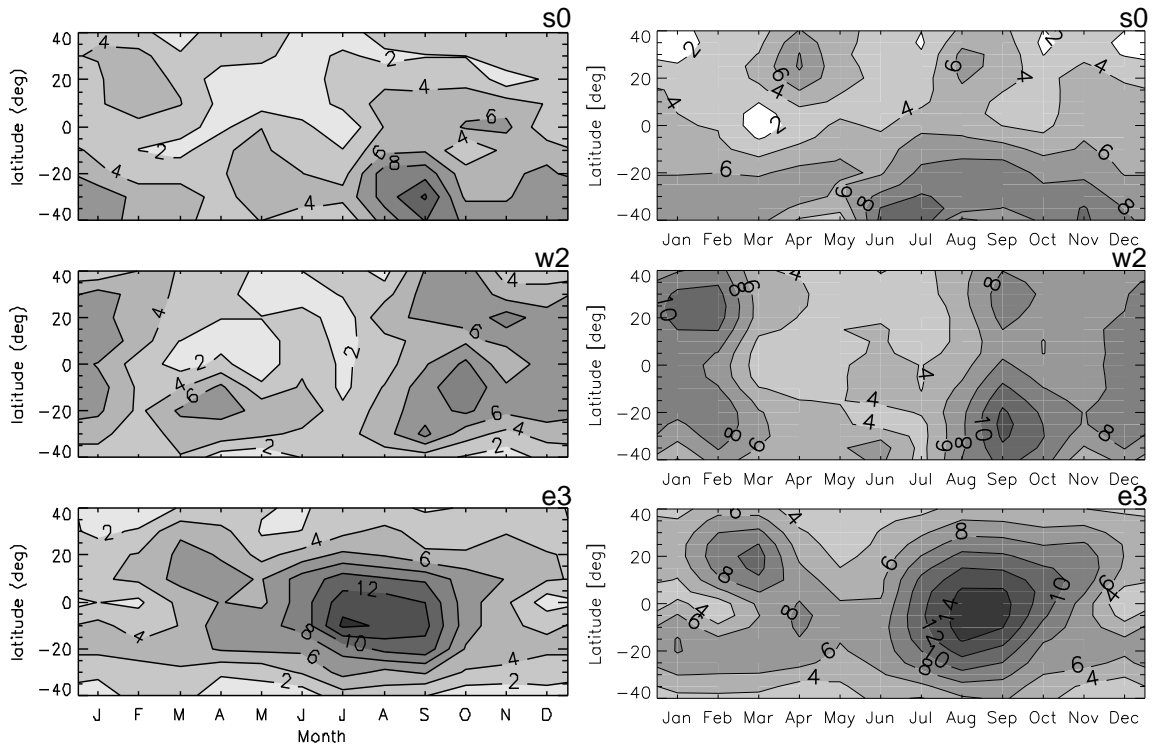


Figure 4.15: As Figure 4.14, but for the zonal wind.

a sharp amplitude peak in September at 30°S that is much broader in the TIDI data. Nevertheless, the agreement between TIDI and the UARS analysis is quite encouraging. Both data sets show an almost identical seasonal variation for several components. Considering the 11-year time lag, this points to a remarkable seasonal cycle stability of the nonmigrating tides.

#### 4.3.5 Model/observation comparison

The interpretation of the TIDI tidal diagnostics and the elucidation of the associated processes on the MLT requires complementary modeling efforts. One question to be answered in this context is what tidal sources and forcing mechanisms are responsible for the observed relative strength and seasonal variation of the tides. The TIDI climatologies are therefore compared to the tidal predictions from the GSWM, TIME-GCM, and extended CMAM.

As a climatological, linear tidal model, GSWM does not account for non-linear processes such as wave-wave interaction forcing and it does not produce inter-annual variations. The model version used here is overviewed in section 3.2.1. The only tidal source included is latent heat release due to tropical deep convection. GSWM provides monthly amplitudes and phases for 13 diurnal and 13 semidiurnal tidal components (w6 to e6).

Non-linear wave-wave interaction forcing is the dominant source of nonmigrating tides in TIME-GCM that, on the other hand, does not include the latent heat source. *Hagan and Roble* [2001] show that the w2 and s0 diurnal components in TIME-GCM are predominantly forced by the non-linear interaction between the migrating tide and QSPWs. For this study, TIME-GCM was run for the years 2002 and 2003 with the migrating tides at the lower boundary specified by GSWM (radiative forcing only) and 10 hPa temperature and geopotential data from NCEP. The simulations are overviewed in section 3.2.2. They include realistic solar and geomagnetic forcing based upon the conditions that prevailed in 2002 and 2003. Daily model output was generated with one hour time resolution. Fast Fourier transform then provides daily tidal amplitudes and phases that were averaged into monthly bins.

As a full GCM, the extended CMAM accounts for all the tidal sources included in the GSWM and TIME-GCM simulations except for ionospheric and auroral processes. It may thus be expected that the extended CMAM simulations provide a more complete description of the tidal fields in the MLT, although GSWM and TIME-GCM results are better suited to identify the tidal sources responsible for the magnitude and distribution of a specific tidal component. Section 3.2.3 gives an overview of the model. Nonmigrating tide simulations are described by *Ward et al.* [2005].

Time series of GSWM and TIME-GCM tidal predictions at 95 km have been compared to preliminary TIDI meridional wind tides in an earlier paper [*Oberheide et al.*, 2005]. Neither model alone could reproduce the seasonal variation of the w2 and s0 components. The combined model results described the observed amplitudes well during equinox, but they underestimated the w2 and s0 tides during winter solstice. The e3 component was solely forced by latent heat release. Because the TIDI climatology has been extended here, it is worthwhile to redo this comparison and to

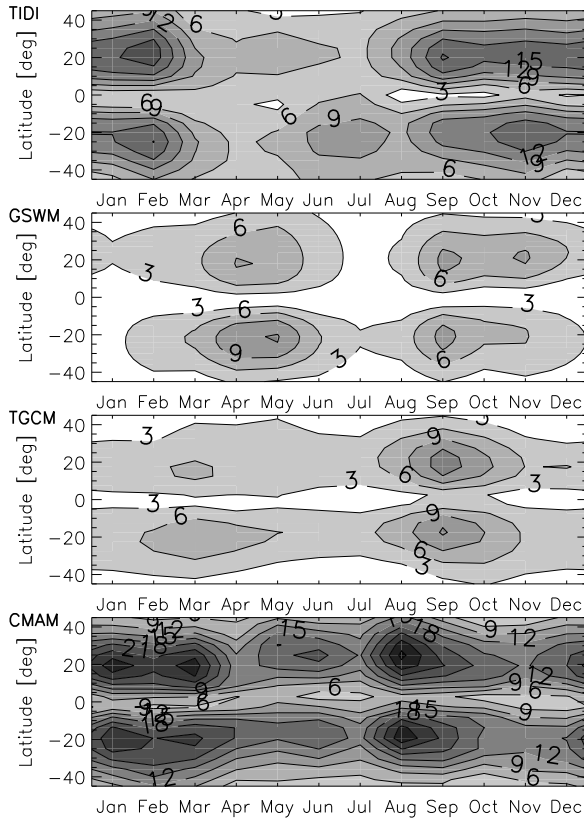
Table 4.6: Leading tidal forcing mechanisms for the diurnal w2, s0, e2, and e3 components. LH: latent heat forcing. WW: interaction between the migrating tide and planetary waves.

component	leading forcing mechanism(s)
w2	WW & LH about equally important over the course of the year, LH may be larger during solstices
s0	WW generally more important with increasing LH contribution during equinoxes
e2	predominantly LH, possible contribution of radiative forcing
e3	LH

do a similar one for the zonal wind and with the extended CMAM. Comparisons are only shown for w2, s0, e2, and e3. These components already give a general overview of the model strengths and shortcomings, and the tidal forcing mechanisms. Time series are compared at 95 km which is close to the peak altitude of most components. Comparisons of the vertical amplitude and phase structures are provided for two exemplary months: January and September.

The models partly agree and partly disagree with the observation. It may thus be helpful to summarize the basic findings (Table 4.6) of the comparisons before discussing the details: (i) the interaction between the migrating tide and planetary waves is an important contribution to the forcing of the standing (s0) and westward propagating components. (ii) Eastward propagating components are predominantly forced by latent heat release in the tropical troposphere. This result comes not unexpected because the interaction between QSPW-1 with the migrating tide may result in a forcing of w2 and s0 (see section 2.2). Forcing e2 or e3 by wave-wave interaction would require QSPWs of wavenumbers 3 or 4 that usually have small amplitudes (compared to QSPW-1). Global analysis of diurnal rainfall rates (as a proxy for latent heat release), on the other hand, shows the largest power at w2, s0, e2, e3, and e4 [*Forbes et al.*, 1997].

**w2, meridional (Figures 4.16 and 4.17)** TIDI amplitudes maximize at about 20° North and South. This and the anti-symmetric phase behavior about the equator is well reproduced by all models that also agree in the vertical wavelength. The observed w2 component maximizes in Jan-Feb (15-18 m/s) and in Sep-Dec with a secondary peak in Jun-Jul (9 m/s). GSWM and TIME-GCM fail to reproduce the secondary peak but the amplitudes from both models together match the observation in the Sep-Dec period. The modeled maxima in Mar-May occur two months later than in the TIDI data. As a result, the January response from GSWM and TIME-GCM (2-4 m/s each, Figure 4.17a) are much smaller than in the TIDI data. The September model predictions (Figure 4.17b) are between 8 m/s (GSWM) and 16 m/s (TIME-GCM) which comes close to the observation although both models maximize about 5 km higher in altitude. From this comparison, both latent heat release in the tropical troposphere and wave-wave interaction forcing are about equally important



## w2 meridional

Figure 4.16: Diurnal tidal amplitudes (m/s) for w2, meridional wind, 95 km. From top to bottom: TIDI, GSWM, TIME-GCM, extended CMAM. Contour interval is 3 m/s.

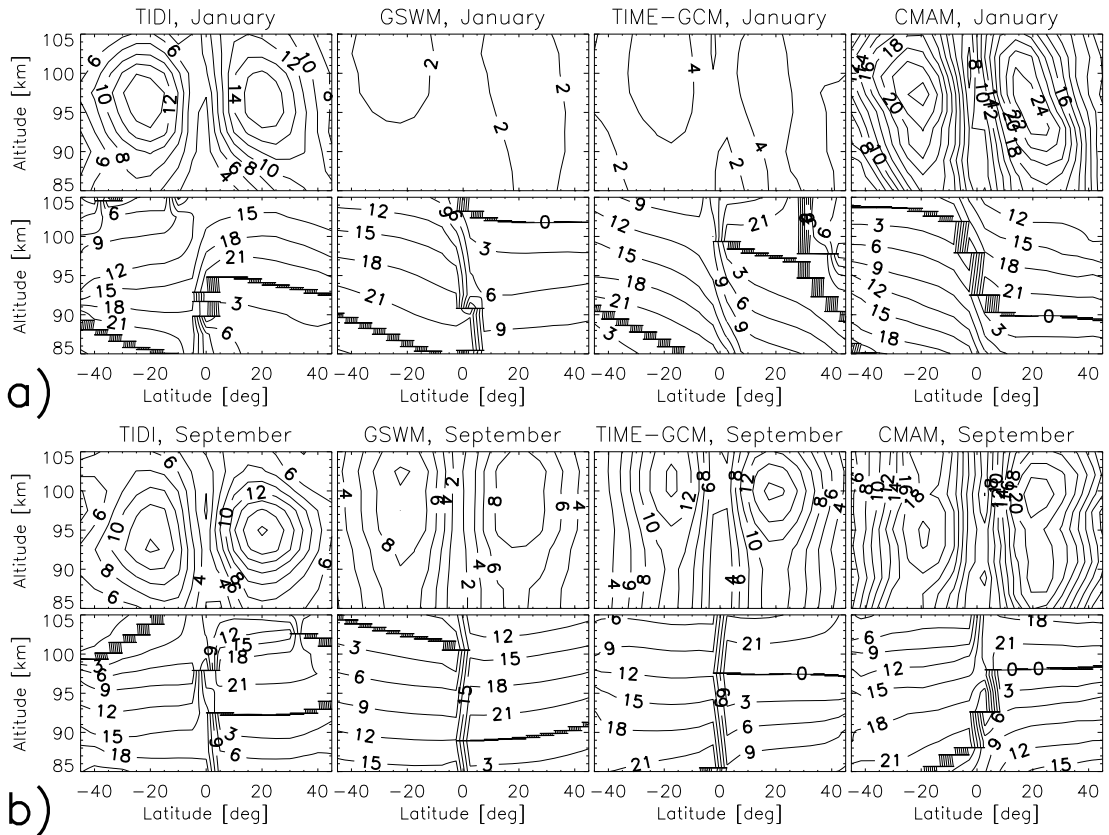
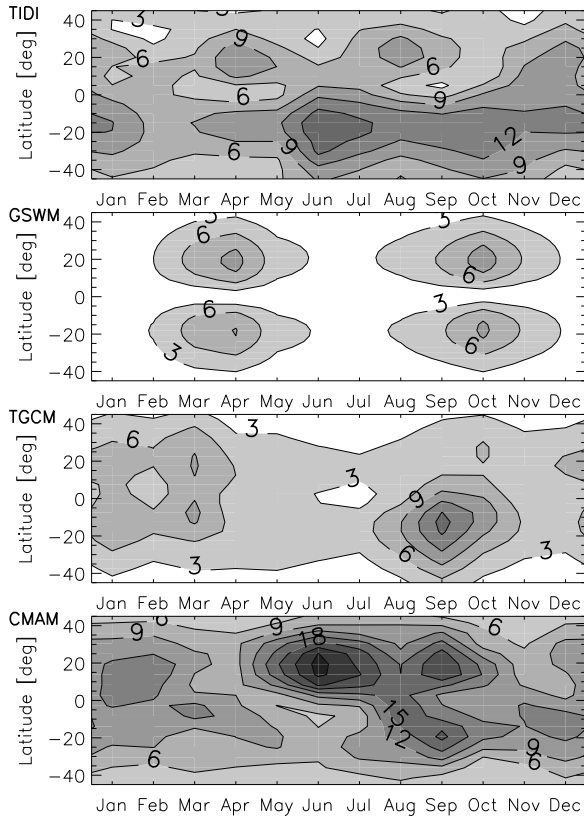


Figure 4.17: Amplitudes (top, m/s) and phases (bottom, UT of max. at 0° longitude) for w2, meridional wind. a) January. b) September. Contours are 2 m/s and 3 h.



**s0 meridional**

Figure 4.18: As Figure 4.16, but for the s0 meridional component.

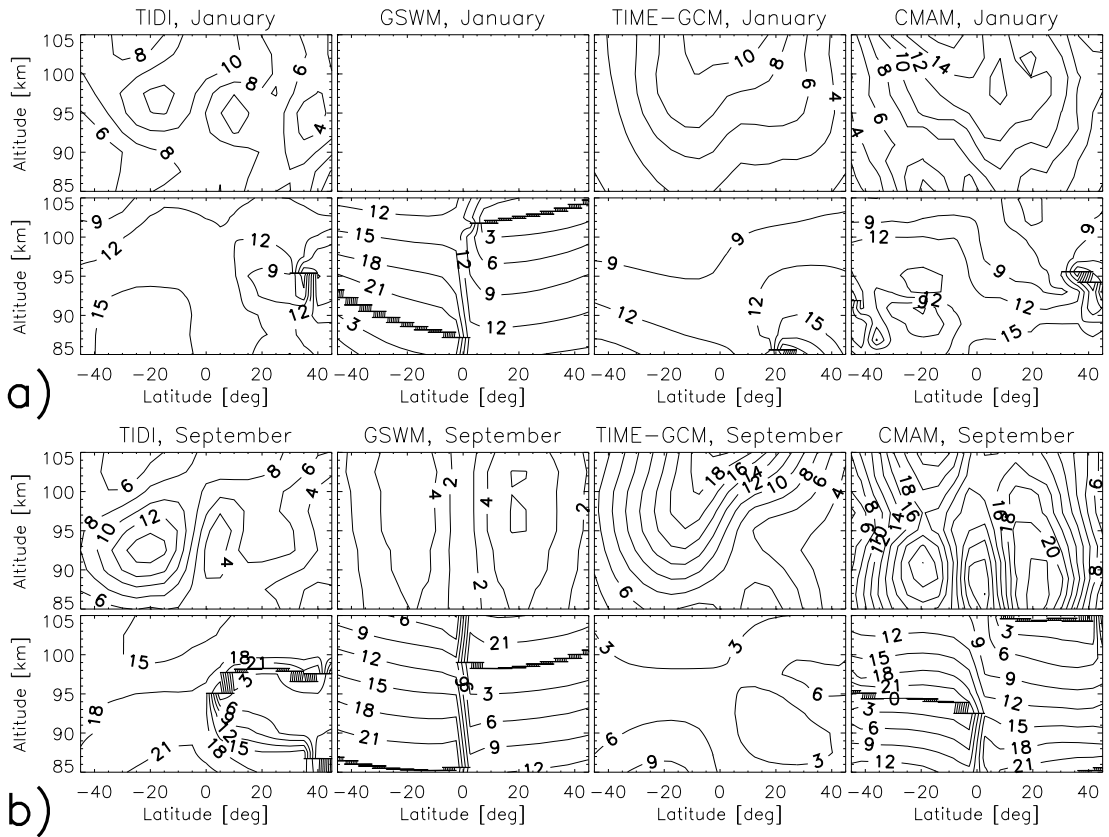
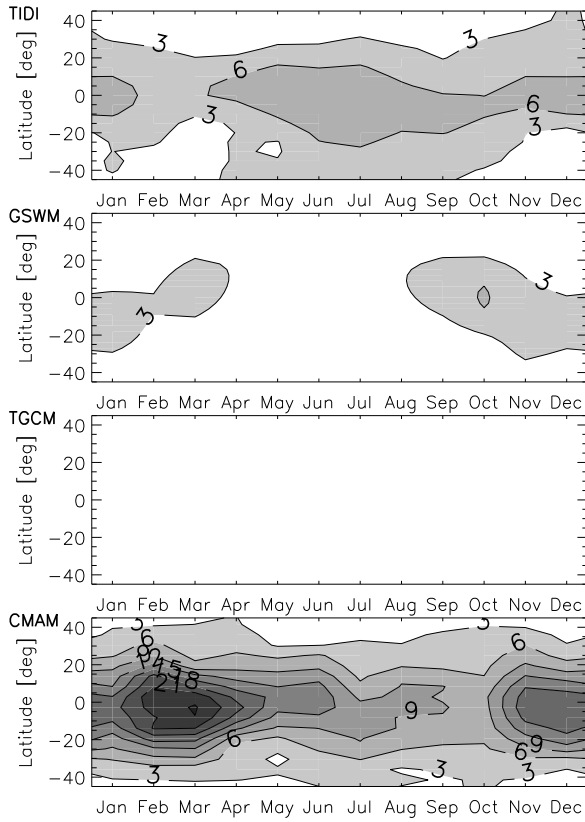


Figure 4.19: As Figure 4.17, but for the s0 meridional component.



**e2 meridional**

Figure 4.20: As Figure 4.16, but for the e2 meridional component.

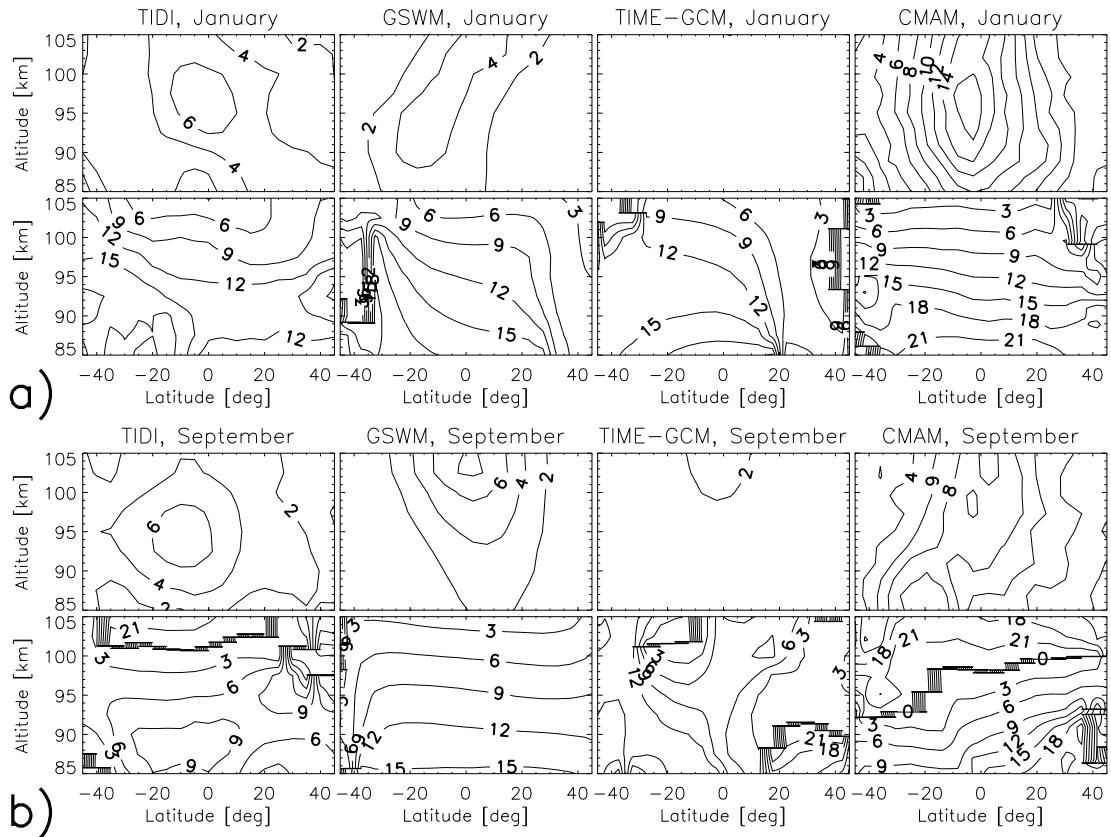
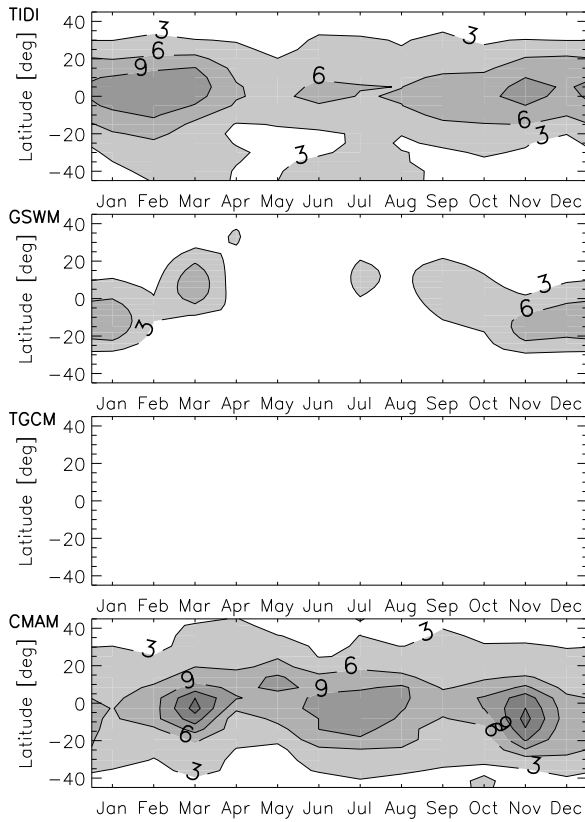


Figure 4.21: As Figure 4.17, but for the e2 meridional component.



### e3 meridional

Figure 4.22: As Figure 4.16, but for the e3 meridional component.

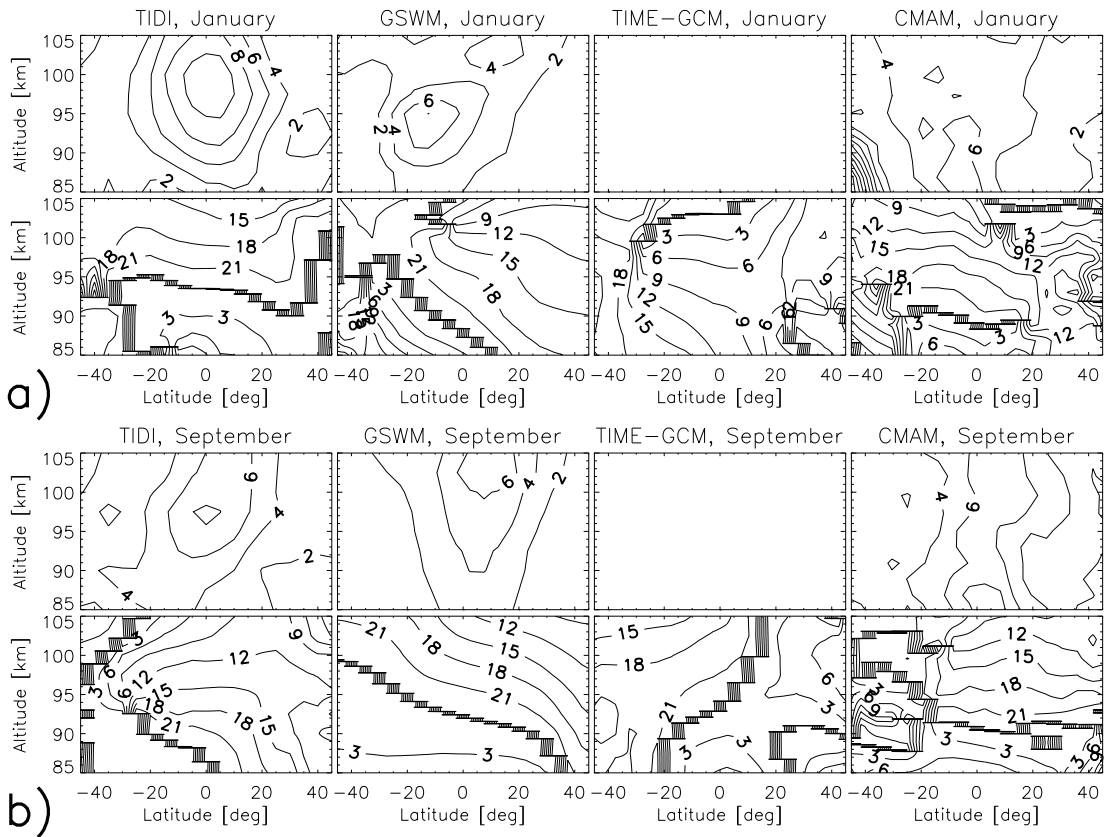
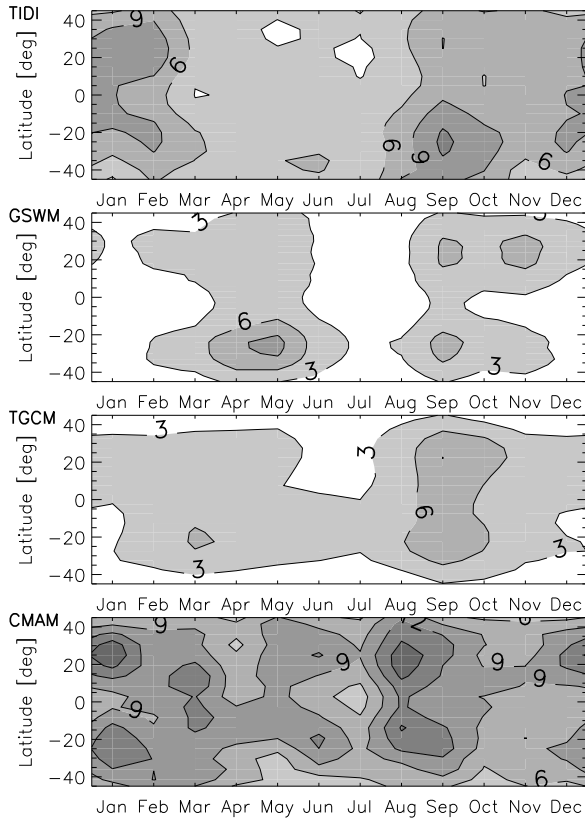


Figure 4.23: As Figure 4.17, but for the e3 meridional component.



w2 zonal

Figure 4.24: Diurnal tidal amplitudes (m/s) for w2, zonal wind, 95 km. From top to bottom: TIDI, GSWM, TIME-GCM, extended CMAM. Contour interval is 3 m/s.

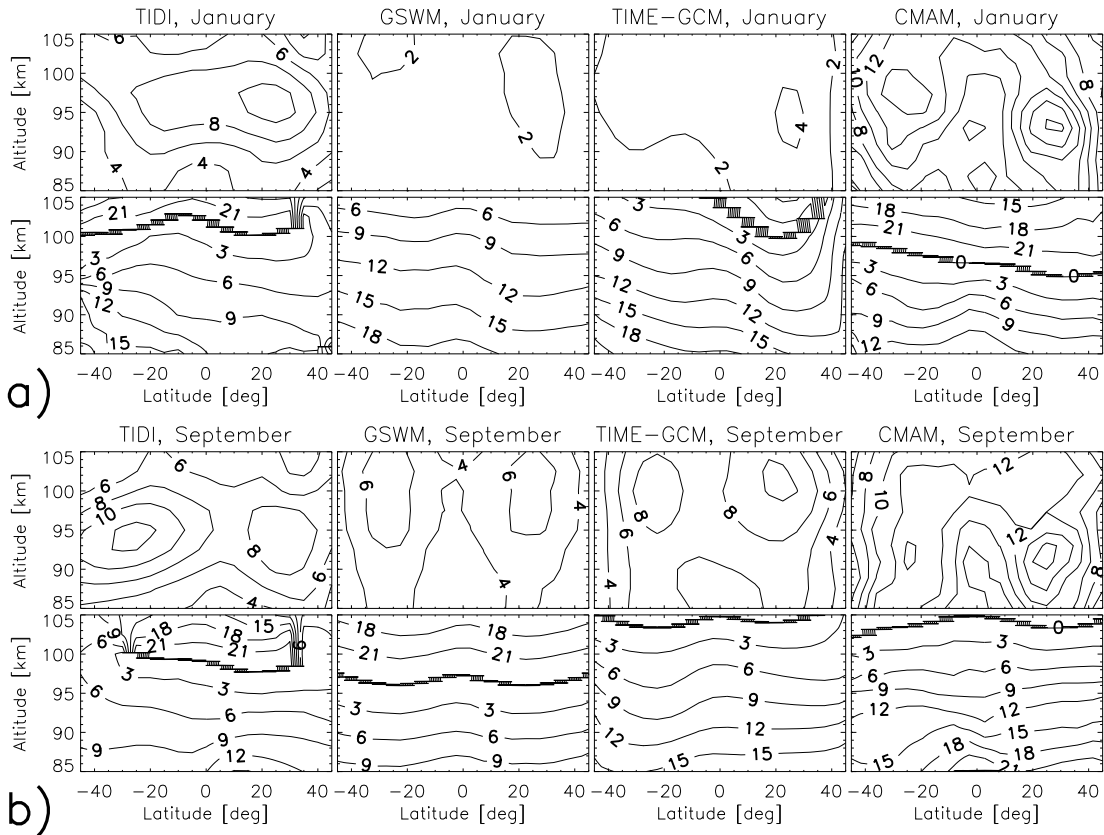
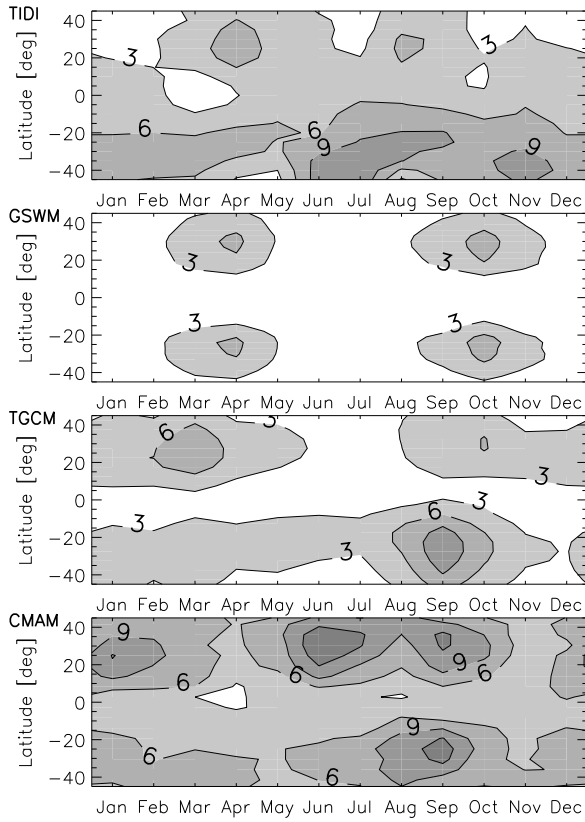


Figure 4.25: Amplitudes (top, m/s) and phases (bottom, UT of max. at 0° longitude) for w2, zonal wind. a) January. b) September. Contours are 2 m/s and 3 h.



s0 zonal

Figure 4.26: As Figure 4.24, but for the s0 zonal component.

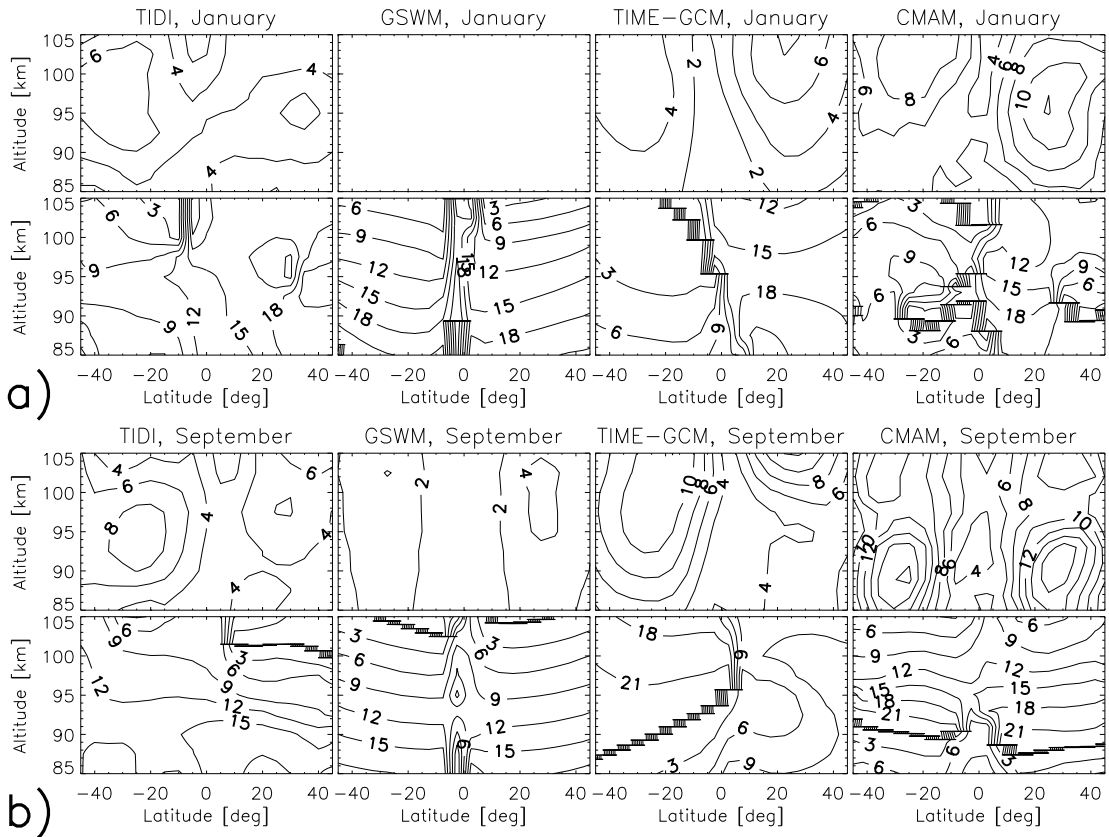
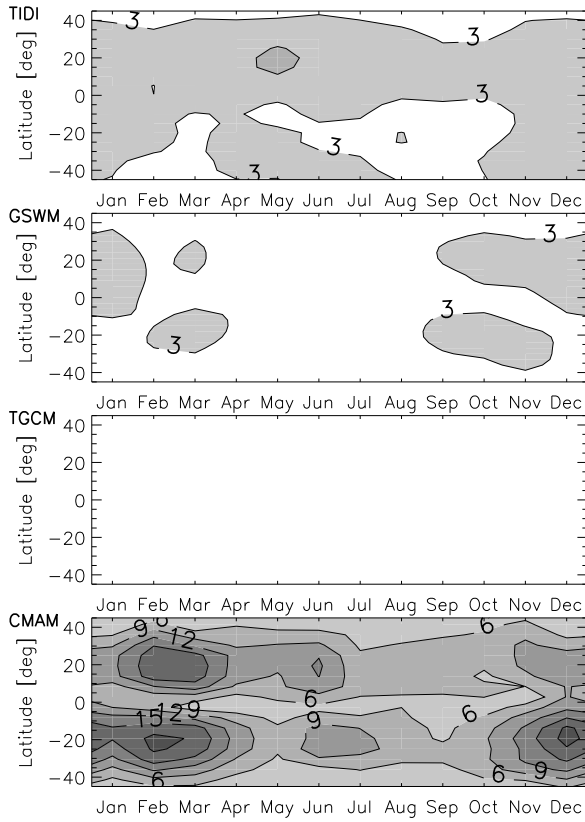


Figure 4.27: As Figure 4.25, but for the s0 zonal component.



**e2 zonal**

Figure 4.28: As Figure 4.24, but for the e2 zonal component.

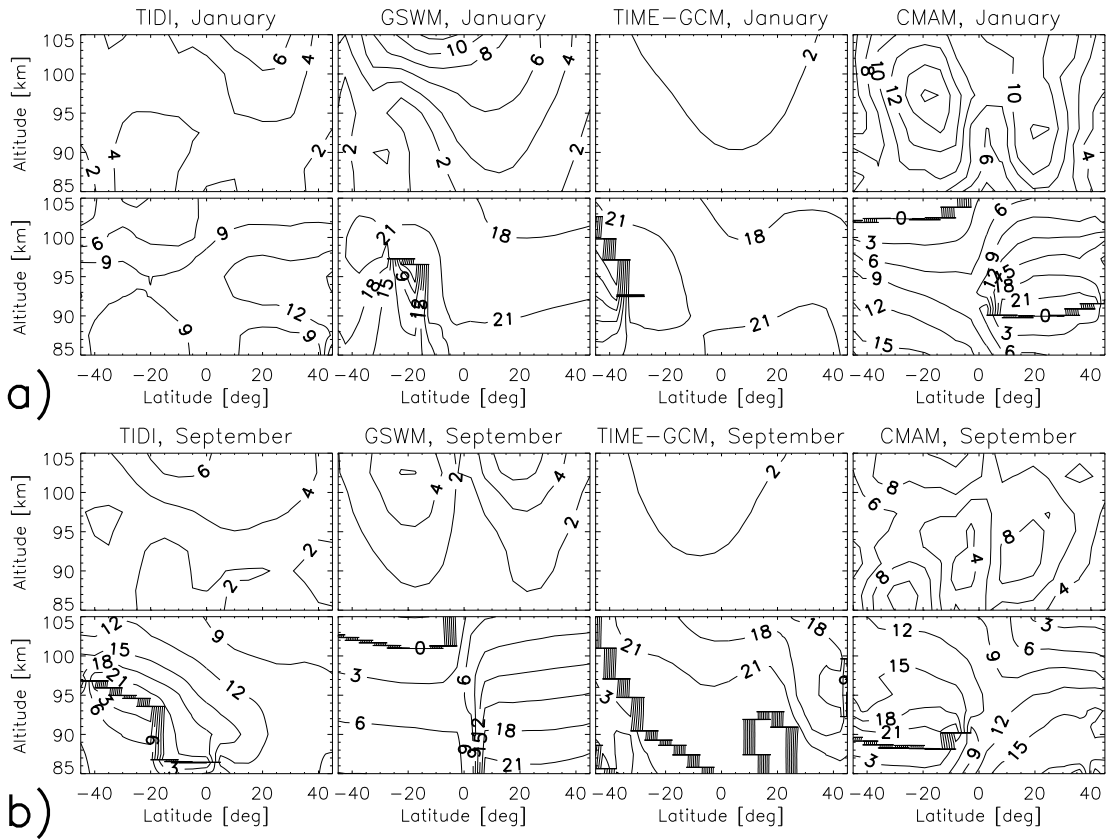
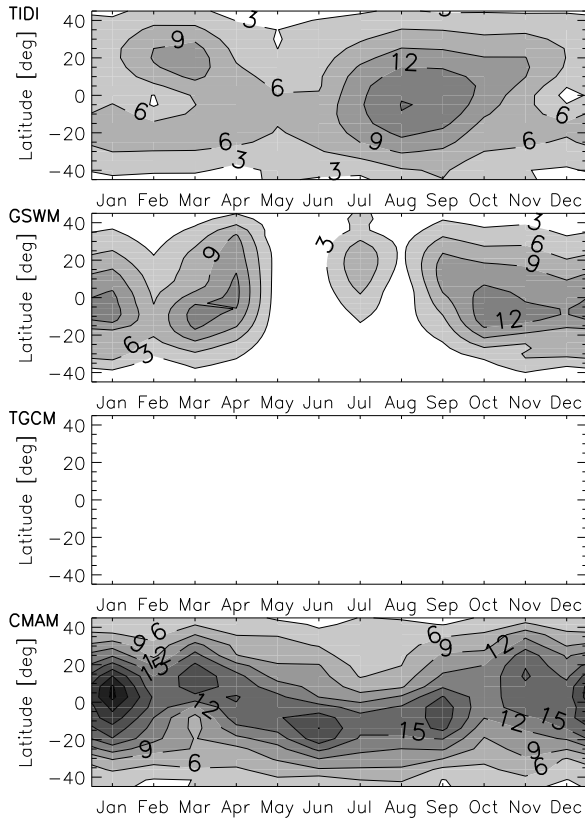


Figure 4.29: As Figure 4.25, but for the e2 zonal component.



**e3 zonal**

Figure 4.30: As Figure 4.24, but for the e3 zonal component.

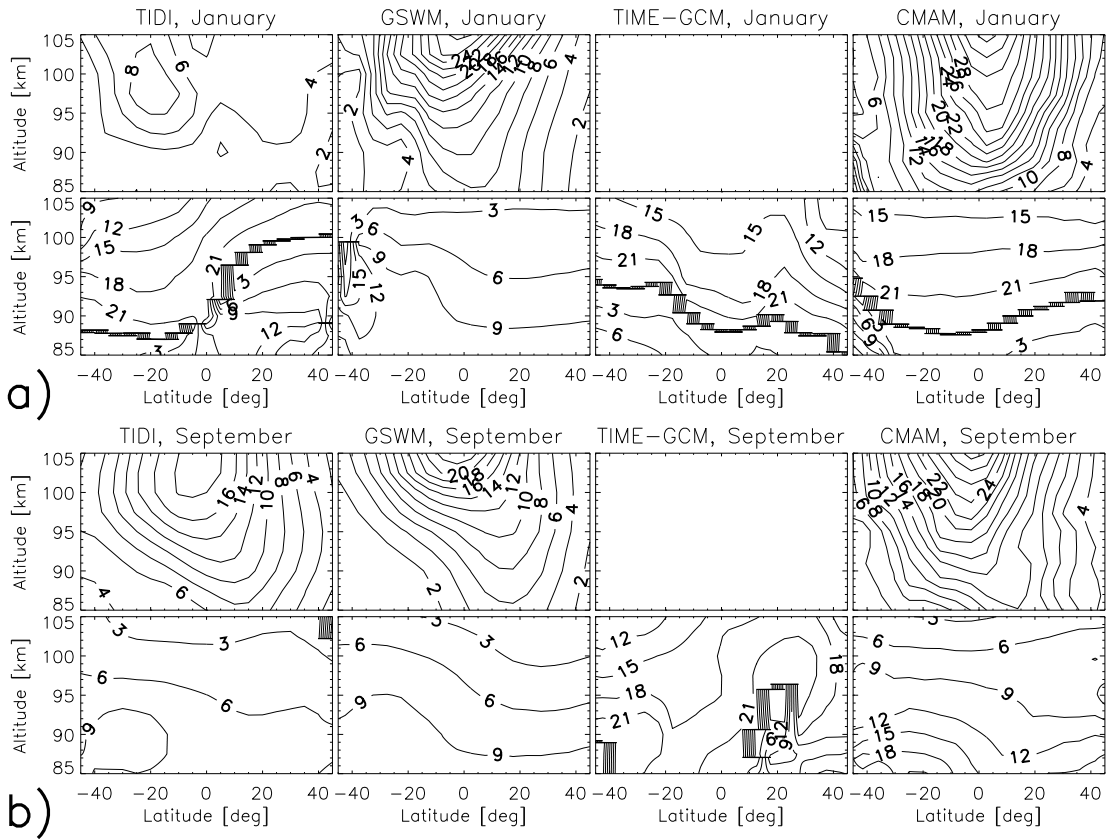


Figure 4.31: As Figure 4.25, but for the e3 zonal component.

over the course of the year. This is consistent with the result of the CRISTA/model intercomparison of equatorial temperatures discussed in section 4.1.3.

The extended CMAM, on the other hand, gives a very good description of the observed temporal evolution and vertical structure although the model overestimates the  $w_2$  amplitude by about 30%. With few exceptions, observed and modeled peak altitudes agree within 1-2 km. The model even predicts the secondary maximum in boreal summer that is not reproduced by GSWM and TIME-GCM. It is not entirely clear whether this is more related to the tidal forcing and propagation in the extended CMAM or whether it is more a result of the relative phasing between the latent heat and non-linear interaction contributions. However, the model predicts similar boreal summer maxima for other components (i.e.,  $e_3$  meridional,  $e_2$  zonal, see below) where a significant contribution of wave-wave interaction forcing is rather unlikely. The  $w_2$  secondary amplitude maximum in boreal summer may thus be more associated with latent heat forcing.

**s0, meridional (Figures 4.18 and 4.19)** GSWM predicts two equinox maxima (8 m/s) around  $20^\circ$  North and South with an anti-symmetric phase behavior about the equator. The model response during solstices is negligible. TIME-GCM shows a distinct SH amplitude maximum in September (15 m/s) and a broad equatorial maximum between Jan-Mar (Figure 4.18). The phases are symmetric about the equator which is consistent with the latitude-height distribution of the amplitudes (Figure 4.19). A single amplitude maximum peaks above 105 km at the equator with a latitudinal shift into the SH at altitudes below. The quite different GSWM and TIME-GCM predictions now allow to interpret the TIDI observation.

Although the time evolution (Figure 4.18) may suggest the presence of two maxima at  $20^\circ$  North and South in January, the latitude-height amplitude and phase distributions in Figure 4.19a show that only a single maximum exists that is shifted toward Southern latitudes at altitudes below 100 km. This, the symmetric phase behavior about the equator, and the long vertical wavelength are consistent with the TIME-GCM simulation. The interpretation of the September observations (Figure 4.19b) is less unequivocal. As in the TIME-GCM, the TIDI amplitude at 95 km maximizes around  $20^\circ$ S with a shift toward the equator at altitudes above. However, the observed peak altitude of 93 km is in contrast to the model simulation. The long vertical wavelength in the SH decreases in the NH with an equatorial phase jump occurring between 87 km and 97 km. The observed phases become again symmetric about the equator above 97 km. All these discrepancies to the TIME-GCM predictions suggest that the latent heat source also plays a role in forcing the s0 component in September. This is supported by the time evolution of the observed s0 amplitudes and phases shown in appendix A4 (Figure A4.2). The phasing is more anti-symmetric about the equator and the vertical wavelength is shorter during equinoxes when the GSWM predicts the largest latent heat response. Hence, the vertical structure and the time evolution of the observed s0 component is consistent with a combination of latent heat and wave-wave interaction forcing. The latter source is generally more important and causes the inter-hemispheric asymmetry of the amplitudes: a single amplitude maximum is shifted toward Southern latitudes. The secondary amplitude maxima at  $20^\circ$ N are likely caused by an increasing latent heat contribution during equinoxes that also introduces some phase asymmetry about the equator.

The extended CMAM supports this interpretation. In January, it is consistent with the TIME-GCM result although it shows an amplitude shift toward Northern latitudes around 95 km. The September simulation shows an anti-symmetric phase behavior about the equator with short vertical wavelengths and two distinct amplitude maxima at 20° North and South that peak around 90 km. Its general structure agrees with the GSWM result but with much larger amplitudes (22 m/s). The different phase behavior compared to the observation suggests that the model overestimates the latent heat forcing of  $s_0$ . This is similar to the result obtained for  $w_2$ . It is interesting to note that the extended CMAM again predicts a boreal summer maximum that is not present in GSWM and TIME-GCM. However, the summer maximum in the model occurs in the NH whereas the observed maximum is in the SH. One may speculate about the reason for this discrepancy, that is, the specifics of the PW-migrating tide interaction in the model, but it is so far not understood.

**e2, meridional (Figures 4.20 and 4.21)** The observed broad amplitude distribution is symmetric about the equator. This is reproduced by the GSWM although the model does not predict the tidal maximum in boreal summer. GSWM amplitudes (4 m/s at 95 km) are slightly smaller than the observed ones (6 m/s) and maximize about 5-10 km higher in altitude. Observed and modeled vertical wavelengths are in good agreement. The TIME-GCM response is negligible thus indicating that the  $e_2$  component is predominantly forced by latent heat release. The extended CMAM predicts about the same tidal distribution as the GSWM but with larger amplitudes. It better reproduces the peak altitude in January but with much larger amplitudes (16 m/s). As for  $w_2$  and  $s_0$ , the model generally overestimates the observed amplitudes.

**e3, meridional (Figures 4.22 and 4.23)** As for  $e_2$ , the TIME-GCM response is negligible with GSWM predicting equatorial amplitudes of about 6 m/s peaking around 95 km (January, Figure 4.23a) and 105 km (Figure 4.23b). The model phase distribution is basically symmetric about the equator but with some slope in it. TIDI amplitudes agree well with the model prediction although they are slightly larger (10 m/s in January, 8 m/s in September). The model amplitudes maximize partly below (September) and partly above (September) the observation. Vertical wavelengths and phase symmetries are similar to GSWM. TIDI and GSWM time evolutions are similar to  $e_2$  and agree with each other. GSWM now reproduces a weak secondary maximum in July. The comparison indicates that the  $e_3$  component is forced by latent heat release alone. As for  $e_2$ , the extended CMAM prediction is similar to GSWM but it again tends to overestimate the tidal amplitude

**w2, zonal (Figures 4.24 and 4.25)** The  $w_2$ , zonal component is symmetric about the equator and thus different from its meridional counterpart that was anti-symmetric about the equator. Apart from that, both the observed and modeled time evolution and vertical structure are generally similar in the zonal and meridional directions. This is expected from the tidal theory and shows the internal consistency of the TIDI data. The discussion provided for the  $w_2$ , meridional component also applies here: both latent heat release in the tropical troposphere and wave-wave interaction forcing are about equally important over the course of the year.

**s0, zonal (Figures 4.26 and 4.27)** As for  $w_2$ , the  $s_0$  zonal component has a different symmetry (compared to  $s_0$ , meridional) about the equator in the models and the observation. The vertical phase lines in the equatorial GSWM results are

not significant because the model result is close to zero. A discussion identical to the one provided above leads to the same conclusions and is thus not repeated again: migrating tide - PW interaction forcing is generally more important with an increasing latent heat contribution during equinoxes.

**e2, zonal (Figures 4.28 and 4.29)** Comparing the observed e2, zonal component to the models provides additional information to the meridional case. TIDI generally observes a single, broad amplitude maximum with a symmetric phase behavior about the equator although the peak latitude is shifted into the SH or NH (about  $20^\circ$ , height and season dependent, compare Figure A4.7 in appendix A4). However, there are now significant differences between the TIDI, the GSWM, and the extended CMAM results. GSWM slightly overestimates the TIDI amplitudes in January, but generally reproduces their latitude-height distribution including the peak altitude well above 105 km. Vertical wavelength and phase symmetry about the equator are also similar. This is different in September when GSWM predicts two mid-latitude maxima and an anti-symmetric phase behavior about the equator. The TIDI observation still shows a single maximum and symmetric phases about the equator. The extended CMAM, on the other hand, always predicts anti-symmetric phases about the equator and two mid-latitude maxima. It is unclear why these model-observation and model-model discrepancies occur. The specifics of the background atmosphere, particularly of the background zonal winds, may play a role in this context by favoring the upward propagation of either symmetric or anti-symmetric wind expansion Hough modes. It is also possible that radiative forcing processes contribute to the differences. This may be supported by the small (but non-negligible) TIME-GCM response above 90 km. A tidal/PW interaction forcing of e2 is rather unlikely and the only other nonmigrating tidal source in the model is solar insolation absorption. The general latitude-height distribution of TIME-GCM amplitudes and phases is similar to the TIDI observation.

**e3, zonal (Figures 4.30 and 4.31)** The TIME-GCM response is negligible such that wave-wave interaction does not play much of a role. GSWM and extended CMAM results are internally consistent with a broad amplitude maximum around the equator, a peak altitude above 105 km, and symmetric phases about the equator. The extended CMAM amplitudes are always larger than those of the GSWM which is most striking in boreal summer (similar to the meridional case). The model-observation comparison in general and the time evolution in particular is less favorable. The agreement during equinoxes is good (Figure 4.31b) with more or less the same amplitudes and phases thus indicating a leading role of latent heat release in forcing this component. Significant differences occur during solstices. The GSWM response in boreal summer is too small and the extended CMAM amplitude is too large. This is so far consistent with the findings for the meridional component but the most striking difference occurs in Jan-Feb. The observation shows two distinct maxima around  $20\text{-}25^\circ$ , a peak altitude of 97 km, and an anti-symmetric phase behavior about the equator. This structure is also present in the UARS data shown in Figure 4.15 and thus not an artifact of the data analysis. It is rather a persistent signature because the UARS and TIDI observations are 11 years apart. The failure of both models to reproduce it remains unexplained so far. It may indicate that the atmosphere rather favors the upward propagation of anti-symmetric wind expansion Hough modes (compared to the symmetric ones in the models) or that other unknown mechanisms play a role.

### 4.3.6 Some conclusions from the diurnal analyses

TIDI winds provide a data set that is unprecedented in that it is amenable to global nonmigrating tidal analysis over a range of MLT altitudes. A comparison with the UARS results at 95 km yields a good agreement and provides additional confidence in the TIDI results. The derived monthly climatologies of zonal and meridional diurnal tides for seven nonmigrating components show that the amplitude of a single nonmigrating tidal component can reach 20 m/s. Their aggregate effects can easily exceed the amplitude of the radiatively forced migrating tide. Nonmigrating tides therefore introduce a considerable amplitude and phase modulation of the tidal fields in the MLT. This is particularly important when comparing ground-based observations with satellite data or with models, and for data assimilation approaches. First comparisons of the TIDI tides with a chain of MF-radar instruments in the Indian/Indonesian sector show that large parts of longitude dependent amplitude differences between these ground-based instruments could be explained by nonmigrating tides (T. Nakamura, private communication).

Observed and modeled phases point to an upward energy and momentum transport with tidal forcing in the lower atmosphere. Hence, nonmigrating tides provide an important mechanism for coupling the lower with the upper atmosphere. Large-scale tropospheric systems that do not propagate into the MLT nevertheless influence the dynamics, chemistry, and energetics in this height region via their imprint upon the tidal fields. The model/observation comparisons indicate that for the w2 and s0 components both latent heat release in the tropical troposphere and wave-wave interaction forcing need to be considered. Their relative contribution may differ from month to month but these sources can basically explain the observations. The eastward propagating components e2 and e3, however, appear to be mostly governed by the latent heat source, although some differences between the model predictions and the observation exist. These findings are consistent with the results obtained from CRISTA and LIMS. A correlation analysis between QSPWs and the tides, similar to the LIMS analysis in section 4.2, has already been started and will hopefully provide further insight into the non-linear wave-wave interaction source in the future.

The quantitative agreement between the model predictions and the TIDI observations is good for some months and rather bad for other months. This is not very surprising because GSWM and TIME-GCM do not account for all tidal sources (i.e., latent heat release tidal/PW interaction forcing is missing) and interactions with the background atmosphere (GSWM is a linear model). The extended CMAM generally reproduces more realistic tidal amplitudes and phases but has a tendency to overestimate the amplitudes which is likely due to the latent heat source and/or the tidal dissipation in the model. There is an obvious need to further improve tidal forcing and dissipation schemes in the future. Ongoing collaborations with the GSWM, TIME-GCM, and extended CMAM owners pursuit this goal with the TIDI climatologies providing the necessary guidance for such efforts.

Analyzing the propagation characteristics, variability, and forcing mechanisms of the nonmigrating tides requires a componentwise treatment. Many studies, however, rather require information about the total tidal wind field in the MLT region, that is, the superposition of the nonmigrating tides with the migrating tide. The latter

component cannot be analyzed with the approach used here but it is currently being processed with a different method (Q. Wu, private communication). It may be possible to merge both data sets in the future to provide the community with an easily accessible tidal wind reference based upon TIDI data via a web interface. Future work will also focus on analyzing interannual variations of the nonmigrating tides and how they are related to variations in the atmospheric background state, to tidal source variations, and to the solar cycle. This is particularly interesting because TIDI will be the only satellite instrument measuring MLT winds for some time to come.

#### 4.4 Semidiurnal tidal climatologies from TIDI wind data

Semidiurnal nonmigrating tides in the TIDI wind data are analyzed in exactly the same way as the diurnal tides. Climatologies of monthly mean amplitudes and phases in the zonal and meridional directions are derived for six tidal components each (w4, w3, w1, s0, e1, e2) at altitudes between 85 and 105 km and latitudes between 45°S and 45°N. As for the diurnal tide, it is not possible to derive the migrating component (w2 for the semidiurnal tide) with the analysis method. Error analysis and subsequent calculation of the scaling factors follow the approach presented in section 4.3.2. Table 4.7 gives the results. They do not differ very much from those for the diurnal tides. The slightly larger absolute error is related to the generally smaller semidiurnal tidal amplitudes that usually maximize in boreal winter or fall equinox. Secondary maxima are frequently observed in boreal summer.

An in-depth model/observation comparison has not yet been performed. The following discussion thus focuses on the observational results. It is rather qualitative and intended as an overview. Most semidiurnal components reveal a considerable spatio-temporal variability that renders a more quantitative discussion difficult without providing much more detail information. Latitude-height plots of the semidiurnal monthly climatologies are omitted from the running text, for better readability. They are shown in appendix A5. Time-series of the tidal amplitudes are provided in Figures 4.32 and 4.33 at altitudes where the basic features of a specific component are most pronounced.

**w4, meridional (Figures 4.32a and A5.1)** The largest amplitudes (8-10 m/s) are found between October and March at about 40°S and 40°N. In most cases, the

Table 4.7: As Table 4.5, but for the semidiurnal tide.

component	scaling factor		amplitude accuracy		amplitude precision		phase precision	
	$v$	$u$	$v$ [%]	$u$ [%]	$v$ [ $\frac{m}{s}$ ]	$u$ [ $\frac{m}{s}$ ]	$v$ [hours]	$u$ [hours]
w4	1.50	1.54	17	14	0.8	0.7	1.8	1.6
w3	1.27	1.25	19	17	0.8	0.7	2.0	2.0
w1	1.29	1.33	17	23	0.9	0.7	2.0	1.9
s0	1.51	1.54	13	18	0.8	0.6	2.0	2.0
e1	2.05	2.10	20	13	0.7	0.5	2.2	2.0
e2	3.22	3.10	13	17	0.8	0.6	2.3	1.7

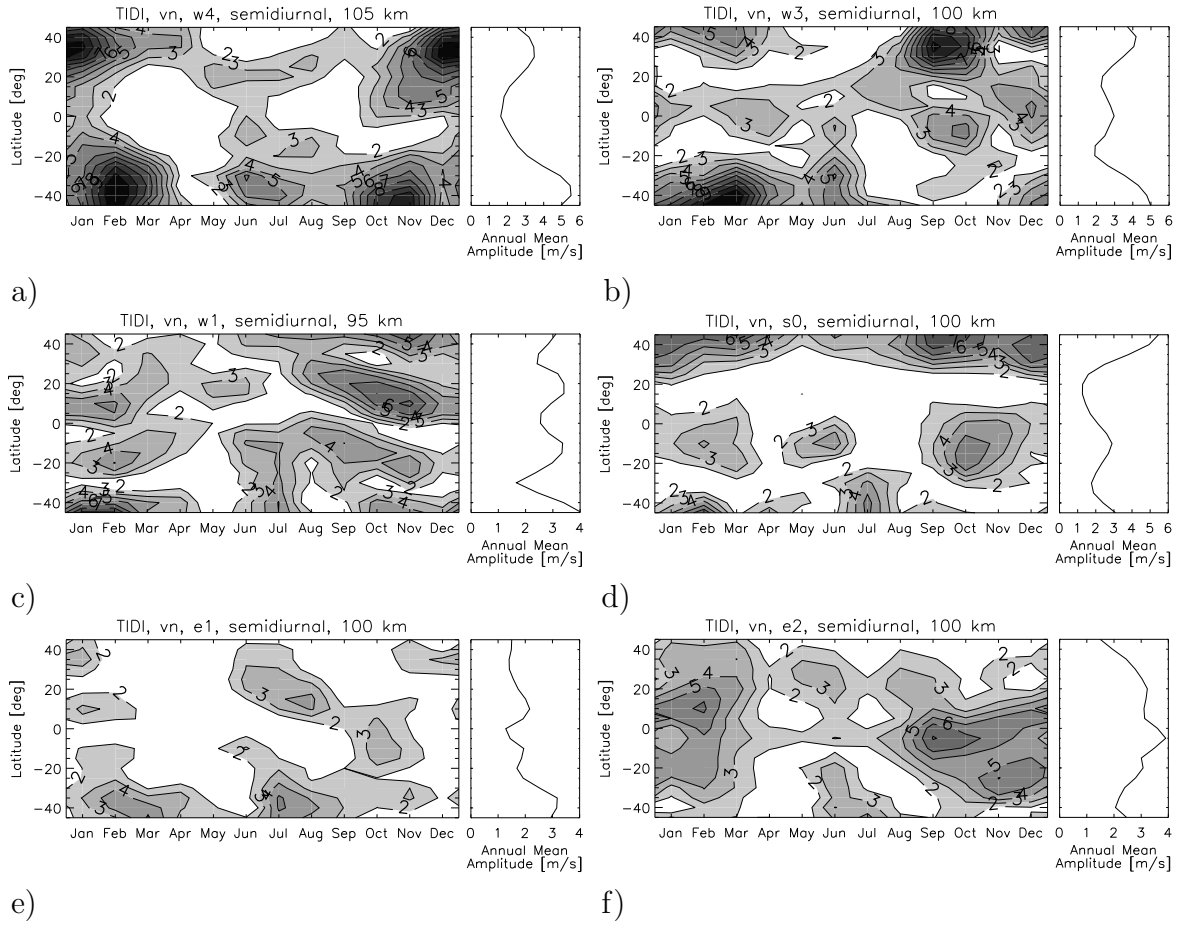


Figure 4.32: Time evolution of semidiurnal amplitudes for the meridional wind and annual mean amplitude. Contour interval is 1 m/s. Components are given at different altitudes. a) w4, 105 km; b) w3, 100 km; c) w1, 95 km; d) s0, 100 km; e) e1, 100 km; f) e2, 100 km.

peak altitude is above the upper boundary of the analyzed height interval. During these months, the amplitude minimizes at the equator and the component is anti-symmetric with respect to the equator. Phases decrease with increasing altitude but with a comparably long vertical wavelength of 40 km or even more. Amplitudes between April and September are generally smaller (3-4 m/s) and show an additional peak at equatorial latitudes. Accordingly, the component is rather symmetric about the equator with phase transitions at 20°S and 20°N (i.e., August).

**w3, meridional (Figures 4.32b and A5.2)** Again, largest amplitudes of 8-10 m/s are found at 105 km altitude and at 40°S and 40°N between September and April. Boreal summer amplitudes are smaller (2-5 m/s) but an equatorial maximum persists during the whole year. Phase transitions occur at roughly 20°S and 20°N such that this component is generally symmetric about the equator. Phases decrease with increasing altitude and the vertical wavelength is long.

**w1, meridional (Figures 4.32c and A5.3)** Similar to w4 and w3, largest amplitudes occur between September and April at high latitudes (40°S and 40°N) and altitudes (105 km) but secondary mid-latitude maxima (20°S and 20°N) are frequently observed that are most pronounced between 90 and 100 km altitude. Hence, three

phase transitions occur at roughly the equator and  $30^{\circ}\text{S}$  and  $30^{\circ}\text{N}$  although the exact location may differ from month to month (see October for a clear signature). Phase lines are almost vertical thus indicating a very long vertical wavelength.

**s0, meridional (Figures 4.32d and A5.4)** This component generally shows two maxima at or poleward of  $45^{\circ}\text{S}$  and  $45^{\circ}\text{N}$  with the latter being more pronounced and an additional equatorial maximum. Amplitudes reach 5-7 m/s in boreal winter with a considerable month-to-month variation of the peak altitude from 90-95 km to above 105 km. Phases generally decrease with increasing altitude and phase jumps occur at latitudes of minimum amplitude. Vertical wavelengths are usually very large.

**e1, meridional (Figures 4.32e and A5.5)** Maximum amplitudes at 105 km reach 4-5 m/s in February and July. The latitudinal distribution changes from three peaks at high ( $40^{\circ}$ ) and equatorial latitudes in January to two peaks at  $20^{\circ}\text{N}$  and  $30^{\circ}\text{S}$  in July to a single and rather symmetric peak in November. Phase jumps occur at latitudes of minimum amplitudes and may be shifted by several degrees latitude from one month to another. Phases generally decrease with increasing altitude but the vertical wavelengths vary between relatively short (i.e., July) and very long (i.e., January). A more quantitative assessment is difficult due to the large variability.

**e2, meridional (Figures 4.32f and A5.6)** Boreal winter and fall equinox amplitudes show a broad distribution symmetric about the equator. This behavior is also present in the phases that reveal a very long vertical wavelength during these months. Maximum amplitudes of 7 m/s are observed at the upper boundary of the analysis interval. The latitudinal distribution changes to a three peak structure in boreal summer ( $30^{\circ}\text{S}$ ,  $30^{\circ}\text{N}$ , equator) with phase jumps occurring at latitudes in between. Vertical wavelengths in boreal summer are much smaller than in winter.

**w4, zonal (Figures 4.33a and A5.7)** In contrast to its meridional counterpart, this component is symmetric about the equator in boreal winter with maximum amplitudes of 10 m/s around  $35^{\circ}\text{N}$  and  $40^{\circ}\text{S}$  and 105 km altitude. Phase jumps are not observed. Vertical wavelengths during the winter months are on the order of 40 km. Tidal response is small in boreal summer except for high Southern latitudes where the component has a different phase compared to latitudes equatorward of  $30^{\circ}\text{S}$ .

**w3, zonal (Figures 4.33b and A5.8)** Maximum amplitudes of 10 m/s are observed between September and March at  $40^{\circ}\text{S}$  and  $40^{\circ}\text{N}$  and 105 km altitude. An equatorial maximum of up to 6 m/s is present at lower altitudes ( $\sim 95$  km). Phase transitions usually occur at latitudes of minimum amplitude. Hence, the general behavior is anti-symmetric about the equator during some months and rather symmetric (i.e., October) during other months, depending on the exact location of the amplitude maxima. In most cases, a long vertical wavelength is observed.

**w1, zonal (Figures 4.33c and A5.9)** Boreal winter amplitudes maximize at high latitudes ( $\sim 40^{\circ}$ ) and 105 km (up to 10 m/s). Equatorial maxima between 95 and 105 km are observed during some months. Phase transitions usually occur at latitudes of minimum amplitude. The large variability of this component makes a further discussion difficult. Vertical wavelengths are sometimes short (i.e., February) and sometimes long (i.e., December). Boreal summer amplitudes are relatively small and maximize at lower altitudes (90-95 km) although there are exceptions from this general behavior (i.e., August).

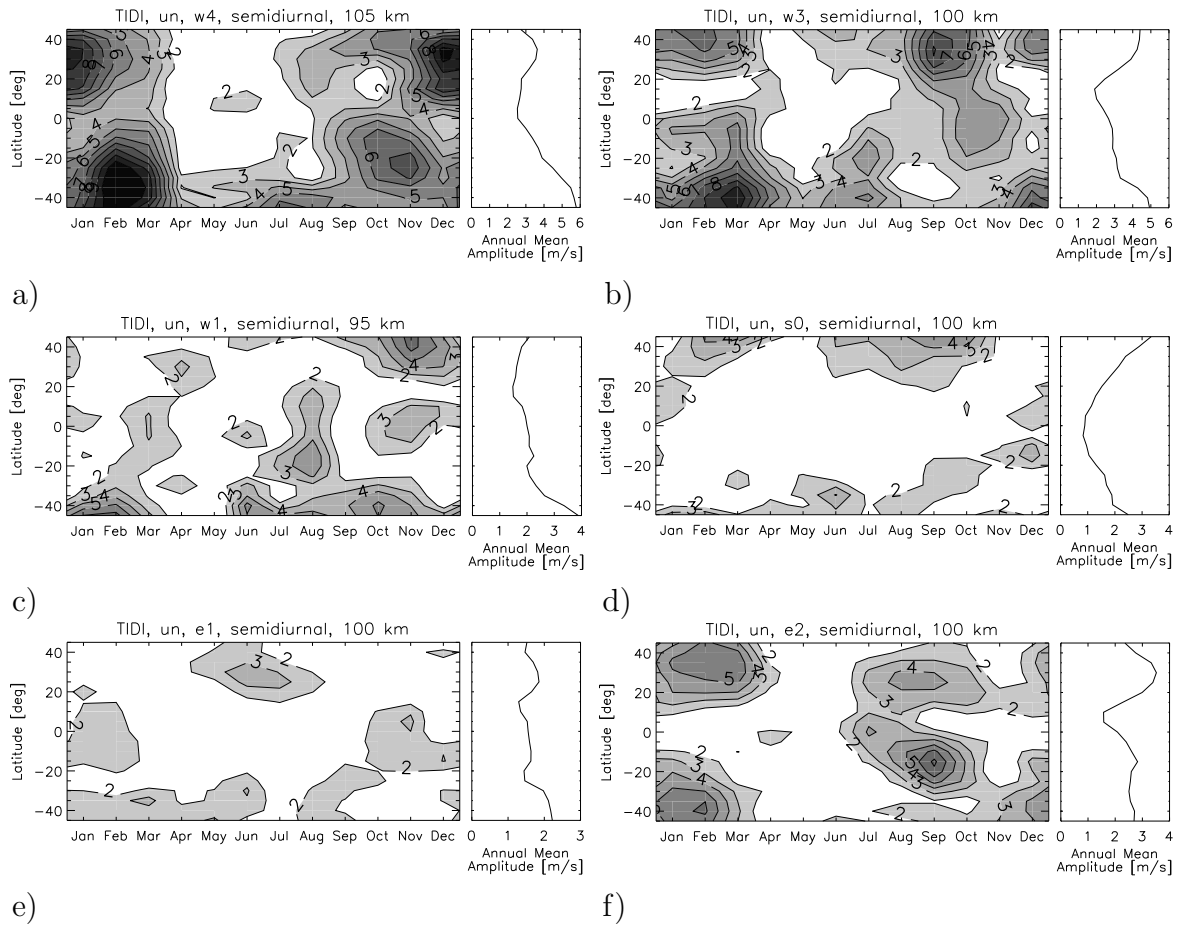


Figure 4.33: As Figure 4.32, but for the zonal wind amplitudes.

**s0, zonal (Figures 4.33d and A5.10)** The amplitudes of the zonal component peak poleward of  $45^{\circ}\text{S}$  and  $45^{\circ}\text{N}$ , similar to the meridional wind. The small amplitudes on the order of 1-2 m/s during most months, latitudes and altitudes prevent a further discussion. However, long vertical wavelengths are observed.

**e1, zonal (Figures 4.33e and A5.11)** The basic latitude-time distribution of the e1, zonal component is similar to its signature in the meridional wind. Amplitudes are usually on the order of 1-2 m/s which prevents a further discussion.

**e2, zonal (Figures 4.33f and A5.12)** As in the meridional wind, e2 zonal amplitudes are comparatively large. Although peak values of 5 m/s are observed in boreal winter, the most pronounced response (9 m/s) occurs in September at 105 km. Amplitude growth starts in July and therefore somewhat earlier than observed in most other components. The general phase behavior is anti-symmetric about the equator with amplitude maxima at  $30^{\circ}\text{N}$  and  $20\text{-}40^{\circ}\text{S}$ . Vertical wavelengths are long.

The large variability of the derived semidiurnal components in space and time together with their narrow latitudinal structure (i.e., 3-4 peaks between  $45^{\circ}\text{S}$  and  $45^{\circ}\text{N}$  for a number of components) will make the future analysis of their principle forcing mechanisms more difficult than for the diurnal tide. This particularly applies to the months with small amplitudes when the tidal structure is more sensitive to external disturbances. Nevertheless, both the latitude-height structures and the time

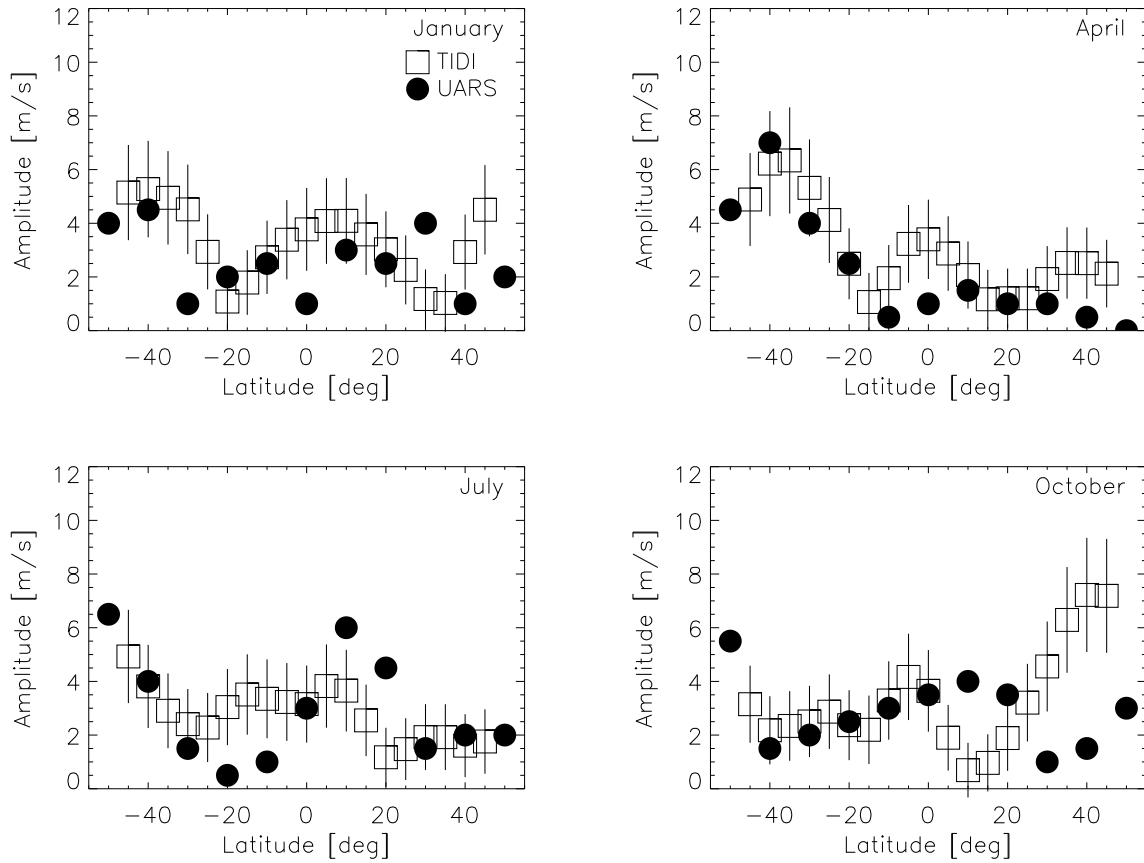


Figure 4.34: Meridional wind amplitudes from TIDI and UARS [*Angelats i Coll and Forbes, 2002*] for w3, semidiurnal at 95 km. TIDI error bars are from Table 4.7. UARS error bars are unknown.

evolutions presented above show in most cases coherent amplitude and phase structures that in turn give additional confidence in the derived tidal fields. A comparative model/observation analysis such as presented in section 4.3.5 for the diurnal tides thus appears feasible and will be done in the future. It will be interesting to see how well the different models can reproduce the basic features evident in the observations, that is, the long vertical wavelengths, a narrow latitudinal structure, and peak altitudes at or above 105 km for many components. The classical tidal theory [*Chapman and Lindzen, 1970*] already predicts this general behavior such that there may be some prospect.

A cross-check of the semidiurnal climatologies from TIDI is more difficult than for the diurnal tide. *Angelats i Coll and Forbes* [2002] provide w1 and w3 amplitudes and phases at 95 km from UARS analysis but not for the zonal wind component. A comparison altitude of 95 km is also less favorable for the semidiurnal tide than for the diurnal tide because it is well below the peak altitude. The amplitude distribution as function of latitude is partly different at 95 and 105 km (see appendix A5). However, the 95 km UARS results are the only global data available for comparison. They represent monthly averages of the December 1991 through September 1994 time period. Hence, the TIDI comparison with UARS does not meet the hard requirements of validation but it is helpful to verify the consistency of both data sets, as for the diurnal tide (section 4.3.4).

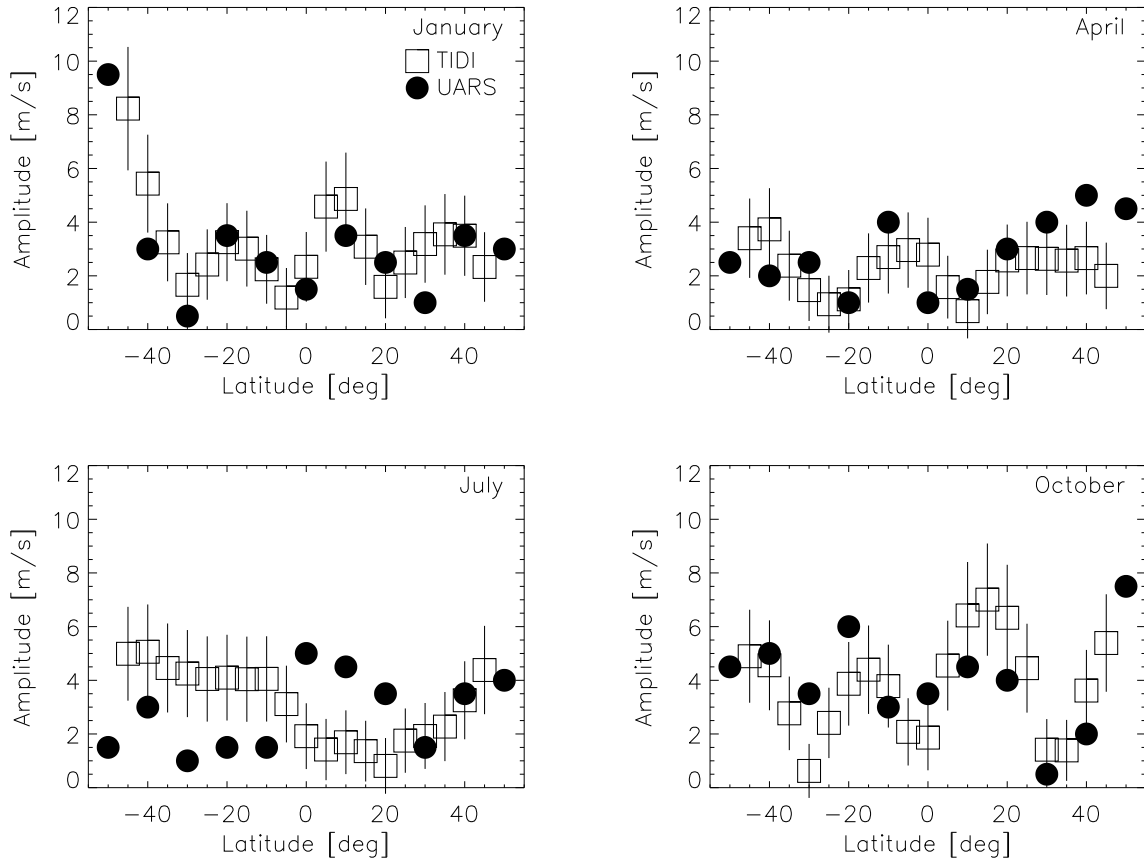


Figure 4.35: As Figure 4.34 but for w1, semidiurnal.

Figure 4.34 shows the amplitude comparison for the w3 component in January, April, July, and October. Phase comparisons are not included because the *Angelats i Coll and Forbes* [2002] phase definition is not entirely clear. TIDI and UARS amplitudes range from almost zero to 8 m/s with a similar latitudinal distribution in most cases. However, the UARS minimum at  $0^\circ$  and the maximum at  $30^\circ\text{N}$  in January are not observed by TIDI. This discrepancy is not of much concern because the UARS amplitudes in February (not shown) are very similar to the January and February amplitudes from TIDI. It may thus be related to the 11-year time lag between both data sets. TIDI and UARS amplitudes in April have three maxima in April that are located within about  $10^\circ$  latitude. The amplitude distributions in July are also similar with large amplitudes at high Southern latitudes, a second maximum at low Northern latitudes and another maximum at high Northern latitudes. Latitudes of minimum amplitudes differ by only  $10^\circ$ . The UARS NH amplitude minimum is  $20^\circ$  poleward of the TIDI observation but the UARS and TIDI amplitudes behave nevertheless similar: amplitudes increase poleward and equatorward of  $40^\circ$ , and toward high Northern latitudes.

The TIDI/UARS agreement for w1 (Figure 4.35) is even better. Both data sets show almost the same latitudinal distribution in January, April, and October. The comparison in July is less favorable but becomes better in August (not shown). A more quantitative assessment than discussing pattern similarities is not meaningful here, owing to the 11-year time lag between the measurements. Considering that, the amplitude agreement between TIDI and UARS is remarkable. A similar stability of

the nonmigrating tides was also found for the diurnal components (section 4.3.4). *Angelats i Coll and Forbes* [2002] established that the non-linear interaction between the migrating tide and PW-1 significantly contributes to the generation of the w3 and w1 semidiurnal tides observed in the 95 km UARS data. Hence, the same processes will likely be of importance in forcing the tides observed in the TIDI data. The relative contribution of other mechanisms, i.e. the latent heat source, and the height dependency of their imprints upon the tidal fields in the MLT still needs to be quantified. This is the focus of ongoing work.

## 5 Mesospheric surf zone and inversion layers

Upward propagating planetary waves do not only affect the mesosphere and lower thermosphere through their interaction with the tides (see section 4) but also through various other mechanisms. Two of these mechanisms, wave breaking and GW filtering, and their resulting effects on the atmospheric mean state are considered more closely in the following. Special emphasis is given to the generation of the mesospheric surf zone and to the simultaneous occurrence of mesospheric temperature inversion layers (MILs) at altitudes just above the surf zone.

During wintertime, PWs may propagate into the mesosphere thus redistributing energy and momentum from the lower atmosphere into the MLT when dissipating. One important dissipation mechanism is wave breaking that leads to the formation of distinct surf zones in the stratosphere and mesosphere [McIntyre and Palmer, 1984]. Wave breaking occurs when a wave propagates into a region where its speed matches the mean flow (critical wind line). Air parcels then undergo large and rapid excursions and strong, irreversible mixing occurs thus forming a thoroughly mixed "surf zone" region.

The stratospheric surf zone is formed on the equatorward side of the polar night jet when refracted PWs encounter a critical wind line (i.e.,  $\bar{u} = 0$  for quasi-stationary planetary waves, QSPWs) at low latitudes. It has been frequently observed in satellite measurements, e.g. in LIMS observations of long-lived tracers [Leovy *et al.*, 1985] and potential vorticity [Dunkerton and Delisi, 1986] as well as in aircraft measurements combined with trajectory-following methods [Waugh *et al.*, 1994]. The presence of a low latitude zero wind line in the stratosphere is a reflection of wave-mean flow interaction by GWs and Kelvin waves which finally leads to the quasi-biennial oscillation (QBO) and semiannual oscillation (SAO) phenomena.

The mesospheric surf zone is located between approximately 60-80 km altitude. Its existence eventually manifests the interaction between GWs and PWs. GWs may propagate through the stratospheric polar night jet and break in the lower mesosphere thus decelerating the jet and reversing the zonal circulation at altitudes above about 75 km. The critical wind line in the mesosphere is therefore caused by the deposition of easterly momentum by small-scale GWs [Holton, 1983; Garcia and Solomon, 1985]. Without such a critical wind line, upward propagating PWs would dissipate throughout the upper mesosphere and lower thermosphere such producing a surf zone extending well above 100 km altitude. In this sense, the formation and mechanism of the mesospheric surf zone are reminiscent of the stratospheric surf zone although they may behave somewhat independently [Dunkerton and Delisi, 1985].

Recent analyses of satellite measurements show that the existence of a distinct mesospheric surf zone is often accompanied by mesospheric temperature inversions just above the surf zone [Wu, 2000; Salby *et al.*, 2002; Oberheide *et al.*, 2006a] suggesting a linkage between both phenomena. Inversions in the mesosphere are characterized by an inversion of the vertical temperature gradient from negative to positive and such by a negative lapse rate.

Mesospheric inversion layers have been reported as early as in the late 1960's and early 1970's deduced from acoustic grenades, pitot probe, and falling sphere measure-

ments [*Schmidlin*, 1976]. Lidar observations [*Hauchecorne et al.*, 1987; *Meriwether et al.*, 1994; *Leblanc and Hauchecorne*, 1997] show that they may also occur during summer and in the tropics although they are stronger during winter at higher latitudes. Space-borne MIL observations have been reported by *Clancy et al.* [1994], *Leblanc et al.* [1995], and *Leblanc and Hauchecorne* [1997] using data from the Solar Mesosphere Explorer (SME) and the Upper Atmosphere Research Satellite (UARS) instruments. Their results show that, in spite of the limited vertical resolution, satellite data in general can resolve MILs that are usually only a few kilometers thick.

Model results by *Sassi et al.* [2002] indicate that the occurrence of wintertime MILs may be a direct consequence of rapidly decaying PWs. Strong inversion layers should be generated in the Arctic during winter. Rayleigh lidar observations obtained in the High Arctic, however, disagree with these model results, particularly in lapse rates and the extent of the MIL [*Duck and Greene*, 2004]. The presence of a persistent, well-defined turbulent layer within the mesosphere [*Whiteway et al.*, 1995], GW-tidal interactions [*Liu and Hagan*, 1998; *Liu et al.*, 2000], turbulent heating by GW breaking [*Hauchecorne et al.*, 1987], and chemical heating [*Meriwether and Mlynczak*, 1995] may also be important for the MIL generation. The review by *Meriwether and Gardner* [2000] gives a detailed discussion of these possible origins. Recently, *Ward et al.* [2005] emphasized the possible role of nonmigrating tides for the mesospheric inversions. The variety of the proposed production mechanisms may be indicative for the fact that several types of MILs of different origins may exist.

One approach to shed some light on the MIL generation and their relationship to the mesospheric surf zone is to perform case studies. Such a case study was recently carried out for a Canadian warming event during early November 1994 using CRISTA and TIME-GCM data [*Oberheide et al.*, 2006a]. Subtropical and high latitude MILs are analyzed. The case study is summarized in the following section 5.1. Section 5.2 makes an attempt to generalize the results.

## 5.1 November 1994 case study

The NH stratosphere during early November 1994 was characterized by a Canadian warming [*Baldwin*, 2000]. Accordingly, PW analyses from Freie Universität Berlin (FUB) [*Naujokat et al.*, 1995] show a large increase of PW-1 amplitude during the first half of November with the PW-2 amplitude and the wave phases remaining almost constant. Geostrophic winds derived from the CRISTA data indicate an already wintertime circulation pattern with NH westerly winds in the stratosphere and mesosphere with a high (low) latitude wind reversal at about 80 (90) km with easterlies above. This general situation is reasonably well reproduced by the TIME-GCM with the jet located at the same latitude and altitude as in the observation but with a wind reversal about 5-10 km higher in altitude (Figure 5.1).

The version of the model used here has  $5^\circ$  by  $5^\circ$  horizontal and four grid points per scale height vertical resolution, the latter being twice as good as in the standard model version. The GW parameterization scheme has been tuned such that the model winds better match the geostrophic CRISTA winds. TIME-GCM results used here are obtained by extracting the model fields along the CRISTA footprints ("flying the

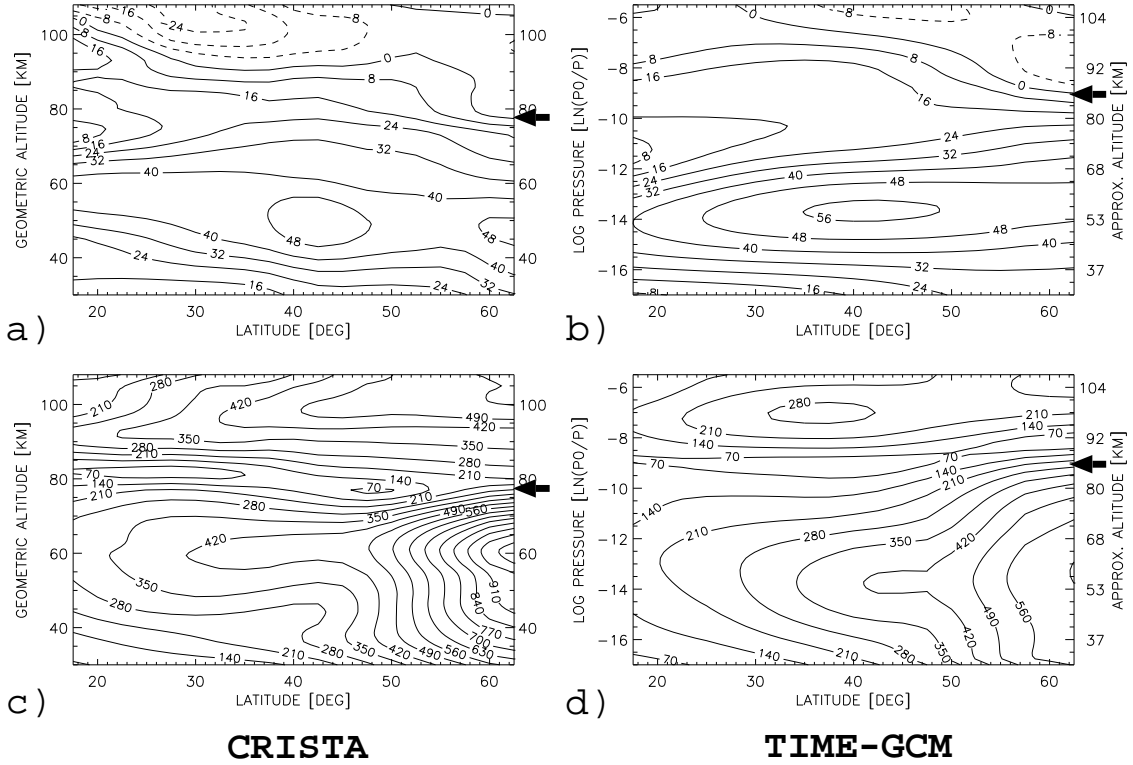


Figure 5.1: a) Zonal mean geostrophic zonal wind from CRISTA (9 November 1994). b) Zonal mean zonal wind from TIME-GCM (9 November 1994, sampled along the CRISTA footprints). c) PW-1 geopotential amplitude from CRISTA (geopotential meters). d) PW-1 geopotential amplitude from TIME-GCM (geopotential meters). Thick arrows point to the zero wind lines at 60°N. Dashed lines indicate easterlies. CRISTA data are plotted on geometric height levels. TIME-GCM data are on log-pressure levels.

satellite through the model”), that is by interpolating the model data to the time, latitude, and longitude of the satellite measurements. This is particularly helpful in avoiding tidal aliasing when comparing the observation with the model prediction. For a more detailed description of the model sampling and aliasing issues see sections 3.2.2 and 3.3.

The TIME-GCM geopotential wave 1 amplitudes in Figure 5.1 show basically the same structure as in the CRISTA data but with significantly smaller amplitudes (50%). This discrepancy must be at least in part attributable to the NCEP specified TIME-GCM lower boundary forcing because it is already present at 30 km altitude. In both the observation and the model simulation, a band of large wave amplitudes extends well into mid- and subtropical latitudes. The upward propagating PW-1 rapidly decays when approaching the region of slow wind speeds (black arrows in Figure 5.1). The PW amplitude increases again above the critical wind level. CRISTA and TIME-GCM PWs are quasi-stationary.

The zonal mean acceleration due to the PW dissipation can be approximated by using the geostrophic CRISTA winds and by setting the vertical wind speed  $w$  and horizontal friction  $X$  to zero in the transformed Eulerian-Mean Equations [i.e.,

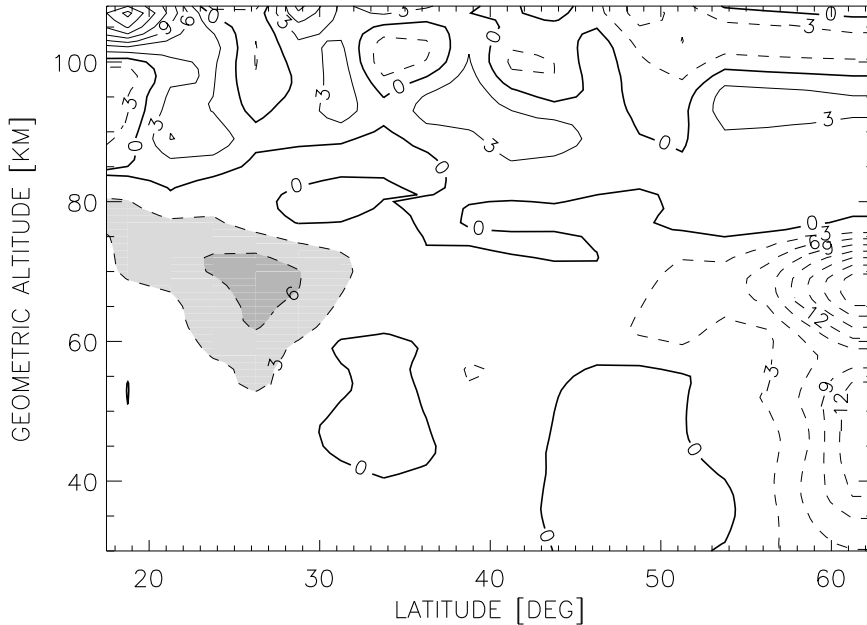


Figure 5.2: Zonal mean zonal momentum tendency  $\partial\bar{u}/\partial t$  from CRISTA geostrophic winds (9 November 1994). The shading indicates the mesospheric surf zone in the subtropics. Contour interval is  $3 \text{ ms}^{-1}\text{day}^{-1}$ . Dashed lines indicate easterly forcing.

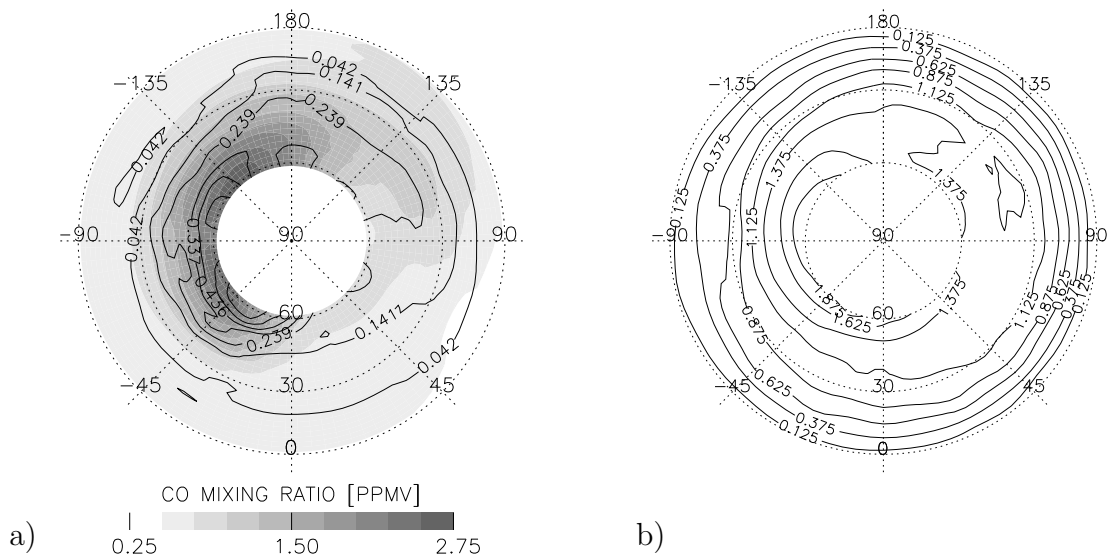
Equation 3.5.2a, *Andrews et al.*, 1987]:

$$\frac{\partial\bar{u}}{\partial t} + \bar{v}^* \left[ \frac{1}{a \cos \phi} \frac{\partial(\bar{u} \cos \phi)}{\partial \phi} - f \right] + \bar{w}^* \frac{\partial\bar{u}}{\partial z} - \bar{X} = \frac{1}{\rho_0 a \cos \phi} \vec{\nabla} \cdot \vec{F}, \quad (5.1)$$

with Coriolis parameter  $f$ , latitude  $\phi$ , Earth radius  $a$ , zonal wind  $u$ , meridional wind  $v$ , and density  $\rho_0$ . Zonal mean values are denoted by an overbar.  $\vec{F}$  is the Eliassen-Palm flux, and  $\bar{v}^*$ ,  $\bar{w}^*$  is the residual mean meridional circulation. All these quantities can be calculated from the CRISTA data using the aforementioned approximations.

The resulting (Equation 5.1) zonal mean zonal momentum tendency  $\partial\bar{u}/\partial t$  is largely easterly below 80-85 km (Figure 5.2). It can be attributed to PWs alone because GWs and tides are smoothed out in geostrophic CRISTA winds (see *Oberheide et al.* [2002a] for details). Regions of enhanced wave dissipation (surf zones) are found in subtropical latitudes ( $20^\circ$ - $30^\circ\text{N}$ ) between 60 and 75 km and poleward of  $55^\circ\text{N}$  below 75-80 km. The observed compact subtropical surf zone agrees well with simulations of the whole atmosphere community climate model (WACCM) for the month of January [*Sassi et al.*, 2002].

Figure 5.3 shows the horizontal structure of the mesospheric surf zone in measured and modeled carbon monoxide (CO) and potential vorticity (PV) data. In the observation, a tongue of polar air extends from North America ( $\sim 90^\circ\text{W}$ ) over the Pacific ( $\sim 180^\circ\text{E}$ ) into subtropical latitudes in the Indonesian sector ( $\sim 90^\circ\text{E}$ ). Flat and even inverted meridional gradients are observed in both PV (computed from CRISTA geostrophic winds) and CO mixing ratio. The latter is the first direct observation of the mesospheric surf zone in a trace constituent (see *Grossmann et al.* [2006] for retrieval details and error estimates). The good match of PV and CO also indicates that PV, as in the stratosphere, is a suitable proxy for studying large-scale dynamics



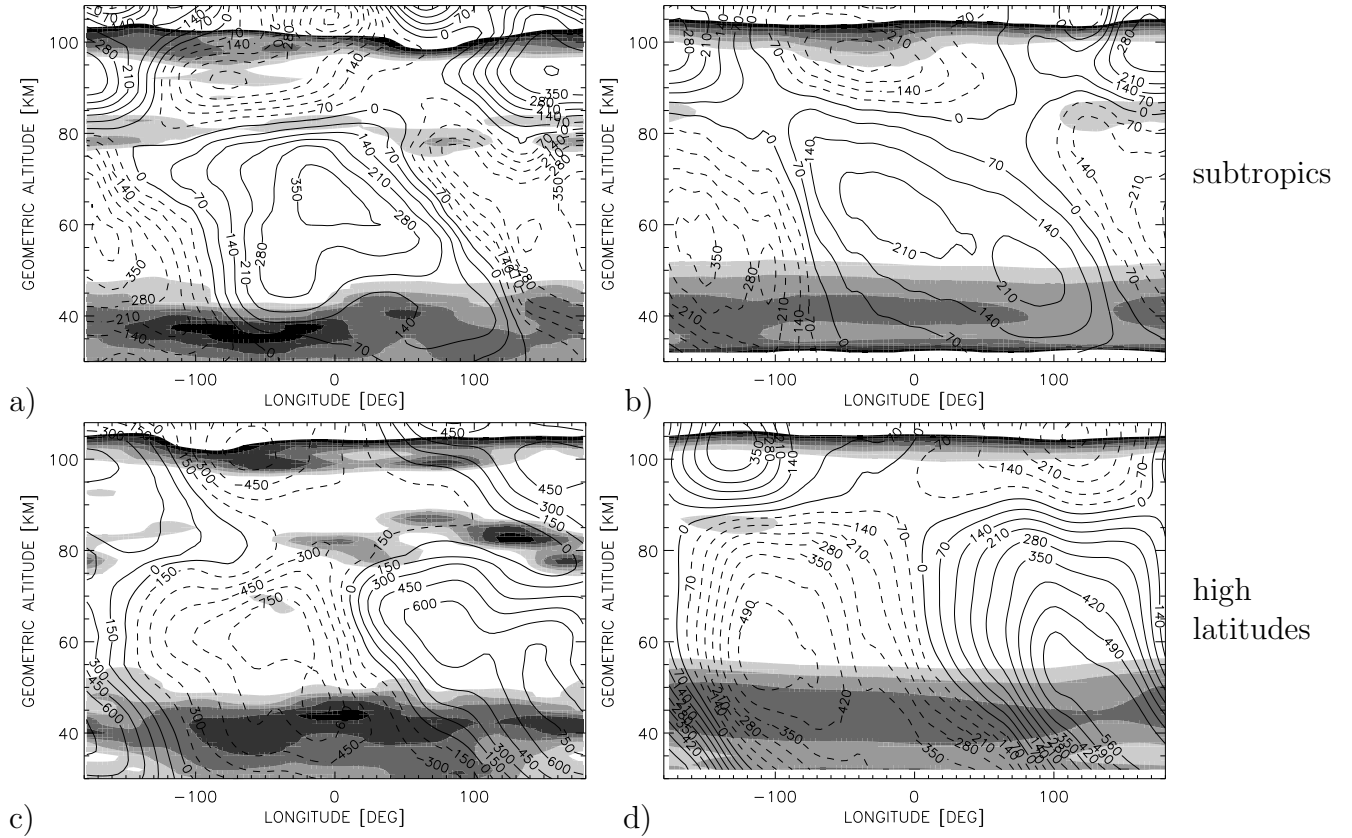


Figure 5.4: Geopotential perturbation measured by CRISTA at 26°N (a) and 56°N (c) in geopotential meters. Corresponding TIME-GCM results at 30°N (b) and 56°N (d). The shading indicates negative lapse rates (-1 K/km interval). Values  $< -5 \text{ K/km}$  are omitted. Note the mesospheric inversion layer (MIL) around 80 km.

the thermosphere. The interesting parts are the thin layers of inverted temperature gradients around 80 km altitude in the observation and in the model. As discussed in detail by *Oberheide et al.* [2006a], these MILs are not artifacts of tidal contamination.

The subtropical observation and model simulation (Figure 5.4a, b) show a relative PW amplitude minimum around 80 km that comes along with a sharp phase transition in the geopotential perturbation which in turn coincides with local temperature perturbation extrema (not shown, see *Oberheide et al.* [2006a] for details). CRISTA and TIME-GCM overall gross structures are very similar with a generally smaller perturbation amplitude in the model. In both cases, the MIL follows the phase transition altitude with its signature more pronounced in the measured data.

MIL and wave perturbations at high latitudes (Figure 5.4c, d) look similar to the subtropical results, although some details differ. The measured geopotential phase transition is smoother and the MIL altitude, though still coinciding with the minimum geopotential altitude of 80 km, no longer coincides with the local temperature perturbation extrema (not shown). The lower mesosphere geopotential PW phase is more eastward than at subtropical latitudes with the upper mesospheric PW phase more or less unchanged. High latitude MILs are stronger than in the subtropics (up to  $-5 \text{ K/km}$ ) and their altitude distribution with longitude is much more variable. The model reproduces the observed lower mesosphere PW phase shift but the phase

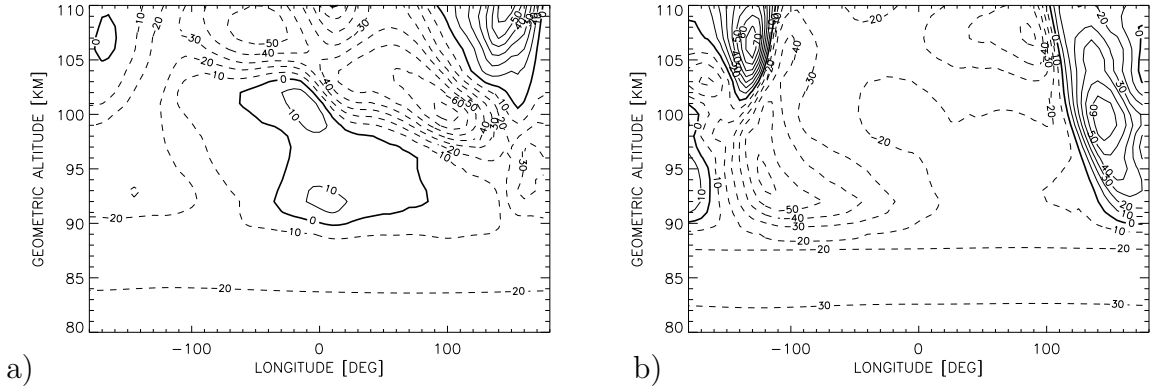


Figure 5.5: TIME-GCM averaged (9 November 1994) net momentum forcing from parameterized GW drag at  $27.5^\circ\text{N}$  (a) and  $57.5^\circ\text{N}$  (b). Contour intervals are  $10 \text{ ms}^{-1}\text{day}^{-1}$ . Solid: eastward, dashed: westward.

transition around 85 km is much sharper than in the observation. A MIL is only weakly present around 85 km ( $< -1 \text{ K/km}$ ) from  $100^\circ\text{W}$  to  $160^\circ\text{W}$ .

Apart from these differences, the overall similarity of the CRISTA and TIME-GCM PW and MIL structure encourages the use of the model results for the interpretation of the observed upper mesospheric PWs, that is, their forcing, and for analyzing the leading MIL generation process. *Smith* [2003] suggested that the upper mesospheric PWs and their out-of-phase behavior with the waves below eventually manifest the filtering of upward propagating GWs by PWs in the stratosphere. The filtering leads to zonal asymmetries in the GW net momentum forcing in the upper mesosphere (where the GWs break) and thus to zonal asymmetries in the background flow. The asymmetric flow in turn is the source for PWs that must be out-of-phase with the waves that provided the initial filtering.

This idea is well supported by the TIME-GCM simulation. Figure 5.5 shows the daily averaged net momentum forcing from parameterized GW drag in the subtropics and at high latitudes. The general model forcing is easterly below 90 km thus contributing to the wind reversal and thus to the PW decay in the surf zone. Wave-1 like signatures of westerly momentum forcing are observed in the upper mesosphere (above 90 km) where the PW activity amplifies again. The sharp phase transition between lower and upper mesospheric PWs in the model data has already been discussed (Figure 5.4). GW drag cannot be measured by CRISTA, but zonal asymmetries in observed temperature standard deviations may be indicative for GW drag asymmetries in the measured data as well [*Offermann et al.*, 2006a].

The combined CRISTA and TIME-GCM data now suggest a hypothesis for the MIL generation mechanism: the abrupt vertical phase transition between lower and upper mesospheric PWs induces a strong geopotential curvature that is sufficiently large, through hydrostatic equilibrium, to invert the thermal structure around 80 km altitude. Its verification is straightforward.

From hydrostatic equilibrium  $\partial\Phi/\partial z = RT/H$  with geopotential  $\Phi$ , temperature  $T$ , mean scale height  $H$ , and gas constant  $R$  one deduces immediately the lapse rate

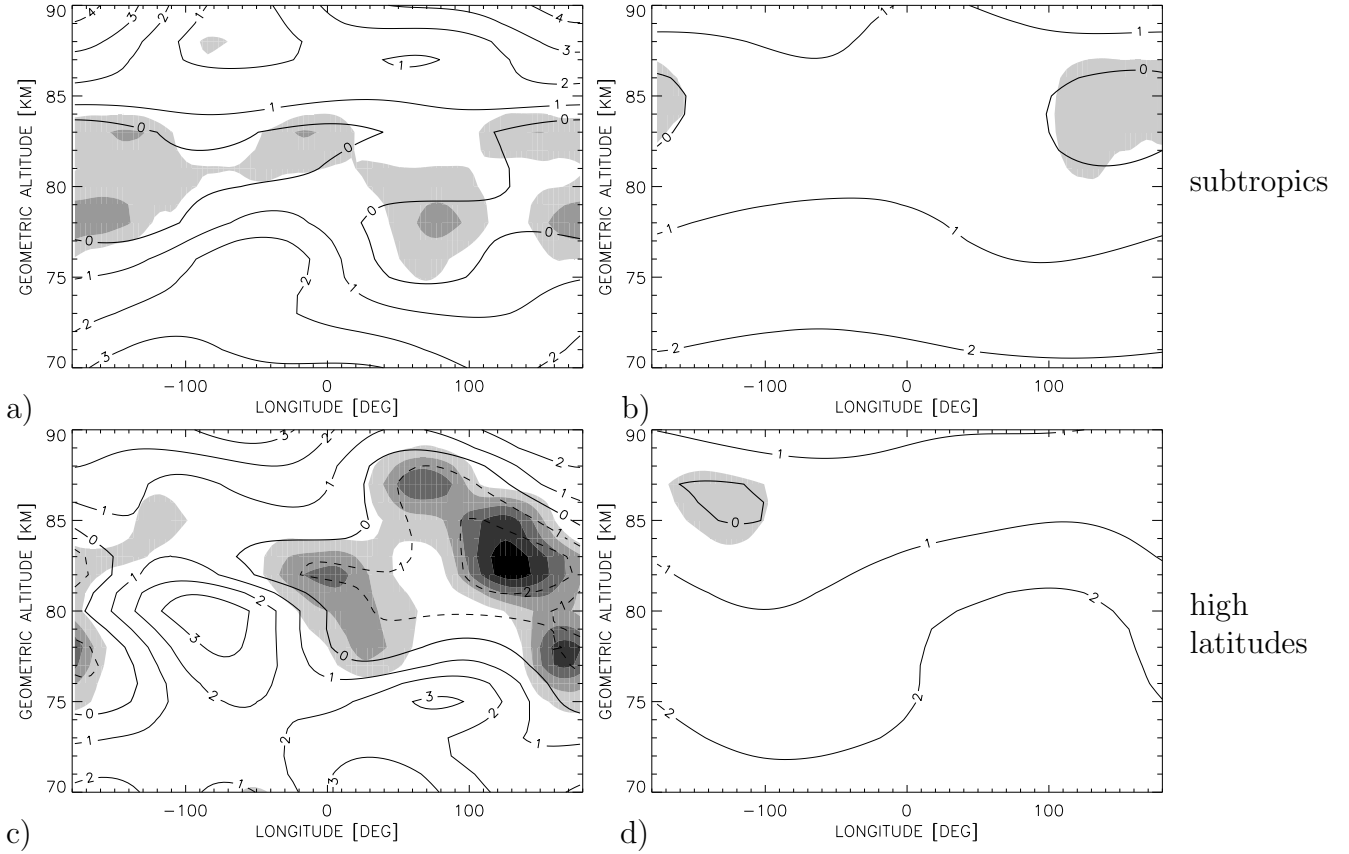


Figure 5.6: Negative lapse rates (shaded, -1 K/km interval) and lapse rates from PW-1 and PW-2 (lines, 1 K/km interval, negative values are dashed) from CRISTA at 26°N (a) and 56°N (c). Corresponding TIME-GCM results at 30°N (b) and 56°N (d).

$\Gamma = -\partial T/\partial z$  as

$$\Gamma = -\frac{H}{R} \frac{\partial^2 \Phi}{\partial z^2}. \quad (5.2)$$

Following the approach of *Salby et al.* [2002] and separating  $\Gamma$  into zonal mean  $\bar{\Gamma}$  and perturbation  $\Gamma'$  components one obtains

$$\Gamma' = -\frac{H}{R} \frac{\partial^2 \Phi'}{\partial z^2} < -\bar{\Gamma} \quad (5.3)$$

as a condition to invert the thermal structure. A sufficiently large geopotential curvature can therefore produce the MILs. The lapse rate due to PW induced geopotential curvature  $\Phi'_{PW}$  is

$$\Gamma_{PW} = \bar{\Gamma} - \frac{H}{R} \frac{\partial^2 \Phi'_{PW}}{\partial z^2}, \quad (5.4)$$

with  $\Phi'_{PW}$  determined from fitting zonal wavenumbers 1 and 2 to  $\Phi'$ . Negative values of  $\Gamma_{PW}$  should correspond to the observed negative lapse rates in both the model and observational data if the MILs are generated by the abrupt vertical PW phase transition.

The comparisons between computed  $\Gamma_{PW}$  (Equation 5.4) and observed  $\Gamma$  for subtropical (Figure 5.6a) and high latitude (Figure 5.6c) CRISTA measurements show indeed a good agreement. Slight altitude shifts (80°E, Figure 5.6a) and deviations

are present, but most parts of the thermal inversions can be attributed to the PW induced geopotential curvature, as hypothesized. The differences between  $\Gamma_{PW}$  and  $\Gamma$  are generally larger at high latitudes. This may be due to additional processes of importance for the MIL generation. The agreement between  $\Gamma_{PW}$  and  $\Gamma$  for the subtropical (Figure 5.6b) and high latitude (Figure 5.6d) TIME-GCM MILs is even better. Additional computations (Figure not shown) indicate that the PW-1 contribution to the MIL generation in both the observational and model data exceeds the PW-2 contribution.

The comparative observation/model analysis thus shows that the increasing PW activity during the Canadian warming not only favors the generation of a compact mesospheric surf zone but also the generation of mesospheric temperature inversions on synoptic scales. Both effects are eventually the result of the interaction of GWs and PWs. Below the wind reversal altitude, the GW net momentum forcing contributes to the reversal of the zonal wind that acts as a critical level for the upward propagating PWs in the stratosphere and lower mesosphere. Their decay in the surf zone region comes along with an amplification of upper mesospheric PWs which in turn is a result of GW filtering. Both effects together result in a sharp PW phase transition around 80 km altitude just above the surf zone. The vertical curvature of the geopotential wave perturbation is sufficiently large to invert the thermal structure, through hydrostatic equilibrium.

Both the observation and the model suggest that this process is the leading MIL generation mechanism in the subtropics. It also contributes significantly to the high latitude MIL generation but the CRISTA data show some indications that additional processes may also play a role. These findings only represent a case study for a very limited time period. It is quite clear that long-term measurements, such as from the TIMED instruments, and complementary modeling efforts are required to verify how representative the observed MIL generation process is. An analysis of the TIMED data (i.e., SABER temperatures) similar to the presented one might therefore be worthwhile but it is beyond the scope of this work. The following attempt to generalize the case study results thus uses model data from the 2003 TIME-GCM simulation (see sections 3.2.2 and 3.3) only.

## 5.2 Generalization of the case study results

The 2003 TIME-GCM simulation provides model fields with one hour time resolution for each day of the year. The model output is averaged into daily means such avoiding tidal contamination but also smoothing fast planetary waves (e.g. the QTDW). Each daily mean horizontal grid point is then analyzed on MILs on a day-by-day basis. All temperature inversions that are below the mesopause and above the stratopause are identified as MILs. This criterion is uncritical for a single, "regular" mesopause, but it introduces some potential shortcomings in the analysis when a two-level mesopause structure [Berger and von Zahn, 1999] is present.

These shortcomings arise because the term "mesopause" is dubious to some extent. A reasonable definition is given by She and von Zahn [1998] with the mesopause being "the altitude of the absolute minimum in temperature, obtained after averaging over

an observation period that is extensive enough to smooth out most of the wave effects”. The present model study strictly follows this definition with an averaging period of 24 hours, as pointed out above.

Observations [*von Zahn et al.*, 1996] and model simulations [*Berger and von Zahn*, 1999] indicate that only two distinct mesopause levels exist without a smooth transition between them. The mesopause is located around 100 km altitude during winter and around 85-87 km during summer [i.e., *Gusev et al.*, 2006; *von Zahn and Meyer*, 1989]. Temperature profiles in the transition region between the summer and winter hemisphere may therefore have two distinct minima of almost the same depth. Interpreting the low-lying temperature minimum (if the temperature of the high-lying minimum is lower) as the bottom of a MIL is thus somewhat misleading. However, several attempts to separate two-level mesopause signatures from ”regular” MILs (means: all the rest) failed to produce unequivocal results. To ensure the reproducibility of the results, particularly in the light of future observational studies, it appears more reasonable to accept this shortcoming and to merely identify the latitudes and months where two-level mesopause artifacts may play a role.

Figure 5.7 shows the monthly variation of the MIL height in the 2003 TIME-GCM simulation. MIL bottom and top altitudes are derived for each horizontal grid point of the daily averaged temperatures. In the few cases with more than one MIL only the highest lying layer is counted. Bottom and top altitudes are then binned into monthly mean zonal averages except that those longitudes and days without MILs are excluded. The mean mesopause height is only calculated from grid points with MILs (black dotted line). Virtually no MILs are present when the mesopause altitude is low (summer). As a result, the mean mesopause is always located around 100 km altitude. The red dotted line in the Figure shows the mean mesopause height for grid points without MILs. It is used to derive a crude proxy for possible two-level mesopause artifacts. A larger contribution of the latter is rather unlikely if both lines do not differ very much, because in that case only a regular, single mesopause is present. In contrast, two-level mesopause artifacts are rather likely in the MIL results if both lines diverge. Such latitudes are indicated by the yellow shading. The interpretation of the MIL results in these regions is uncertain to some extent and they are disregarded in the further discussion. The histogram (blue) gives the MIL occurrence frequency in percent at a given latitude. An occurrence frequency of 100% means that MILs are present during all days of the month at all longitudes, that is, in 2232 cases for January (72 model longitudes  $\times$  31 days).

MILs are more frequent in NH winter than in SH winter with the largest occurrence frequencies (30-100%) observed at middle and high latitudes (Figure 5.7). This is already an indication for a possibly important role of PWs in the MIL generation: PW amplitudes increase toward higher latitudes and the NH vortex is usually more disturbed than in the SH. MIL bottom altitudes decrease toward higher latitudes and are, with few exceptions, between 70 and 80 km. The layer thickness is usually between one and two model grid points (about 3.5-7 km). The model resolution does not allow a discussion of MILs thinner than that. A somewhat larger high latitude MIL thickness in January, February, October, and November is a result of the averaging and thus rather an indication for the variability of the MIL height. The layer thickness of individual temperature profiles does not exceed 2 model grid points.

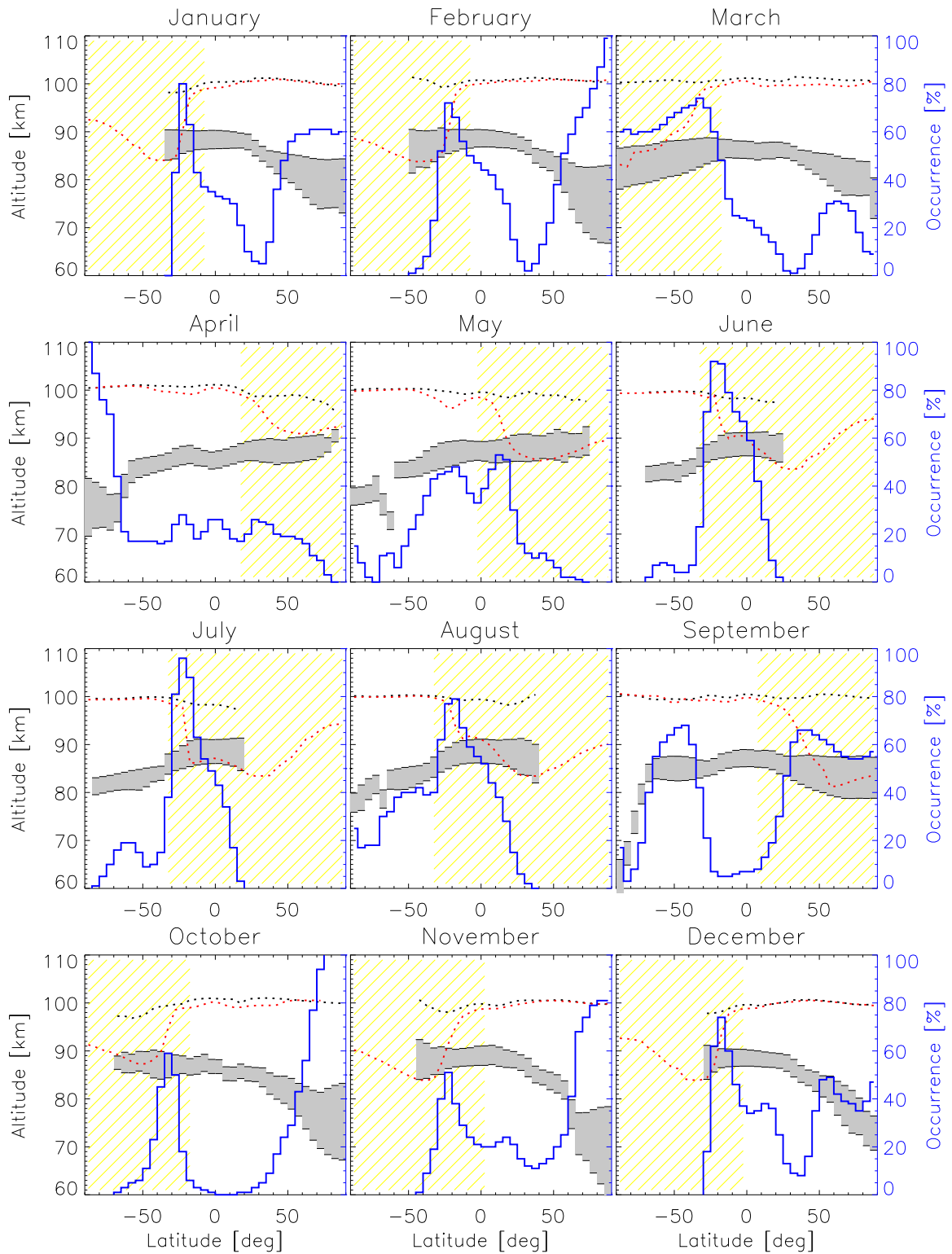


Figure 5.7: Monthly variation of MIL height from the 2003 TIME-GCM simulation. Gray shading: Area between the bottom and top of the MILs. The value plotted is akin to a zonal monthly average except that those longitudes and days without MILs are excluded. Black dotted line: Mean mesopause height from longitudes and days with MILs. Red dotted line: Mean mesopause height from longitudes and days without MILs. Blue line: MIL occurrence frequency. Yellow shading: Latitudes with possible two-level mesopause artifacts. For details see text.

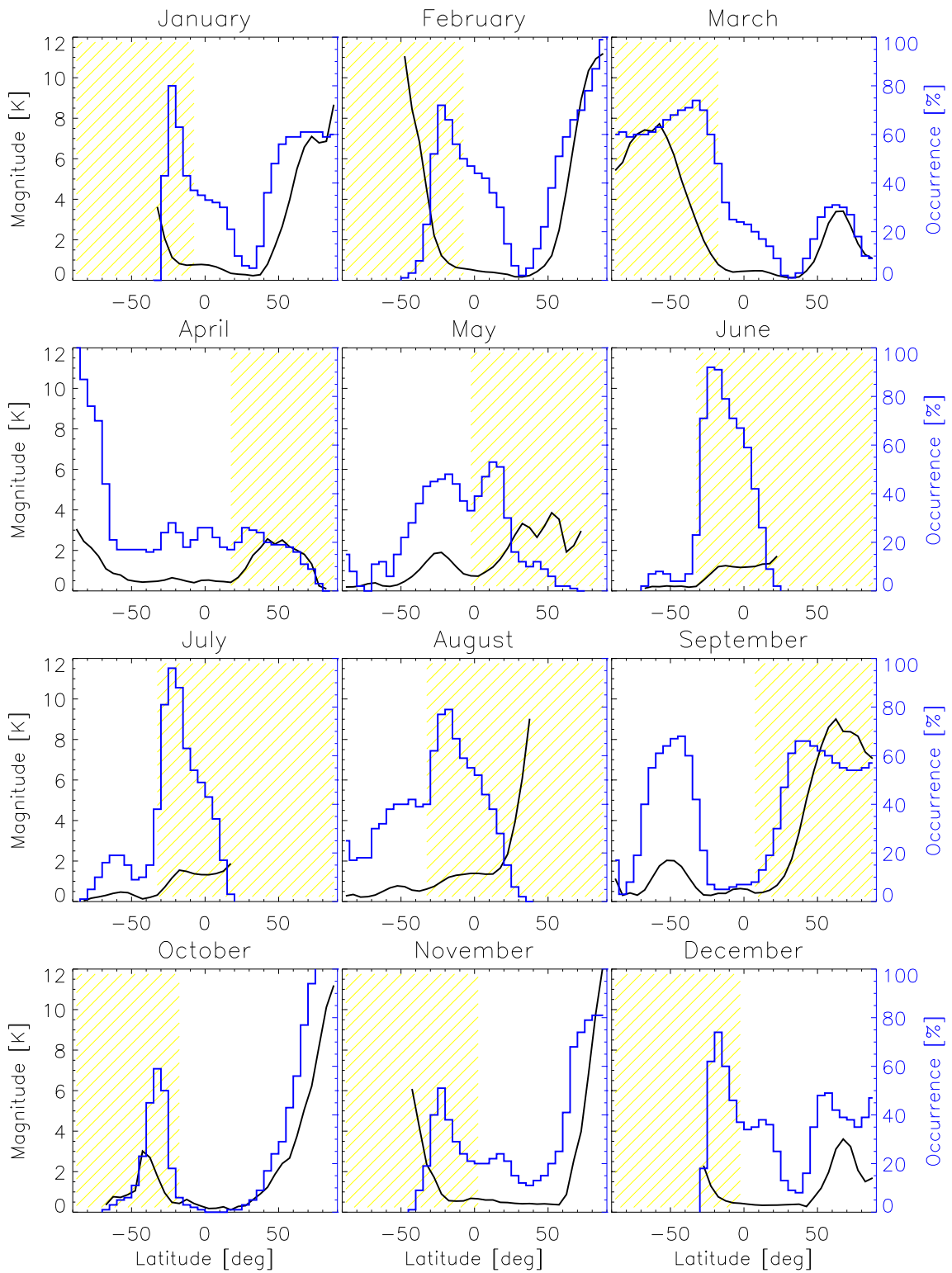


Figure 5.8: Monthly variation of MIL magnitude from the 2003 TIME-GCM simulation. Black: MIL magnitude. The value plotted is akin to a zonal monthly average from longitudes and days with MILs. Longitudes and days without MILs do not enter the average. Blue: MIL occurrence frequency. Yellow shading: Latitudes with possible two-level mesopause artifacts. For details see text.

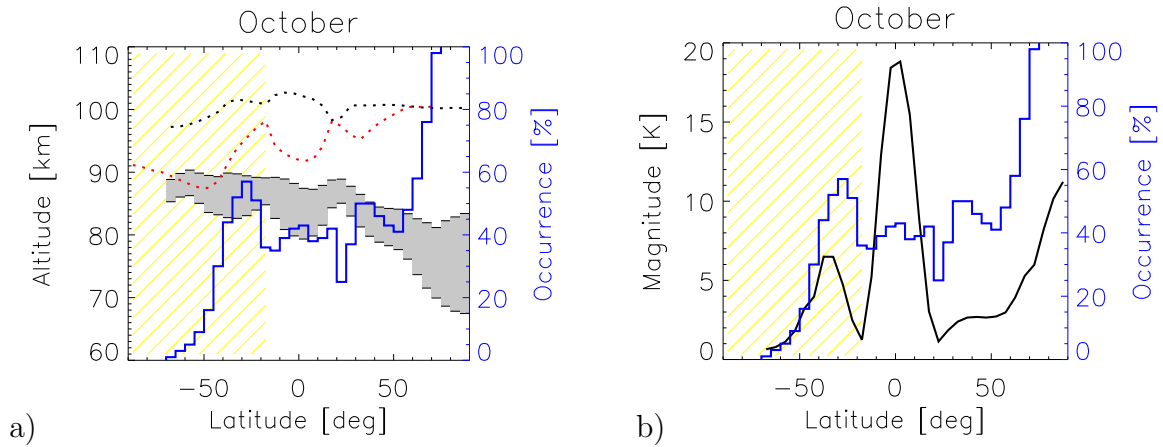


Figure 5.9: As Figure 5.7 (a) and Figure 5.8 (b), but for a fixed UT (0h). Only October results are shown. Tides significantly affect occurrence frequency, height, and magnitude of the MILs.

Figure 5.8 shows the corresponding MIL magnitudes, averaged in the same way as the layer heights. The magnitude is defined as the temperature difference between MIL top and bottom. Its latitudinal distribution basically follows the occurrence frequency which is not unexpected because more processes that are sufficiently large to invert the thermal structure will automatically lead to more pronounced inversions. High latitude magnitudes vary from about 8-12 K in NH winter to small values ( $<2$  K) in SH winter. The January and December MIL heights and magnitudes agree well with observational results of *Wu* [2000] who studied MIL events with Improved Stratospheric and Mesospheric Sounder (ISAMS) and Microwave Limb Sounder (MLS) temperatures. Both UARS instruments show pronounced inversions between about 70 and 80 km altitude that maximize northward of  $40^{\circ}\text{N}$  during December 1991 - January 1992. This time period was characterized by a particularly strong PW activity and, consistent with the expectation, by large MIL magnitudes that are about a factor of two larger than those in TIME-GCM. The comparatively small MIL magnitudes in the model are at least in part attributable to the inherent smoothing introduced by the vertical resolution of only 2 grid points per scale height.

Note that the global MIL distribution in Figure 5.8 differs from the WACCM results of *Sassi et al.* [2002]. WACCM has large magnitudes (up to 30 K) at mid-latitudes in the winter hemisphere and equatorial peaks of about 10 K during equinox. Both features are not present in the TIME-GCM data. One can only speculate about the reasons for this discrepancy because it is not clear whether the *Sassi et al.* [2002] results are calculated from daily averaged model output or from model output for a single Universal Time (UT). One indication for the latter might be that TIME-GCM magnitudes are similar to WACCM if they are derived from model output for a single UT. Figure 5.9 shows as an example the global distribution for October and 0h UT which is now in good agreement with the WACCM data. It is quite obvious that the difference between the daily averaged and fixed UT analyses is caused by tides. They are sufficiently large in TIME-GCM to invert the thermal structure in a number of cases which in turn significantly affect MIL occurrence frequency, height and magnitude.

The interpretation of the MIL signatures in Figures 5.7 and 5.8 now requires a closer examination of the model dynamics in general and the PW activity in particular. Hence, Figure 5.10 shows time series of the zonal mean zonal wind at  $62.5^{\circ}\text{N}$ , the zonal mean temperature at  $72.5^{\circ}\text{N}$ , the PW-1 and PW-2 geopotential amplitudes at  $62.5^{\circ}\text{N}$ , and the MIL magnitudes at  $62.5^{\circ}\text{N}$  and  $32.5^{\circ}\text{N}$ . These latitudes are chosen for three reasons. First, the PW amplitudes in the model are largest around  $62.5^{\circ}\text{N}$ . Second, the temperature at latitudes poleward of  $60^{\circ}\text{N}$  is a good indicator for stratospheric warming events that might be related to MIL occurrence, as in the November 1994 case study. Third, low and high latitude MILs may behave somewhat independently.

The wind reversal height during boreal winter is between 110-120 km with the jet usually located around 70 km (Figure 5.10a). Mid-winter circulation reversals in the stratosphere occur around days 16 and 52. The model also predicts low wind speeds around days 3, 341 and 354. These wind patterns come along with stratospheric warming events as indicated in Figure 5.10b. Using NCEP data, *Manney et al.* [2005] classified the mid-January (day 16) and mid-February (day 52) events as major warmings. The warmings on days 3, 341, and 354 are insufficient to reverse the stratospheric circulation. A classification as minor or Canadian warmings is not required in the present context. The circulation reversal around day 68 has no clear counterpart in the zonal mean temperature and is not further discussed. Figures 5.10c, d show that the identified warmings (indicated by the vertical lines in the Figure) are closely related to periods of enhanced PW-1 and PW-2 activity with the wave 1 being the dominant wave component. Its growth precedes the stratospheric warming events and is probably due to wave resonance. This has been discussed in detail by *Liu and Roble* [2002] using the coupled TIME-GCM/CCM3 model version. These authors also show that the wave decay at or shortly after the peak of the warming leaves a mid-latitude surf zone, as found in the November 1994 cases study results presented in the previous section 5.1.

The stratospheric warmings and the corresponding large PWs are always accompanied by high and middle latitude MILs (Figures 5.10e, f). This becomes particularly clear at  $32.5^{\circ}\text{N}$  where MILs only occur during the marked warmings and during periods of large PW activity (days 310-340). Note that MILs between 1 April and 30 September (days 91-273) are not plotted due to the abovementioned possible double mesopause artifacts. The signature around day 275 (early October) is not a "real" MIL but related to the summer-winter transition in mesospheric temperature (see Figure 5.10b). High latitude MILs (Figure 5.10e) occur more frequent but they also maximize around the warming events. MILs between roughly days 60-90 and 274-300 are artifacts of the winter-summer and summer-winter transitions in the mesosphere (Figure 5.10b).

The results of the year-long model simulation are so far consistent with the November 1994 cases study. It is thus worthwhile to have a closer look into the relationship between PWs and MILs during a stratospheric warming event. Figure 5.11 shows the geopotential PW-1 amplitude, the zonal mean zonal wind field, and the net momentum forcings due to parameterized GW drag and the geopotential perturbations at  $62.5^{\circ}\text{N}$  and  $32.5^{\circ}\text{N}$  for day 341. This particular day is representative for all stratospheric warming events. It was chosen because it corresponds to the period of largest PW-1 amplitudes (Figure 5.10c). The PW-1 amplitude at  $65^{\circ}\text{N}$  and 70 km reaches

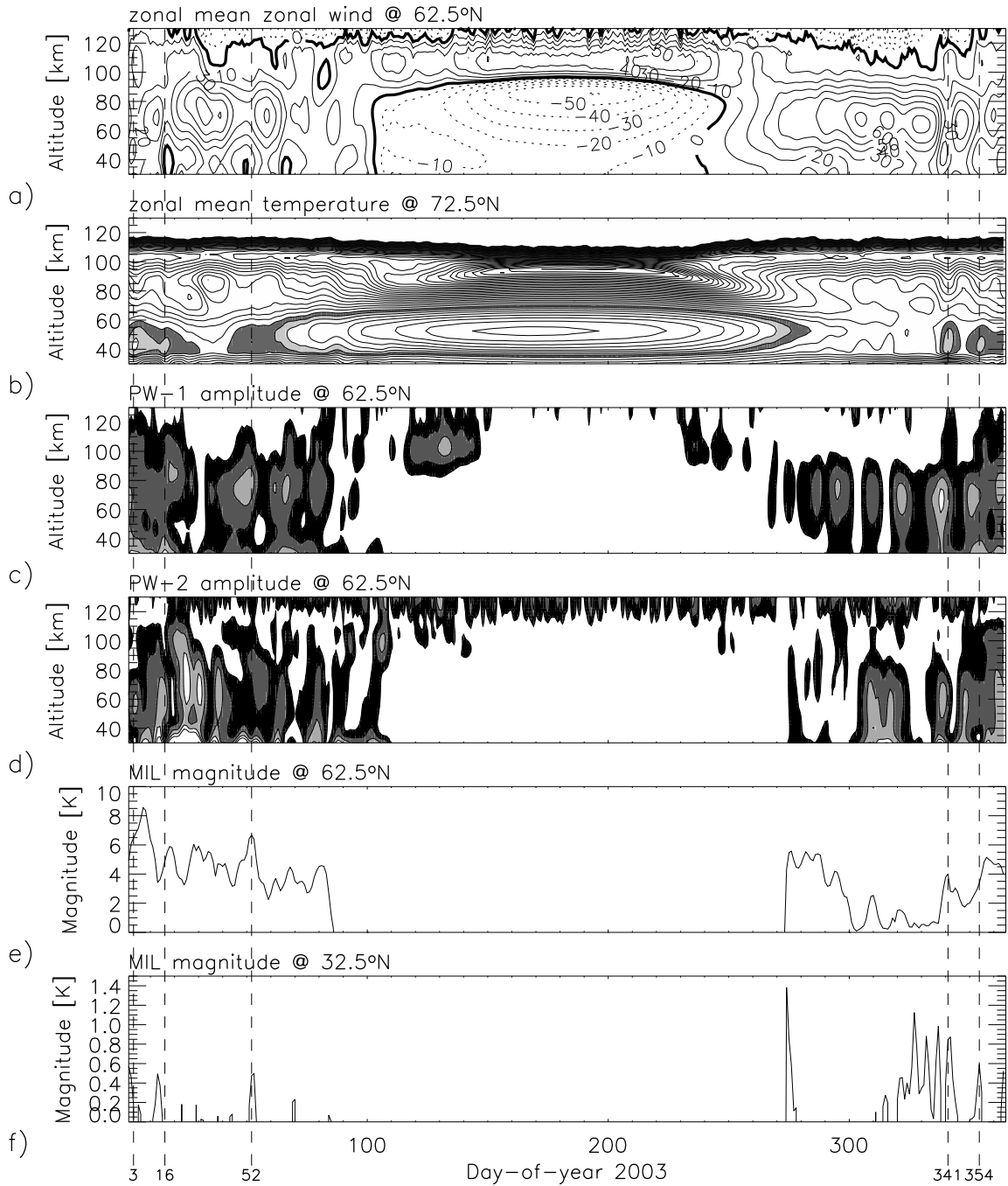


Figure 5.10: NH results from the 2003 TIME-GCM simulation. a) Zonal mean zonal wind at  $62.5^\circ\text{N}$  (solid: eastward, dotted: westward, contour interval: 10 m/s). b) Zonal mean temperature at  $72.5^\circ\text{N}$  (dark grey: 240 K, light grey: 245 K, contour interval: 5 K). c) Geopotential wave-1 amplitude at  $62.5^\circ\text{N}$  (contours from dark to light: 400, 800, 1200, 1600 gpm). d) Geopotential wave-2 amplitude at  $62.5^\circ\text{N}$  (contours from dark to light: 100, 200, 300, 400 gpm). e) MIL magnitude at  $62.5^\circ\text{N}$  in K. f) MIL magnitude at  $32.5^\circ\text{N}$  in K. MILs between 1 April and 30 September are omitted. Large events between days 60-90 and 274-300 are related to the winter-summer and summer-winter transitions (for details see text). Dashed vertical lines indicate stratospheric warmings (maxima of winter stratopause temperatures exceeding 245 K).

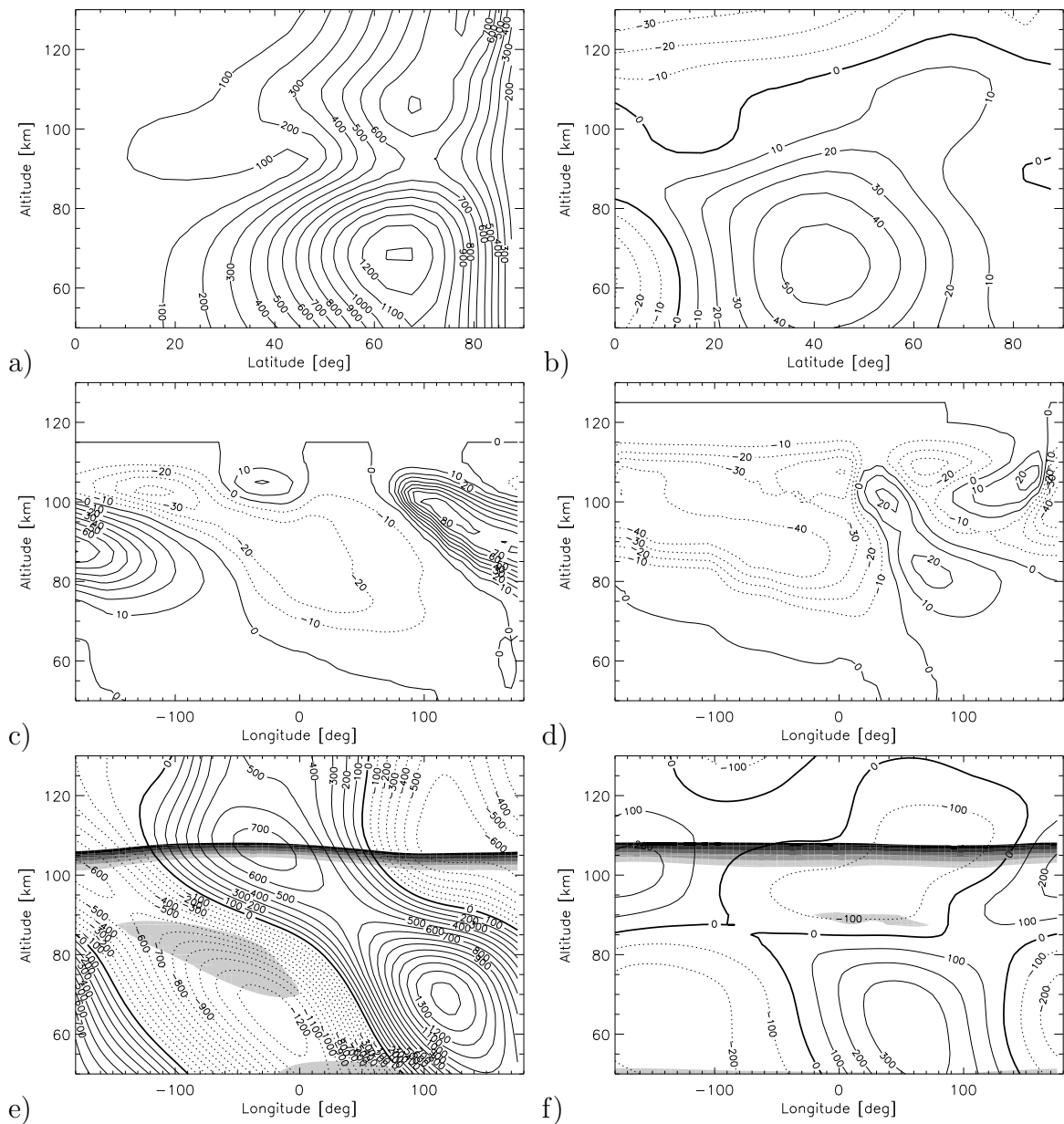


Figure 5.11: TIME-GCM results for the stratospheric warming event on day 341. a) Geopotential wave-1 amplitude (contour interval 100 gpm). b) Zonal mean zonal wind (solid: eastward, dotted: westward, contour interval 10 m/s). c) Net momentum forcing from parameterized GW drag at  $62.5^{\circ}\text{N}$  (solid: eastward, dotted: westward, contour interval:  $10 \text{ ms}^{-1}\text{day}^{-1}$ ). d) Same as c) but at  $32.5^{\circ}\text{N}$ . e) Geopotential perturbation at  $62.5^{\circ}\text{N}$  with negative lapse rates indicated by the shading ( $-1 \text{ K/km}$  interval, values  $< -5 \text{ K/km}$  are omitted). A MIL centered at  $80^{\circ}\text{W}$  and 80 km is present. f) Same as e) but at  $32.5^{\circ}\text{N}$ . A thin MIL centered at  $30^{\circ}\text{E}$  and 88 km is present.

1300 gpm (Figure 5.11a). It decays toward higher altitudes when the wave approaches low wind speed regions that act as critical layers (Figure 5.11b). A secondary wave maximum at 107 km occurs just above the relative minimum height of 93 km. These altitudes decrease toward lower latitudes which is consistent with the zonal mean zonal wind pattern. Figures 5.11c,d show that the wave growth in the upper mesosphere / lower thermosphere is caused by an in-situ forcing due to breaking GWs

that have been filtered by the PW-1 in the stratosphere and lower mesosphere. The wave-1 patterns of westerly momentum forcing become large in the upper mesosphere and the PW activity amplifies again. This is consistent with the case study results in section 5.1. An increasing low latitude contribution of higher wavenumber components also leads to the excitation of PWs with higher zonal wavenumbers in the lower thermosphere (not shown).

The high (e) and low (f) latitude geopotential perturbations in Figure 5.11 undergo a rapid phase transition at the altitude of minimum wave amplitude. This is less pronounced at 62.5°N because the high latitude critical wind layer is comparably thick such that the wave dissipates over a larger altitude range (i.e., compare to the case study wind field in Figure 5.1b). Nevertheless, MILs close to the phase transition altitude occur at both low and high latitudes with the latter being much broader. Although their different magnitude is quite understandable because of the larger wave amplitude and the smaller vertical temperature gradient at higher latitudes, another difference is evident. The high latitude MIL occurs at longitudes where the geopotential perturbation gradient is positive with height and the low latitude MIL occurs at longitudes with a negative gradient. According to Equation 5.4, MILs induced by PWs are governed by the vertical geopotential curvature term  $\partial^2\Phi'_{PW}/\partial z^2$ . Assuming that  $\Phi'_{PW}$  can be approximated by

$$\Phi'_{PW} = \Phi_0 \cos(k\lambda - \varphi) \quad (5.5)$$

with amplitude  $\Phi_0$ , wavenumber  $k = \frac{2\pi}{360^\circ}$ , longitude  $\lambda$  and phase  $\varphi$ , one obtains

$$\begin{aligned} \frac{\partial^2\Phi'_{PW}}{\partial z^2} &= \frac{\partial^2\Phi_0}{\partial z^2} \cos(k\lambda - \varphi) + 2\frac{\partial\Phi_0}{\partial z} \frac{\partial\varphi}{\partial z} \sin(k\lambda - \varphi) \\ &+ \Phi_0 \frac{\partial^2\varphi}{\partial z^2} \sin(k\lambda - \varphi) - \Phi_0 \left(\frac{\partial\varphi}{\partial z}\right)^2 \cos(k\lambda - \varphi). \end{aligned} \quad (5.6)$$

The second term on the right of Equation 5.6 vanishes at altitudes with minimum amplitude. The exact location of the MIL thus depends on the relative strengths of  $\Phi_0$ , its curvature and the vertical phase derivatives. PW induced MILs may therefore occur at any longitude although term 1 in Equation 5.6 usually leads when the wave amplitude is small (i.e., low latitudes,  $\partial^2\Phi_0/\partial z^2 > 0$  close to heights of minimum amplitude) while term 4 (opposite sign compared to term 1) is more important when the wave amplitude is still large (i.e., high latitudes). The MIL signatures in Figures 5.11e, f are well reproduced when computing  $\Phi'_{PW}$  from wave-1 and wave-2 fits (with wave-1 leading) using Equation 5.4 (not included in the Figure for better readability).

The PW decay when approaching the critical wind layer also leads to the formation of a mesospheric surf zone, as in the case study. The model potential vorticity in Figure 5.12 shows an inverted meridional gradient over Central Asia and an almost flat gradient over Europe.

Hence, the year-long TIME-GCM simulation confirms the November 1994 case study results, that is, the close relationship between PW activity, GW filtering processes, MIL occurrence and the mesospheric surf zone as outlined in section 5.1. Additional processes may play a role at high latitudes but the occurrence of low latitude MILs is strongly favored during time periods of enhanced PW-1 activity that precede stratospheric warming events. The same results are obtained for the SH with

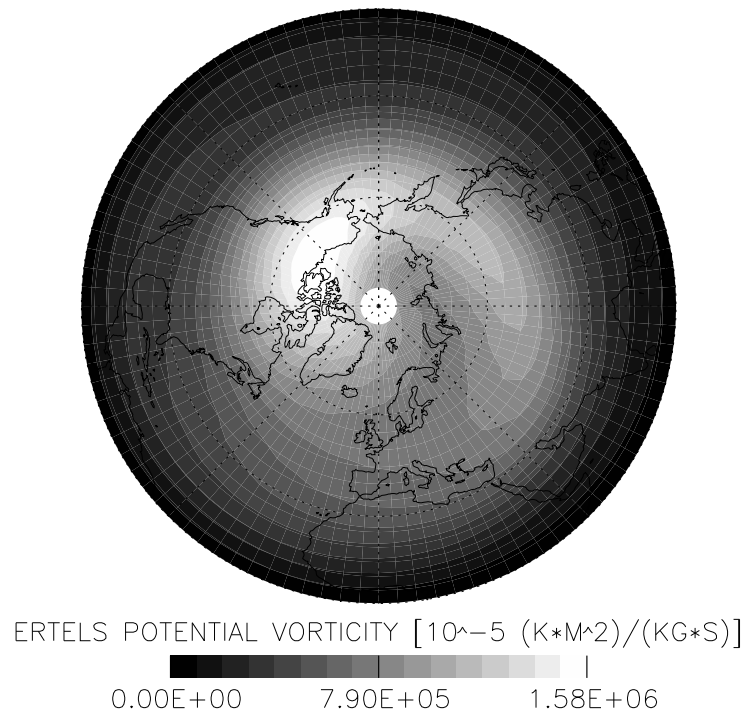


Figure 5.12: PV at 90 km from TIME-GCM during day 341.

the exception that no stratospheric warmings occurred. This comes not as a surprise because the Southern vortex is more stable than the Northern vortex. The only ever recorded SH major warming occurred in September 2002. Nevertheless, the SH MILs are also closely related to the PW activity and the mechanisms are the same. Because the SH results would basically be a repetition of Figures 5.10 to 5.12, they are not shown again.

As outlined in section 3.2.2, TIME-GCM does not include latent heat forced non-migrating tides that may play an additional role in the MIL generation [Ward *et al.*, 2005] and it does not resolve small scale gravity waves. This and the limited vertical model resolution may lead to an underestimate of MIL occurrence and magnitude. Further insight into these potentially important generation processes may come from a future analysis of SABER data similar to the one presented here.

## 6 Comparison of kinetic temperature from 15 $\mu\text{m}$ $\text{CO}_2$ limb emissions and $\text{OH}^*(3,1)$ rotational temperature in nearly coincident air masses

Sophisticated retrieval algorithms nowadays account for the deviation from the local thermodynamical equilibrium (non-LTE) in the MLT. This allows a kinetic temperature retrieval from 15  $\mu\text{m}$   $\text{CO}_2$  limb emissions up to an altitude of 120 km [Gusev *et al.*, 2006]. The prospects of such global data sets for dynamical analyses are quite obvious, as exemplified with CRISTA temperatures in sections 4 and 5. In particular the long-term temperature measurements of the SABER instrument on board the TIMED satellite (see section 3.1.3) will and already have provided invaluable diagnostics of the seasonal and inter-annual variability of tides [Criss *et al.*, 2005; Forbes *et al.*, 2006], PWs [Garcia *et al.*, 2005], GWs [Preusse *et al.*, 2006], and mean temperature [Siskind *et al.*, 2005]. SABER temperatures are also retrieved from 15  $\mu\text{m}$   $\text{CO}_2$  limb emissions and account for the non-LTE conditions in the MLT [Mertens *et al.*, 2004]

On the other hand, a systematic comparison of such satellite-borne temperatures with the data from ground-based instruments is a necessity for (i) validation and (ii) joint analyses of combined data sets. Validation requires that one instrument is more reliable than the instrument to be validated. As pointed out by Scheer *et al.* [2006], this goal is difficult to achieve because the accuracies (systematic errors) of ground-based and space-borne temperature instruments are comparable. Many joint analyses of combined satellite and ground-based observations, however, only require determining the bias between both data sets. The ground-based instrument can then provide the temporal information not accessible to satellites which in turn provide the spatial coverage not accessible to a ground-based instrument. This approach has been successfully implemented to infer MLT wave dynamics [Shepherd *et al.*, 2004] as well as to use satellite data as transfer standard between different ground-based instruments and techniques [Scheer *et al.*, 2006]. Comparing several years of ground-based and satellite temperatures can also provide additional confidence in long-term trend analyses: bias variations with season or year would point to instrumental or method deficiencies of at least one measuring technique.

This basically motivated a three-year (January 2003 to November 2005) comparison of 15  $\mu\text{m}$  kinetic temperatures measured by SABER with  $\text{OH}^*(3,1)$  rotational temperatures measured by the Ground Based Infrared P-Branch Spectrometer (GRIPS) [Offermann *et al.*, 1983] in Wuppertal, Germany (7.2°E, 51.3°N) [Oberheide *et al.*, 2006c]. GRIPS data have been used for various trend studies, that is, for estimating decadal variations of planetary wave activity [Bittner *et al.*, 2002], long-term temperature changes [Beig *et al.*, 2003], and the seasonal dependence of temperature trends (length of summer) [Offermann *et al.*, 2004].

### 6.1 GRIPS instrument and data

The Wuppertal GRIPS instrument (named GRIPS-II) is a 0.3 m Czerny-Turner grating spectrometer that scans the near infrared between 1.05 - 1.74  $\mu\text{m}$  with a spectral

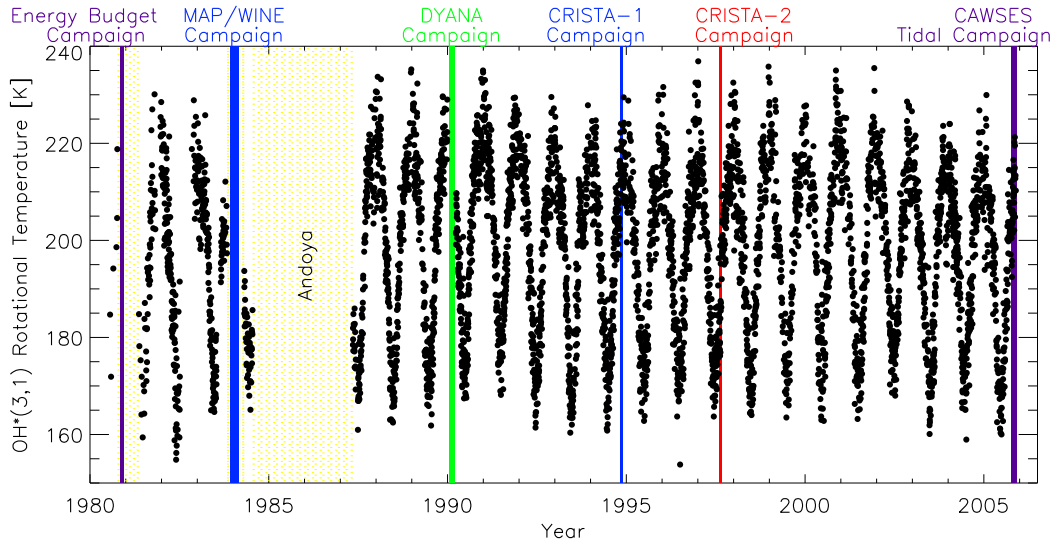
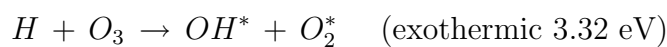


Figure 6.1: Nightly mean OH\*(3,1) rotational temperatures since 1980 as measured by GRIPS instruments in Wuppertal (7.2°E, 51.3°N). Yellow shadings indicate periods when the instruments were moved to different locations. Major campaigns with GRIPS participation are also marked. GRIPS-II measurements started in 1987.

resolution of 450. It is equipped with a liquid nitrogen cooled Ge detector. Measured parameters are the nighttime hydroxyl Meinel band (3,1) rotational temperature from the OH\* emission layer centered near 87 km altitude. The GRIPS-II instrument field-of-view is  $13.5^\circ \times 13.5^\circ$  (29 km  $\times$  41 km at 87 km) with a zenith angle of  $45^\circ$ . One OH\* spectrum is measured in 80 s. OH\* temperature data in Wuppertal are continuously taken since fall 1980 with gaps in 1981, between 1984 and 1987, and early 1990 when the measurements were performed at different locations. Figure 6.1 shows the nightly mean temperatures from 1980 - 2005. Temperatures since 1987 are from GRIPS-II and from an older instrument (named GRIPS-I) before that date. GRIPS-I is currently operated in collaboration with the Deutsche Wetterdienst (DWD) and the Deutsche Zentrum für Luft- und Raumfahrt (DLR) in Hohenpeissenberg in Southern Bavaria, Germany. DLR also operates another instrument that was developed and built by the University of Wuppertal on the Zugspitze mountain in the German Alps.

Only the data set from GRIPS-II in Wuppertal has the continuity for a systematic comparison with the SABER temperatures. It is used in the following, with the "-II" omitted for brevity. GRIPS is operated 365 days per year. The number of measuring nights with data is only limited by the cloud conditions: 232 nights in 2003, 221 nights in 2004, and 190 nights in 2005, totaling 643 nights in the 2003 - 2005 period. The measuring technique is described in detail by *Bittner et al.* [2002]. It may be summarized as follows.

In the upper mesosphere, atomic hydrogen reacts with ozone to form excited hydroxyl molecules in a layer of  $\sim 8$  km thickness and a peak altitude of  $\sim 87$  km.



Chemically excited OH molecules emit near-infrared radiation from several rotational-vibrational transitions. These emissions can be measured from the ground. During nighttime, GRIPS rotational temperatures are derived from the OH\*(3,1) vibrational

P-branch using the relative intensities of the three rotational  $P_1(2)$ ,  $P_1(3)$ , and  $P_1(4)$  lines between  $1.524 \mu\text{m}$  and  $1.543 \mu\text{m}$ . Hence, the derived temperatures are not affected by changes of the spectrometer sensitivity and of atmospheric transmission unless such changes are wavelength dependent. Even then, influences would be small because the three lines are close together. *Sivjee and Hamwey* [1987] give a detailed description of the temperature retrieval. The transition coefficient from *Mies* [1974] and the rotational energy from *Krassovsky et al.* [1962] are used. This and the measuring technique have not been changed since the beginning of the measurements in 1980 to ensure a homogenous time series for long-term trend analysis. Data from the recent GRIPS re-analysis [*Offermann et al.*, 2006b] are used in the following.

Rotational temperatures from  $\text{OH}^*$  emissions are not necessarily equal to the kinetic temperature of the atmosphere. Substantial deviations from the LTE were identified by *Pendleton et al.* [1993] for high-lying vibrational and rotational levels and transitions. Low-lying transitions such as  $\text{OH}^*(3,1)$  are more suitable for temperature derivations because non-LTE effects are less important [*She and Lowe*, 1998]. The systematic error (accuracy) of the GRIPS temperatures is estimated as 2 K [*Bittner et al.*, 2002]. There is, however, some indication that this error might be too low. A comparison of CRISTA temperatures and  $\text{OH}^*(3,1)$  measurements in Wallops Island [*Scheer et al.*, 2006] rather points to a warm bias of  $\sim 3$  K. This value is used in the following. The relative error (precision) of an hourly mean temperature is  $\leq 3.5$  K.

## 6.2 Coincidence criteria

One concern with the interpretation of ground-based  $\text{OH}^*$  rotational temperatures has always been the inherent lack of altitude information of the measurement technique. Exact altitude, shape, and OH layer thickness cannot be determined from these measurements. Hence, the allocation of the measured temperatures remains dubious to some extent. A compilation of various measurements of the mean OH layer altitude leads to a value of  $87.4 \text{ km}$  ( $\pm 2.9 \text{ km}$ ) [*Bittner et al.*, 2002; and references therein]. Sodium lidar -  $\text{OH}^*$  temperature comparisons indicate a mean layer altitude of  $87 \text{ km}$  which agrees with the independent WINDII/UARS satellite measurements [*She and Lowe*, 1998]. It must nevertheless be expected that the vertical displacement of air parcels due to wave activity (tides, PWs, GWs) will disturb the OH layer on various spatio-temporal scales. For example, tides may lead to a local time dependent emission layer height variance over the course of the night. *Zhao et al.* [2005] found values up to  $5 \text{ km}$  at low latitudes although the tidal effect is probably smaller at middle and high latitudes. The atmospheric variability can therefore introduce considerable differences between GRIPS and SABER temperatures data for a specific coincident observation. A systematic comparison between both instruments thus requires a good statistics, that is, several years of data.

The choice of the coincidence criteria is a balance between several arguments. Limiting the comparisons to true spatio-temporal coincidences is not feasible, because (i) only very few exact satellite overpasses occur and (ii) the noise error of a single GRIPS temperature measurement taken from one 80 s spectrum exceeds  $20 \text{ K}$ . On the other hand, relaxed spatio-temporal coincidence criteria increase the number of coincidences, and therefore improve the statistics, but they also add atmospheric

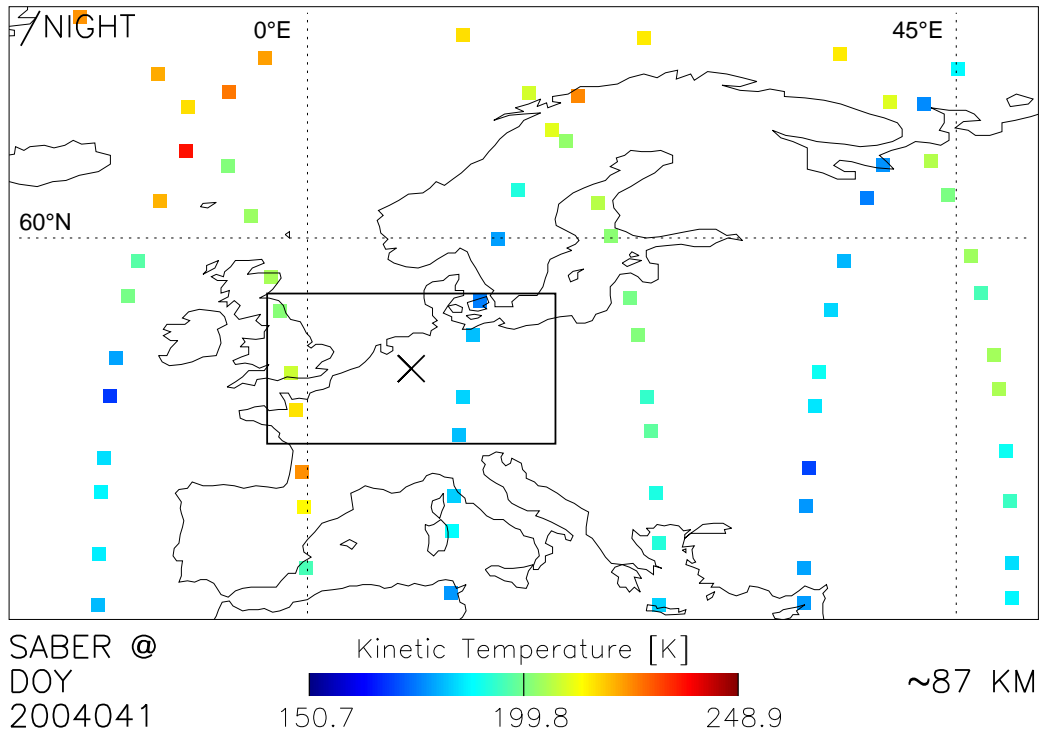


Figure 6.2: Example of SABER coverage over Europe (nighttime values only): temperature measurements made on February 10, 2004. The x marks Wuppertal and the box shows the spatial coincidence criterion (standard case, Table 6.1).

variability to the comparisons. The criteria for the standard case used here (Table 6.1) are a reasonable compromise with the air masses being compared not exactly but nearly coincident: SABER data must be taken within  $\sim 600$  km of Wuppertal. A spatially coincident temperature is then compared to hourly mean GRIPS temperatures centered around the time of the SABER observation. At least 20 single GRIPS temperature measurements must be present to calculate an hourly mean temperature. 330 nights between January 2003 and November 2005 meet these criteria (2003: 128, 2004: 104, 2005: 98) with in average 4.5 coincident SABER profiles (a total of 1490; 2003: 570, 2004: 492, 2005: 428).

Figure 6.2 shows the spatially coincident SABER temperatures for February 10, 2004. Using more rigorous criteria would severely limit the number of coincidences and/or would increase the random error of the GRIPS temperatures (3.5 K for hourly means). The effects of different coincidence criteria are discussed in section 6.4.

### 6.3 GRIPS - SABER comparisons

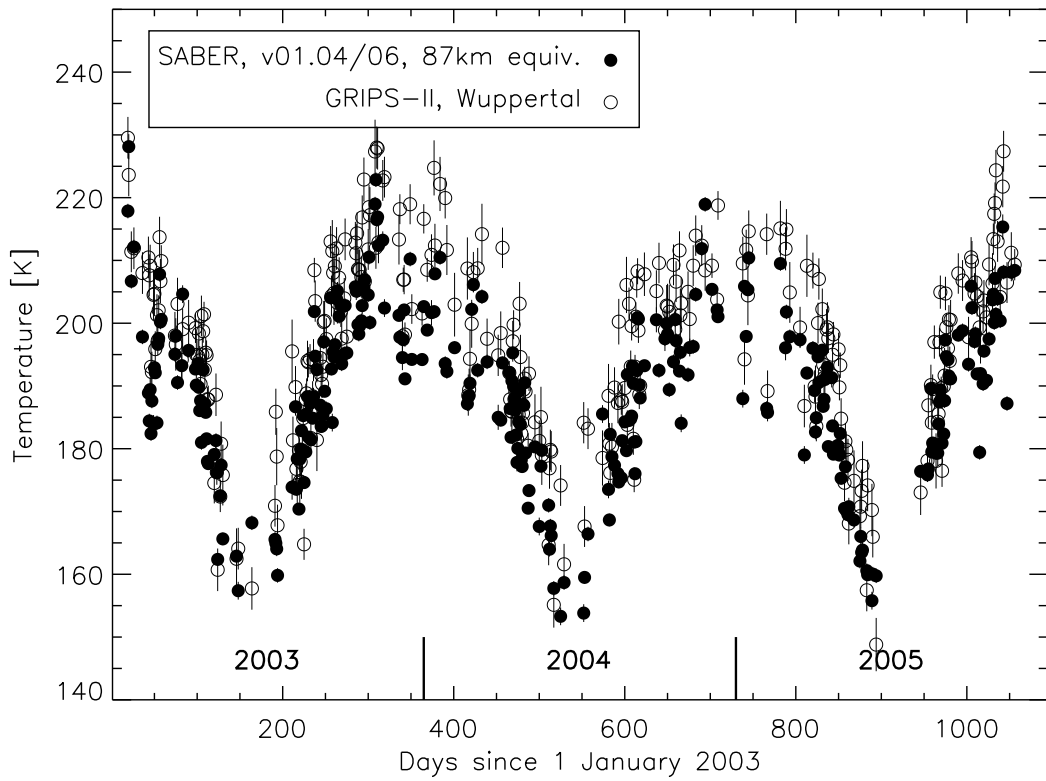
One potential shortcoming of ground-based - satellite comparisons is that the vertical resolution of both techniques is quite different. GRIPS temperatures inherently represent an average over the OH layer. As a limb-scanner, SABER has a vertical resolution of  $\sim 2$  km and its temperatures are allocated to certain altitudes. To mimic the GRIPS geometry, SABER temperatures must be converted into so-called *OH equivalent temperatures*. This is done by vertically averaging the SABER tem-

peratures using a Gaussian shaped weighting function (Full-Width-Half-Maximum = 8.7 km) centered at 87 km altitude. Calculating OH equivalent temperatures that way is simpler than the approach of *von Zahn et al.* [1987] who introduced the concept. It is chosen for practical reasons. Differences in the horizontal field-of-view of GRIPS (29 km × 41 km) and SABER (200 km × 20 km) are moderate with no reasonable way to account for it. The SABER temperatures used in the following are always OH equivalent temperatures, if not stated otherwise. They are calculated from data versions v01.04 (2003, 2004) and v01.06 (2005). Using different data versions does not pose a problem. A comparison of several months of v01.06 SABER data in 2004 and GRIPS yielded almost the same result (well within the error bars) as for v01.04. Recent algorithm improvements of the SABER non-LTE retrieval [*Feofilov et al.*, 2006] toward the forthcoming data version v01.07 resulted in higher polar summer mesopause temperatures. However, the effect is small at 51°N (about 1 K, A. Feofilov, private communication, 2006). It does not affect the results presented here because it is well within the systematic SABER temperature error (5 K, section 3.1.3).

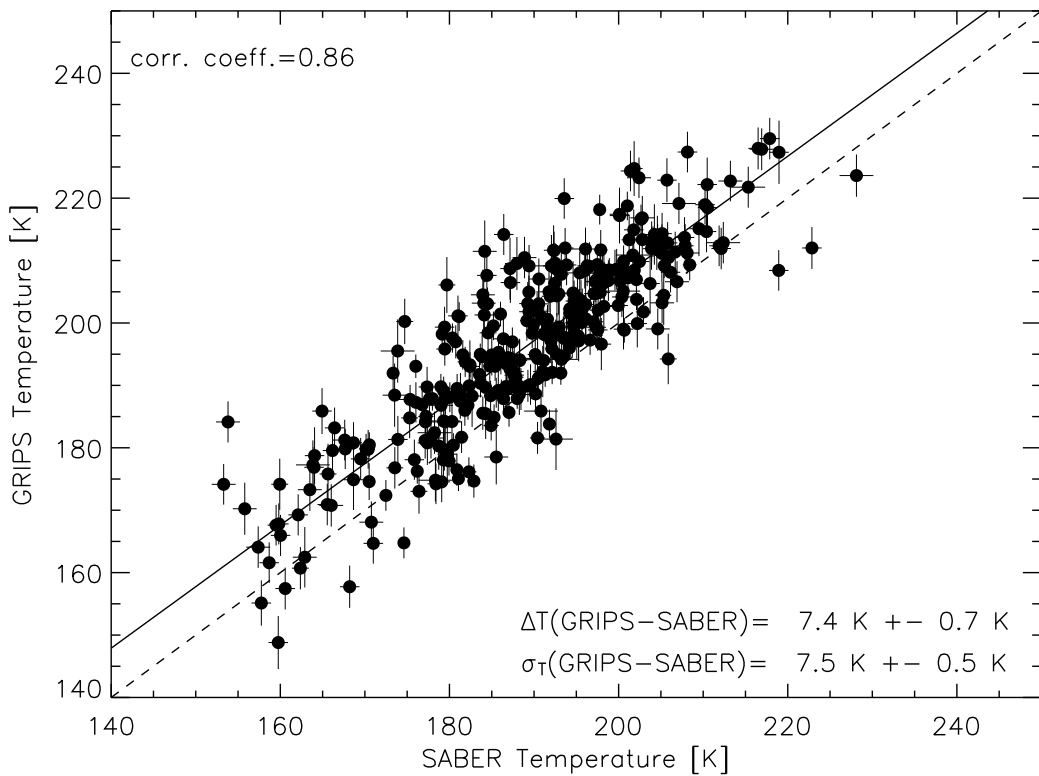
Figure 6.3a shows time series of coincident (standard case, Table 6.1) OH equivalent SABER temperatures and GRIPS OH\*(3,1) rotational temperatures. Owing to the orbit geometry of the TIMED satellite, only few coincidences occur in June and

Table 6.1: Effects of different coincidence criteria and altitudes on the GRIPS - SABER comparisons. † is the standard case, \* is for SABER temperatures at a fixed geometric altitude of 87 km, and ‡ is for weighting with SABER 1.6 μm volume emission rates.

altitude	spatial criterion	temporal criterion	bias [K]	standard deviation [K]	slope	correlation coefficient
†87 km OH equiv.	±5° (lat) ±10° (lon)	±30 min	7.4 ± 0.7	7.5 ± 0.5	0.99 ± 0.01	0.86
”	”	±15 min	7.6 ± 0.8	8.4 ± 0.5	0.97 ± 0.02	0.84
”	±2.5° (lat) ±5° (lon)	±30 min	7.3 ± 0.8	7.7 ± 0.6	0.98 ± 0.02	0.84
”	”	±15 min	7.4 ± 1.0	9.0 ± 0.7	0.99 ± 0.03	0.80
86 km OH equiv.	±5° (lat) ±10° (lon)	±30 min	7.3 ± 0.7	7.5 ± 0.5	0.95 ± 0.01	0.87
88 km OH equiv.	”	”	7.6 ± 0.7	7.8 ± 0.5	1.02 ± 0.01	0.85
*87 km geometric	”	”	7.1 ± 0.8	8.7 ± 0.5	0.83 ± 0.01	0.83
‡1.6 μm VER	”	”	6.2 ± 0.7	7.7 ± 0.5	1.07 ± 0.02	0.86

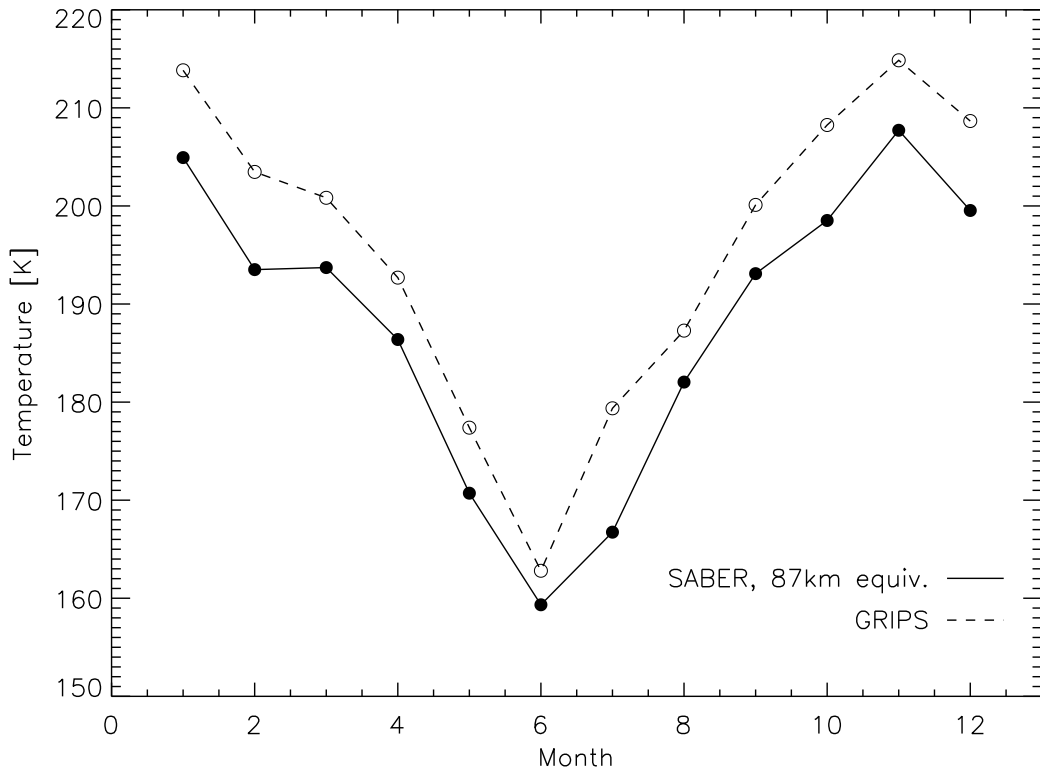


a)

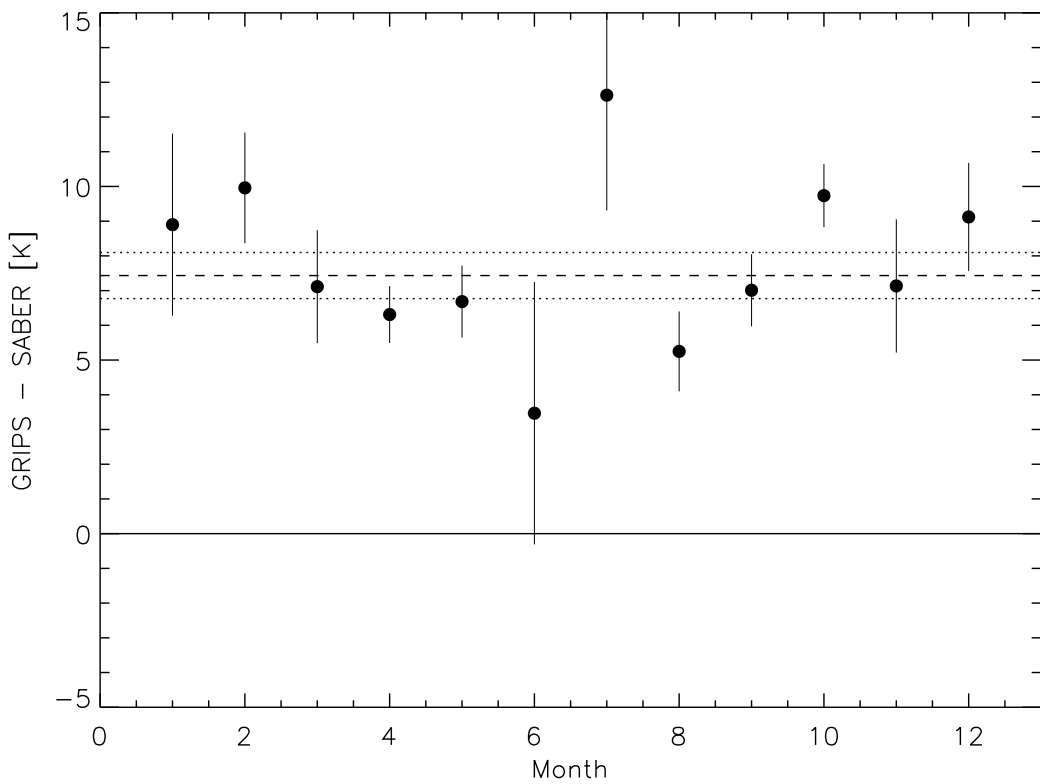


b)

Figure 6.3: a) Coincident (standard case, Table 6.1) OH equivalent SABER temperatures (v01.04: 2003, 2004; v01.06: 2005) and GRIPS OH\*(3,1) rotational temperatures. Only few coincidences occur in June and July. Error bars show noise error (GRIPS) and standard deviation (SABER). b) Scatter between the temperatures shown in a). Mean difference is 7.4 K with a standard deviation of 7.5 K. Bisecting line (dashed) and fit curve (solid, slope = 0.99) are also shown.



a)



b)

Figure 6.4: a) Monthly averaged (2003 - 2005) GRIPS and OH equivalent SABER temperatures. b) Difference between the curves shown in a). Error bars indicate standard deviations. No significant deviation from the mean difference (dashed; standard deviation: dotted) is observed. June and July values are outliers due to poor statistics.

July. Each plot value is an average of all GRIPS and SABER temperatures that meet the coincidence criteria during this night. GRIPS error bars are calculated from the precision and thus indicate the noise error of the plot values. SABER error bars are the standard deviations of the plot values. Hence, they are governed by atmospheric -mostly spatial- variability. The contribution of instrument noise to the SABER error bars is negligible, due to the vertical averaging into OH equivalent temperatures.

Both instruments observe the same seasonal and annual cycles, and similar extreme events such as the low temperatures in early 2005. However, Figure 6.3a already points to some scatter between both data sets with a warm bias of the GRIPS temperatures. This becomes more clear in Figure 6.3b. A linear fit (accounting for both error bars) gives a 7.4 K warm bias of the GRIPS temperatures with a fit uncertainty of 0.7 K. The fit slope is 0.99 ( $\pm 0.01$ ) which is very important because it shows that the offset between both data sets is temperature independent. The GRIPS - SABER standard deviation is 7.5 K ( $\pm 0.5$  K) and the correlation coefficient is 0.86. All these parameters are almost independent of the year, that is, well inside their uncertainties (not shown). Possible reasons for the bias and the scatter are discussed in section 6.4.

Because the differences between GRIPS and SABER do not differ much from year to year, it makes sense to compare monthly mean temperatures (Figure 6.4a). Their agreement is, apart from the systematic bias, remarkable. Both instruments observe the flattened gradient in February and the relative temperature minimum in December. Figure 6.4b provides more details about the monthly mean temperature differences with their standard deviations indicated by the error bars. The June and July values are outliers due to poor statistics. There may be some tendency for a slightly larger difference in winter and a smaller one in summer, but this is statistically not significant. From the current statistics -based upon three years of data- the GRIPS - SABER temperature offset is independent of the month.

## 6.4 Discussion and implications for joint analyses

A different choice of the coincidence criteria (Table 6.1) does not change the comparison results very much. For OH equivalent SABER temperatures centered around 87 km, more restrictive spatio-temporal criteria leave the systematic bias unaltered but increase the standard deviation  $\sigma$  between both data sets. Note that in these cases the fit slope is still very close to one indicating a temperature independent bias. As for the standard case, no statistically significant year-to-year and month-to-month bias variations are found. The increase of  $\sigma$  with decreasing miss time is basically an artifact of the GRIPS noise error  $\sigma_G$ . Assuming that  $\sigma$  is governed by atmospheric variability  $\sigma_v$  (including a small contribution of SABER noise error) and  $\sigma_G$ , it can be expressed as

$$\sigma = \sqrt{\sigma_v^2 + \sigma_G^2} \quad (6.1)$$

if instrument noise and atmospheric variability are uncorrelated. GRIPS data that are averaged over time periods  $\leq 1$  hour comply with the latter condition (D. Offermann, private communication, 2006).

With  $\sigma_G = 3.5$  K for hourly means and  $\sigma = 7.5 \pm 0.5$  K (standard case, Table 6.1), Equation 6.1 results in  $\sigma_v = 6.6 \pm 0.6$  K. Reducing the allowed miss time to

$\pm 15$  minutes increases the GRIPS noise error to  $\sigma_G = 5.0$  K which in turn leads to  $\sigma = 8.3 \pm 0.5$  K (expected). This is close to the observed value of  $8.4 \pm 0.5$  K. The same calculation for the  $\pm 5^\circ$  (lon),  $\pm 2.5^\circ$  (lat) spatial criterion results in  $\sigma = 8.5 \pm 0.5$  K (expected) that is also close to the observed value of  $9.0 \pm 0.7$  K. Without being statistically significant,  $\sigma$  also increases for decreasing miss distance. This tendency is consistent with the smaller number of available coincidences.

The use of OH equivalent temperatures centered around 86 km and 88 km yields very similar results as the standard case (Table 6.1), but the fit slopes slightly deviate from one. Hence, 87 km is the best choice for the centroid altitude when calculating OH equivalent temperatures. The direct comparison of SABER temperatures measured at 87 km (i.e., not converted into OH equivalent temperatures) gives a warm bias similar to the standard case but with a larger standard deviation. However, the slope of the fit curve is only 0.83 such that the bias is now temperature dependent with a larger difference in summer and a smaller one in winter. This emphasizes the need for using OH equivalent temperatures when comparing satellite and ground-based data. Another way to calculate OH equivalent temperatures is to use the vertical shape of the measured OH volume emission rates (VER) from the SABER 1.6  $\mu\text{m}$  channel instead of a Gaussian function centered at a certain altitude to do the weighting. This significantly reduces the bias to 6.2 K but the fit slope becomes 1.07 with larger differences in winter and smaller ones in summer. This may be due to the fact that the SABER 1.6  $\mu\text{m}$  channel has contributions from the (5,3) and (4,2) OH bands that peak at a different altitude. Using a Gaussian shaped weighting function for the comparison is thus more feasible.

The most important finding is that the comparison of OH equivalent SABER temperatures centered at 87 km and OH\*(3,1) rotational temperatures from GRIPS yields a warm bias of 7.5 K of the ground-based instrument. This systematic offset is independent of the specific choice of the coincidence criteria, the year, and the season. It thus gives additional confidence into allocating the mean altitude of the OH layer to 87 km altitude for trend analyses: dynamically induced disturbances of layer altitude, thickness and shape average out in the long term.

A 7.5 K bias is in a sense disappointing but it lies nevertheless just within the combined systematic error bars of both instruments (8 K), that is, 3 K from GRIPS and 5 K from SABER (section 3.1.3). Its stability may prove to be useful for adjusting SABER and GRIPS temperatures to each other for future joint analyses. Because the GRIPS and SABER systematic errors are comparable, the comparison does not represent a validation, but there is some additional indication that the ground-based OH\*(3,1) rotational temperatures are too warm by a few degrees. The observed offset is consistent with the 5 K warm bias between GRIPS and 15  $\mu\text{m}$  kinetic temperatures from CRISTA (O. Gusev, private communication, 2005). Comparisons of GRIPS with OH\*(3,1) rotational temperatures from SCIAMACHY on ENVISAT [*von Savigny et al.*, 2004] show a warm bias of 2.7 K. Using the GRIPS instrument as a transfer standard, these offsets also provide an initial guess of the systematic temperature differences between SABER, CRISTA, and SCIAMACHY. This complements the approach of *Scheer et al.* [2006] who used the CRISTA instrument as a transfer standard between different ground-based stations.

## 7 Summary

Temperature and wind data from four satellite instruments (CRISTA, LIMS, SABER, TIDI) have been analyzed on their spatio-temporal variations in the MLT region with emphasis on large-scale waves. The comparison with the predictions of three models of differing character (GSWM, TIME-GCM, extended CMAM) allows an interpretation of the satellite diagnostics in terms of lower-upper atmosphere coupling across the stratopause. Of particular interest in this context are the nonmigrating or non-Sun-synchronous tides and quasi-stationary planetary waves including their interaction.

The CRISTA case study results base upon a new, non-spectral analysis approach. They show how large diurnal temperature tides may become in an altitude region of Earth's atmosphere that was not accessible to global analysis before. Nonmigrating tides in the equatorial lower thermosphere may exceed the migrating tide by almost an order of magnitude and hence introduce a considerable longitude modulation of the tidal signal. The results always point to an upward energy and momentum transport with tidal forcing lower in the atmosphere. Two important sources of the nonmigrating tides are identified by comparing the observations to the model predictions: latent heat release in the tropical troposphere associated with deep convective systems and the interaction between the migrating tide and quasi-stationary planetary waves. Their relative contribution depends on the propagation direction and zonal wavenumber of the nonmigrating tides. As a general rule, latent heat release is more important in forcing eastward propagating components and the wave-wave interaction source is more important in forcing the standing oscillation and westward propagating components with low zonal wavenumbers. Observed large amplitudes of westward propagating components with high zonal wavenumbers are not reproduced by the models and remain unexplained so far.

Further evidence for the wave-wave interaction forcing comes from observations alone. An application of the analysis method developed for CRISTA to seven month of LIMS temperature data provided nonmigrating tidal amplitudes and phases over a broader latitude range. Two diurnal components are analyzed in that way, the standing oscillation and the westward propagating wave of zonal wavenumber 2 ( $w_2$ ). Highest positive correlations of  $w_2$  with the quasi-stationary planetary wave 1 occur in boreal winter during periods when the latter penetrates into low and middle latitudes where the signal of the migrating tide in either temperature or wind is still significant. This is internally consistent with the CRISTA observations. The wave-wave interaction forcing is most efficient equatorward of  $30^\circ$  and between 45 and 55 km altitude.

The seasonal variability of the nonmigrating tides is studied in MLT region winds. Zonal and meridional wind measurements of the TIDI instrument on board TIMED are Fourier analyzed on diurnal and semidiurnal nonmigrating tides from 85-105 km altitude and between  $45^\circ\text{S}$  and  $45^\circ\text{N}$ . Limitations of previous satellite-borne wind instruments have restricted such analyses to 95 km altitude before. Hence, the TIDI results are unprecedented in that they represent the first observations of the vertical structure of nonmigrating tidal winds over a range of MLT altitudes. Monthly climatologies are derived from three years (2002-2005) of data for 14 diurnal components and 12 semidiurnal components. Amplitudes of a single nonmigrating diurnal com-

ponent can reach 20 m/s. Their aggregate effect can easily exceed the amplitude of the radiatively forced migrating tide although that component could not be analyzed. The TIDI results are consistent with climatologies from HRDI and WINDII at 95 km in spite of the 11 year time gap between the measurements. This points to a seasonal cycle stability of the nonmigrating tides that is remarkable, considering the variability of the tidal sources.

The comparison and interpretation of the diurnal TIDI climatologies with the model predictions yields results that are consistent with the findings from CRISTA and LIMS. It indicates that for the w2 and s0 components both latent heat release in the tropical troposphere and wave-wave interaction forcing need to be considered. Their relative contribution may differ from month to month but these sources can basically explain the observations. Eastward propagating components, on the other hand, are mostly governed by the latent heat source. The quantitative agreement between the model predictions and TIDI is good for some months but rather disappointing for other months. Some of the discrepancies may be attributable to the fact that not all sources and interactions are included in the models. It nevertheless becomes clear that the present understanding of nonmigrating tides is still incomplete. There is an obvious need to further improve the tidal forcing and dissipation schemes in the models. The observation based tidal climatologies from TIDI provide the necessary guidance for such efforts.

The semidiurnal climatologies from TIDI have not yet been interpreted in the same way as the diurnal climatologies. Initial results nevertheless indicate that they are also governed by latent heat release in the tropical troposphere and by the interaction of the migrating semidiurnal tide with the quasi-stationary planetary wave 1. It thus becomes clear from CRISTA, LIMS, and TIDI analyses that nonmigrating tides provide an important mechanism for coupling the lower with the upper atmosphere. Large-scale tropospheric systems that do not propagate into the MLT nevertheless influence the dynamics, chemistry, and energetics in this height region via their imprint upon the tidal fields. Accounting for these coupling processes is a very challenging task for data assimilation approaches in the MLT. One of the next natural steps is a quantification of the momentum transfer and the resulting zonal mean flow acceleration due to nonmigrating tides from observations alone. The TIDI climatologies altogether with similar climatologies [Forbes *et al.*, 2006] derived from SABER temperature measurements provide the necessary database for that.

Space-borne, high spatial resolution temperature and constituent measurements are also ideally suited to study other wave coupling processes. CRISTA measurements during a Canadian warming event in November 1994 showed a compact surf zone in the mesosphere and the presence of mesospheric temperature inversion layers. Both effects are eventually the result of the interaction between quasi-stationary planetary waves, gravity waves, and the mean flow. The decay of upward propagating planetary waves in the surf zone region just beneath the wind reversal altitude comes along with an amplification of upper mesospheric planetary waves that in turn is a result of gravity wave filtering and breaking. This induces a vertical curvature of the geopotential wave perturbation that is sufficiently large to invert the thermal structure in the mesosphere, through hydrostatic equilibrium. A one year-long TIME-GCM simulation supports the case study findings. Low latitude mesospheric temperature inversion

layers are strongly favored during time periods of enhanced quasi-stationary planetary wave 1 activity that precede stratospheric warming events. It is nevertheless quite clear that long-term temperature measurements such as from the SABER instrument are needed to provide the observational database to further confirm this generation mechanism and to investigate additional processes that are not resolved in the model.

A global analysis of the mesospheric dynamics will likely profit from combining the spatial coverage of a satellite instrument with the temporal coverage of a ground-based instrument. As a first step toward such a joint analysis, three years of ground-based GRIPS temperature measurements are compared to coincident SABER temperature measurements. Both instruments agree within their combined error bars with a time-independent systematic bias of 7.5 K. This is consistent with the warm bias between GRIPS and CRISTA, and GRIPS and SCIAMACHY/ENVISAT such that the comparison provides an initial guess for the systematic temperature differences between the three satellite instruments. The bias independency of year and season gives additional confidence into allocating the mean altitude of the OH\* emission layer to a constant value of 87 km for secular trend analyses.

## 8 Acknowledgment

My sincerest thank goes to D. Offermann for his invaluable support during all phases of this thesis. I also thank M.E. Hagan, H.-L. Liu, R.G. Roble, and W.E. Ward for their helpful and friendly collaboration in providing the model simulations. The support of Q. Wu and T.L. Killeen in providing the TIDI data is gratefully acknowledged. This thesis was partly supported by DLR grants 50 OE 8503 and 50 QV 9802 4 and by the DFG priority program CAWSES through grant OB 299/2-1.

## Appendix

- A1 List of acronyms
- A2 Classical tidal theory
- A3 Tidal component deconvolution
- A4 TIDI climatologies: diurnal
- A5 TIDI climatologies: semidiurnal

## A1 List of acronyms

CAWSES	Climate and Weather of the Sun-Earth System
CMAM	Canadian Middle Atmosphere Model
CRISTA	Cryogenic Infrared Spectrometers and Telescopes for the Atmosphere
EUV	extreme ultraviolet
GCM	general circulation model
GRIPS	Ground Based Infrared P-Branch Spectrometer
GSWM	Global Scale Wave Model
GW	gravity wave
LST	local solar time
IR	infrared
LIMS	Limb Infrared Monitor of the Stratosphere
MIL	mesospheric inversion layer
MLT	mesosphere and lower thermosphere
NH	northern hemisphere
PSMOS	Planetary Scale Mesopause Observing System
PW	planetary wave
QTDW	quasi two-day wave
QSPW	quasi-stationary planetary wave
SABER	Sounding the Atmosphere Using Broadband Emission Radiometry
SH	southern hemisphere
TIDI	TIMED Doppler Interferometer
TIME-GCM	Thermosphere-Ionosphere-Mesosphere-Electrodynamics General Circulation Model
TIMED	Thermosphere, Ionosphere, Mesosphere, Energetics and Dynamics
UARS	Upper Atmosphere Research Satellite
UT	universal time
UV	ultraviolet
vis	visible

## A2 Classical tidal theory

In the following, a sketch of the classical tidal theory is given by summarizing the review of *Forbes* [1995] whereas some intermediate steps of the math are also provided. Neglecting mechanical forcing and dissipation, the classical tidal theory assumes that atmospheric wave motions can be considered as linear perturbations of an initially motionless zonal mean state that is horizontally stratified and isothermal. The linearized equations, then, for perturbations on a spherical isothermal atmosphere are [*Holton*, 1975]:

$$\frac{\partial u'}{\partial t} - 2\Omega \sin \varphi v' + \frac{1}{a \cos \varphi} \frac{\partial \Phi'}{\partial \lambda} = 0, \quad (\text{A2.1})$$

$$\frac{\partial v'}{\partial t} + 2\Omega \sin \varphi u' + \frac{1}{a} \frac{\partial \Phi'}{\partial \varphi} = 0, \quad (\text{A2.2})$$

$$\frac{\partial^2}{\partial t \partial z} \Phi' + N^2 w' = \frac{\kappa J'}{H}, \quad (\text{A2.3})$$

$$\frac{1}{a \cos \varphi} \left( \frac{\partial u'}{\partial \lambda} + \frac{\partial}{\partial \varphi} (v' \cos \varphi) \right) + \frac{1}{\varrho_o} \frac{\partial}{\partial z} (\varrho_o w') = 0, \quad (\text{A2.4})$$

with

- $u$  eastward zonal wind
- $v$  northward meridional wind
- $w$  upward vertical wind
- $\Phi$  geopotential,  $\int g(z, \varphi) dz$
- $N^2$  square of Brunt-Vaisala (buoyancy) frequency =  $\kappa g/H$
- $\Omega$  angular velocity of the Earth
- $\varrho_o$  density  $\propto \exp(-z/H)$
- $z$  altitude
- $\lambda$  longitude
- $\varphi$  latitude
- $\kappa$   $R/c_p \approx 2/7$
- $J$  heating rate per unit mass
- $a$  radius of the Earth
- $g$  gravity acceleration
- $H$  constant scale height
- $t$  time

Equations A2.1 and A2.2 describe the local momentum conservation in the zonal and meridional direction, Equation A2.3 describes the thermodynamics and Equation A2.4 is the continuity equation. Primed parameters are perturbations. The set of equations can be solved for longitudinally propagating waves of zonal wavenumber  $s$  and frequency  $\sigma$ :

$$\{u', v', w', \Phi'\} = \{\hat{u}, \hat{v}, \hat{w}, \hat{\Phi}\} e^{i(s\lambda - \sigma t)}. \quad (\text{A2.5})$$

Zonal wavenumber  $s$  is a positive integer so that positive values for  $\sigma$  correspond to eastward propagating waves and negative values to westward propagating waves. This nomenclature differs from the one used throughout the remainder of this work where

frequencies are always positive and negative (positive) values of  $s$  represent westward (eastward) propagation. It is used for consistency with *Forbes* [1995].

Using Equation A2.5, the partial time and longitude derivatives of winds and geopotential can be determined. Substitution in Equations A2.1 and A2.2 leads to

$$\hat{u} = \frac{\sigma}{4\Omega^2 a (\eta^2 - \sin^2 \varphi)} \left[ \frac{s}{\cos \varphi} + \frac{\sin \varphi}{\eta} \frac{\partial}{\partial \varphi} \right] \hat{\Phi} \quad (\text{A2.6})$$

$$\hat{v} = \frac{-i\sigma}{4\Omega^2 a (\eta^2 - \sin^2 \varphi)} \left[ \frac{s \tan \varphi}{\eta} + \frac{\partial}{\partial \varphi} \right] \hat{\Phi} \quad (\text{A2.7})$$

with  $\eta = \sigma/(2\Omega)$ . Separating out the latitude and height variables gives

$$\hat{\Phi} = \Theta(\varphi) G(z). \quad (\text{A2.8})$$

Using  $\mu = \sin \varphi$ ,  $\epsilon = (2\Omega a)^2/gh$  ( $h$  is an arbitrary constant here, its meaning becomes clear in Equation A2.17) and Equation A2.8, the following is obtained:

$$\begin{aligned} \frac{1}{a \cos \varphi} \frac{\partial u'}{\partial \lambda} &= \frac{is\hat{u}}{a \cos \varphi} e^{i(s\lambda - \sigma t)} \\ &= \frac{i\sigma}{\epsilon gh (\eta^2 - \mu^2)} \left[ \frac{s^2}{(1 - \mu^2)} + \frac{s\mu}{\eta} \frac{\partial}{\partial \mu} \right] \Theta(\mu) G(z) e^{i(s\lambda - \sigma t)} \end{aligned} \quad (\text{A2.9})$$

$$\begin{aligned} \frac{1}{a \cos \varphi} \frac{\partial}{\partial \varphi} (v' \cos \varphi) &= \frac{1}{a \cos \varphi} \frac{\partial}{\partial \varphi} (\hat{v} \cos \varphi) e^{i(s\lambda - \sigma t)} \\ &= -\frac{i\sigma}{\epsilon gh (\eta^2 - \mu^2)} \left[ \frac{s\mu}{\eta} + (1 - \mu^2) \frac{\partial}{\partial \mu} \right] \Theta(\mu) G(z) e^{i(s\lambda - \sigma t)} \\ &= -\frac{i\sigma}{\epsilon gh} \left[ \frac{s(\eta^2 + \mu^2)}{\eta(\eta^2 - \mu^2)^2} + \frac{s\mu}{\eta(\eta^2 - \mu^2)} \frac{\partial}{\partial \mu} \right. \\ &\quad \left. + \frac{\partial}{\partial \mu} \left( \frac{(1 - \mu^2)}{(\eta^2 - \mu^2)} \frac{\partial}{\partial \mu} \right) \right] \Theta(\mu) G(z) e^{i(s\lambda - \sigma t)} \end{aligned} \quad (\text{A2.10})$$

Hence, Equation A2.4 can be rewritten as

$$-\left( \frac{i\sigma}{\epsilon gh} \mathcal{L} \right) \Theta(\mu) G(z) e^{i(s\lambda - \sigma t)} + \frac{1}{\rho_o} \frac{\partial}{\partial z} (\rho_o w') = 0, \quad (\text{A2.11})$$

$$\mathcal{L} = \frac{\partial}{\partial \mu} \left[ \frac{(1 - \mu^2)}{(\eta^2 - \mu^2)} \frac{\partial}{\partial \mu} \right] - \frac{1}{\eta^2 - \mu^2} \left[ -\frac{s}{\eta} \frac{(\eta^2 + \mu^2)}{(\eta^2 - \mu^2)} + \frac{s^2}{1 - \mu^2} \right]. \quad (\text{A2.12})$$

Separating out the latitude and height variables in the vertical wind  $\hat{w} = \tilde{w}(\varphi) w^*(z)$ , Equation A2.11 yields ( $\rho_o \propto e^{-z/H}$ , see above)

$$-\left( \frac{i\sigma}{\epsilon gh} \mathcal{L} \right) \Theta(\mu) G(z) e^{i(s\lambda - \sigma t)} + \tilde{w}(\varphi) \left( \frac{\partial w^*(z)}{\partial z} - \frac{1}{H} w^*(z) \right) e^{i(s\lambda - \sigma t)} = 0. \quad (\text{A2.13})$$

Because of the separated variables in Equation A2.13, and without loss of generality, one can now choose

$$G(z) = \frac{\partial w^*(z)}{\partial z} - \frac{1}{H} w^*(z) \quad (\text{A2.14})$$

and, after omission of the time-dependent parts, Equation A2.11 yields

$$-\left(\frac{i\sigma}{\epsilon gh}\mathcal{L}\right)\Theta(\mu) + \tilde{w}(\mu) = 0. \quad (\text{A2.15})$$

With the substitutions for  $\hat{\Phi}$ ,  $\hat{w}$ , and setting  $J' = 0$  for the moment, Equation A2.3 can be expressed as

$$-i\sigma\Theta(\varphi)\frac{\partial G(z)}{\partial z}e^{i(s\lambda-\sigma t)} + N^2\tilde{w}(\varphi)w^*(z)e^{i(s\lambda-\sigma t)} = 0 \quad (\text{A2.16})$$

that immediately results in

$$\frac{\partial G(z)/\partial z}{N^2w^*(z)} = -\frac{i\tilde{w}(\varphi)}{\sigma\Theta(\varphi)} = -\frac{1}{gh}. \quad (\text{A2.17})$$

Equation A2.17 can only be satisfied by a constant value, that is,  $-1/gh$  which then defines the separation constant  $h$  introduced in Equation A2.9. Hence,

$$\tilde{w}(\varphi) = -\frac{i\sigma}{gh}\Theta(\varphi) \quad (\text{A2.18})$$

$$w^*(z) = -\frac{gh}{N^2}\frac{\partial G(z)}{\partial z}. \quad (\text{A2.19})$$

Substitution of Equation A2.18 and  $\mu = \sin\varphi$  into Equation A2.15 yields *Laplace's tidal equation* (horizontal structure equation)

$$\mathcal{L}\hat{\Theta} + \epsilon\hat{\Theta} = 0. \quad (\text{A2.20})$$

For this eigenfunction-eigenvalue problem of specified wavenumber  $s$  and frequency  $\sigma$ , a complete orthogonal set of eigenfunctions  $\{\Theta_n\}$  (*Hough functions*) and eigenvalues  $\epsilon_n$  can be found. For a proof, see *Flattery* [1967] who also provides tabulated values. Hough functions are defined as an infinite sum of associated Legendre polynomials. The separation constants  $h_n$  (sometimes referred to as *equivalent depths*) couple the horizontal part with the vertical part.

Since  $\{\Theta_n\}$  is a complete orthogonal set, the amplitude of the thermal excitation  $J' = \hat{J}e^{i(s\lambda-\sigma t)}$  can be expanded as

$$\hat{J} = \sum_n \Theta_n(\varphi) J_n(z). \quad (\text{A2.21})$$

and Equations A2.6, A2.7, and A2.8 transform to

$$\hat{\Phi} = \sum_n \Theta_n(\varphi) G_n(z), \quad (\text{A2.22})$$

$$\hat{u} = \frac{\sigma}{4\Omega^2 a} \sum_n U_n(\varphi) G_n(z), \quad (\text{A2.23})$$

$$\hat{v} = \frac{-i\sigma}{4\Omega^2 a} \sum_n V_n(\varphi) G_n(z) \quad (\text{A2.24})$$

with

$$U_n = \frac{1}{(\eta^2 - \sin^2 \varphi)} \left[ \frac{s}{\cos \varphi} + \frac{\sin \varphi}{\eta} \frac{\partial}{\partial \varphi} \right] \Theta_n \quad (\text{A2.25})$$

$$V_n = \frac{1}{(\eta^2 - \sin^2 \varphi)} \left[ \frac{s \tan \varphi}{\eta} + \frac{\partial}{\partial \varphi} \right] \Theta_n. \quad (\text{A2.26})$$

Using the expansion in Equation A2.21, Equation A2.3 (now with external forcing) immediately results in a general expression of A2.19:

$$w_n^*(z) = -\frac{gh}{N^2} \left( \frac{\partial G_n(z)}{\partial z} - \frac{i\kappa}{\sigma H} J_n(z) \right) \quad (\text{A2.27})$$

Substitution of Equation A2.27 into Equation A2.14 yields

$$i\sigma H \left[ \frac{1}{\rho_0} \frac{\partial}{\partial z} \rho_0 \frac{\partial}{\partial z} G_n \right] + \frac{1}{\rho_0} \frac{\partial}{\partial z} (\rho_0 \kappa J_n) = -\frac{i\sigma \kappa}{h_n} G_n, \quad (\text{A2.28})$$

that is, the *vertical structure equation* for an isothermal atmosphere. With the definitions

$$\alpha_n^2 = \kappa H / h_n - 1/4 \quad (\text{A2.29})$$

$$x = z/H \quad (\text{A2.30})$$

$$G_n^* = G_n \varrho_o^{1/2} N^{-1} \quad (\text{A2.31})$$

$$F_n(x) = -\frac{\varrho_o^{-1/2}}{i\sigma N} \frac{\partial}{\partial x} (\varrho_o J_n), \quad (\text{A2.32})$$

Equation A2.28 can be rewritten in its canonical form as

$$\frac{\partial^2 G_n^*}{\partial x^2} + \alpha_n^2 G_n^* = F_n(x). \quad (\text{A2.33})$$

with solutions of the form

$$G_n^*(x) \sim A e^{i\alpha_n x} + B e^{-i\alpha_n x} \quad (\text{A2.34})$$

which leads to

$$G_n^*(x) \sim \begin{cases} e^{-|\alpha_n| x} & : \alpha_n^2 < 0 \\ e^{i\alpha_n x} & : \alpha_n^2 > 0 \\ e^{(\kappa - \frac{1}{2})x} & : h_n = H/(1 - \kappa), F_n(x) = 0 \forall x \end{cases} \quad (\text{A2.35})$$

for bounded solutions and at altitudes above the source region. Obviously, three classes of solutions exist: (i) evanescent or trapped ( $\alpha_n^2 < 0$ ); (ii) propagating ( $\alpha_n^2 > 0$ ), and (iii) Lamb waves (free solutions).

Tides are eigenmodes or eigenoscillations of the atmosphere. Each wavenumber/frequency pair (a tidal *component*) is a superposition of associated Hough functions (often called tidal *modes* in the literature) of index  $n$ . The nomenclature is such that a negative value of  $n$  refers to evanescent modes (no vertical propagation) and a positive value to propagating modes. The equivalent depth  $h_n$  is linked to the vertical wavelength, since  $\alpha_n/H$  is the vertical wavenumber:

$$\lambda_{z,n} = \frac{2\pi H}{\alpha_n} = \frac{2\pi H}{\sqrt{\frac{\kappa H}{h_n} - \frac{1}{4}}}. \quad (\text{A2.36})$$

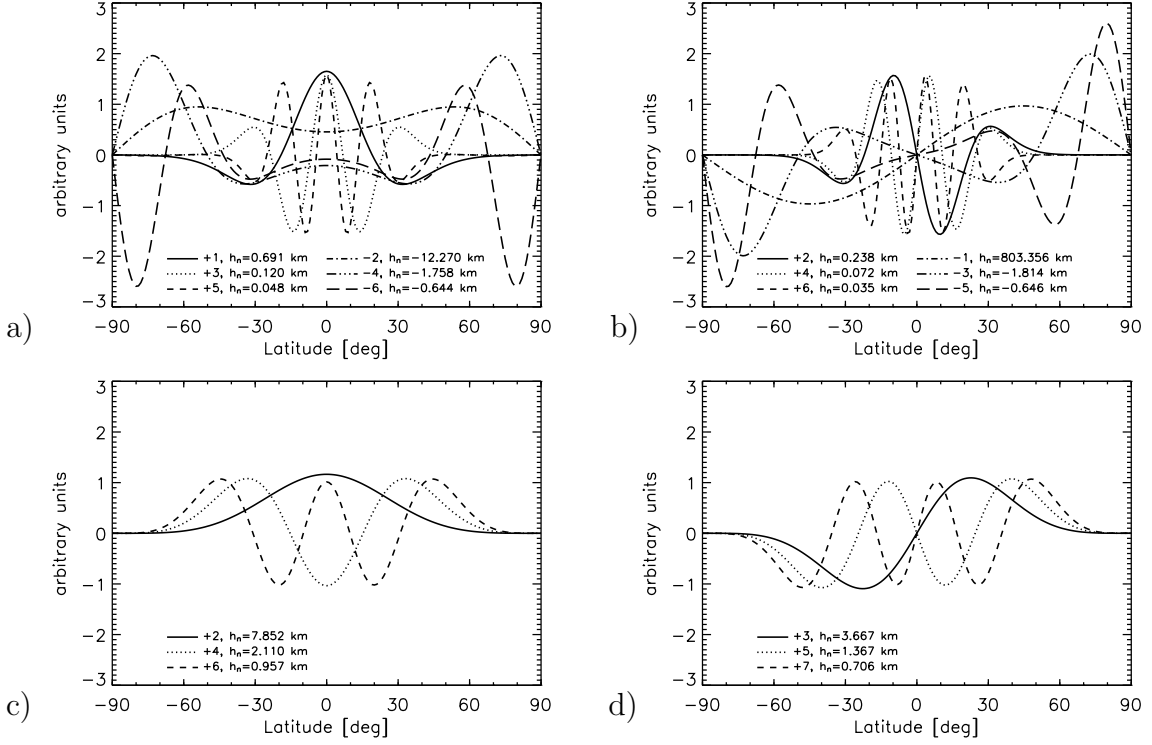


Figure A2.1: Hough functions for migrating tides and corresponding equivalent depths  $h_n$ . a) symmetric,  $s = 1$ , diurnal period. b) anti-symmetric,  $s = 1$ , diurnal. c) symmetric,  $s = 2$ , semidiurnal. d) anti-symmetric,  $s = 2$ , semidiurnal.

For propagating solutions ( $\alpha_n^2 > 0$ ), the vertical group velocity

$$c_{gz,n} = H \frac{\partial \sigma}{\partial \alpha_n} \quad (\text{A2.37})$$

becomes positive (upward energy propagation) only if  $\alpha_n > 0$  for westward ( $\sigma < 0$ ) or if  $\alpha_n < 0$  for eastward ( $\sigma > 0$ ) propagating waves (see *Forbes* [1995] for details). At a given height  $x = z/H$ , the wave maximizes for

$$K_n = s\lambda + \alpha_n x - \sigma t = 0. \quad (\text{A2.38})$$

For a fixed longitude  $\lambda$ , this in turn always results in downward phase progression as time progresses, independent of the propagation direction. This is an important result for the interpretation of observations: *downward phase progression in time means an upward propagation of energy and therefore a tidal forcing lower in the atmosphere*. According to Equations A2.31 and A2.35, amplitude increases with height  $\sim e^{z/2H}$ , as density decreases.

Figure A2.1 shows the first symmetric and anti-symmetric (with respect to the equator) tidal modes for the diurnal (top row) and semidiurnal (bottom row) migrating tide. An equivalent depth of  $h_n = 0.691$  km corresponds to a vertical wavelength of  $\lambda_z = 27.9$  km. The vertical wavelength increases with increasing (positive) equivalent depth. The wind expansion functions (Equations A2.25 and A2.26) are basically the meridional derivatives of  $\Theta_n$ . See *Forbes* [1995] for plots. As a general rule, propagating Hough functions maximize at low latitudes whereas trapped or evanescent modes maximize at middle to high latitudes.

### A3 Tidal component deconvolution

In the following, more details of the tidal component deconvolution outlined in *Oberheide et al.* [2002b] are given. From Equation 3.4 on page 22, one can immediately deduce an expression for the observed temperature difference using trigonometric transformations:

$$\begin{aligned}\Delta T &= \tilde{T}(t_{asc}) - \tilde{T}(t_{dsc}) \\ &= 2 \sum_{s,n} T_{s,n} \sin\left(\omega_n \frac{\Delta t}{2}\right) \sin\left(\omega_n(t_{asc} - t_{s,n}) + \omega_n \frac{\Delta t}{2} - (s+n)\lambda\right) \quad (\text{A3.1})\end{aligned}$$

with LSTs  $t_{asc}$  and  $t_{dsc}$  for the asc and dsc orbit nodes and  $\Delta t = t_{dsc} - t_{asc}$ . The background atmosphere, including PWs, is assumed to be the same for the asc and dsc measurements and thus vanishes in  $\Delta T$ . For diurnal frequency ( $n = 1$ ,  $\omega_1 = \pi/12$ ) and  $\Delta t = 12$  hours, Equation A3.1 simplifies to

$$\Delta T = 2 \sum_{s,1} T_{s,1} \sin\left(\frac{\pi}{12}(t_{asc} - t_{s,1}) + \frac{\pi}{2} - (s+1)\lambda\right). \quad (\text{A3.2})$$

According to Table 4.1, an observed zonal wavenumber  $s'$  is a superposition of real zonal wavenumbers  $s_1 = -s' - 1$  and  $s_2 = s' - 1$ . The fitted temperature difference  $\Delta T_{s'}$  (Figure 4.1, fit amplitude  $T_0(s')$ , fit phase  $\Phi_0(s')$ ) can thus be described as

$$\begin{aligned}\Delta T_{s'} &= 2T_{s_1,1} \cos\left(\frac{\pi}{12}(t_{asc} - t_{s_1,1}) - (s_1+1)\lambda\right) + \\ &\quad 2T_{s_2,1} \cos\left(\frac{\pi}{12}(t_{asc} - t_{s_2,1}) - (s_2+1)\lambda\right) \\ &= 2T_{-s'-1,1} \cos\left(\frac{\pi}{12}(t_{asc} - t_{-s'-1,1}) + s'\lambda\right) + \\ &\quad 2T_{s'-1,1} \cos\left(\frac{\pi}{12}(t_{asc} - t_{s'-1,1}) - s'\lambda\right) \\ &= 2T_0(s') \cos(s'\lambda - \Phi_0(s')) \quad (\text{A3.3})\end{aligned}$$

with

$$\begin{aligned}T_0^2(s') &= T_{-s'-1,1}^2 + T_{s'-1,1}^2 + 2T_{-s'-1,1}T_{s'-1,1} \cos(\Psi(s')) \quad (\text{A3.4}) \\ \Psi(s') &= \varphi_{-s'-1,1} - \varphi_{s'-1,1}\end{aligned}$$

$$\varphi_{-s'-1,1} = \frac{\pi}{2} + \frac{\pi}{12}(t_{asc} - t_{-s'-1,1}) \quad (\text{A3.5})$$

$$\varphi_{s'-1,1} = \frac{\pi}{2} - \frac{\pi}{12}(t_{asc} - t_{s'-1,1}) \quad (\text{A3.6})$$

and

$$\cot \Phi_0(s') = \frac{T_{-s'-1,1} \sin \varphi_{-s'-1,1} + T_{s'-1,1} \sin \varphi_{s'-1,1}}{T_{-s'-1,1} \cos \varphi_{-s'-1,1} + T_{s'-1,1} \cos \varphi_{s'-1,1}}. \quad (\text{A3.7})$$

Known parameters (from the fit to the data) are amplitude  $T_0(s')$  and phase  $\Phi_0(s')$ . They must be deconvolved into the tidal component amplitudes ( $T_{-s'-1,1}$ ,  $T_{s'-1,1}$ ) and phases ( $\varphi_{-s'-1,1}$ ,  $\varphi_{s'-1,1}$ ).

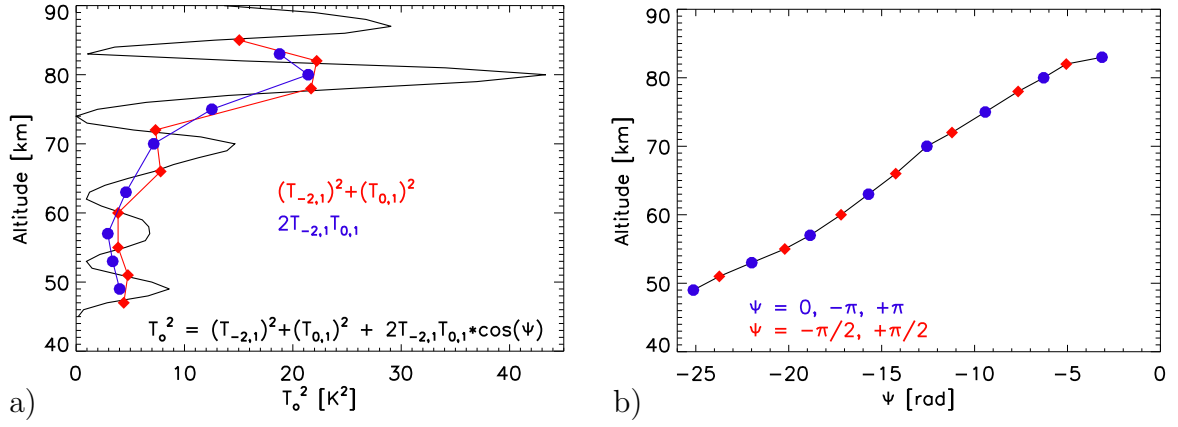


Figure A3.1: Principle of deconvolution for the  $s' = 1$  case and 9 November 1994 (CRISTA-1). a) Squared fit amplitude (black), its mean value (red) and the oscillation amplitude (blue) at altitudes below 90 km. Red and blue lines are from linear interpolation. b) Phase. See text for details.

Equation A3.4 describes an oscillation around the mean value  $\bar{T}^2(s')$  defined by

$$\bar{T}^2(s') = T_{-s'-1,1}^2 + T_{s'-1,1}^2 \quad (\text{A3.8})$$

with amplitude

$$A(s') = 2T_{-s'-1,1}T_{s'-1,1} \quad (\text{A3.9})$$

and phase  $\Psi(s')$ . The three parameters  $\bar{T}^2(s')$ ,  $A(s')$ , and  $\Psi(s')$  are deduced from the squared fit amplitude  $T_0^2(s')$ :

At altitudes  $z_0$  with  $\Psi(s') = \pm\pi/2$ , the cosine term in Equation A3.4 vanishes and  $T_0^2(s') = \bar{T}^2(s')$ . The altitudes  $z_0$  are in good approximation the altitudes where the oscillating amplitude  $T_0^2(s')$  equals the average value of the next minimum and maximum amplitudes at the altitudes above and below. Figure A3.1a shows this for the  $s' = 1$  case in the stratosphere and mesosphere (red diamonds). The complete height profile of  $\bar{T}^2(s')$  is then calculated by linear interpolation (red line). At maxima/minima levels  $z_m$  of  $T_0^2(s')$ , the cosine term in Equation A3.4 is in good approximation  $\pm 1$  ( $\Psi(s') = 0, \pm\pi$ ) and  $A(s', z_m) = T_0^2(s', z_m) \mp \bar{T}^2(s', z_m)$  can easily be calculated (blue circles in Figure A3.1). Again, the height profile of  $A(s')$  is computed by linear interpolation (blue line).

Equation A3.4 also defines the phase  $\Psi(s')$  except for its sign because the cosine function is even. The sign is chosen as shown in Figure A3.1b. Tidal forcing usually occurs in the lower atmosphere with the tides propagating up and away from their source region. Upward propagation implies that the phases of the two components to be deconvolved decrease with height

$$\frac{\partial t_{-s'-1,1}}{\partial z} \leq 0$$

$$\frac{\partial t_{s'-1,1}}{\partial z} \leq 0.$$

With that, Equation A3.4 yields

$$\frac{\partial \Psi(s')}{\partial z} \geq 0 \quad (\text{A3.10})$$

which defines the slope of  $\Psi(s')$  and therefore the sign. Note the  $2\pi$ -periodicity of  $\Psi(s')$ . Assuming tidal forcing in the lower atmosphere, although reasonable, nevertheless puts an important constraint to the deconvolution: *the derived amplitudes and phases are only valid for upward propagating tides.*

The deconvolution method inherently assumes reasonably small vertical gradients  $\partial T_{-s'-1,1}/\partial z$  and  $\partial T_{s'-1,1}/\partial z$ . No large amplitude oscillations with height of a specific tidal component are allowed:  $A(s')$  and  $\bar{T}^2(s')$  are exact for constant tidal amplitudes only. More realistic vertical gradients introduce an uncertainty in the altitudes  $z_0$  and  $z_m$  where the cosine function in Equation A3.4 equals 0 or  $\pm 1$ . This uncertainty, combined with the necessary linear interpolations, cause an error in  $A(s')$  and  $\bar{T}^2(s')$ . The effects of neglecting vertical gradients on the derived tidal amplitudes can be estimated from the classical tidal theory where the vertical amplitude increase is  $\sim \exp(z/2H)$  with scale height  $H$  ( $\sim 8$  km). The resulting height uncertainties in  $z_m$  and  $z_0$  are about 1 km and the corresponding tidal amplitude errors are  $\sim 10\%$ . This is consistent with the quantitative error estimates shown in section 4 (Table 4.2).

With  $\bar{T}^2(s')$ ,  $A(s')$ , and  $\Psi(s')$  determined, Equations A3.8 and A3.9 can be solved for the squared tidal component amplitudes:

$$T_{-s'-1,1}^2 = \frac{\bar{T}^2(s')}{2} \pm \frac{1}{2} \sqrt{\bar{T}^4(s') - A^2(s')} \quad (\text{A3.11})$$

$$T_{s'-1,1}^2 = \frac{A^2(s')}{4T_{-s'-1,1}^2(s')} \quad (\text{A3.12})$$

with the positive sign in Equation A3.11 for  $T_{-s'-1,1} \geq T_{s'-1,1}$  and with negative sign for  $T_{-s'-1,1} < T_{s'-1,1}$ . The relative magnitude (fraction) of both amplitudes is not yet known. Its further calculation requires to derive the phases first.

As a first step, it is helpful to rewrite Equation A3.7. Substitution of  $\varphi_{s'-1,1} = \varphi_{-s'-1,1} - \Psi(s')$  (Equation A3.4) and additional trigonometric transformations yield

$$\begin{aligned} \cot \Phi_0(s') &= \\ &= \frac{T_{-s'-1,1} \sin \varphi_{-s'-1,1} + T_{s'-1,1} \sin \varphi_{-s'-1,1} \cos \Psi(s') - T_{s'-1,1} \cos \varphi_{-s'-1,1} \sin \Psi(s')}{T_{-s'-1,1} \cos \varphi_{-s'-1,1} + T_{s'-1,1} \cos \varphi_{-s'-1,1} \cos \Psi(s') + T_{s'-1,1} \sin \varphi_{-s'-1,1} \sin \Psi(s')} \\ &= \frac{(T_{-s'-1,1} + T_{s'-1,1} \cos \Psi(s')) \sin \varphi_{-s'-1,1} - T_{s'-1,1} \sin \Psi(s') \cos \varphi_{-s'-1,1}}{(T_{-s'-1,1} + T_{s'-1,1} \cos \Psi(s')) \cos \varphi_{-s'-1,1} \left( 1 + \frac{T_{s'-1,1} \sin \Psi(s')}{T_{-s'-1,1} + T_{s'-1,1} \cos \Psi(s')} \tan \varphi_{-s'-1,1} \right)} \\ &= \frac{\tan \varphi_{-s'-1,1} - \frac{T_{s'-1,1} \sin \Psi(s')}{T_{-s'-1,1} + T_{s'-1,1} \cos \Psi(s')}}{1 + \frac{T_{s'-1,1} \sin \Psi(s')}{T_{-s'-1,1} + T_{s'-1,1} \cos \Psi(s')} \tan \varphi_{-s'-1,1}} \\ &= \frac{\alpha - \beta}{1 + \alpha\beta} \end{aligned} \quad (\text{A3.13})$$

with

$$\begin{aligned} \alpha &= \tan \varphi_{-s'-1,1}, \\ \beta &= \frac{\gamma}{\delta}, \\ \gamma &= T_{s'-1,1} \sin \Psi(s') \\ \delta &= T_{-s'-1,1} + T_{s'-1,1} \cos \Psi(s'). \end{aligned}$$

Further substitution of

$$\chi = \arctan \beta + \begin{cases} 0 & : \delta \geq 0 \\ \pi & : \delta < 0 \end{cases}$$

such that  $\chi$  has  $2\pi$ -periodicity (as  $\Phi_0(s')$ ,  $\varphi_{-s'-1,1}$  and  $\Psi(s')$  do) results in

$$\cot \Phi_0(s') = \frac{\tan \varphi_{-s'-1,1} - \tan \chi}{1 + \tan \varphi_{-s'-1,1} \tan \chi} = \tan (\varphi_{-s'-1,1} - \chi) \quad (\text{A3.14})$$

and finally in

$$\Phi_0(s') = \frac{\pi}{2} - \varphi_{-s'-1,1} + \arctan \beta + \begin{cases} 0 & : \delta \geq 0 \\ \pi & : \delta < 0 \end{cases} \quad (\text{A3.15})$$

that satisfies Equation A3.3. Equation A3.15 relates the known phases  $\Phi_0(s')$ ,  $\Psi(s')$ , the unknown tidal component amplitude fraction (Equations A3.11, A3.12) and the tidal component phases. It is now solved at altitudes  $z_m$  (blue circles, Figure A3.1) and  $z_0$  (red diamonds).

*Maxima:*  $z = z_m$ ,  $\Psi(s') = 0$

In this case,  $\beta = 0$  and  $\delta \geq 0$ . Equation A3.15 yields

$$\Phi_0(s') = \frac{\pi}{2} - \varphi_{-s'-1,1}$$

which immediately (Equations A3.5, A3.6) leads to the tidal phases (in hours):

$$t_{-s'-1,1} = t_{asc} + \frac{12}{\pi} \Phi_0(s'), \quad (\text{A3.16})$$

$$t_{s'-1,1} = 2t_{asc} - t_{-s'-1,1}. \quad (\text{A3.17})$$

*Minima:*  $z = z_m$ ,  $\Psi(s') = \pm\pi$

In this case,  $\beta = 0$  and Equation A3.15 yields

$$\Phi_0(s') = \frac{\pi}{2} - \varphi_{-s'-1,1} + \begin{cases} 0 & : T_{-s'-1,1} \geq T_{s'-1,1} (\equiv \delta \geq 0) \\ \pi & : T_{-s'-1,1} < T_{s'-1,1} (\equiv \delta < 0) \end{cases},$$

resulting in the tidal phases (in hours):

$$t_{-s'-1,1} = t_{asc} + \frac{12}{\pi} \Phi_0(s') + \begin{cases} 0 & : T_{-s'-1,1} \geq T_{s'-1,1} \\ 12 & : T_{-s'-1,1} < T_{s'-1,1} \end{cases}, \quad (\text{A3.18})$$

$$t_{s'-1,1} = 2t_{asc} - t_{-s'-1,1} + 12. \quad (\text{A3.19})$$

*Intermediate:*  $z = z_0$ ,  $\Psi(s') = \pm\frac{\pi}{2}$

In this case,  $\beta = \pm T_{s'-1,1}/T_{-s'-1,1}$  and  $\delta \geq 0$ . Equation A3.15 yields

$$\Phi_0(s') = \frac{\pi}{2} - \varphi_{-s'-1,1} \pm \arctan \left( \frac{T_{s'-1,1}}{T_{-s'-1,1}} \right)$$

and tidal phases (in hours):

$$t_{-s'-1,1} = t_{asc} + \frac{12}{\pi} \Phi_0(s') + \begin{cases} -\frac{12}{\pi} \arctan \frac{T_{s'-1,1}}{T_{-s'-1,1}} & : \Psi(s') = +\frac{\pi}{2} \\ +\frac{12}{\pi} \arctan \frac{T_{s'-1,1}}{T_{-s'-1,1}} & : \Psi(s') = -\frac{\pi}{2} \end{cases}, \quad (\text{A3.20})$$

$$t_{s'-1,1} = 2t_{asc} - t_{-s'-1,1} + \begin{cases} -6 & : \Psi(s') = +\frac{\pi}{2} \\ +6 & : \Psi(s') = -\frac{\pi}{2} \end{cases}. \quad (\text{A3.21})$$

The phases still depend on the  $T_{s'-1,1}/T_{-s'-1,1}$  fraction at altitudes with  $\Psi(s') = \pm\pi$  (Equation A3.18) and  $\Psi(s') = \pm\pi/2$  (Equation A3.20), but they are known at altitudes with  $\Psi(s') = 0$  (Equation A3.16). Assuming that the (decreasing) tidal phases are about linear between consecutive altitudes with  $\Psi(s') = 0$ , the minimum deviation from linearity of the phases in Equations A3.18 - A3.21 gives the information whether  $T_{-s'-1,1} \geq T_{s'-1,1}$  or  $T_{-s'-1,1} < T_{s'-1,1}$  applies at altitudes in between. This becomes particularly clear for  $z = z_m$  with  $\Psi(s') = \pm\pi$ , owing to the 12 hour phase difference between both cases (Equation A3.18). If  $T_{-s'-1,1}$  and  $T_{s'-1,1}$  are close together, this approach may fail to produce unambiguous results at altitudes  $z = z_0$  (Equation A3.20), but the tidal amplitude and phase errors introduced by that are well within the error bars discussed in section 4.1.2 (Table 4.2). With the phases determined and the amplitude fraction known, Equations A3.11 and A3.12 immediately provide the amplitudes except for altitudes  $z = z_m$  with  $\Psi(s') = 0$ . They are interpolated from altitudes below and above.

## A4 TIDI climatologies: diurnal

The plots of the TIDI diurnal nonmigrating tidal climatologies appear in the order they have been discussed in section 4.3.3. Amplitudes are given in m/s and phases as Universal time (in hours) of maximum amplitude at  $0^\circ$  longitude.

w2, meridional: Figure A4.1

s0, meridional: Figure A4.2

e2, meridional: Figure A4.3

e3, meridional: Figure A4.4

w2, zonal: Figure A4.5

s0, zonal: Figure A4.6

e2, zonal: Figure A4.7

e3, zonal: Figure A4.8

w4, meridional: Figure A4.9

w3, meridional: Figure A4.10

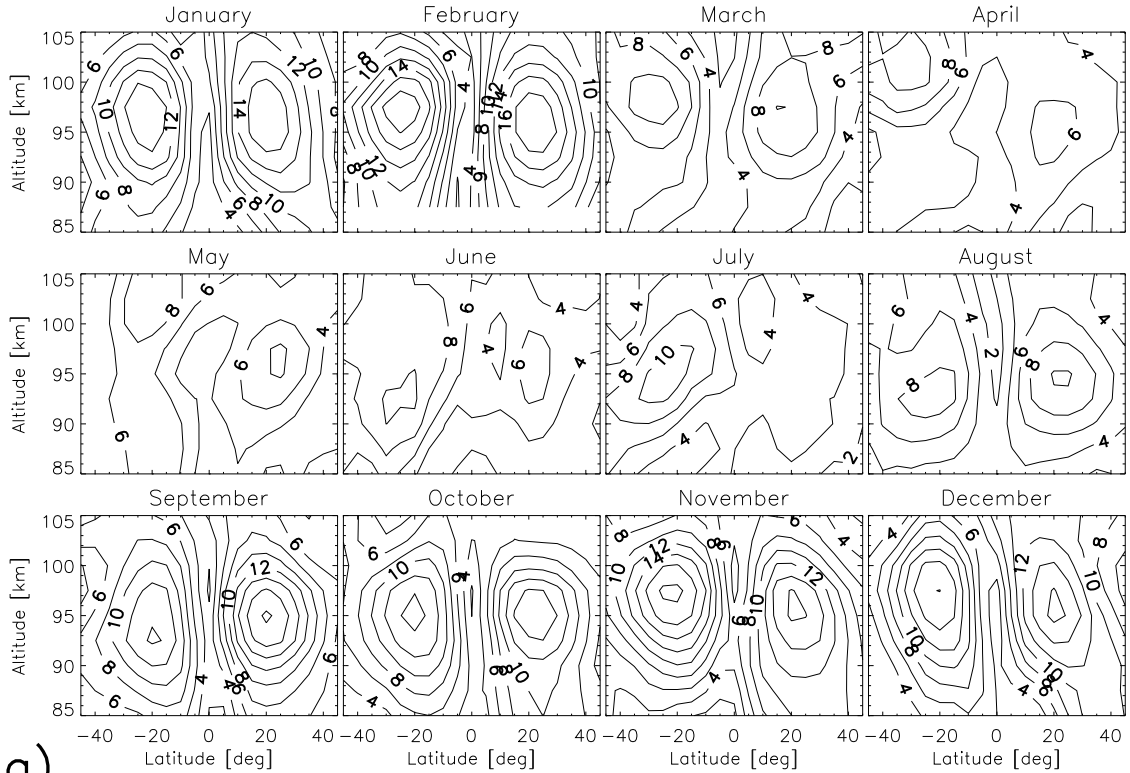
e1, meridional: Figure A4.11

w4, zonal: Figure A4.12

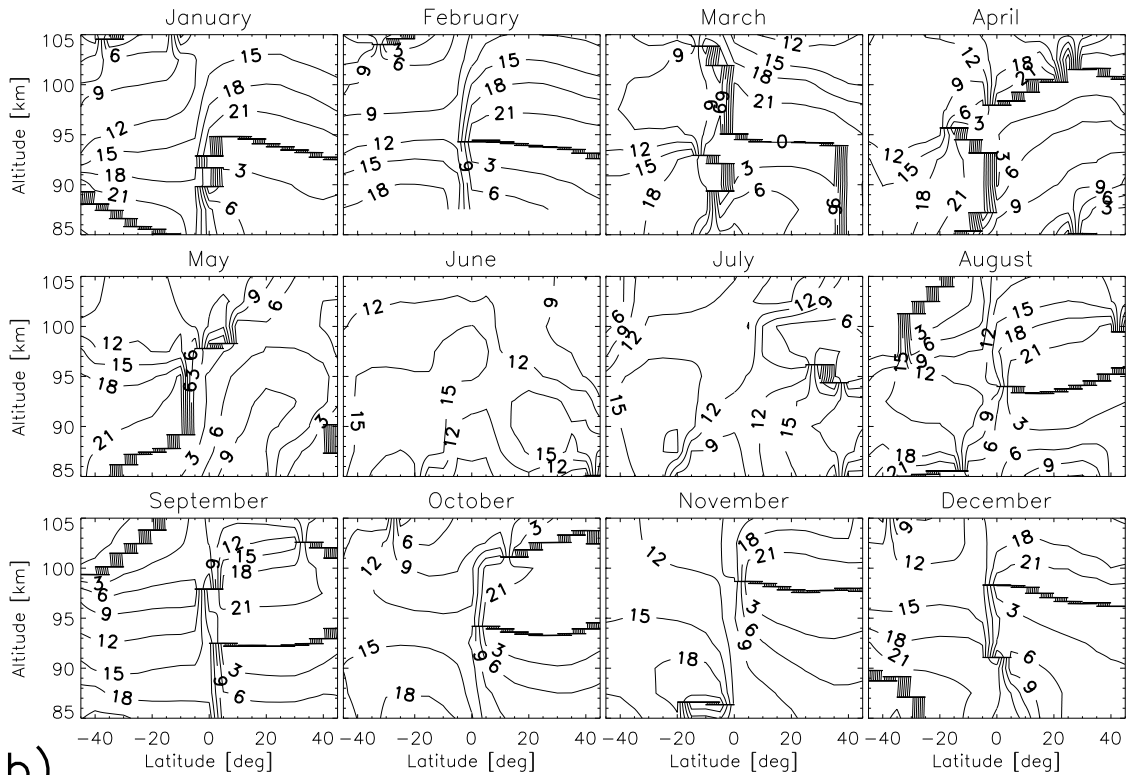
w3, zonal: Figure A4.13

e1, zonal: Figure A4.14

# w2 meridional



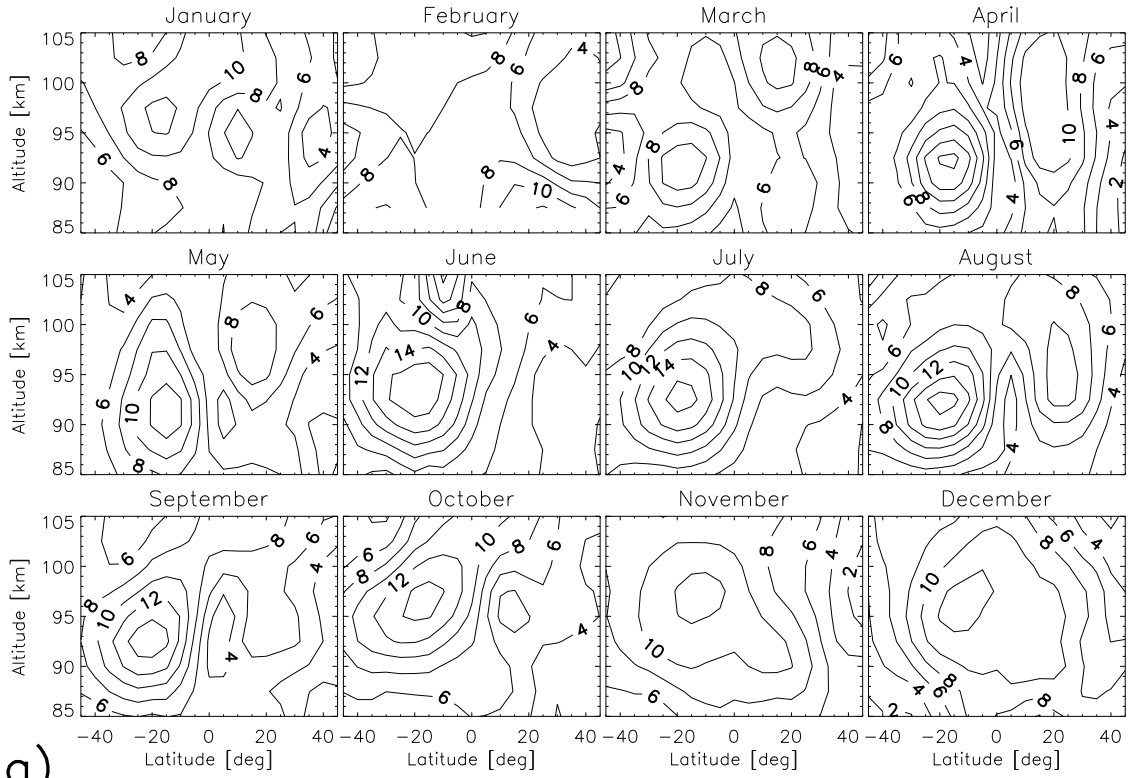
a)



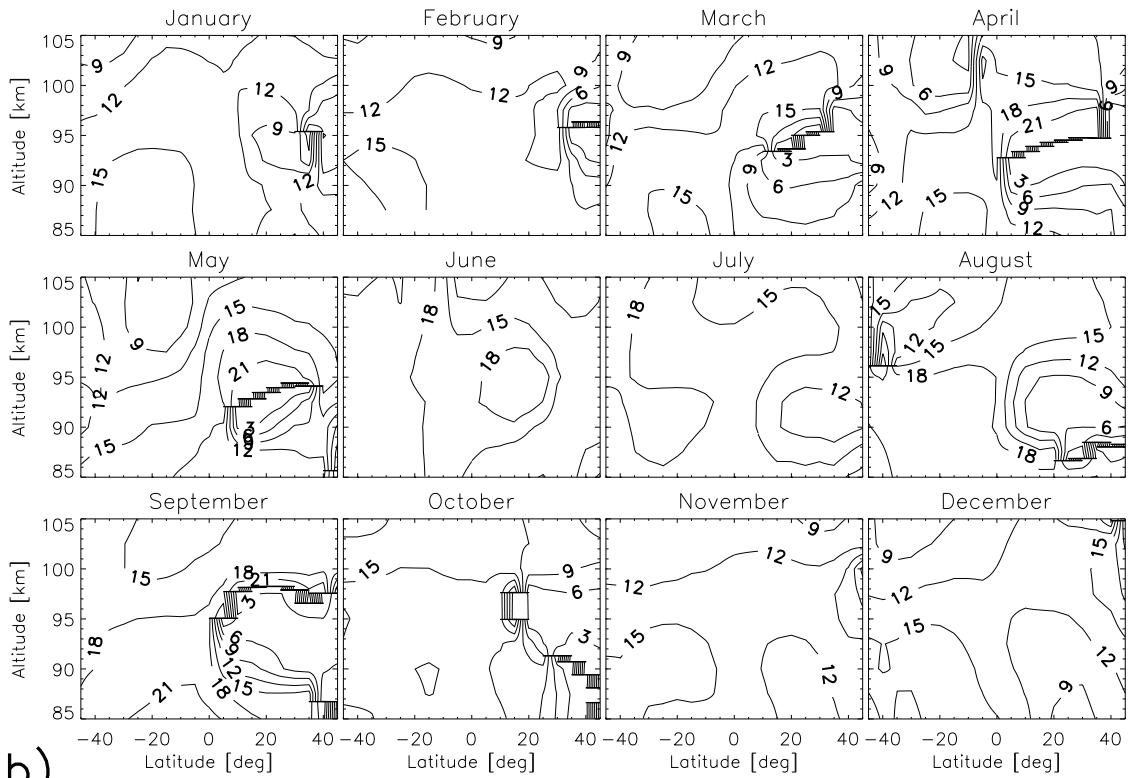
b)

Figure A4.1: a) Monthly mean diurnal amplitudes (m/s) and b) phases (Universal time of maximum amplitude at 0° longitude) for w2 meridional wind. Multiple phase contours adjacent to each other indicate the transition from 0 to 24 hours.

# s0 meridional



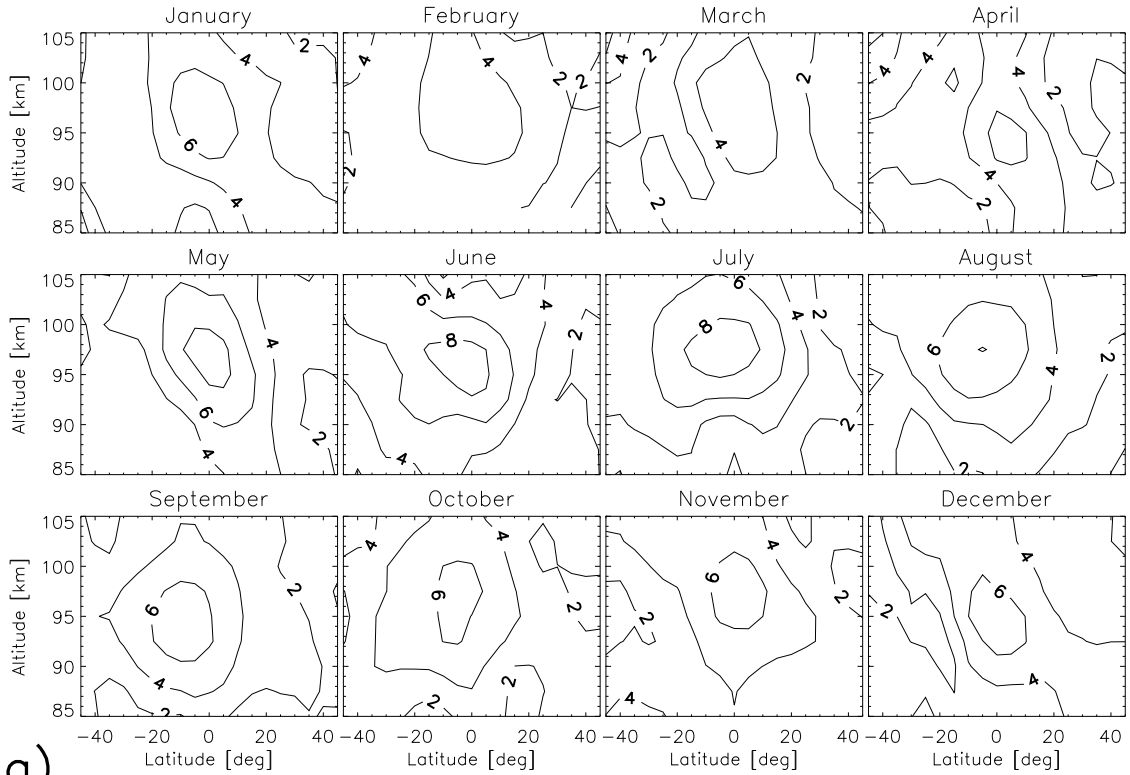
a)



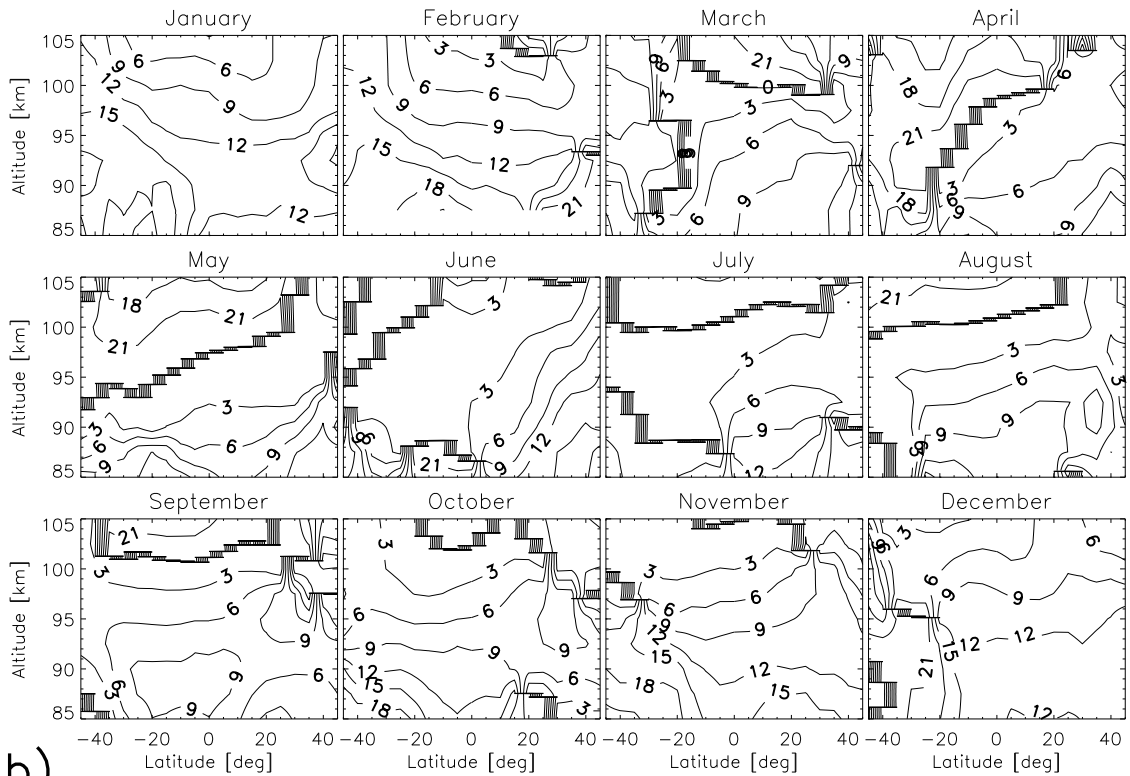
b)

Figure A4.2: As Figure A4.1, but for s0 meridional wind.

## e2 meridional



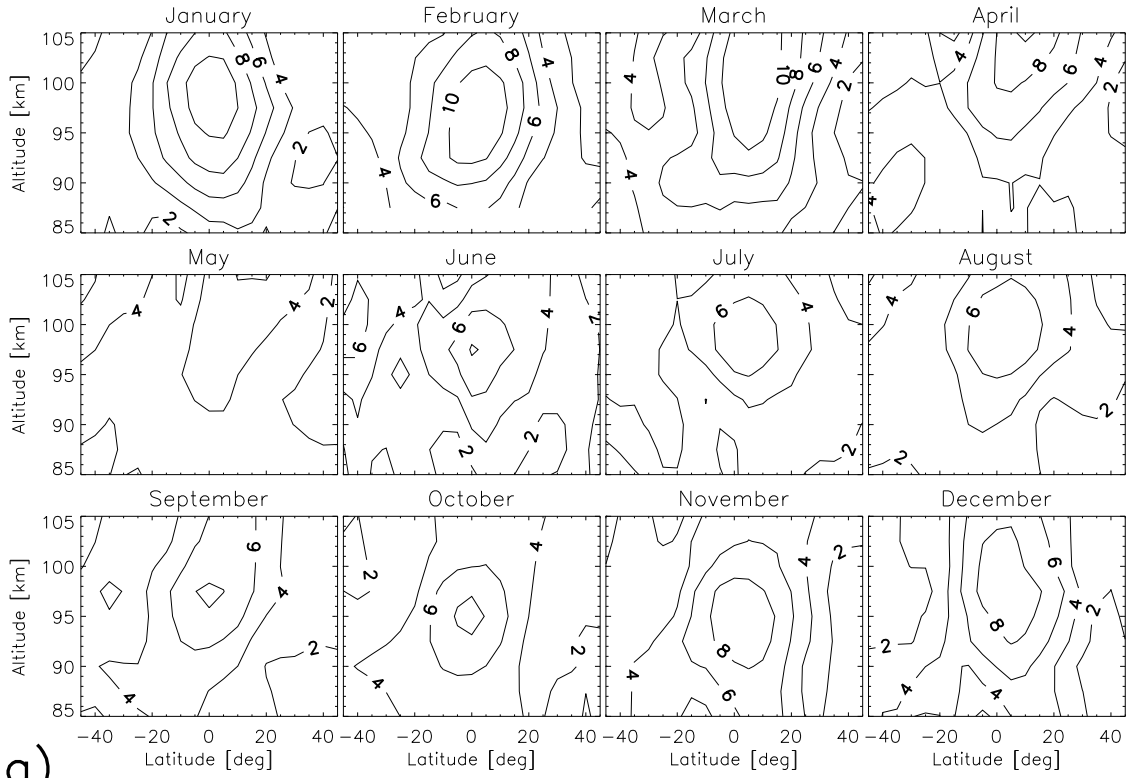
a)



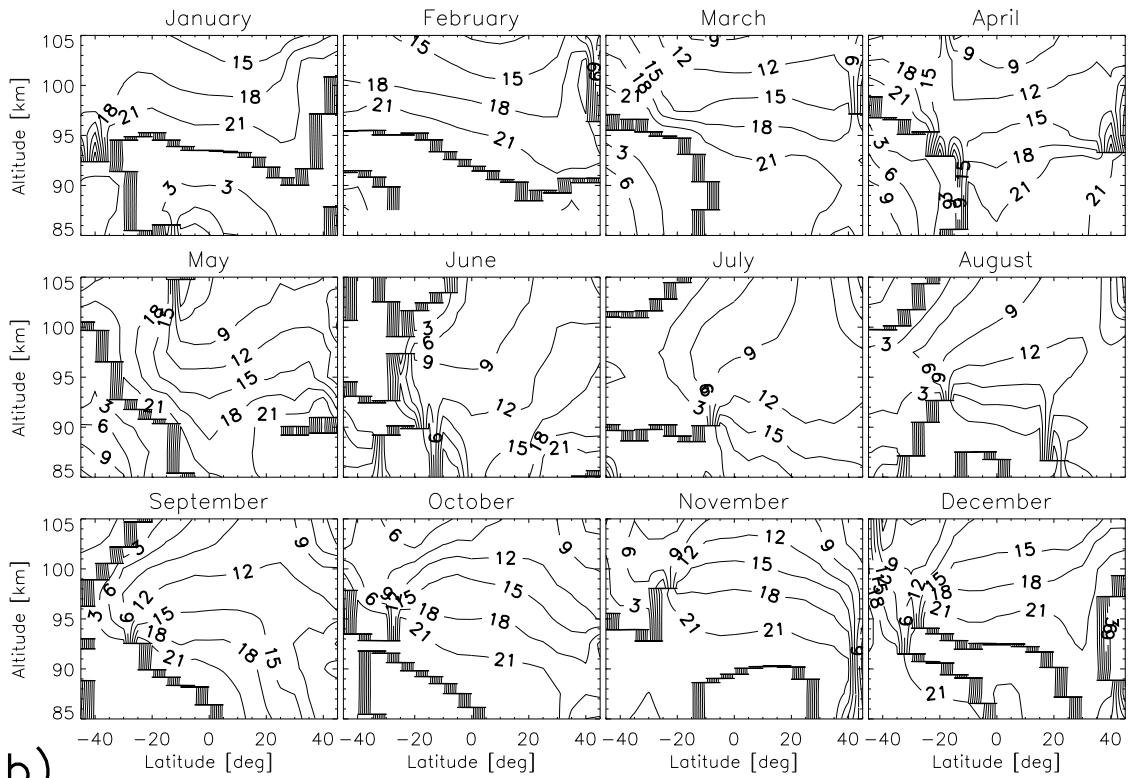
b)

Figure A4.3: As Figure A4.1, but for e2 meridional wind.

### e3 meridional



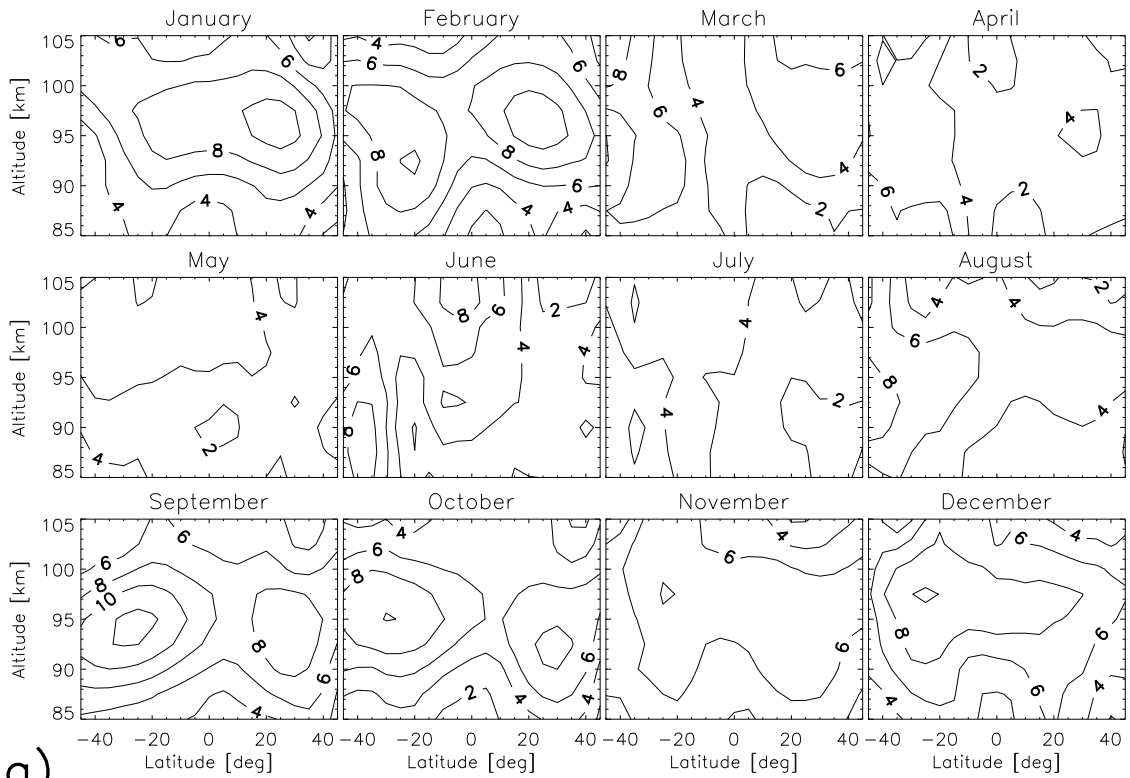
a)



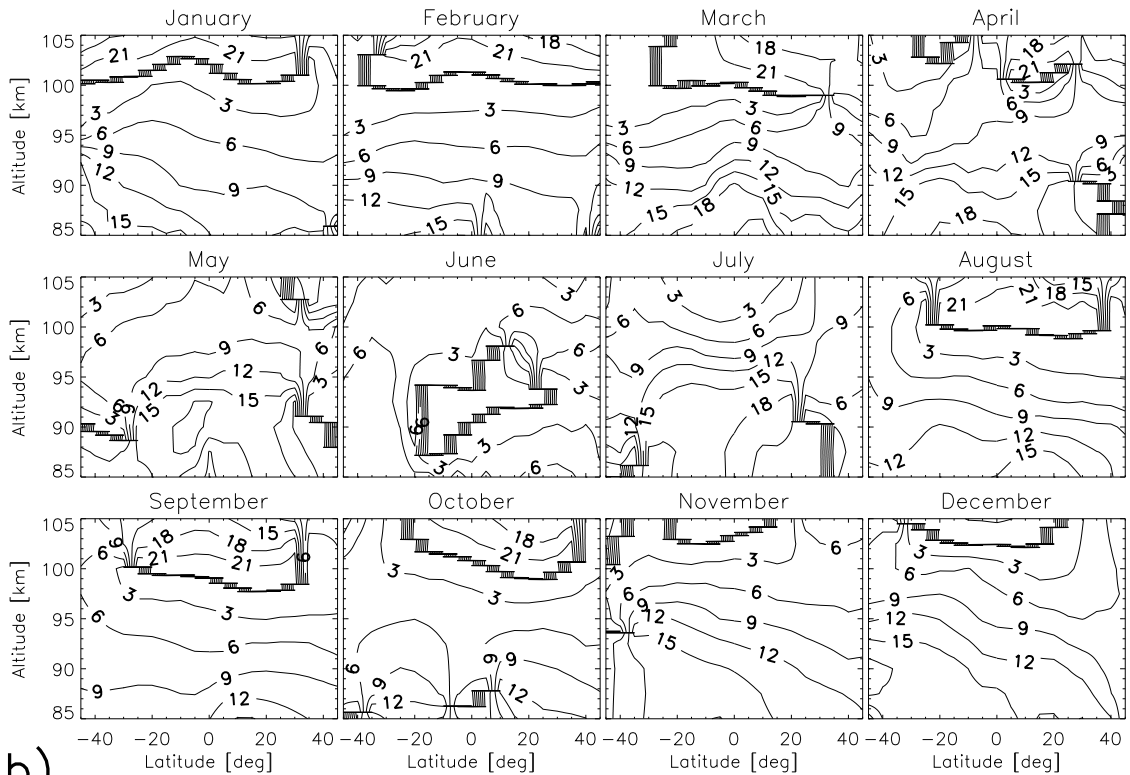
b)

Figure A4.4: As Figure A4.1, but for e3 meridional wind.

## w2 zonal



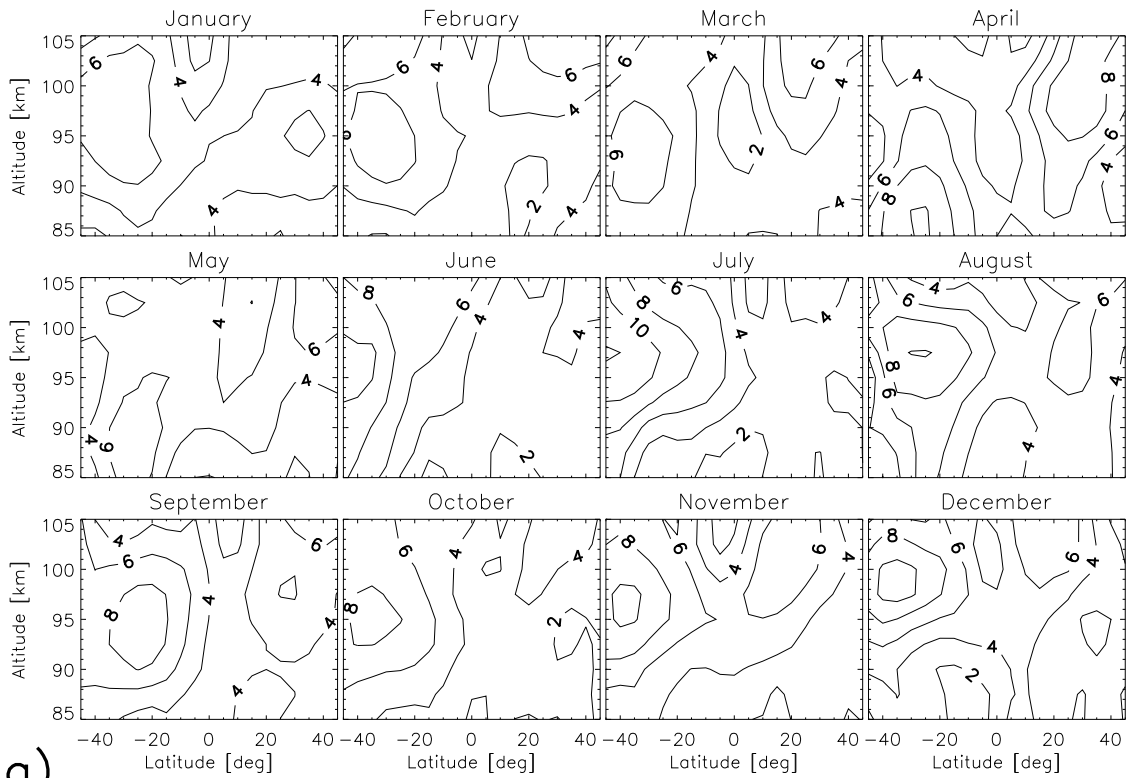
a)



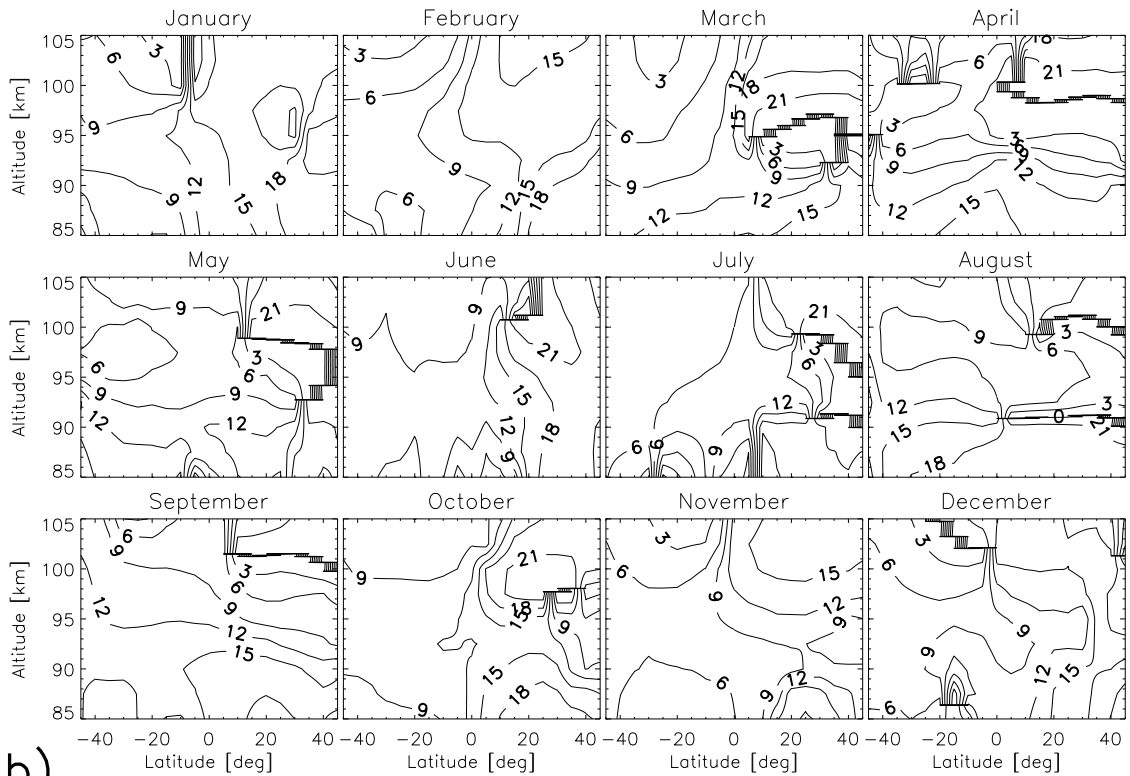
b)

Figure A4.5: a) Monthly mean diurnal amplitudes (m/s) and b) phases (Universal time of maximum amplitude at 0° longitude) for w2 zonal wind.

# s0 zonal



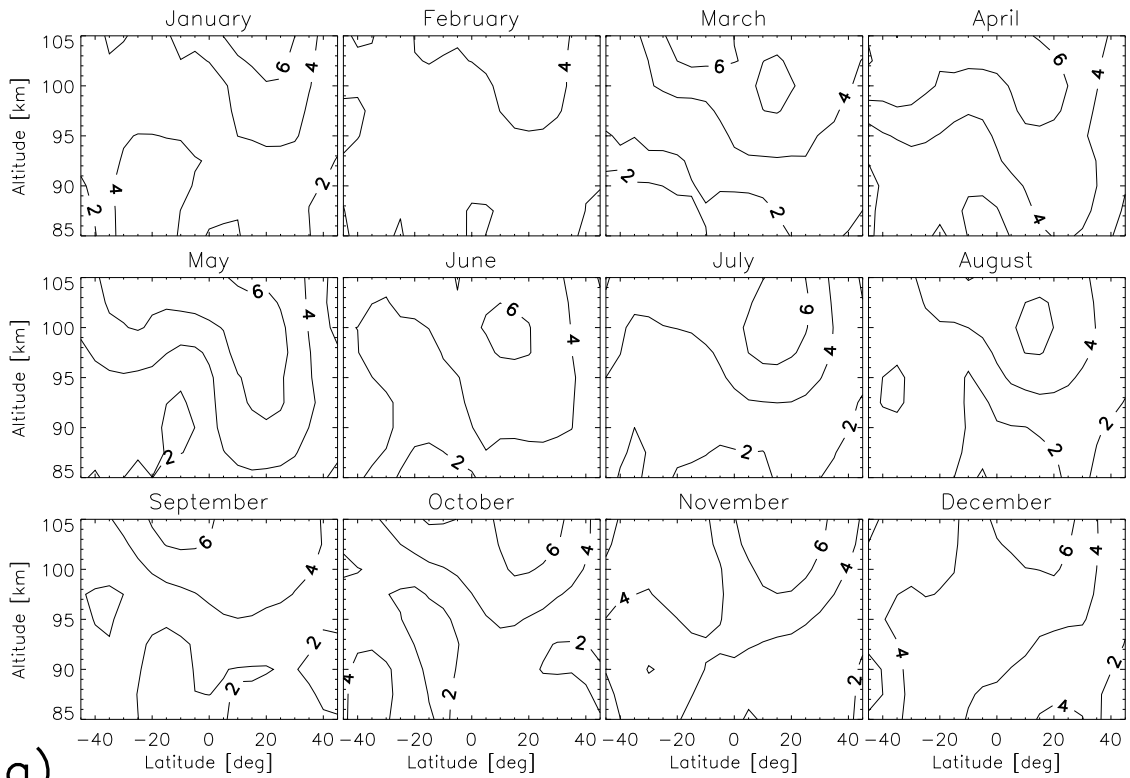
a)



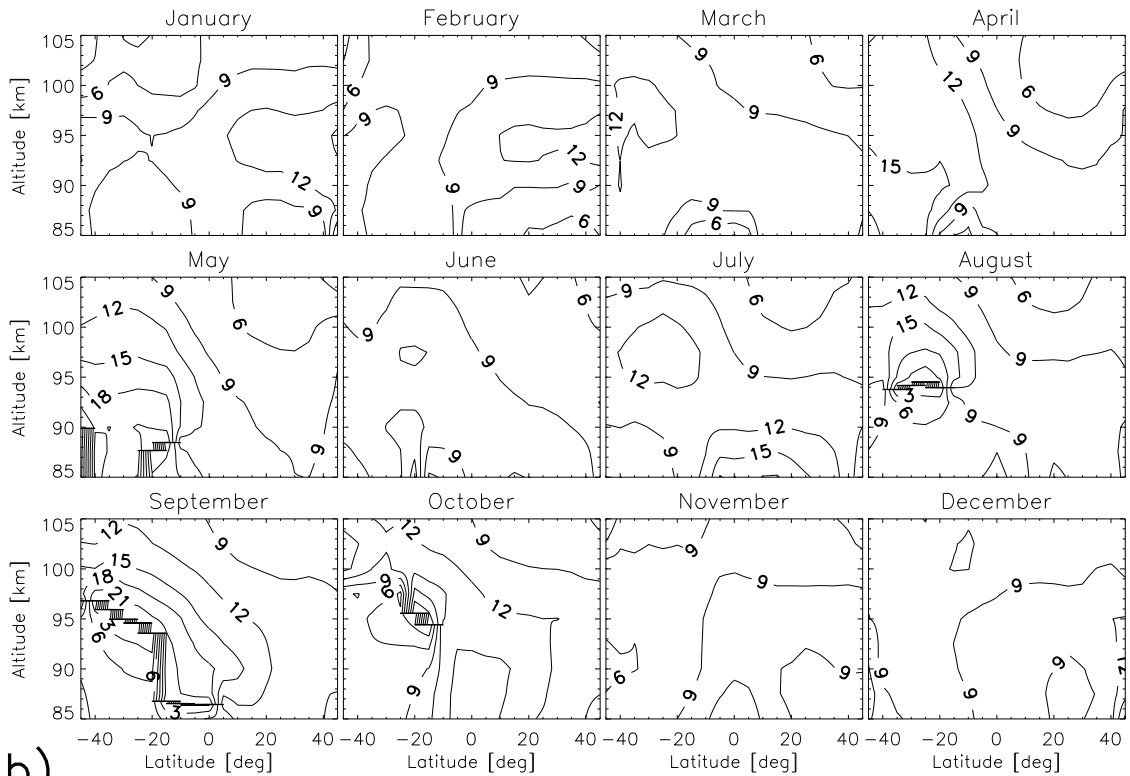
b)

Figure A4.6: As Figure A4.5, but for s0 zonal wind.

## e2 zonal



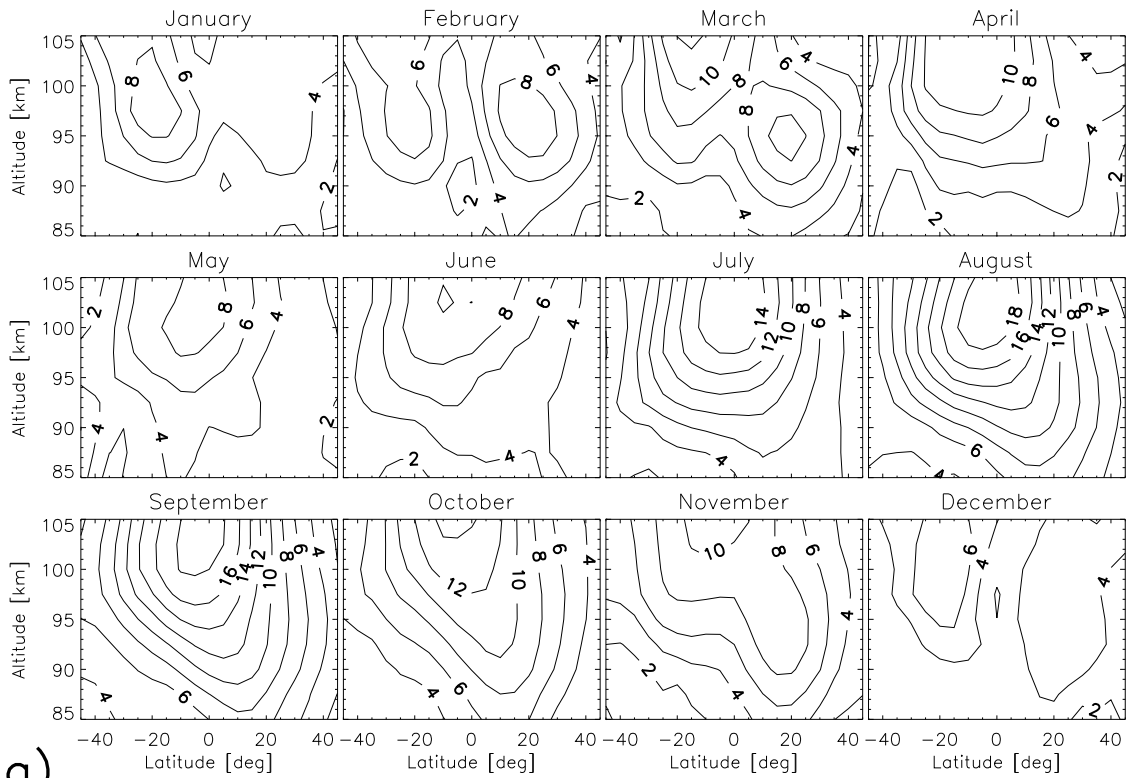
a)



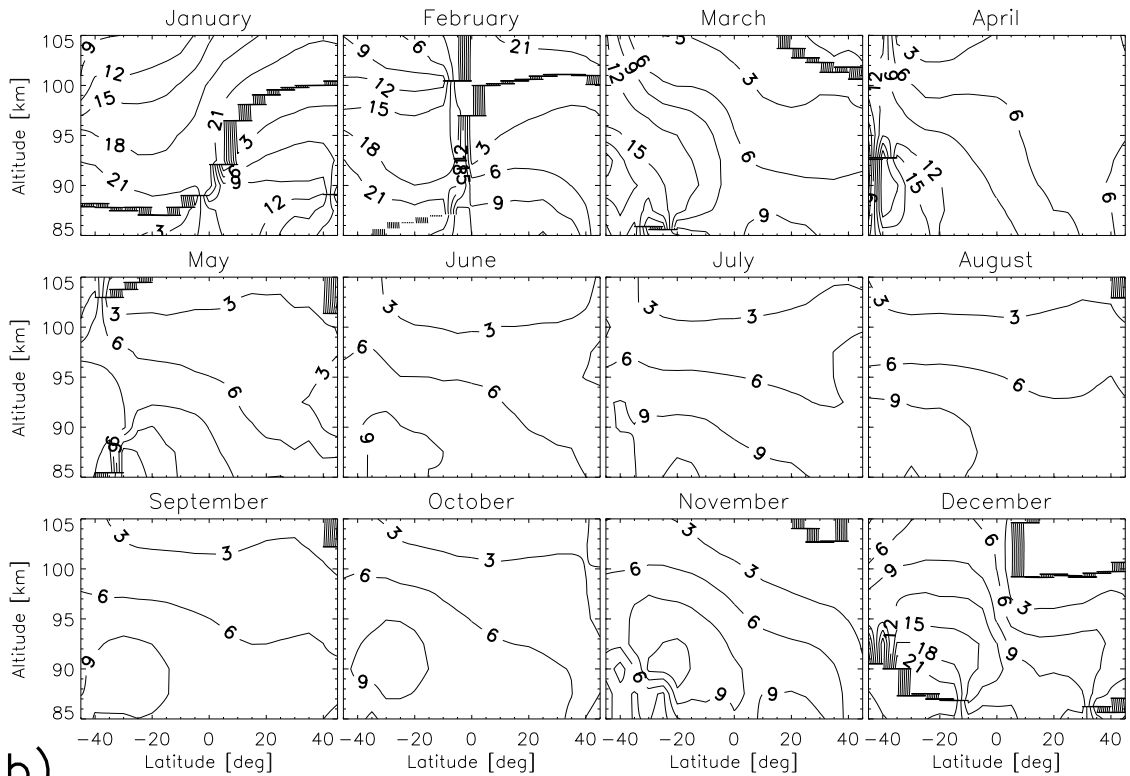
b)

Figure A4.7: As Figure A4.5, but for e2 zonal wind.

### e3 zonal



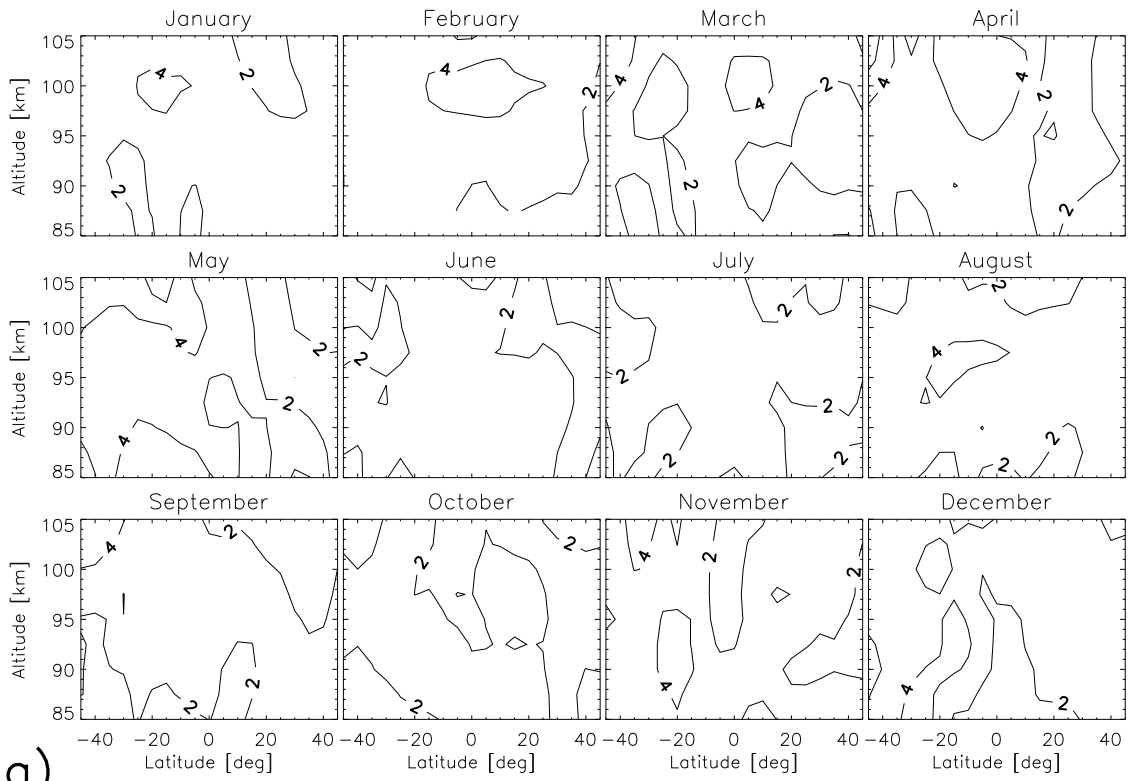
a)



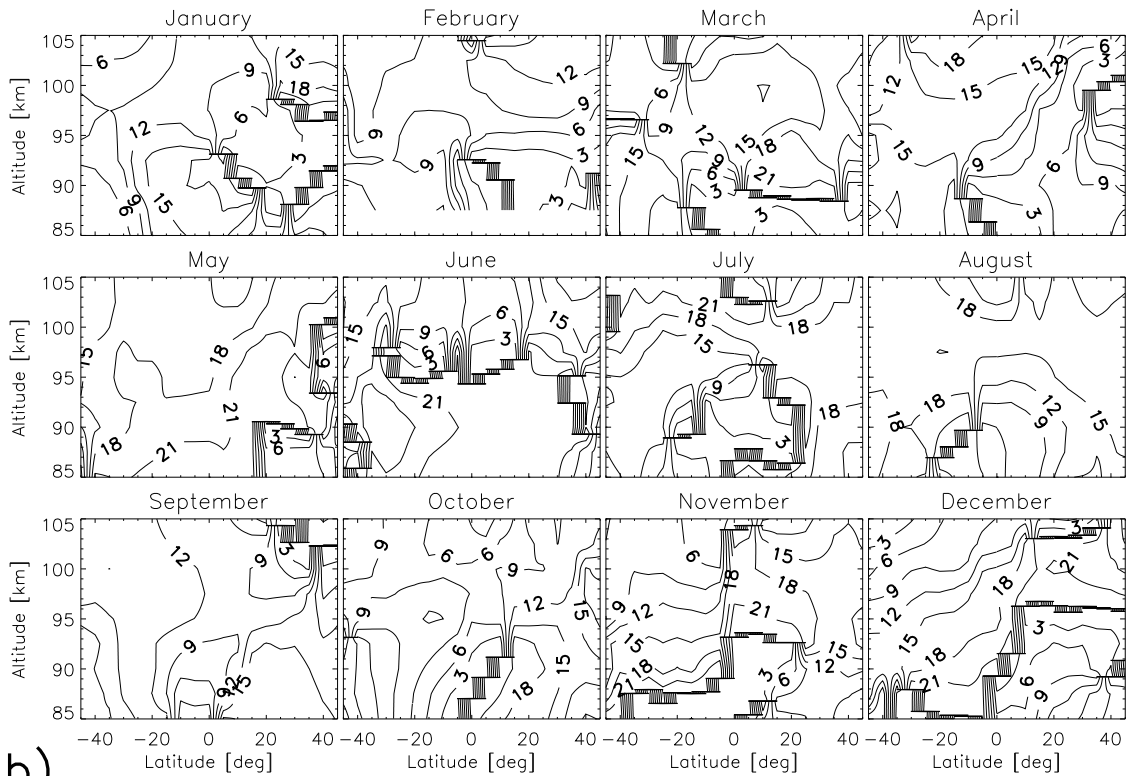
b)

Figure A4.8: As Figure A4.5, but for e3 zonal wind.

# w4 meridional



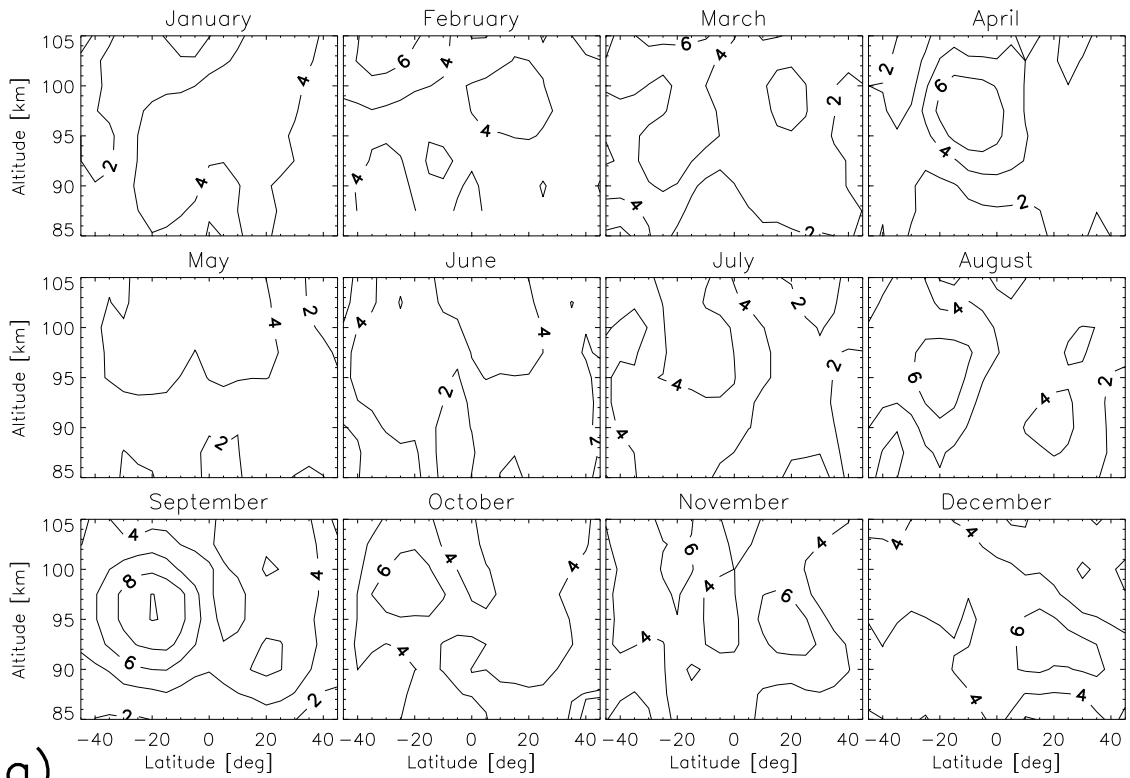
a)



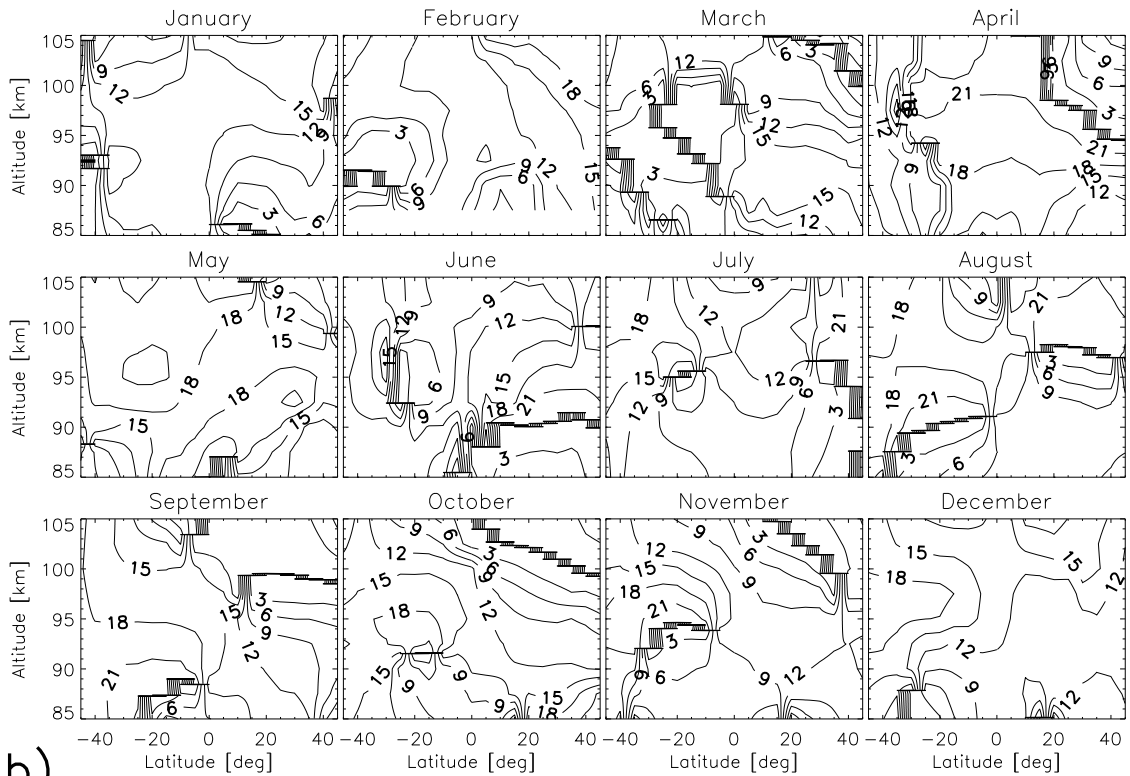
b)

Figure A4.9: As Figure A4.1, but for w4 meridional wind.

### w3 meridional



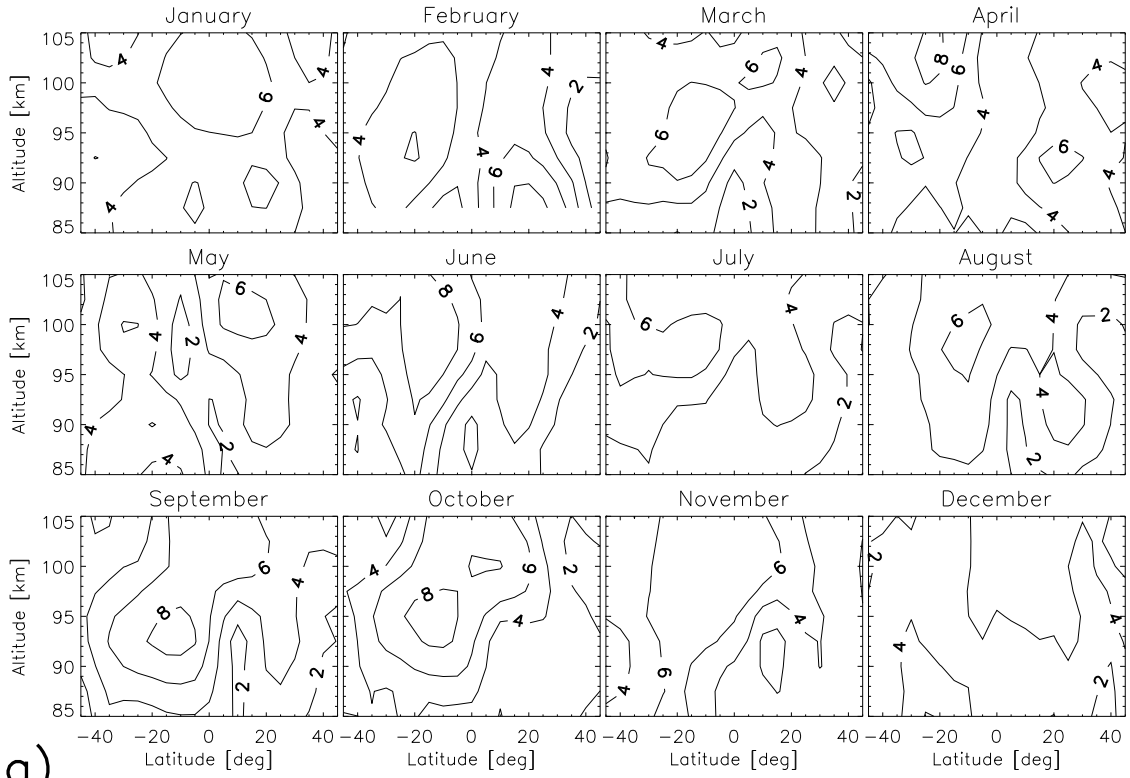
a)



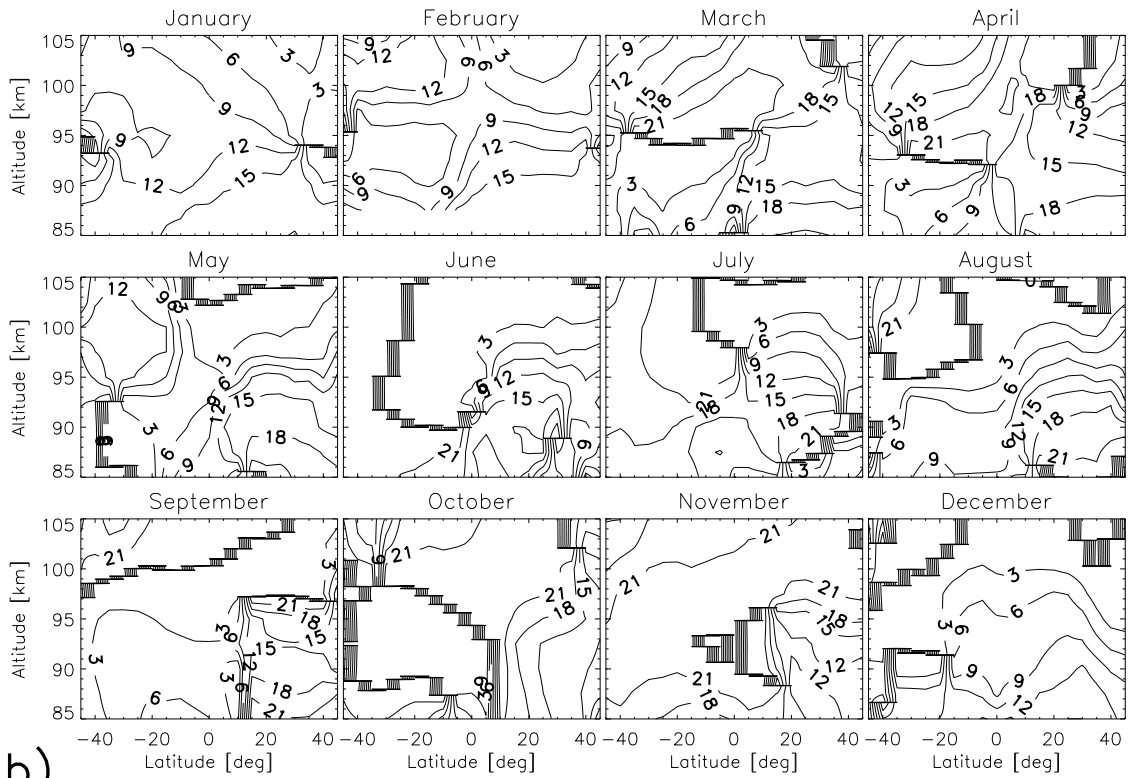
b)

Figure A4.10: As Figure A4.1, but for w3 meridional wind.

# e1 meridional



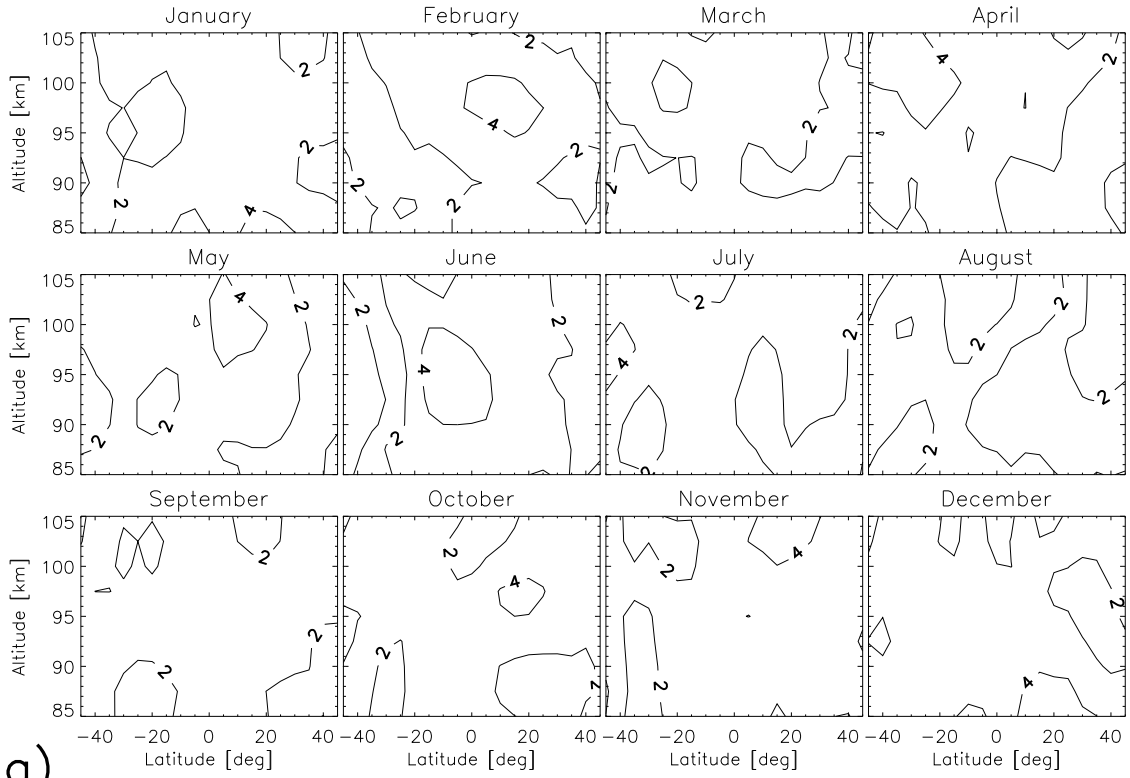
a)



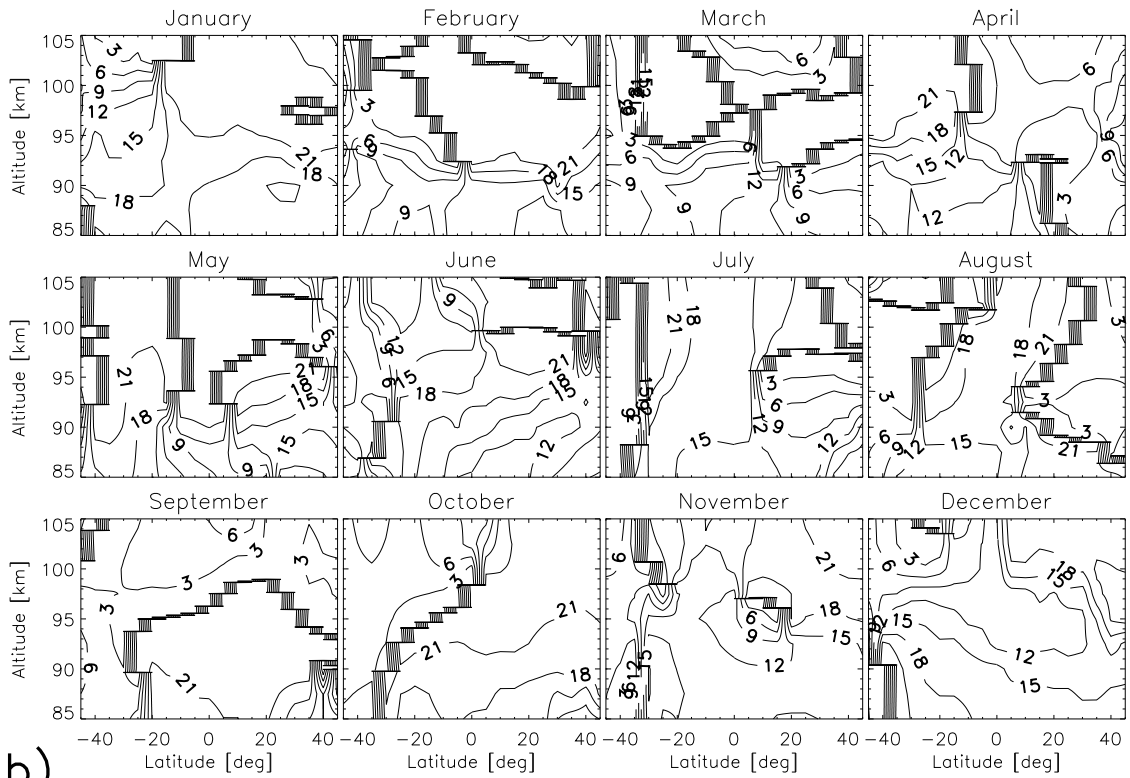
b)

Figure A4.11: As Figure A4.1, but for e1 meridional wind.

# w4 zonal



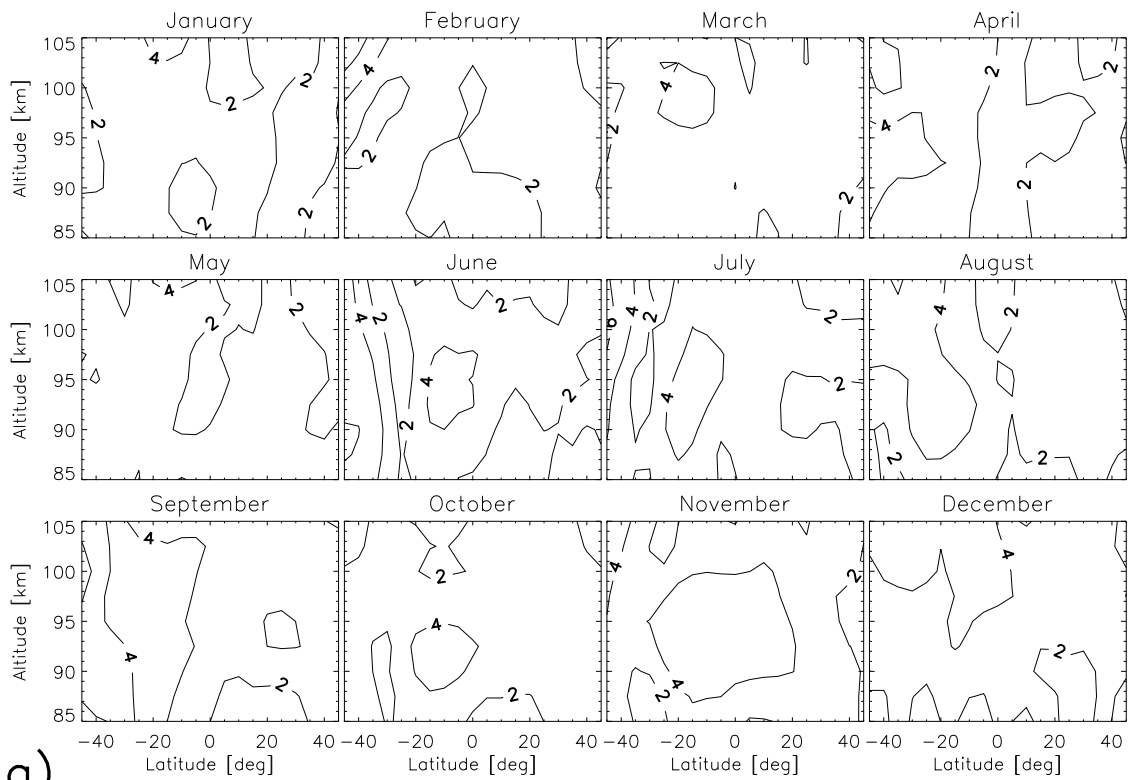
a)



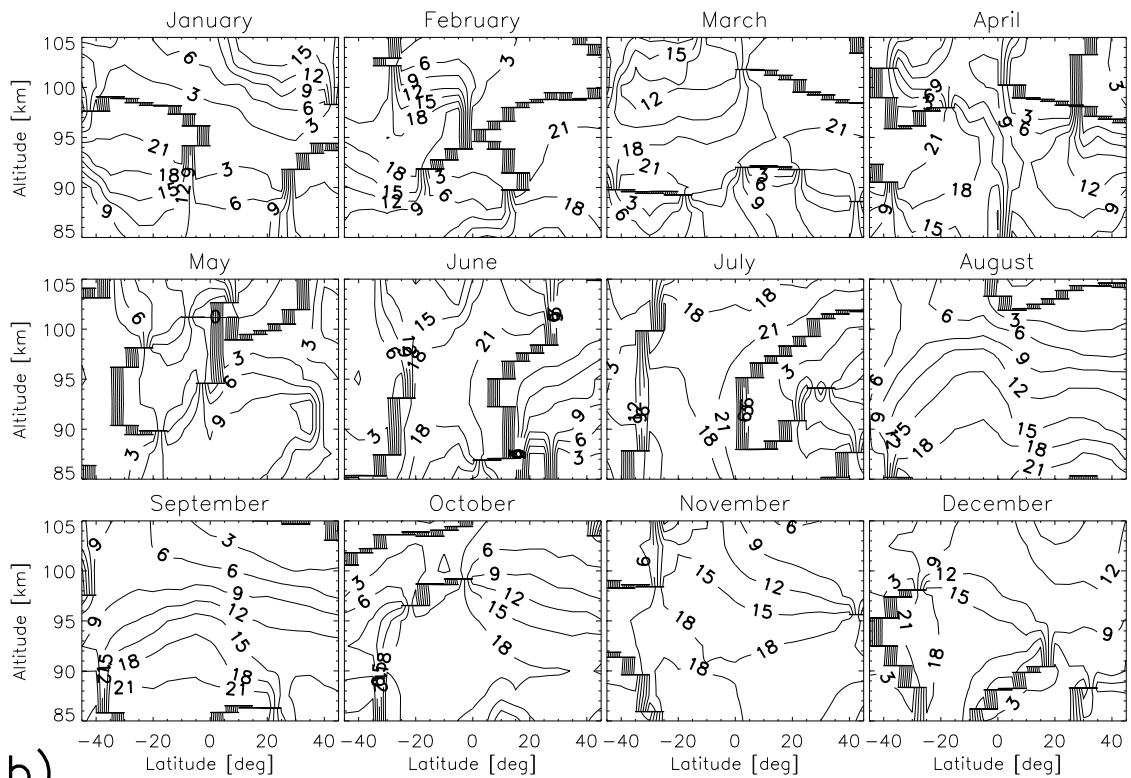
b)

Figure A4.12: As Figure A4.5, but for w4 zonal wind.

# w3 zonal



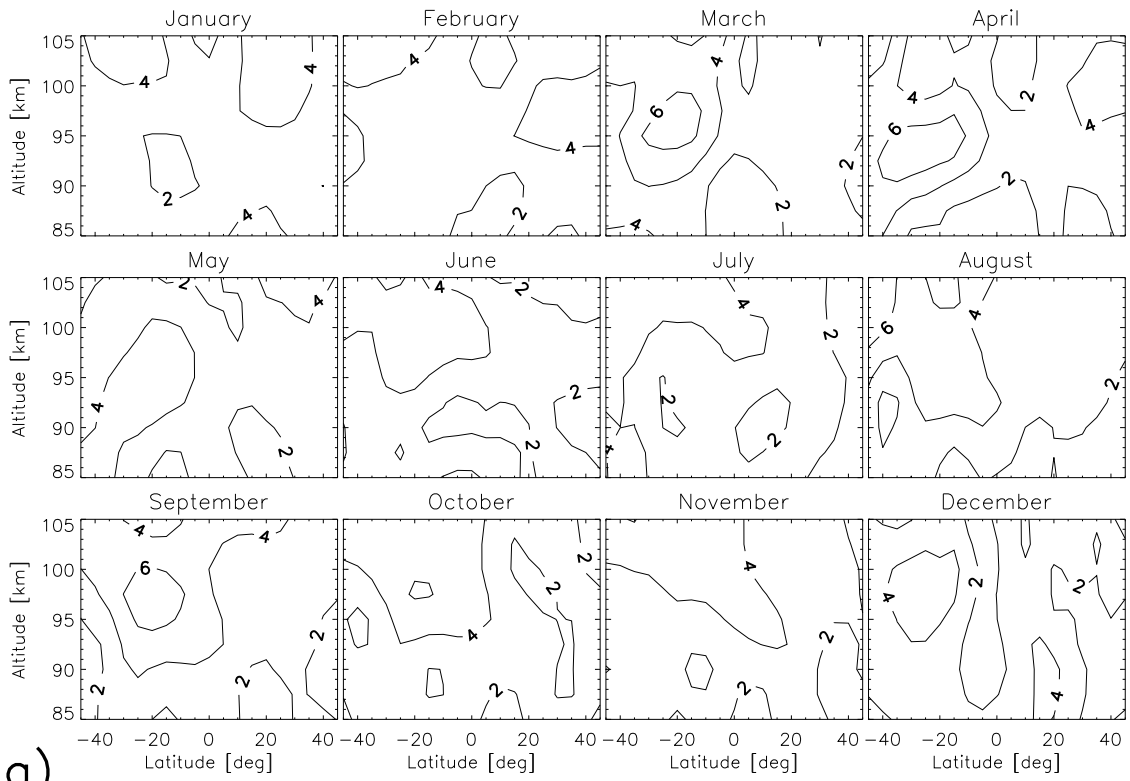
a)



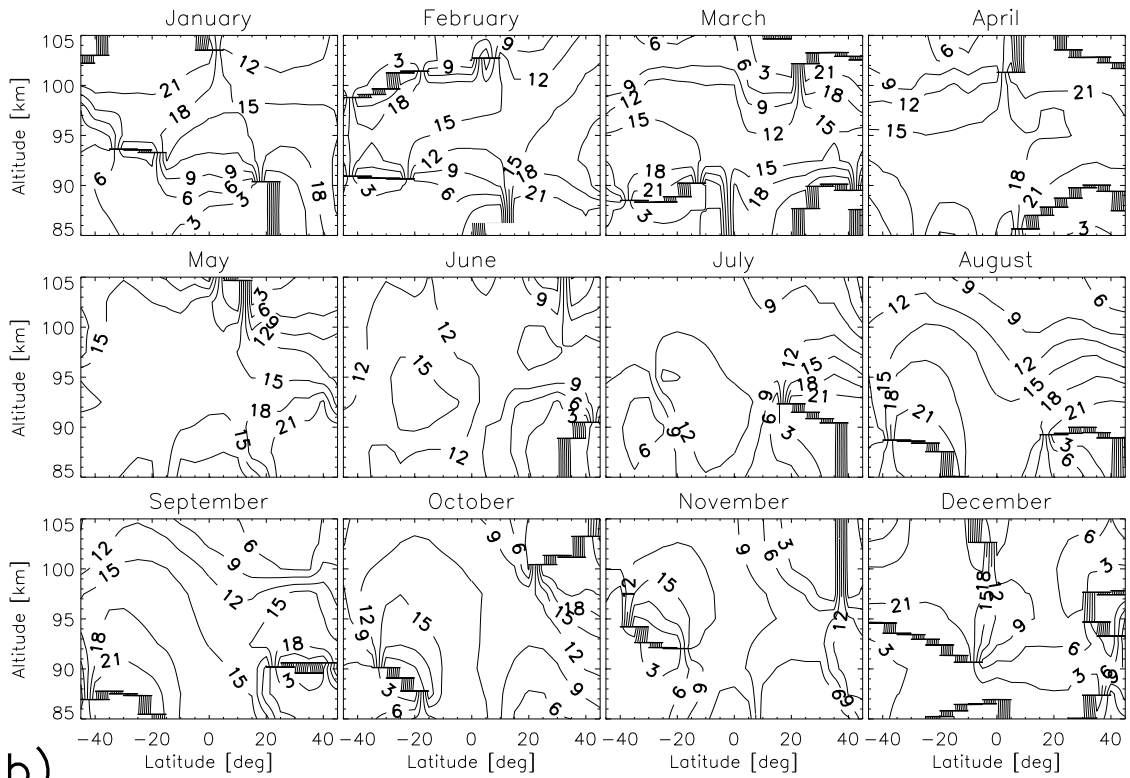
b)

Figure A4.13: As Figure A4.5, but for w3 zonal wind.

# e1 zonal



a)



b)

Figure A4.14: As Figure A4.5, but for e1 zonal wind.

## A5 TIDI climatologies: semidiurnal

Amplitudes are given in m/s and phases as Universal time (in hours) of maximum amplitude at  $0^\circ$  longitude.

w4, meridional: Figure A5.1

w3, meridional: Figure A5.2

w1, meridional: Figure A5.3

s0, meridional: Figure A5.4

e1, meridional: Figure A5.5

e2, meridional: Figure A5.6

w4, zonal: Figure A5.7

w3, zonal: Figure A5.8

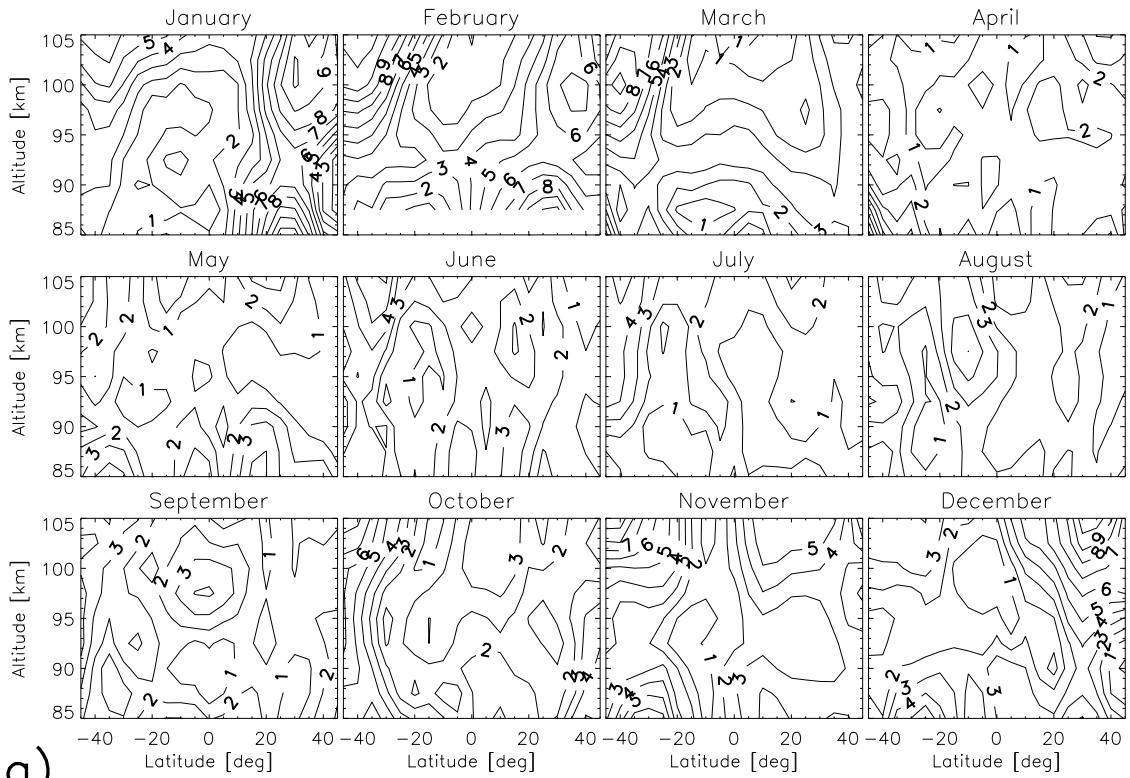
w1, zonal: Figure A5.9

s0, zonal: Figure A5.10

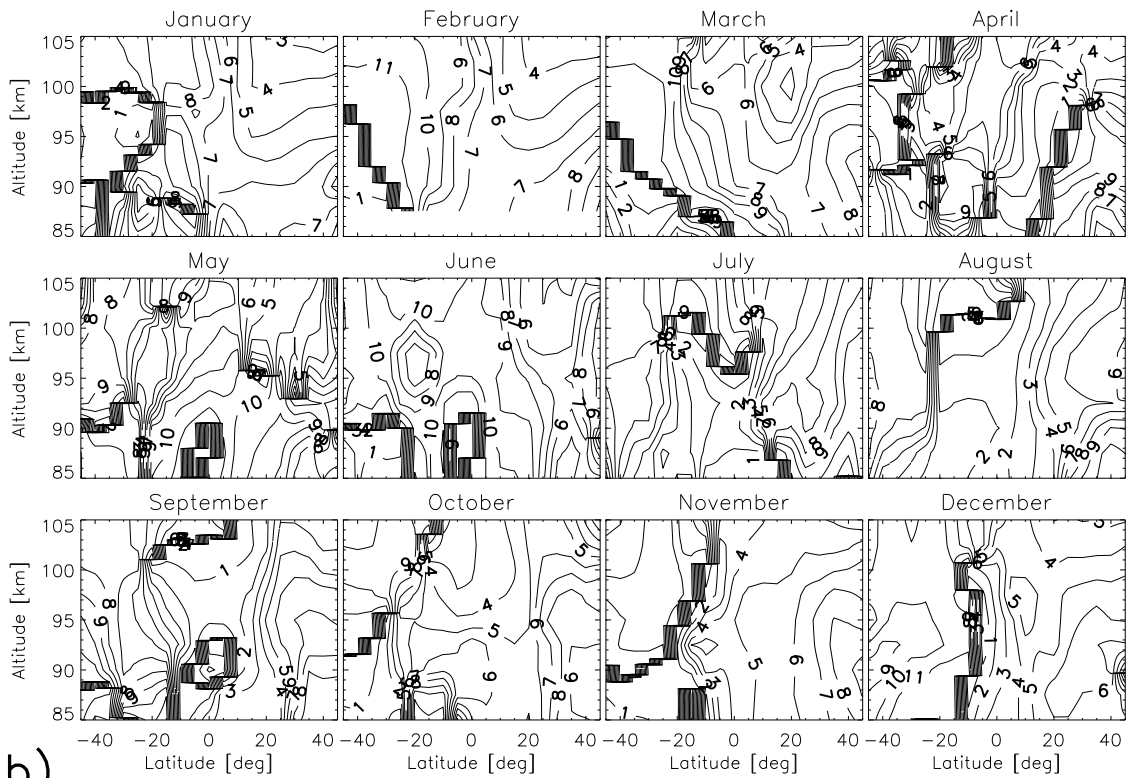
e1, zonal: Figure A5.11

e2, zonal: Figure A5.12

# w4 meridional



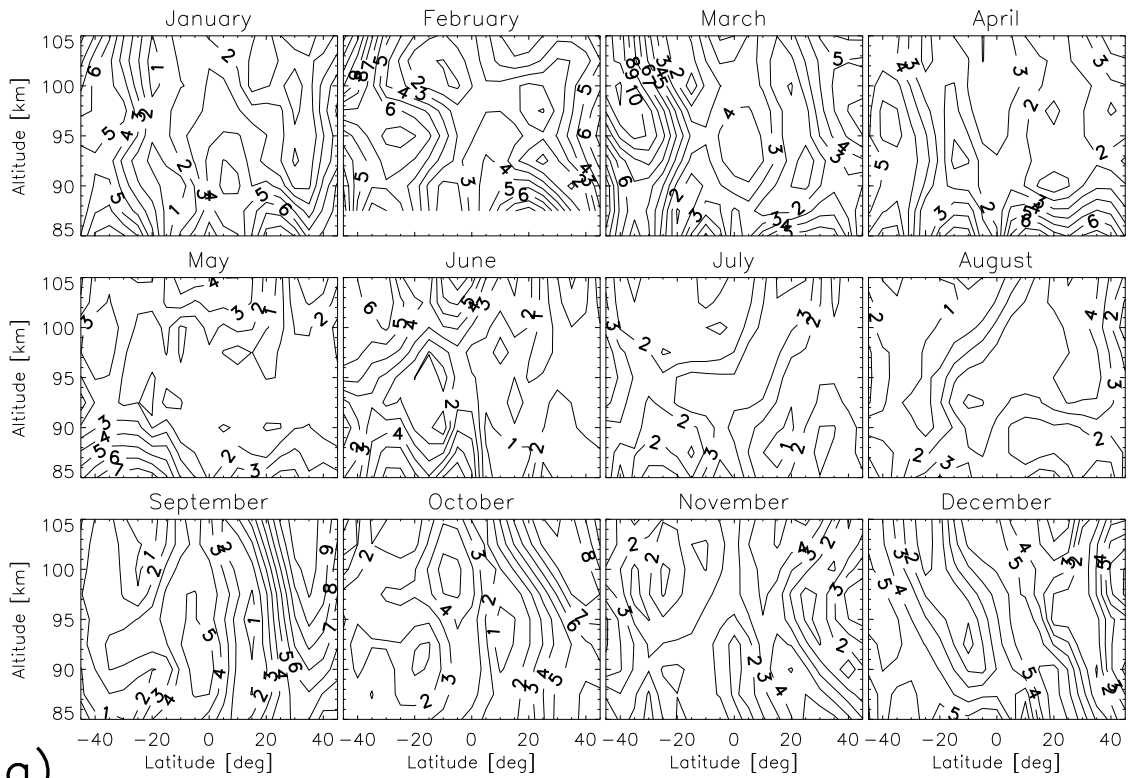
a)



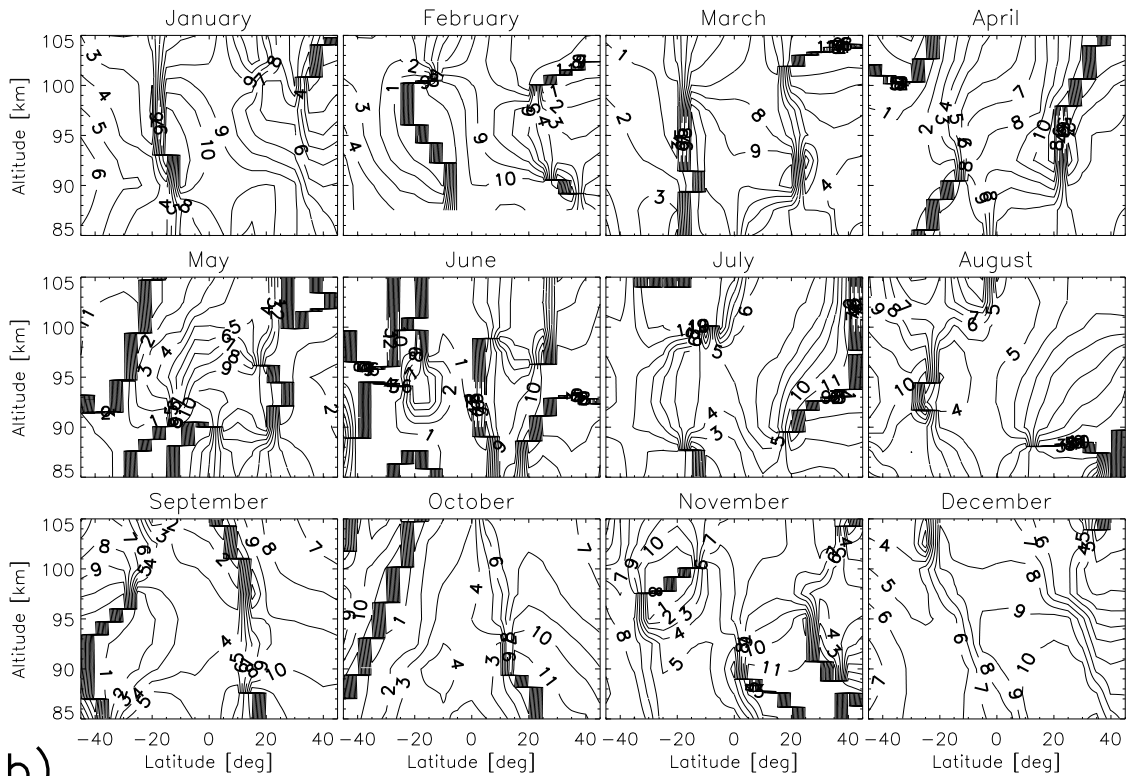
b)

Figure A5.1: a) Monthly mean semidiurnal amplitudes (m/s) and b) phases (Universal time of maximum amplitude at 0° longitude) for w4 meridional wind. Multiple phase contours adjacent to each other indicate the transition from 0 to 12 hours. Contour intervals are 1 m/s and 1 hours respectively.

# w3 meridional



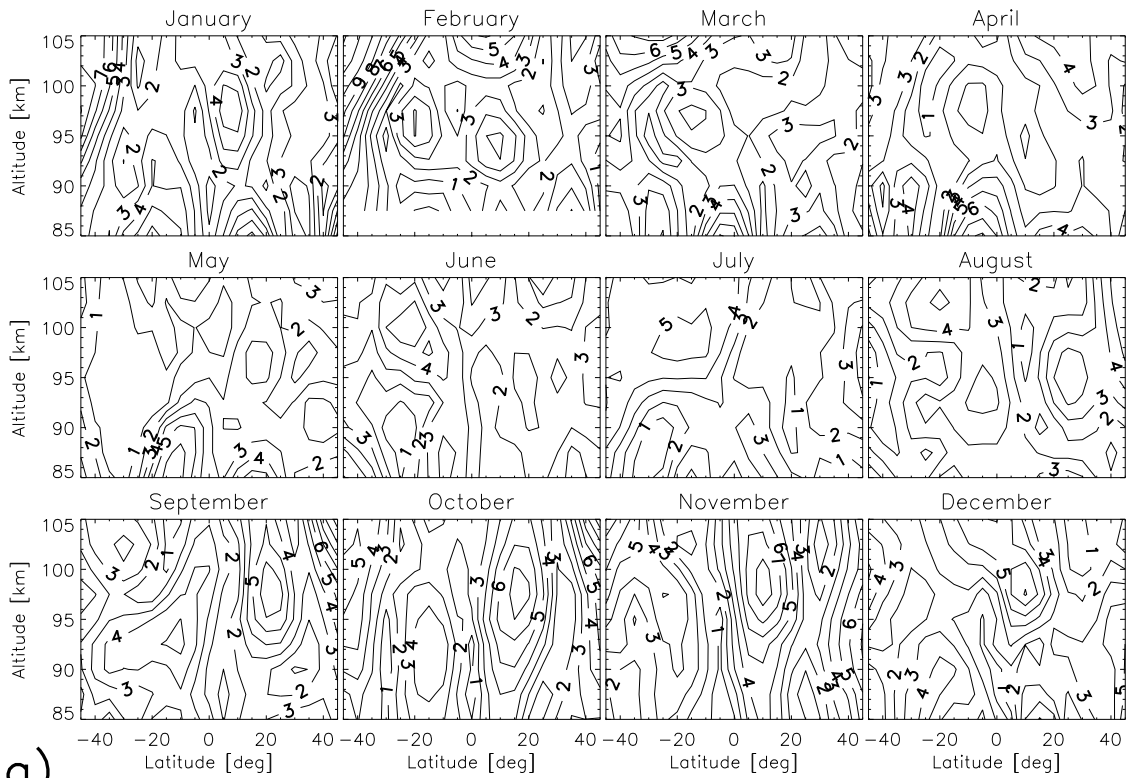
a)



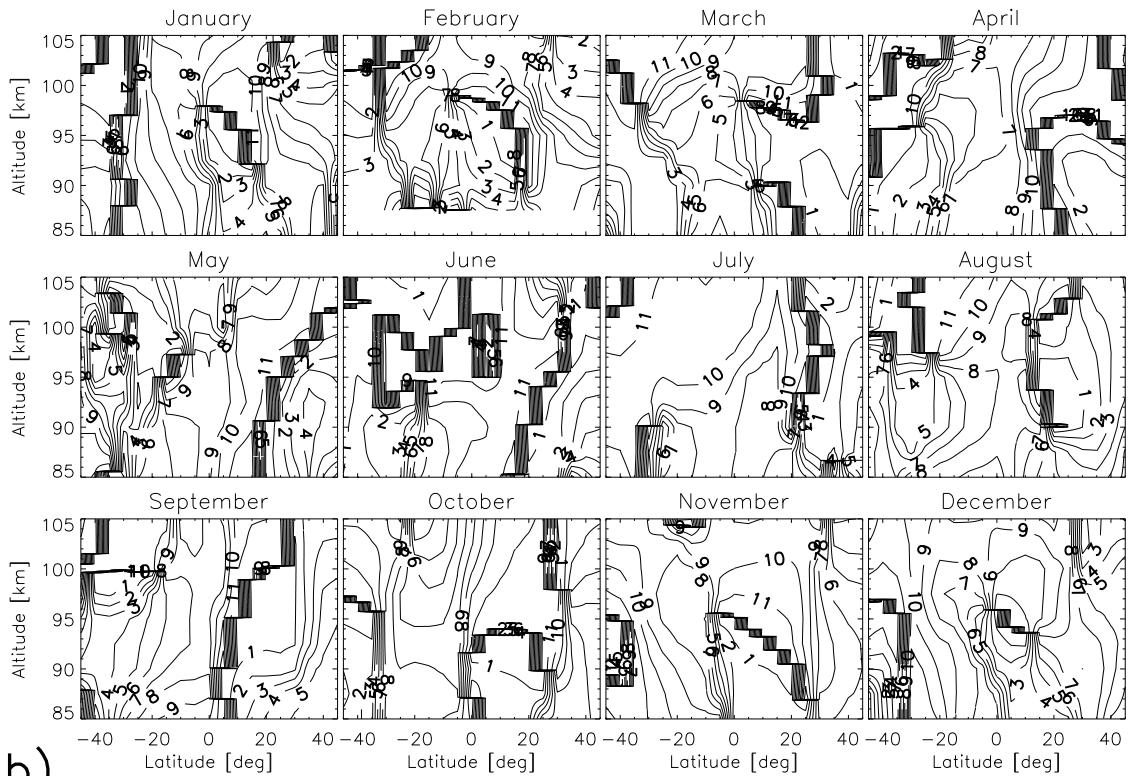
b)

Figure A5.2: As Figure A5.1, but for w3 meridional wind.

# w1 meridional



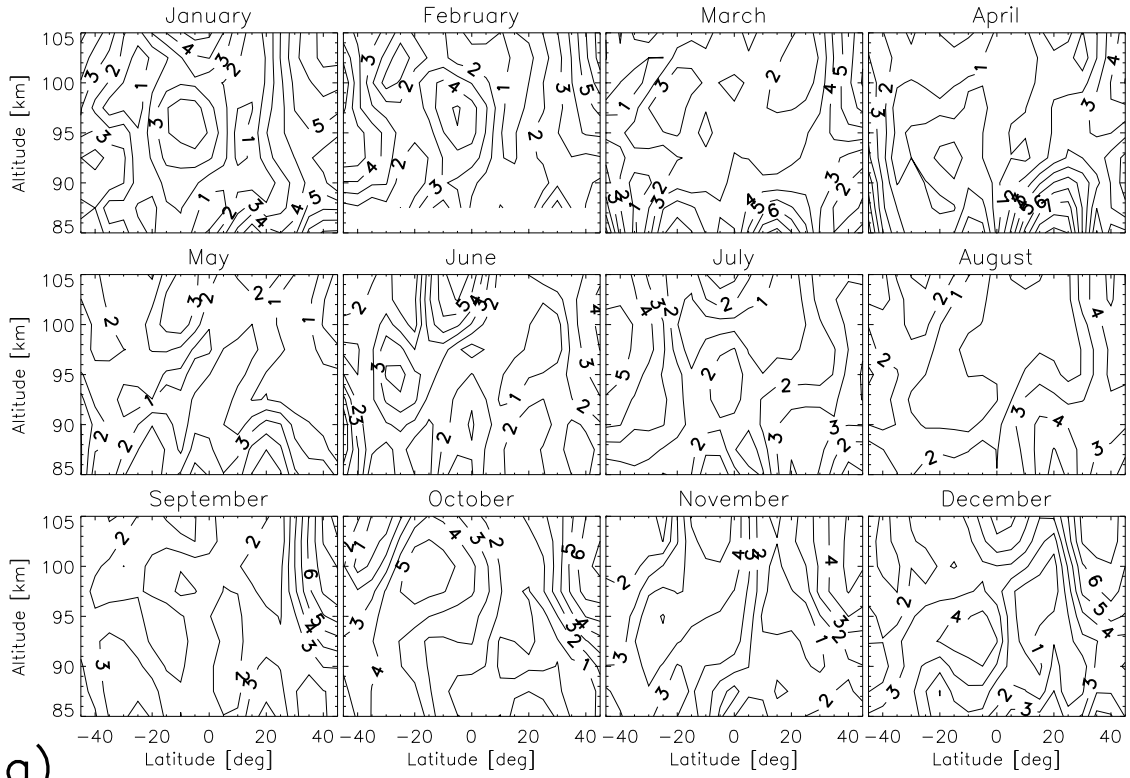
a)



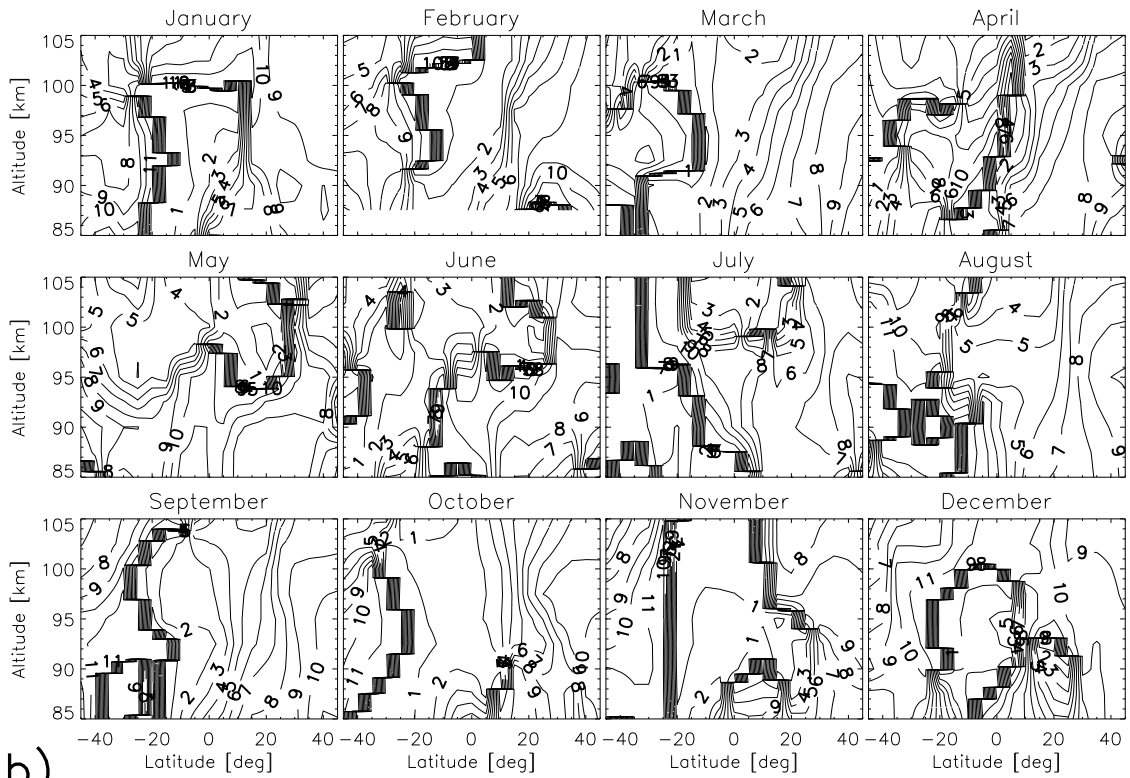
b)

Figure A5.3: As Figure A5.1, but for w1 meridional wind.

# s0 meridional



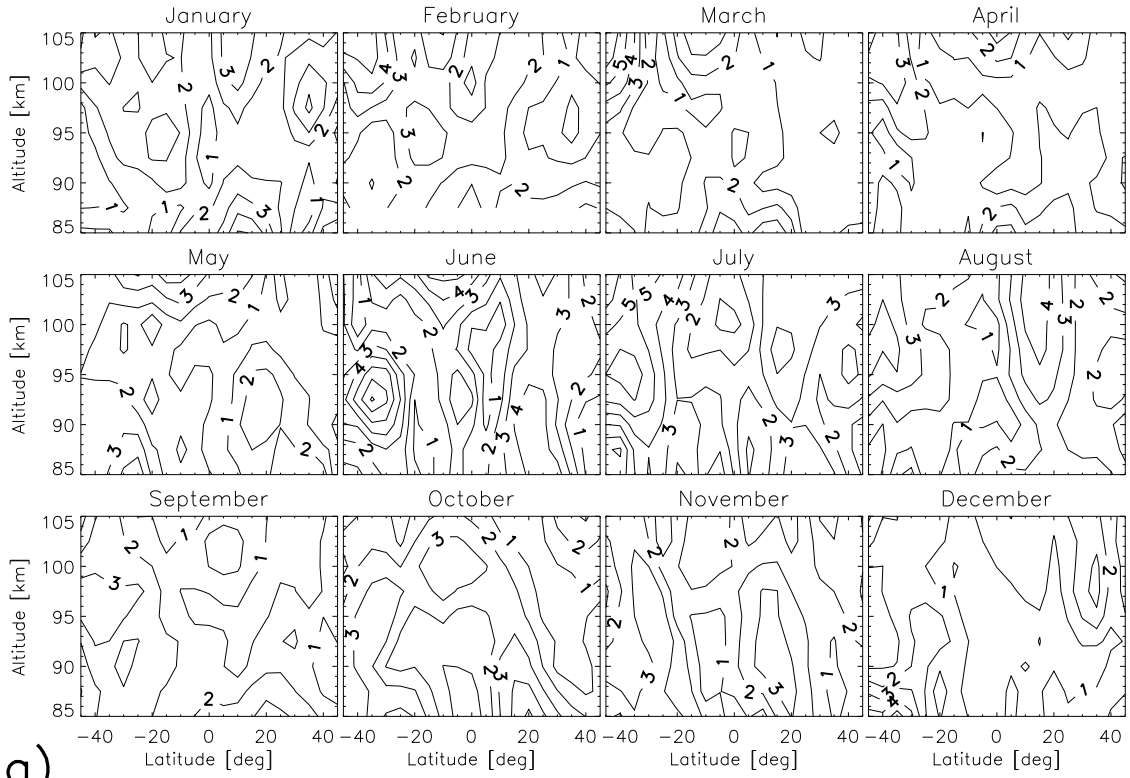
a)



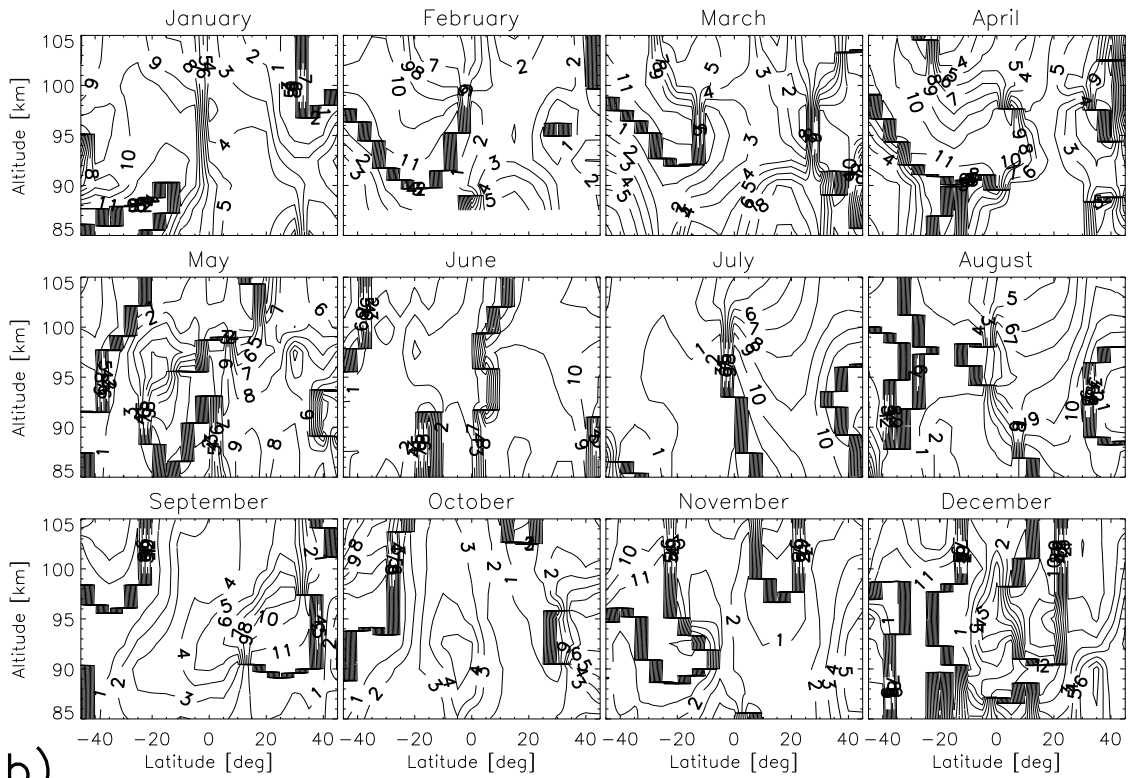
b)

Figure A5.4: As Figure A5.1, but for s0 meridional wind.

# e1 meridional



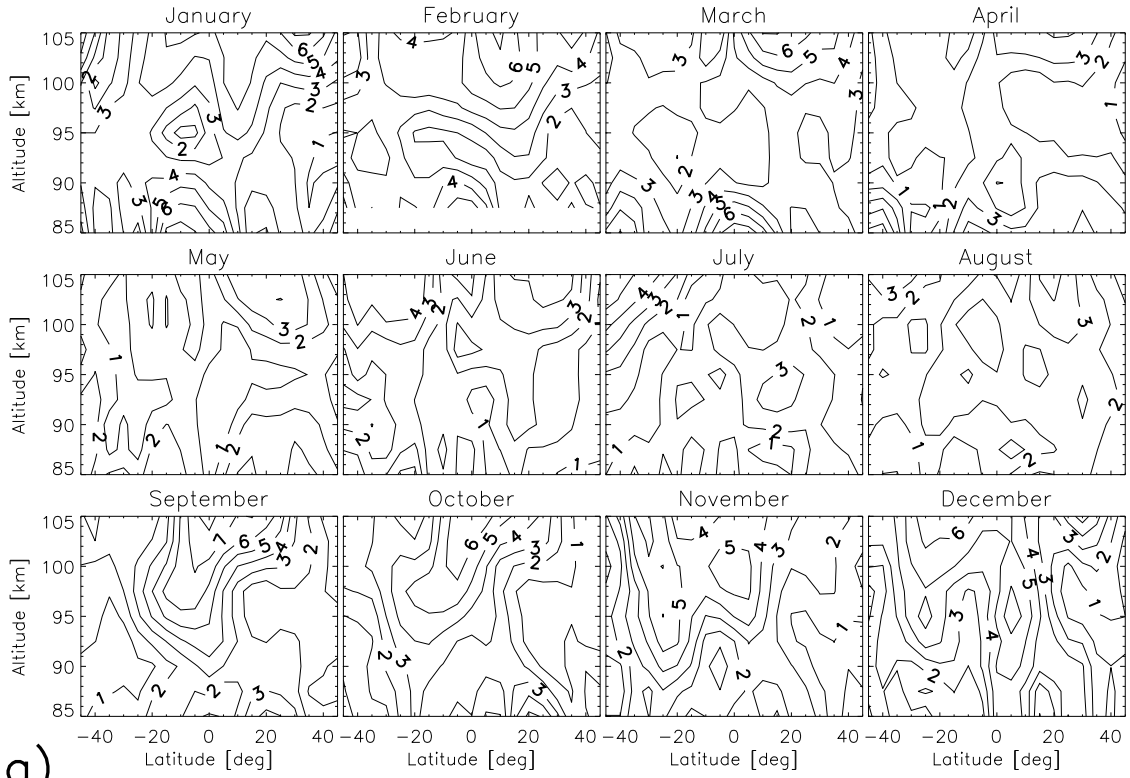
a)



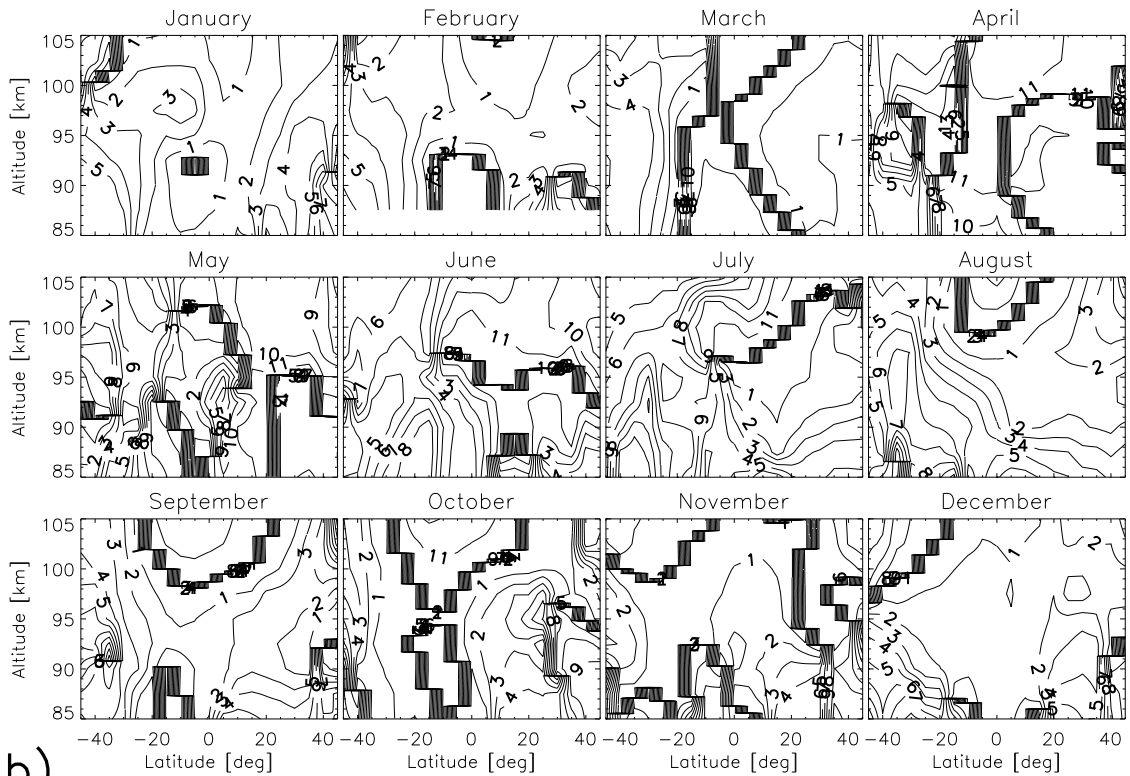
b)

Figure A5.5: As Figure A5.1, but for e1 meridional wind.

# e2 meridional



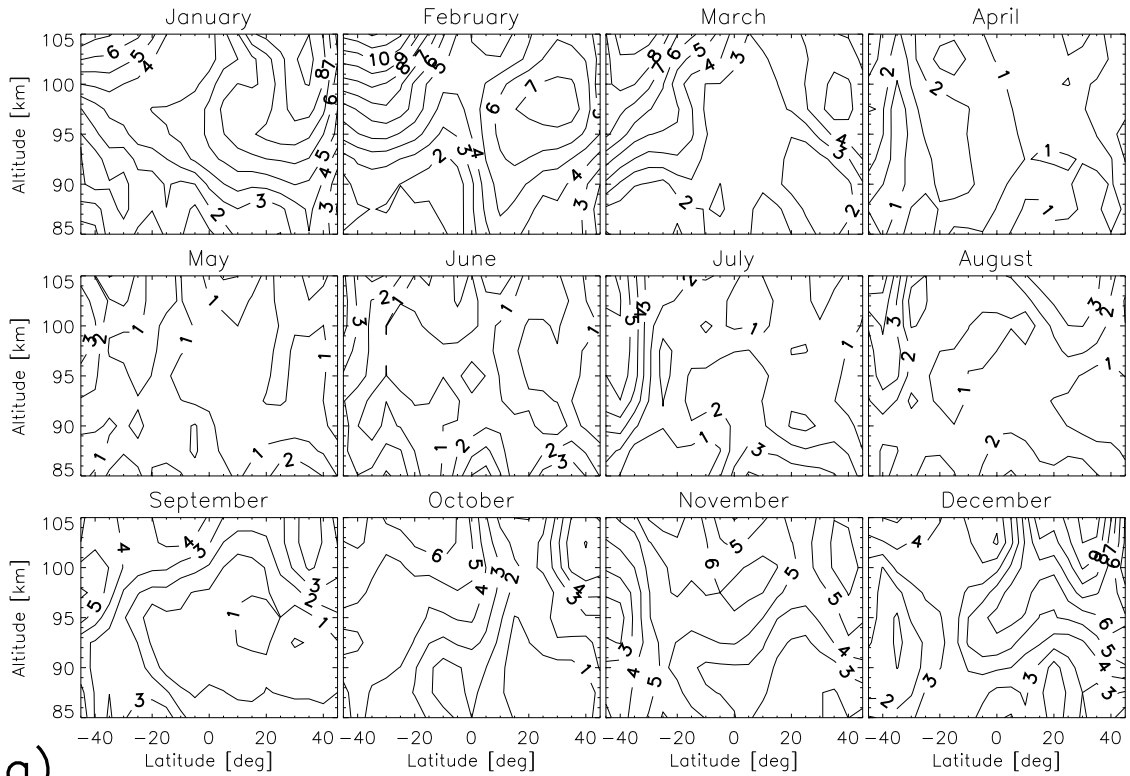
a)



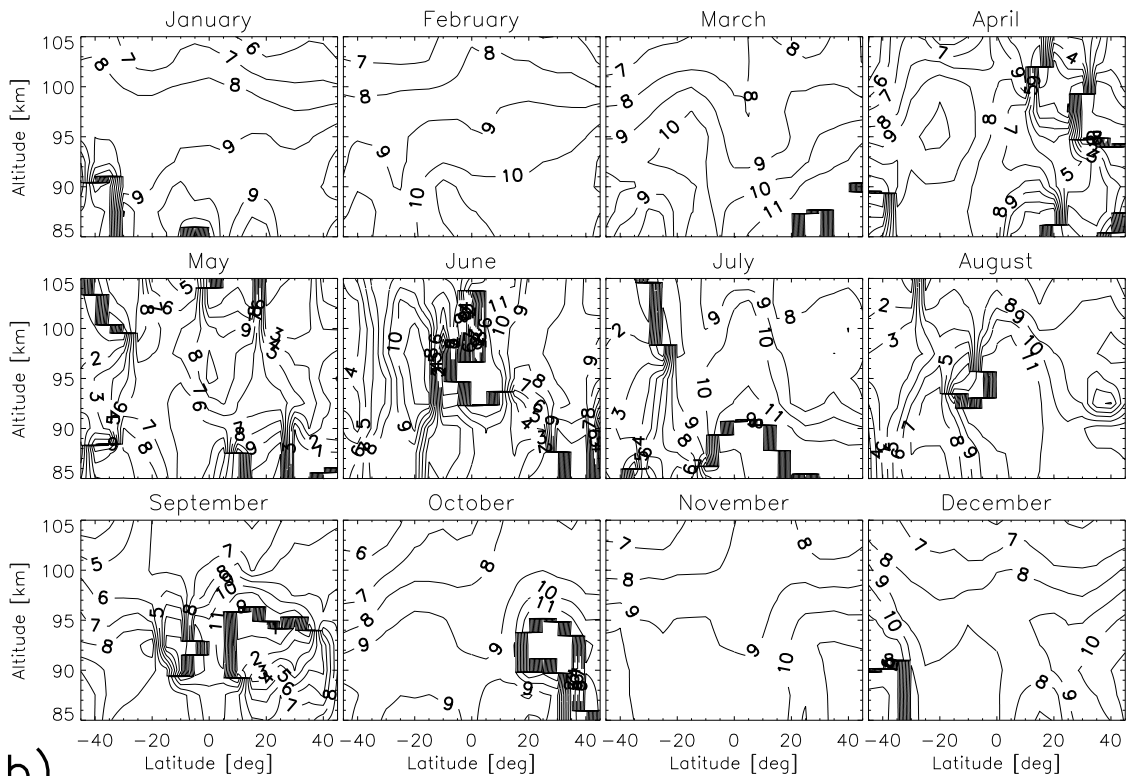
b)

Figure A5.6: As Figure A5.1, but for e2 meridional wind.

# w4 zonal



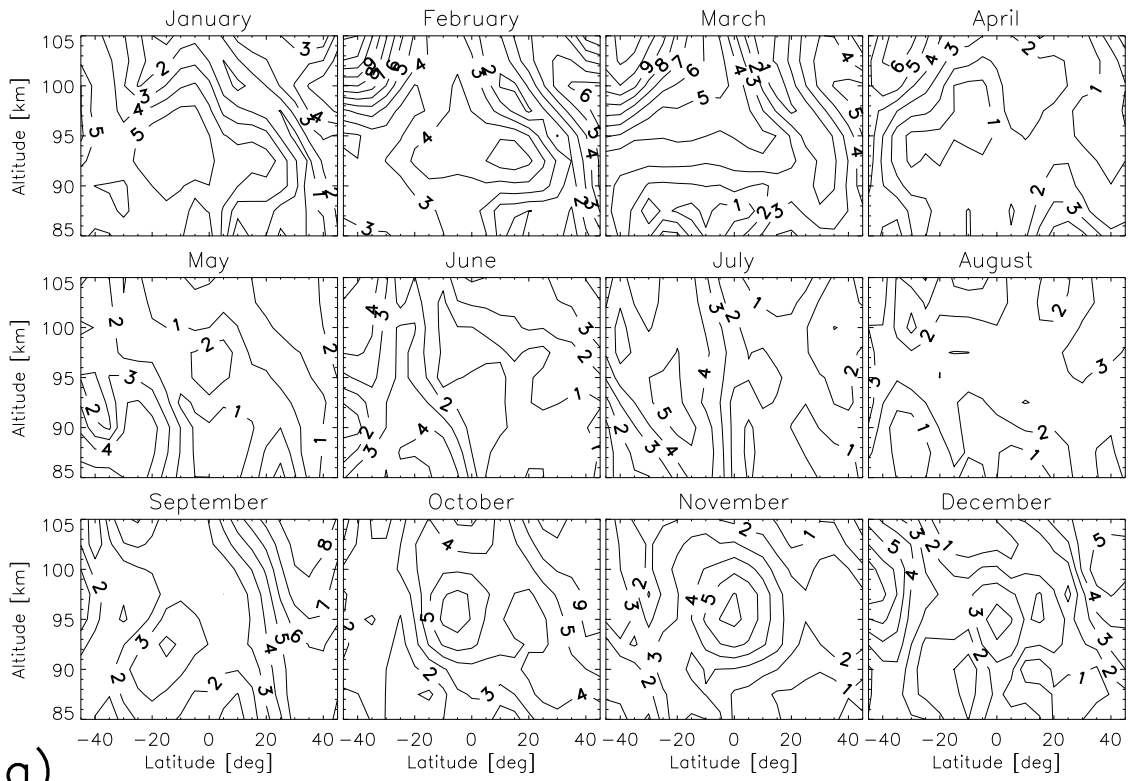
a)



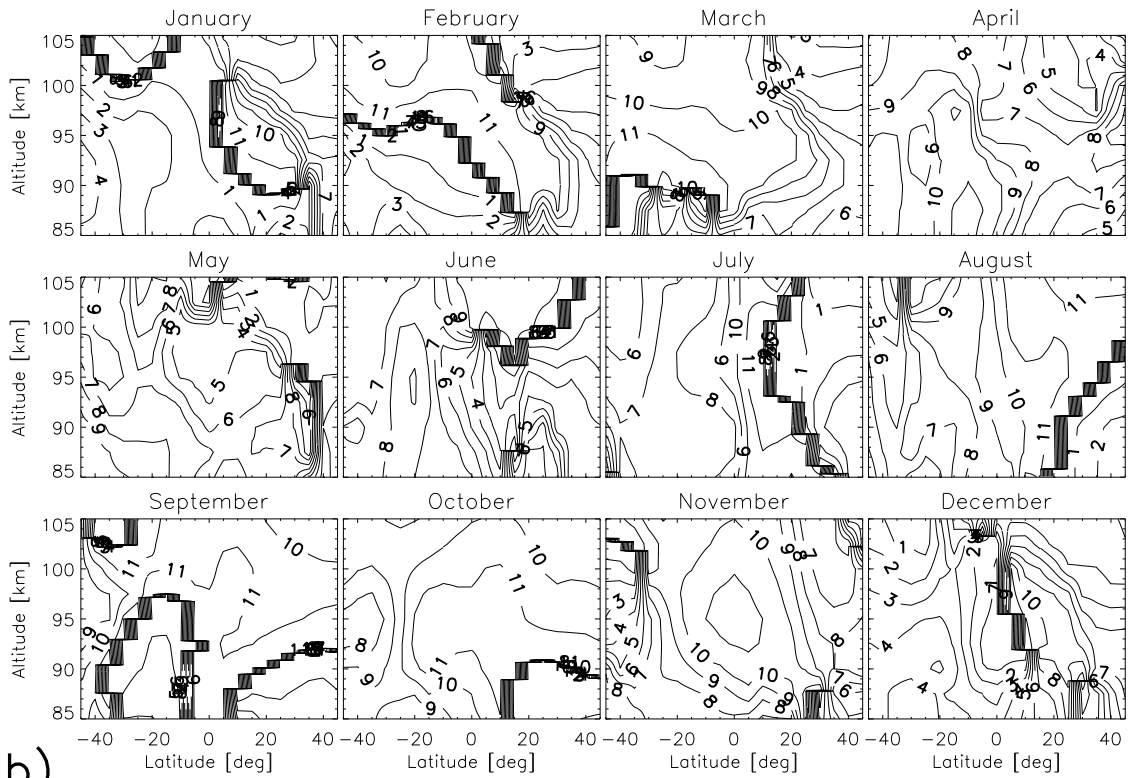
b)

Figure A5.7: a) Monthly mean semidiurnal amplitudes (m/s) and b) phases (Universal time of maximum amplitude at 0° longitude) for w4 zonal wind. Contour intervals are 1 m/s and 1 hours respectively.

# w3 zonal



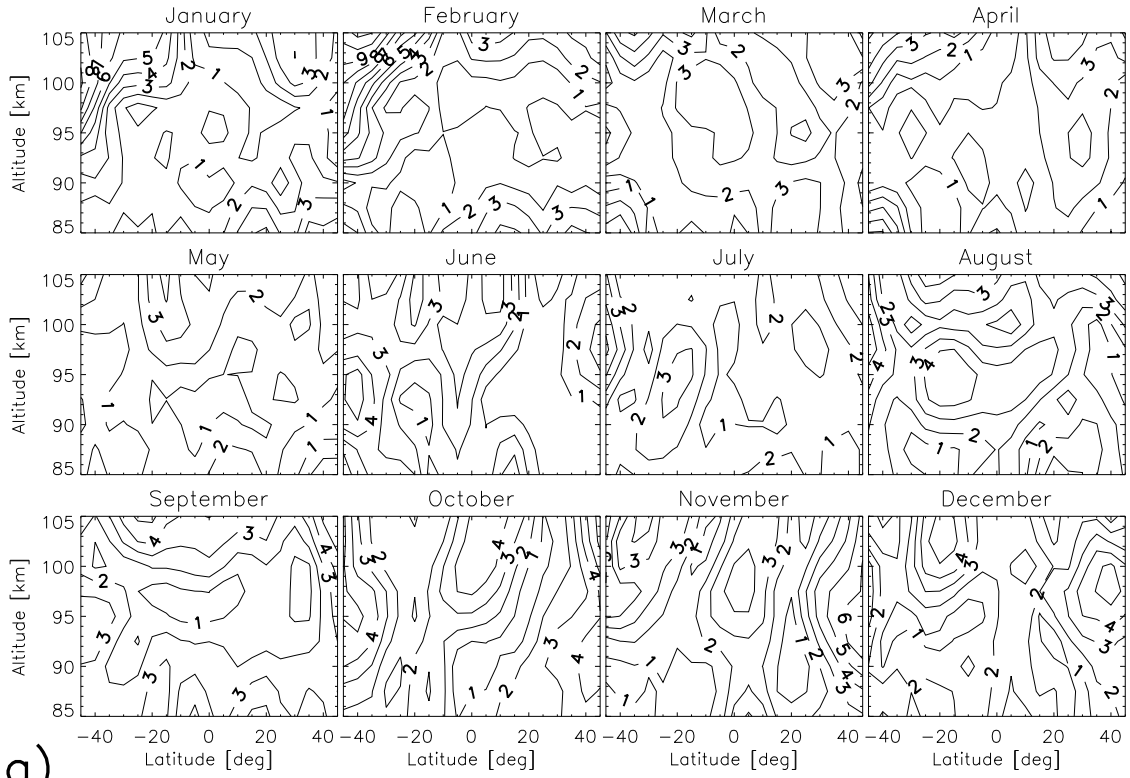
a)



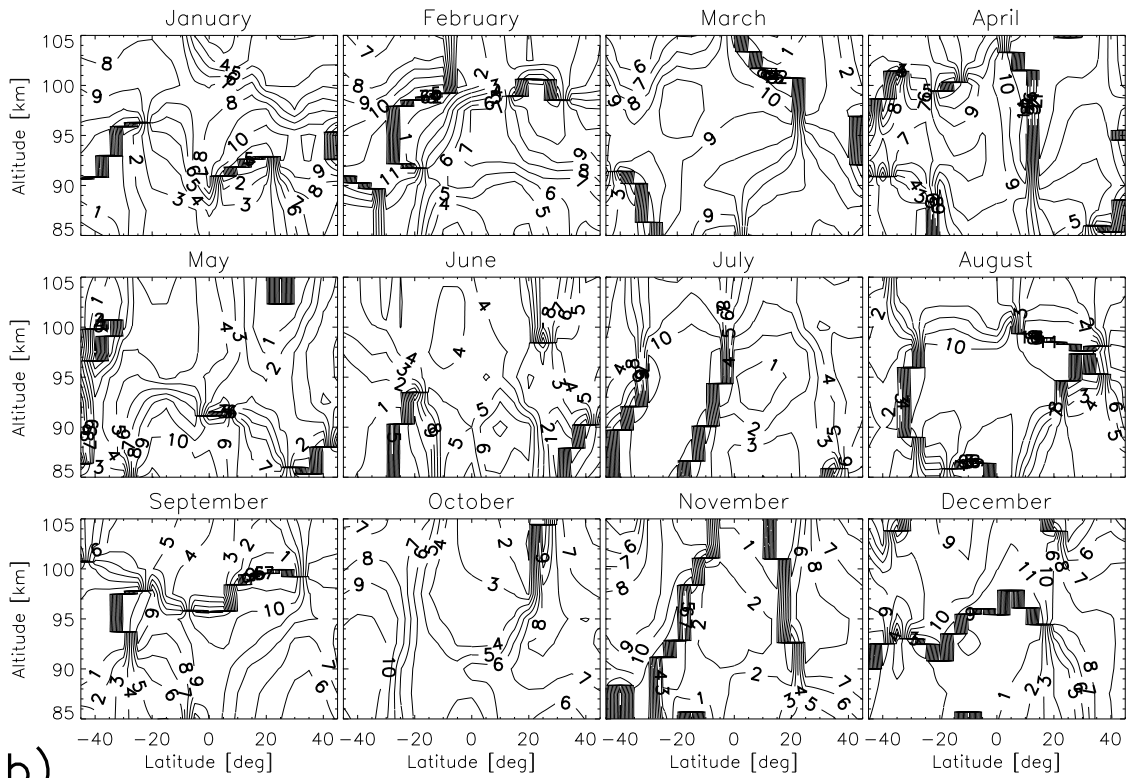
b)

Figure A5.8: As Figure A5.7, but for w3 zonal wind.

# w1 zonal



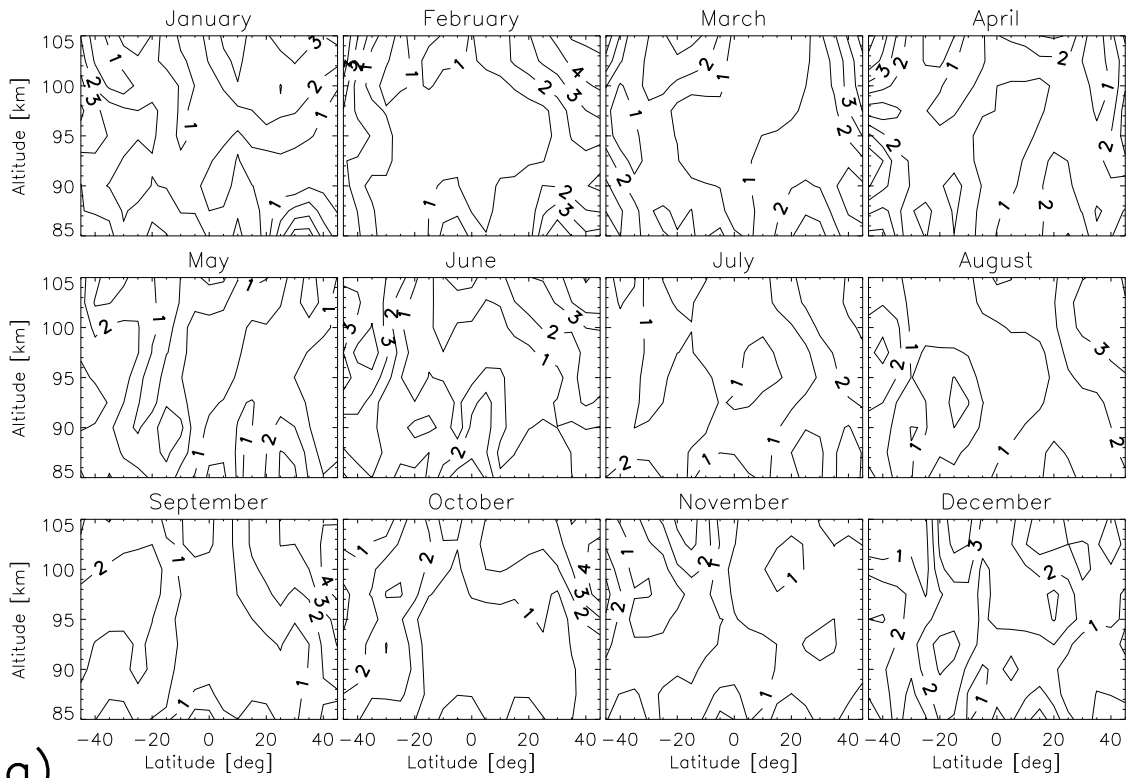
a)



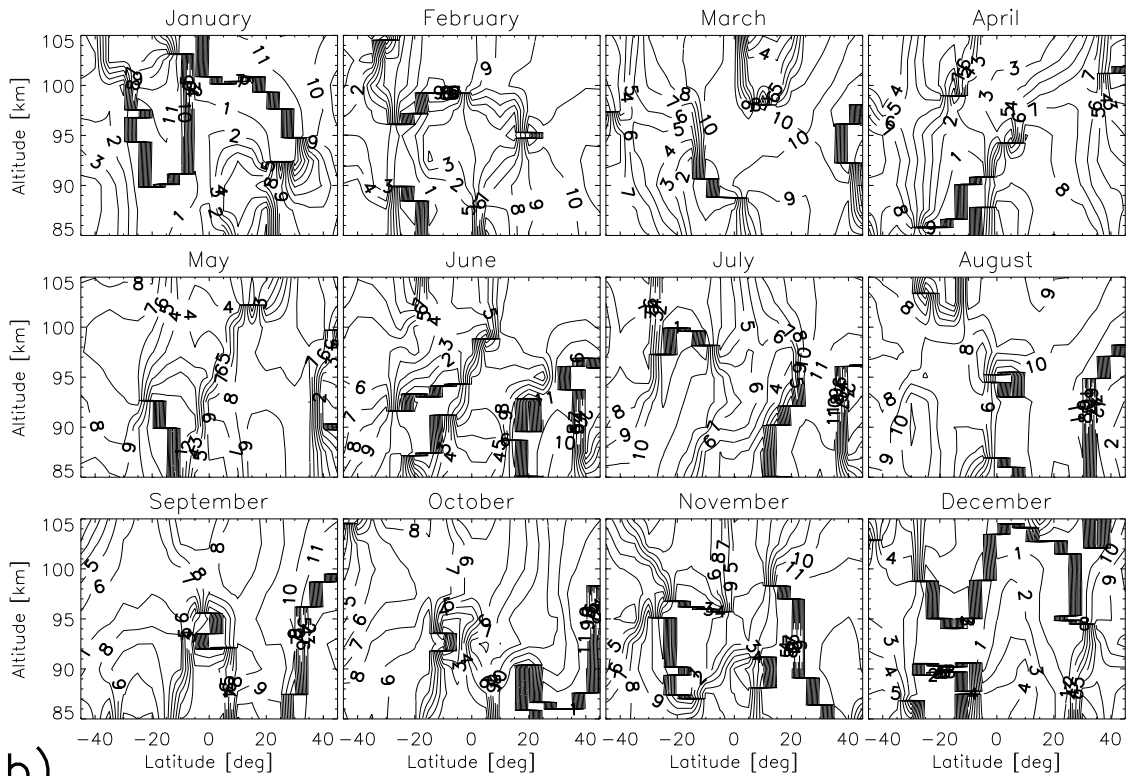
b)

Figure A5.9: As Figure A5.7, but for w1 zonal wind.

# s0 zonal



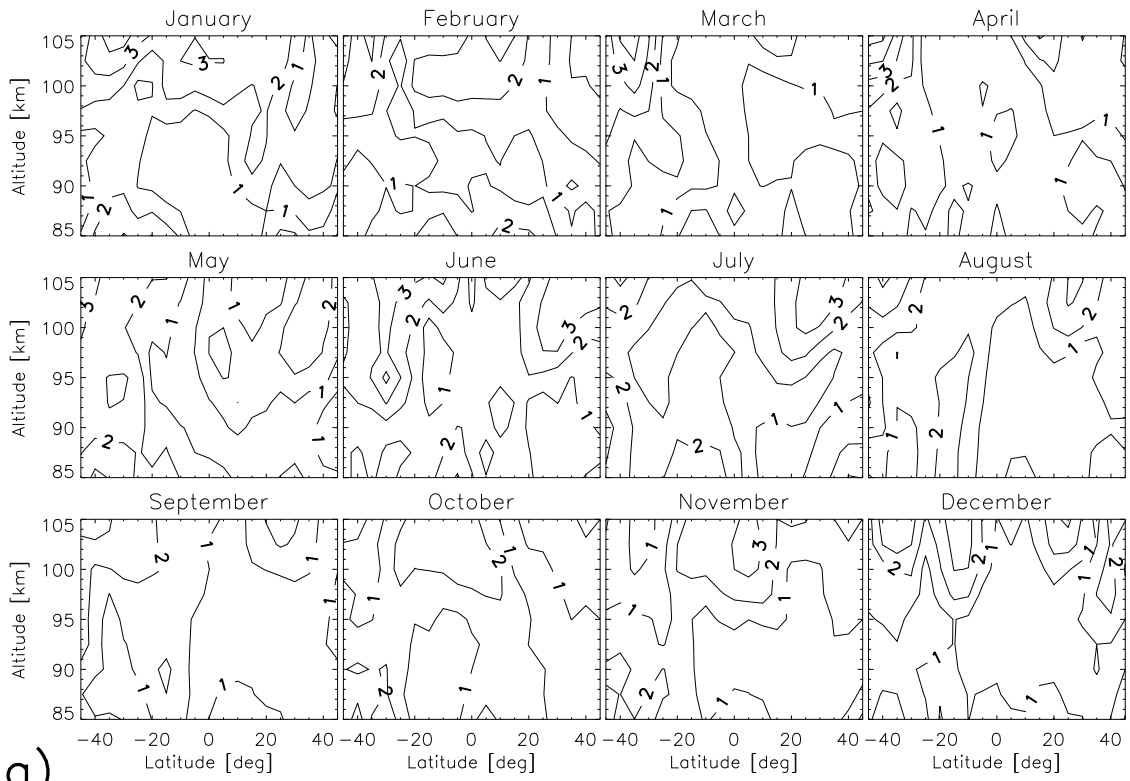
a)



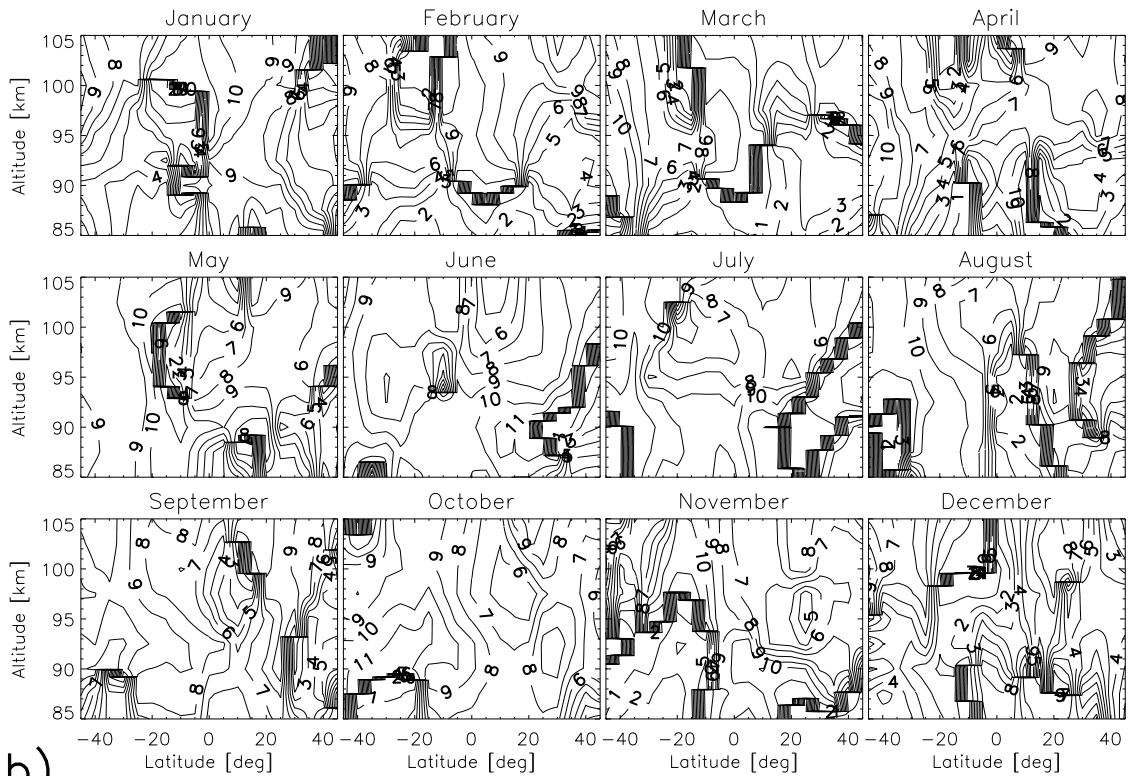
b)

Figure A5.10: As Figure A5.7, but for s0 zonal wind.

# e1 zonal



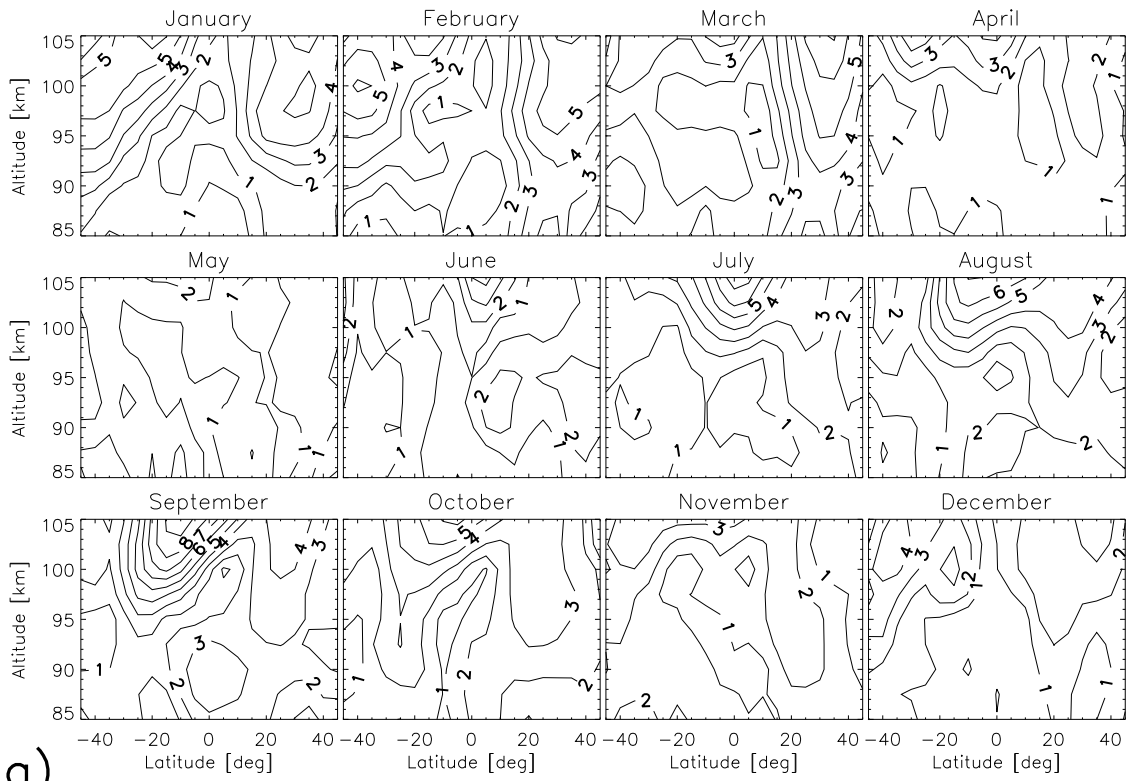
a)



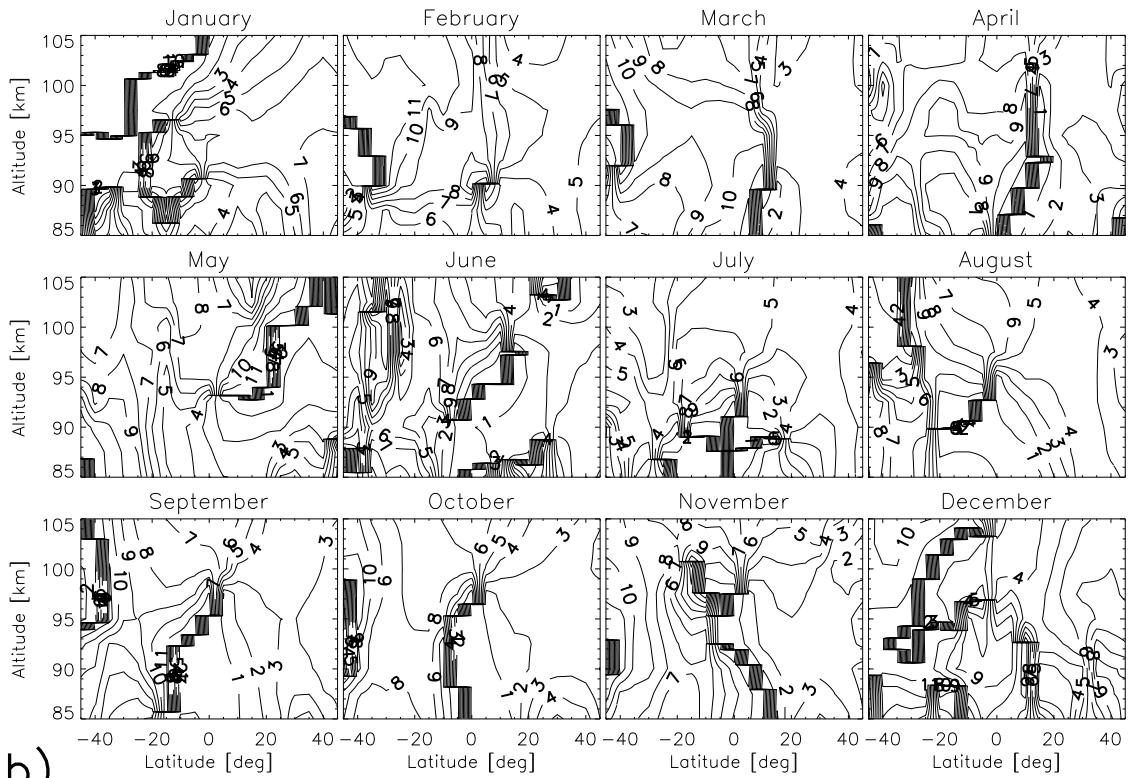
b)

Figure A5.11: As Figure A5.7, but for e1 zonal wind.

# e2 zonal



a)



b)

Figure A5.12: As Figure A5.7, but for e2 zonal wind.

## 9 References

- Akmaev, R. A., J. M. Forbes, and M. E. Hagan, Simulation of tides with a spectral mesosphere/lower thermosphere model, *Geophys. Res. Lett.*, *23*, 2173-2176, 1996.
- Andrews, D. G., J. R. Holton, and C. B. Leovy, Middle Atmosphere Dynamics, *Academic Press*, San Diego, California, 1987.
- Angelats i Coll, M., and J. M. Forbes, Dynamical influences on atomic oxygen and 5577 angstrom emission rates in the lower thermosphere, *Geophys. Res. Lett.*, *25*, 461-464, 1998.
- Angelats i Coll, M., and J. M. Forbes, Nonlinear interactions in the upper atmosphere: The s=1 and s=3 nonmigrating semidiurnal tides, *J. Geophys. Res.*, *107*(A8), doi:10.1029/2001JA900179, 2002.
- Baldwin, M. P., The Arctic Oscillation and its role in stratosphere-troposphere coupling, *SPARC Newsletter*, *14*, 2000.
- Baldwin, M. P., D. W. J. Thompson, E. F. Shuckburgh, W. A. Norton, and N. P. Gillett, Weather from the stratosphere?, *Science*, *301*, 317-318, 2003a.
- Baldwin, M. P., D. B. Stephenson, D. W. J. Thompson, T. J. Dunkerton, A. J. Charlton, A. O'Neill, Stratospheric Memory and Skill of Extended-Range Weather Forecasts, *Science*, *301*, 636-640, 2003b.
- Basu, S., and D. Pallamraju, Science rationale for CAWSES (Climate and Weather of the Sun-Earth System): SCOSTEP's interdisciplinary program for 2004-2008, *Adv. Space Res.*, in press, 2006.
- Beig, G., and 18 co-authors, Review of mesospheric temperature trends, *Rev. Geophys.*, *41*(4), 1015, doi:10.1029/2002RG000121, 2003.
- Berger, U., and U. von Zahn, The two-level structure of the mesopause: A model study, *J. Geophys. Res.*, *104*(D18), 22,083-22,093, 1999.
- Bittner, M., D. Offermann, H.-H. Graef, M. Donner, and K. Hamilton, An 18-year time series of OH rotational temperatures and middle atmosphere decadal variations, *J. Atmos. Sol. Terr. Phys.*, *64*, 1147-1166, 2002.
- Burrage, M. D., M. E. Hagan, W. R. Skinner, D. L. Wu, and P. B. Hays, Long-term variability in the solar diurnal tide observed by HRDI and simulated by the GSWM, *Geophys. Res. Lett.*, *22*, 2641-2644, 1995.
- Chang, J. L., and S. K. Avery, Observations of the diurnal tide in the mesosphere and lower thermosphere over Christmas Island, *J. Geophys. Res.*, *102*(D2), 1895-1907, 1997.
- Chapman, S., and R. S. Lindzen, Atmospheric Tides, *D. Reidel, Norwell, Mass.*, 1970.
- Charney, J. G., and P. G. Drazin, Propagation of planetary-scale disturbances from the lower into the upper atmosphere, *J. Geophys. Res.*, *66*, 83-109, 1961.

- Clancy, R. R., D. W. Rusch, and M. T. Callan, Temperature minima in the average thermal structure of the middle mesosphere (70-80 km) from analysis of 40- to 92-km SME global temperature profiles, *J. Geophys. Res.*, *99*(D9), 19,001-19,020, 1994.
- Criss, A., J. Yee, E. R. Talaat, M. Mlynczak, L. Gordley, C. Mertens, and J. M. Russell, Seasonal and Interannual Variations of Migrating Diurnal Tide in the Mesosphere as Seen from the TIMED/SABER Temperature Measurements, *Eos Trans. AGU*, *86*(52), Fall Meet. Suppl., Abstract SA43A-1099, 2005.
- Dickinson, R. E., E. C. Ridley, and R. G. Roble, A three-dimensional general circulation model of the thermosphere, *J. Geophys. Res.*, *86*, 1499-1512, 1981.
- Duck, T. J., and M. D. Greene, High Arctic observations of mesospheric inversion layers, *Geophys. Res. Lett.*, *31*, L02105, doi:10.1029/2003GL018481, 2004.
- Dudhia, A., S. E. Smith, A. R. Wood, and F. W. Taylor, Diurnal and semi-diurnal temperature variability of the middle atmosphere as observed by ISAMS, *Geophys. Res. Lett.*, *20*, 1251-1254, 1993.
- Dunkerton, T. J. and D. P. Delisi, The subtropical mesospheric jet observed by the Nimbus 7 Limb Infrared Monitor of the Stratosphere, *J. Geophys. Res.*, *99*, 10,681-10,692, 1985.
- Dunkerton, T. J., and D. P. Delisi, Evolution of potential vorticity in the winter stratosphere of January-February 1979, *J. Geophys. Res.*, *91*, 1199-1208, 1986.
- Feofilov, A. G., A. A. Kutepov, B. T. Marshall, L. L. Gordley, W. D. Pesnell, R. A. Goldberg, and J. M. Russell III, Specifics of temperature retrievals in the polar summer mesosphere and lower thermosphere: application to TIMED SABER, *Geophysical Research Abstracts*, *8*, 08428, 2006.
- Flattery, T. W., Hough functions, *PhD thesis*, University of Chicago, Dept. of the Geophysical Sciences, 1967.
- Fomichev, V. I., W. E. Ward, S. R. Beagley, C. McLandress, J. C. McConnell, N. A. McFarlane, and T. G. Shepherd, The extended Canadian Middle Atmosphere Model: Zonal-mean climatology and physical parameterizations, *J. Geophys. Res.*, *107*(D10), 4087, doi:10.1029/2001JD000479, 2002.
- Forbes, J. M., Atmospheric tides, 1, Model description and results for the solar diurnal component, *J. Geophys. Res.*, *87*, 5222-5240, 1982.
- Forbes, J. M., Tidal and Planetary Waves, *Geophys. Monograph*, *87*, American Geophysical Union, 67-87, 1995.
- Forbes, J. M., Wave Coupling in Terrestrial Planetary Atmospheres, *Geophys. Monograph*, *130*, American Geophysical Union, 171-190, 2002.
- Forbes, J. M., and D. L. Wu, Solar Tides as Revealed by Measurements of Mesosphere Temperature by the MLS Experiment on UARS, *J. Atmos. Sci.*, in press, 2006.

- Forbes, J. M., M. E. Hagan, X. Zhang, and K. Hamilton, Upper atmospheric tidal oscillations due to latent heat release in the tropical troposphere, *Ann. Geophys.*, *15*, 1165-1175, 1997.
- Forbes, J. M., X. Zhang, E. R. Talaat, and W. Ward, Nonmigrating diurnal tides in the thermosphere, *J. Geophys. Res.*, *108*(A1), 1033, 2003.
- Forbes, J. M., J. Russell, S. Miyahara, X. Zhang, S. Palo, M. Mlynczak, C. J. Mertens, and M. E. Hagan, Troposphere-Thermosphere Tidal Coupling as Measured by the SABER instrument on TIMED during July-September 2002, *J. Geophys. Res.*, in press, 2006.
- Fritts, D. C., and R. A. Vincent, Mesospheric momentum flux studies at Adelaide, Australia: Observations and a gravity wave-tidal interaction model, *J. Atmos. Sci.*, *44*, 605-619, 1987.
- Garcia, R. R., and S. Solomon, The effects of breaking waves on the dynamics and chemical composition of the mesosphere and lower thermosphere, *J. Geophys. Res.*, *90*, 3850-3868, 1985.
- Garcia, R. R., R. Lieberman, J. M. Russell, and M. G. Mlynczak, Large-scale waves in the mesosphere and lower thermosphere observed by SABER, *J. Atmos. Sci.*, *62*(12), 4384-4399, 2005.
- Gille, J. C., and J. M. Russell, The limb infrared monitor of the stratosphere: experiment description, performance, and results, *J. Geophys. Res.*, *89*, 5125-5140, 1984.
- Grieger, N., G. Schmitz, and U. Achatz, The Dependence of the Nonmigrating Diurnal Tide in the Mesosphere and Lower Thermosphere on Stationary Planetary Waves, *J. Atmos. Sol. Terr. Phys.*, *66*(6-9), 733-754, 2004.
- Grossmann, K. U., D. Offermann, O. Gusev, J. Oberheide, M. Riese, and R. Spang, The CRISTA-2 mission, *J. Geophys. Res.*, *107*(D23), 8173, doi:10.1029/2001JD-000667, 2002.
- Grossmann, K. U., P. Knieling, O. A. Gusev, and M. Jarisch, The distribution of carbon monoxide in the upper mesosphere and lower thermosphere during CRISTA-1 and CRISTA-2, *J. Atmos. Sol. Terr. Phys.*, in press, 2006.
- Gusev, O. A., M. Kaufmann, K. U. Grossmann, F. J. Schmidlin, and M. G. Shepherd, Atmospheric neutral temperature distribution at the mesopause altitude, *J. Atmos. Sol. Terr. Phys.*, in press, 2006.
- Hagan, M. E., Comparative effects of migrating solar sources on tidal signatures in the middle and upper atmosphere, *J. Geophys. Res.*, *101*, 21,213-21,222, 1996.
- Hagan, M. E., and R. G. Roble, Modeling the diurnal tidal variability with the National Center for Atmospheric Research thermosphere-ionosphere-mesosphere-electrodynamics general circulation model, *J. Geophys. Res.*, *106*, 24,869-24,882, 2001.

- Hagan, M. E., and J. M. Forbes, Migrating and nonmigrating diurnal tides in the middle and upper atmosphere excited by tropospheric latent heat release, *J. Geophys. Res.*, 107(D24), 4754, doi:10.1029/2001JD001236, 2002.
- Hagan, M. E., and J. M. Forbes, Migrating and nonmigrating semidiurnal tides in the upper atmosphere excited by tropospheric latent heat release, *J. Geophys. Res.*, 108(A2), 1062, doi:10.1029/2002JA009466, 2003.
- Hagan, M. E., J. M. Forbes, and F. Vial, On modeling migrating solar tides, *Geophys. Res. Lett.*, 22, 893-896, 1995.
- Hagan, M. E., J. L. Chang, and S. K. Avery, GSWM estimates of nonmigrating tidal effects, *J. Geophys. Res.*, 102, 16,439-16452, 1997.
- Hagan, M. E., M. D. Burrage, J. M. Forbes, J. Hackney, W. J. Randel, and X. Zhang, GSWM-98: Results for migrating solar tides, *J. Geophys. Res.*, 104, 6813-6828, 1999.
- Hagan, M. E., R. G. Roble, and J. Hackney, Migrating thermospheric tides, *J. Geophys. Res.*, 106, 12,739-12,752, 2001.
- Hagan, M. E., R. G. Roble, C. Hartsough, J. Oberheide, and M. Jarisch, Dynamics of the middle atmosphere during CRISTA-2 as simulated by the National Center for Atmospheric research thermosphere-ionosphere-mesosphere-electrodynamics general circulation model, *J. Geophys. Res.*, 107(D23), 8181, doi:10.1029/2001JD000679, 2002.
- Hauchecorne, A., M. L. Chanin, and R. Wilson, Mesospheric temperature inversions and gravity wave breaking, *Geophys. Res. Lett.*, 14(9), 933-936, 1987.
- Hitchman, M. H., and C. B. Leovy, Diurnal tide in the equatorial middle atmosphere as seen in LIMS temperatures, *J. Atmos. Sci.*, 42, 557-561, 1985.
- Holton, J. R., The Dynamic Meteorology of the Stratosphere and Mesosphere, *Meteor. Monog.*, 15(37), American Meteorological Society, MA, 1975.
- Holton, J. R., The influence of gravity wave breaking on the general circulation of the middle atmosphere, *J. Atmos. Sci.*, 40, 2497-2507, 1983.
- Holton, J. R., and M. J. Alexander, The Role of Waves in the Transport Circulation of the Middle Atmosphere, *Geophys. Monograph*, 123, American Geophysical Union, 21-35, 2000.
- Horinouchi, T., S. Pawson, K. Shibata, U. Langematz, E. Manzini, M. A. Giorgetta, F. Sassi, R. J. Wilson, K. Hamilton, J. de Grandpre, and A. A. Scaife, Tropical cumulus convection and upward-propagating waves in middle-atmosphere GCMs, *J. Atmos. Sci.*, 60, 2765-2782, 2003.
- Huang, F. T., and C. A. Reber, Nonmigrating semidiurnal and diurnal tides at 95 km based on wind measurements from the High Resolution Doppler Imager on UARS, *J. Geophys. Res.*, 109, D10110, doi:10.1029/2003JD004442, 2004.

- Jarvis, M. J., Bridging the Atmospheric Divide, *Science*, 293(5538), 2218-2219, 2001.
- Johnson, R. M., and T. L. Killeen, editors, The upper mesosphere and lower thermosphere: A review of experiment and theory, *Geophys. Monograph*, 87, American Geophysical Union, 1995.
- Kato, S., T. Tsuda, and F. Watanabe, Thermal excitation of nonmigrating tides, *J. Atmos. Terr. Phys.*, 44, 131-146, 1982.
- Keating, G. M., R. H. Tolson, and M. S. Bradford, Evidence for long term global decline in the Earth's thermospheric densities apparently related to anthropogenic effects, *Geophys. Res. Lett.*, 27(10), 1523-1526, 2000.
- Khattatov, B. V., M. A. Geller, V. A. Yudin, P. B. Hays, W. R. Skinner, M. D. Burrage, S. J. Franke, D. C. Fritts, J. R. Isler, A. H. Manson, C. E. Meek, R. McMurray, W. Singer, P. Hoffmann, R. A. Vincent, Dynamics of the mesosphere and lower thermosphere as seen by MF radars and by the high-resolution Doppler imager/UARS, *J. Geophys. Res.*, 101(D6), 10,393-10,401, 1996.
- Khattatov, B. V., M. A. Geller, V. A. Yudin, and P. B. Hays, Diurnal migrating tide as seen by the high-resolution Doppler imager/UARS, 2, Monthly mean global zonal and vertical velocities, pressure, temperature, and inferred dissipation, *J. Geophys. Res.*, 102(D4), 4423-4435, 1997.
- Khosravi, R., G. Brasseur, A. Smith, D. Rusch, S. Walters, S. Chabrilat, and G. Kockarts, Response of the mesosphere to human-induced perturbations and solar variability calculated by a 2-D model, *J. Geophys. Res.*, 107(D18), 4358, doi: 10.1029/2001JD001235, 2002.
- Killeen, T. L., W. R. Skinner, R. M. Johnson, C. J. Edmonson, Q. Wu, R. J. Niciejewski, H. J. Grassl, D. A. Gell, P. E. Hansen, J. D. Harvey, and J. F. Kafkalidis, TIMED Doppler Interferometer (TIDI), *Proc. SPIE*, 3756, 289-301, 1999.
- Killeen, T. L., Q. Wu, S. C. Solomon, D. A. Ortland, W. R. Skinner, and R. J. Niciejewski, The TIMED Doppler Interferometer: Overview and Recent Results, *J. Geophys. Res.*, submitted, 2006.
- Krassovsky, V. I., N. N. Shefov, and V. I. Yarin, Atlas of the airglow spectrum 3000-12400 Å, *Planet. Space Sci.*, 9, 883-915, 1962.
- Labitzke, K., Climatology of the stratosphere and mesosphere, *Philos. Trans. Roy. Soc. London*, A296, 7-18, 1980.
- Leblanc, T., and A. Hauchecorne, Recent observations of mesospheric temperature inversions, *J. Geophys. Res.*, 102(D16), 19,471-19,482, 1997.
- Leblanc, T., A. Hauchecorne, M.-L. Chanin, C. Rodgers, F. Taylor, and N. Livesey, Mesospheric temperature inversions as seen by ISAMS in December 1991, *Geophys. Res. Lett.*, 22(12), 1485-1488, 1995.

- Leovy, C. B., C.-R. Sun, M. H. Hitchman, E. E. Remsberg, J. M. Russell III, L. L. Gordley, J. C. Gille, and L. V. Lyjak, Transport of ozone in the middle stratosphere: evidence for planetary wave breaking, *J. Atmos. Sci.*, *42*, 230-244, 1985.
- Lieberman, R. S., Nonmigrating diurnal tides in the equatorial middle atmosphere, *J. Atmos. Sci.*, *48*, 1112-1123, 1991.
- Lieberman, R. S., D. A. Ortland, E. S. Yarosh, Climatology and interannual variability of diurnal water vapor heating, *J. Geophys. Res.*, *108*(D3), 4123, 2003.
- Lieberman, R. S., J. Oberheide, M. E. Hagan, E. E. Remsberg, and L. L. Gordley, Variability of diurnal tides and planetary waves during November 1978 – May 1979, *J. Atmos. Sol. Terr. Phys.*, *66*, 517-528, 2004.
- Liu, H.-L., and M. E. Hagan, Local heating/cooling of the mesosphere due to gravity wave and tidal coupling, *Geophys. Res. Lett.*, *25*(15), 2941-2944, 1998.
- Liu, H.-L. and R. G. Roble, A study of a self-generated stratospheric sudden warming and its mesospheric-lower thermospheric impacts using the coupled TIME-GCM/CCM3, *J. Geophys. Res.*, *107*(D23), 4695, doi:10.1029/2001JD001533, 2002.
- Liu, H.-L., and R. G. Roble, Dynamical coupling of the stratosphere and mesosphere in the 2002 Southern Hemisphere major stratospheric sudden warming *Geophys. Res. Lett.*, *32*(13), L13804, doi:10.1029/2005GL022939, 2005.
- Liu, H.-L., M. E. Hagan, and R. G. Roble, Local mean state changes due to gravity wave breaking modulated by the diurnal tide, *J. Geophys. Res.*, *105*(D10), 12,381-12,296, 2000.
- Lübken, F. J., Thermal structure of the Arctic summer mesosphere, *J. Geophys. Res.*, *104*(D8), 9135-9149, 1999.
- Madden, R., and K. Labitzke, A free Rossby wave in the troposphere and stratosphere during January 1979, *J. Geophys. Res.*, *86*, 1247-1254, 1981.
- Manney, G. L., K. Krueger, J. L. Sabutis, S. A. Sena, and S. Pawson, The remarkable 2003-2004 winter and other recent warm winters in the Arctic stratosphere since the late 1990s, *J. Geophys. Res.*, *110*, D04107, doi:10.1029/2004JD005367, 2005.
- Manson, A., C. Meek, M. Hagan, C. Hall, W. Hocking, J. MacDougall, S. Franke, D. Riggin, D. Fritts, R. Vincent, and M. Burrage, Seasonal variations of the semi-diurnal and diurnal tides in the MLT: multi-year MF radar observations from 2 to 70 degrees N, and the GSWM tidal model, *J. Atmos. Sol. Terr. Phys.*, *61*(11), 809-828, 1999.
- Manson, A. H., Y. Luo, and C. Meek, Global distributions of diurnal and semi-diurnal tides: Observations from HRDI-UARS of the MLT region, *Ann. Geophys.*, *20*(11), 1877-1890, 2002.
- Manson, A. H., C. Meek, M. Hagan, X. Zhang, and Y. Luo, Global distributions of diurnal and semidiurnal tides: Observations from HRDI-UARS of the MLT region and comparison with GSWM-02 (migrating, nonmigrating components), *Ann. Geophys.*, *22*(5), 1529-1548, 2004.

- Marsh, D. R., and J. M. Russell III, A tidal explanation for the sunrise/sunset anomaly in HALOE low-latitude nitric oxide observations, *Geophys. Res. Lett.*, *27*, 3197-3200, 2000.
- McIntyre, M. E., and T. N. Palmer, The "surf zone" in the stratosphere, *J. Atmos. Terr. Phys.*, *46*, 825-849, 1984.
- McLandress, C., Seasonal variability of the diurnal tide: Results from the Canadian middle atmosphere circulation model, *J. Geophys. Res.*, *102*, 29,747-29,764, 1997.
- McLandress, C., and W. E. Ward, Tidal/gravity wave interactions and their influence on the large-scale dynamics of the middle atmosphere: Model results, *J. Geophys. Res.*, *99*(D4), 8139-8155, 1994.
- McLandress, C., W. E. Ward, V. I. Fomichev, K. Semeniuk, S. R. Beagley, N. A. McFarlane, and T. G. Shepherd, Large-Scale Dynamics of the MLT: An analysis using the extended Canadian Middle Atmosphere Model, *J. Geophys. Res.*, in press, 2006.
- Meriwether, J. W., and M. G. Mlynczak, Is chemical heating a major cause of the mesosphere inversion layer?, *J. Geophys. Res.*, *100*, 1379-1387, 1995.
- Meriwether, J. W., and C. S. Gardner, A review of mesospheric inversion layer phenomena, *J. Geophys. Res.*, *105*, 12,405-12,416, 2000.
- Meriwether, J. W., P. D. Dao, R. T. McNutt, W. Klemetti, W. Moskowitz, and G. Davidson, Rayleigh lidar observations of mesospheric temperature structure, *J. Geophys. Res.*, *99*, 16,973-16,987, 1994.
- Mertens, C. J., and 11 co-authors, SABER observations of mesospheric temperatures and comparisons with falling sphere measurements taken during the 2002 summer MacWAVE campaign, *Geophys. Res. Lett.*, *31*, L03105, doi:10.1029/2003GL018605, 2004.
- Mies, F. H., Calculated vibrational transition probabilities of OH(X<sup>2</sup>Π), *J. Mol. Spectros.*, *53*, 150-188, 1974.
- Miyahara, S., D. Yamamoto, and Y. Miyoshi, On the Geostrophic Balance of Mean Zonal Winds in the Mesosphere and Lower Thermosphere, *J. Meteor. Soc. Japan*, *78*(5), 683-688, 2000.
- Mlynczak, M. G., Energetics of the mesosphere and lower thermosphere and the SABER experiment, *Adv. Space Res.*, *20*, 1177-1183, 1997.
- Murphy, D. J., M. Tsutsumi, D. M. Riggin, G. O. L. Jones, R. A. Vincent, M. E. Hagan, and S. K. Avery, Observations of a nonmigrating component of the semidiurnal tide over Antarctica, *J. Geophys. Res.*, *108*(D8), 4241, doi:10.1029/2002JD003077, 2003.
- Naujokat, B., K. Labitzke, R. Lenschow, B. Rajewski, M. Wiesner, and R.-C. Wohlfahrt, The stratospheric winter 1994/95: A cold winter with a strong minor warming, *Beilage Berliner Wetterkarte*, *SO 24/95*, 1995.

- Oberheide, J., and O. A. Gusev, Observation of migrating and nonmigrating diurnal tides in the tropical middle atmosphere, *Geophys. Res. Lett.*, 29(24), 2167, doi:10.1029/2002GL016213, 2002.
- Oberheide, J., M. E. Hagan, W. E. Ward, M. Riese, and D. Offermann, Modeling the diurnal tide for the Cryogenic Infrared Spectrometers and Telescopes for the Atmosphere (CRISTA) 1 time period, *J. Geophys. Res.*, 105(A11), 24,917-24,929, 2000.
- Oberheide, J., G. A. Lehmacher, D. Offermann, K. U. Grossmann, A. H. Manson, C. E. Meek, F. J. Schmidlin, W. Singer, P. Hoffmann, and R. A. Vincent, Geostrophic wind fields in the stratosphere and mesosphere from satellite data, *J. Geophys. Res.*, 107(D23), doi:10.1029/2001JD000655, 2002a.
- Oberheide, J., M. E. Hagan, R. G. Roble, and D. Offermann, The sources of nonmigrating tides in the tropical middle atmosphere, *J. Geophys. Res.*, 107(D21), 4567, doi: 10.1029/2002JD002220, 2002b.
- Oberheide J., M. E. Hagan, R. G. Roble, and O. A. Gusev, A global view of tidal temperature perturbations above the mesopause: Preliminary model/observation intercomparison, *Adv. Space Res.*, 32(5), 857-862, 2003a.
- Oberheide, J., M. E. Hagan, and R. G. Roble, Tidal signatures and aliasing in temperature data from slowly precessing satellites, *J. Geophys. Res.*, 108(A2), 1055, doi:10.1029/2002JA009585, 2003b.
- Oberheide, J., Q. Wu, D. A. Ortland, T. L. Killeen, M. E. Hagan, R. G. Roble, R. J. Niciejewski, and W. R. Skinner, Non-migrating diurnal tides as measured by the TIMED Doppler interferometer: Preliminary results, *Adv. Space Res.*, 35, 1911-1917, doi:10.1016/j.asr.2005.01.063, 2005.
- Oberheide, J., H.-L. Liu, O. A. Gusev, and D. Offermann, Mesospheric surf zone and temperature inversion layers in early November 1994, *J. Atmos. Sol. Terr. Phys.*, in press, doi:10.1016/j.jastp.2005.11.013, 2006a.
- Oberheide, J., Q. Wu, T. L. Killeen, M. E. Hagan, and R. G. Roble, Diurnal nonmigrating tides from TIDI wind data: Monthly climatologies and seasonal variations, *J. Geophys. Res.*, in press, doi:10.1029/2005JA011491, 2006b.
- Oberheide, J., D. Offermann, J. M. Russell III, and M. G. Mlynczak, Intercomparison of kinetic temperature from 15  $\mu\text{m}$  CO<sub>2</sub> limb emissions and OH\*(3,1) rotational temperature in nearly coincident air masses: SABER, GRIPS, *Geophys. Res. Lett.*, 33, L14811, doi:10.1029/2006GL026439, 2006c.
- Offermann, D., R. Gerndt, G. Lange, and H. Trinks, Variations of mesopause temperatures in Europe, *Adv. Space Res.*, 3, 21-23, 1983.
- Offermann, D., K.-U. Grossmann, P. Barthol, P. Knieling, M. Riese, and R. Trant, Cryogenic Infrared Spectrometers and Telescopes for the Atmosphere (CRISTA) experiment and middle atmosphere variability, *J. Geophys. Res.*, 104(D13), 16,311-16,325, 1999.

- Offermann, D., M. Donner, P. Knieling, and B. Naujokat, Middle atmosphere temperature changes and the duration of summer, *J. Atmos. Sol. Terr. Phys.*, *66*, 437-450, 2004.
- Offermann, D., M. Jarisch, J. Oberheide, O. Gusev, I. Wohltmann, J. M. Russell III, and M. G. Mlynczak, Global wave activity from upper stratosphere to lower thermosphere: A new turbopause concept, *J. Atmos. Sol. Terr. Phys.*, in press, doi:10.1016/j.jastp.2006.01.13, 2006a.
- Offermann, D., M. Jarisch, M. Donner, W. Steinbrecht, and A. I. Semenov, OH Temperature Re-Analysis Forced by Recent Variance Increases, *J. Atmos. Sol. Terr. Phys.*, in press, doi:10.1016/j.jastp.2006.03.007, 2006b.
- Pendleton Jr., W. R., P. J. Espy, and M. R. Hammond, Evidence of non-local-thermodynamical-equilibrium rotation in the OH airglow, *J. Geophys. Res.*, *98*, 11,567-11,579, 1993.
- Preusse, P., S. D. Eckermann, J. Oberheide, M. E. Hagan, and D. Offermann, Modulation of gravity waves by tides as seen in CRISTA temperatures, *Adv. Space Res.*, *27*(10), 1773-1778, 2001.
- Preusse, P., M. Ern, S. D. Eckermann, C. D. Warner, R. H. Picard, P. Knieling, M. Krebsbach, J. M. Russell III, M. G. Mlynczak, C. J. Mertens, and M. Riese, Tropopause to mesopause gravity waves in August: measurement and modeling, *J. Atmos. Sol. Terr. Phys.*, in press, 2006.
- Remsberg, E. E., L. L. Gordley, B. T. Marshall, R. E. Thompson, J. Burton, P. Bhatt, V. L. Harvey, G. S. Lingenfelter, and M. Natarajan, The Nimbus 7 LIMS Version 6 radiance conditioning and temperature retrieval methods and results, *J. Quant. Spectros. Rad. Transf.*, *86*(4), 395-424, doi:10.1016/j.jqsrt.2003.12.007, 2004.
- Richmond, A. D., Assimilative mapping of ionospheric electrodynamics, *Adv. Space Res.*, *12*(6), 59-68, 1992.
- Richmond, A. D., E. C. Ridley, and R. G. Roble, A thermosphere/ionosphere general circulation model with coupled electrodynamics, *Geophys. Res. Lett.*, *19*, 601-604, 1992.
- Riese, M., R. Spang, P. Preusse, M. Ern, M. Jarisch, D. Offermann, and K. U. Grossmann, Cryogenic Infrared Spectrometers and Telescopes for the Atmosphere (CRISTA) data processing and atmospheric temperature and trace gas retrieval, *J. Geophys. Res.*, *104*(D13), 16,439-16,367, 1999.
- Riese, M., G. L. Manney, J. Oberheide, X. Tie, R. Spang, and V. Küll, Stratospheric transport by planetary wave mixing as observed during CRISTA-2, *J. Geophys. Res.*, *107*(D23), 8179, doi:10.1029/2001JD000629, 2002.
- Roble, R. G., The NCAR Thermosphere-Ionosphere-Mesosphere-Electrodynamics General Circulation Model (TIME-GCM), Ionosphere Models, in *STEP Handbook of Ionospheric Models*, edited by R. W. Schunk, 281-288, Utah State Univ., Logan, 1996.

- Roble, R. G., and E. C. Ridley, A thermosphere-ionosphere-mesosphere-electrodynamics general circulation model (TIME-GCM): Equinox solar cycle minimum simulations (30-500 km), *Geophys. Res. Lett.*, *21*, 417-420, 1994.
- Roble, R. G., E. C. Ridley, A. D. Richmond, and R. E. Dickinson, A coupled thermosphere/ionosphere general circulation model, *Geophys. Res. Lett.*, *15*, 1325-1328, 1988.
- Salby, M. L., Sampling theory for asymptotic satellite observations. I, Space-time spectra, resolution, and aliasing, *J. Atmos. Sci.*, *39*, 2577-2600, 1982.
- Salby, M., F. Sassi, P. Callaghan, D. Wu, P. Keckhut, and A. Hauchecorne, Mesospheric inversions and their relationship to planetary wave structure, *J. Geophys. Res.*, *107*(D4), 4041, doi:10.1029/2001JD000756, 2002.
- Sassi, F., R. R. Garcia, B. A. Boville, and H. Liu, On temperature inversions and the mesospheric surf zone, *J. Geophys. Res.*, *107*(D19), 4380, doi:10.1029/2001JD001525, 2002.
- Scheer, J., E. R. Reisin, O. A. Gusev, W. J. R. French, G. Hernandez, R. Huppi, P. Ammosov, G. A. Gavrilyeva, and D. Offermann, Use of CRISTA mesopause region temperatures for the intercalibration of ground-based instruments, *J. Atmos. Sol. Terr. Phys.*, in press, 2006.
- Schmidlin, F. J., Temperature inversions near 75 km, *Geophys. Res. Lett.*, *3*(3), 173-176, 1976.
- Scott, R. K., and P. H. Haynes, The Seasonal Cycle of Planetary Waves in the Winter Stratosphere, *J. Atmos. Sci.*, *59*, 803-822, 2002.
- She, C. Y., and U. von Zahn, Concept of a two-level mesopause: Support through new lidar observations, *J. Geophys. Res.*, *103*, 5855-5863, 1998.
- She, C. Y., and R. P. Lowe, Seasonal temperature variations in the mesopause region at mid-latitudes: Comparison of lidar and hydroxyl rotational temperatures using WINDII/UARS OH height profiles, *J. Atmos. Sol. Terr. Phys.*, *60*(16), 1573-1583, 1998.
- She, C. Y., Initial full-diurnal-cycle mesopause region lidar observations: Diurnal-means and tidal perturbations of temperature and winds over Fort Collins, CO (41°N, 105°W), *J. Atmos. Sol. Terr. Phys.*, *66*(6-9), 663-674, 2004.
- Shepherd, M. G., W. E. Ward, B. Prawirosoehardjo, R. G. Roble, S. P. Zhang, and D. Y. Wang, Planetary scale and tidal perturbations in mesospheric temperatures observed by WINDII, *Earth, Planets and Space*, *51*(7-8), 593-610, 1999.
- Shepherd, G. G., M. E. Hagan, and Y. Portnyagin, editors, Special Issue: PSMOS 2000 Workshop - Planetary Scale Mesopause Observing System, *J. Atmos. Sol. Terr. Phys.*, *64*(8-11), 873-1307, 2002.

- Shepherd, M. G., Y. J. Rochon, D. Offermann, M. Donner, and P. J. Espy, Longitudinal variability of mesospheric temperatures during equinox at middle and high latitudes, *J. Atmos. Sol. Terr. Phys.*, *66*(6-9), 463-479, 2004.
- Siskind, D. E., S. D. Eckermann, and M. E. Summers, editors, Atmospheric science across the stratopause, *Geophys. Monograph*, *123*, American Geophysical Union, 2000.
- Siskind, D. E., L. Coy, and P. Espy, Observations of stratospheric warmings and mesospheric coolings by the TIMED SABER instrument, *Geophys. Res. Lett.*, *32*(9), L09804, doi:10.1029/2005GL022399, 2005..
- Sivjee, G. G., and R. M. Hamwey, Temperature and chemistry of the polar mesopause OH, *J. Geophys. Res.*, *92*, 4663-4672, 1987.
- Skinner, W. R., and 11 co-authors, Operational Performance of the TIMED Doppler Interferometer (TIDI), *Proc. SPIE*, *5157*, 47-57, 2003.
- Smith, A. K., Wave transience and wave-mean flow interaction caused by the interference of stationary and traveling waves, *J. Atmos. Sci.*, *42*, 529-535, 1985.
- Smith, A. K., The Origin of Stationary Planetary Waves in the Upper Mesosphere, *J. Atmos. Sci.*, *60*, 3033-3041, 2003.
- Smith, A. K., D. R. Marsh, A. C. Szymczak, Interaction of chemical heating and the diurnal tide in the mesosphere, *J. Geophys. Res.*, *108*(D5), 4164, doi:10.1029/2002-JD002664, 2003.
- Song, P., H. J. Singer, and G. L. Siscoe, editors, Space Weather, *Geophys. Monograph*, *125*, American Geophysical Union, 2001.
- Swinbank, R., and A. O'Neill, A stratosphere-troposphere data assimilation system, *Mon. Weather Rev.*, *122*(4), 686-702, 1994.
- Takahashi, H., G. G. Shepherd, M. E. Hagan, and P. P. Batista, editors, Special Issue: Dynamics and Chemistry of the MLT Region - PSMOS 2002 International Symposium, *J. Atmos. Sol. Terr. Phys.*, *66*(6-9), 425-804, 2004.
- Talaat, E. R., and R. S. Lieberman, Nonmigrating diurnal tides in mesospheric and lower-thermospheric winds and temperatures, *J. Atmos. Sci.*, *56*, 4073-4087, 1999.
- Tsuda, T., and S. Kato, Diurnal non-migrating tides excited by a differential heating due to land-sea distribution, *J. Meteor. Soc. Japan*, *67*, 43-54, 1989.
- Tsuda, T., K. Ohnishi, F. Isoda, T. Nakamura, R. A. Vincent, I. M. Reid, S. W. B. Harijono, T. Sribimawati, A. Nurzanto, and H. Wiryosumarto, Coordinated radar observations of atmospheric diurnal tides in equatorial regions, *Earth, Planets and Space*, *51*, 579-592, 1999.
- Vial, F., and J. M. Forbes, Recent progress in tidal modelling, *J. Atmos. Terr. Phys.*, *51*, 663-671, 1989.

- von Savigny, C., K. U. Eichmann, E. J. Llewellyn, H. Bovensmann, J. P. Burrows, M. Bittner, K. Hoepfner, D. Offermann, M. J. Taylor, Y. Zhao, W. Steinbrecht, and P. Winkler, First near-global retrieval of OH rotational temperatures from satellite-based Meinel band emission measurements, *Geophys. Res. Lett.*, *31*, L15111, doi:10.1029/2004GL020410, 2004.
- von Zahn, U., and W. Meyer, Mesopause temperatures in polar summer, *J. Geophys. Res.*, *94*, 14,647-14,651, 1989.
- von Zahn, U., K. H. Fricke, R. Gerndt, and T. Blix, Mesospheric temperatures and the OH layer height as derived from ground-based lidar and OH\* spectrometry, *J. Atmos. Sol. Terr. Phys.*, *49*(7/8), 863-869, 1987.
- von Zahn, U., J. Hoeffner, V. Eska, and M. Alpers, The mesopause altitude: Only two distinctive levels worldwide?, *Geophys. Res. Lett.*, *23*, 3231-3234, 1996.
- Ward, W. E., A simple model of diurnal variations in the mesospheric oxygen night-glow, *Geophys. Res. Lett.*, *26*, 3565-3568, 1999.
- Ward, W. E., J. Oberheide, M. Riese, P. Preusse, and D. Offermann, Tidal signatures in temperature data from CRISTA 1 mission, *J. Geophys. Res.*, *104*(D13), 16,391-16,403, 1999.
- Ward, W. E., V. I. Fomichev, and S. Beagley, Nonmigrating tides in equinox temperature fields from the Extended Canadian Middle Atmosphere Model (CMAM), *Geophys. Res. Lett.*, *32*(3), L03803, doi:10.1029/2004GL021466, 2005.
- Waugh, D. W., R. A. Plumb, R. J. Atkinson, M. R. Schoeberl, L. R. Lait, P. A. Newman, M. Loewenstein, D. W. Toohey, L. M. Avallone, C. R. Webster, and R. D. May, Transport out of the lower stratospheric Arctic vortex by Rossby wave breaking, *J. Geophys. Res.*, *99*, 1071-1088, 1994.
- Whiteway, J. A., A. I. Carswell, and W. E. Ward, Mesospheric temperature inversions with overlaying nearly adiabatic lapse rate: An indication of a well-mixed turbulent layer, *Geophys. Res. Lett.*, *22*(10), 1201-1204, 1995.
- Wu, D. L., Mesospheric temperature inversion layers: Recent observations from UARS ISAMS and MLS, *Recent Res. Devel. Geophys.*, *3*, 37-44, 2000.
- Wu, D. L., C. McLandress, E. F. Fishbein, W. G. Read, J. W. Waters, and L. Froidevaux, Equatorial diurnal variations observed in UARS MLS temperature during 1991-1994 and simulated by the CMAM, *J. Geophys. Res.*, *103*, 8909-8917, 1998.
- Wu, Q., T. L. Killeen, S. Nozawa, D. McEwen, W. Guo, S. C. Solomon, Observations of mesospheric neutral wind 12-hour wave in the Northern Polar Cap, *J. Atmos. Sol. Terr. Phys.*, *65*(8), 971-978, 2003.
- Zhang, G. J., and N. A. McFarlane, Sensitivity of climate simulations to the parameterization of cumulus convection in the Canadian Climate Center General Circulation Model, *Atmos.-Ocean*, *33*, 407-446, 1995.

- Zhang, S. P. P., and G. G. Shepherd, Variations of the mean winds and diurnal tides in the mesosphere and lower thermosphere observed by WINDII from 1992 to 1996, *Geophys. Res. Lett.*, *32*(14), L14111, 2005.
- Zhang, S. P. P., R. G. Roble, and G. G. Shepherd, Tidal influence on the oxygen and hydroxyl nightglows: Wind Imaging Interferometer observations and thermosphere-ionosphere-mesosphere-electrodynamics general circulation model, *J. Geophys. Res.*, *106*, 21,381-21,393, 2001.
- Zhao, Y., M. J. Taylor, and X. Chu, Comparison of simultaneous Na lidar and mesospheric nightglow temperature measurements and the effects of tides on the emission layer heights, *J. Geophys. Res.*, *110*, D09S07, doi:10.1029/2004JD005115, 2005.